Spring 5-18-2012

An Investigation of Mist/Air Film Cooling with Application to Gas Turbine Airfoils

lei zhao
lzhao@uno.edu

An Investigation of Mist/Air Film Cooling with Application to Gas Turbine Airfoils

A Dissertation

Submitted to the Graduate Faculty of the
University of New Orleans
in partial fulfillment of the
requirements for the degree of

Doctor of Philosophy
in
Engineering and Applied Science
Mechanical Engineering

by

Lei Zhao

B.S. University of Science and Technology of China, Hefei, China, 2005
M.S. University of New Orleans, New Orleans, LA, 2008

May, 2012

DEDICATION

To my lovely wife: 黄婉

ACKNOWLEDGEMENT

First of all, I would like to show my thankfulness to my advisor Dr. Ting Wang for the opportunity to work with him through this interesting project. It was a long journey but full of memorable moments. His patience with me, thoughtful guidance for my academic development and wise suggestions for my career will always be deeply appreciated.

I would like to thank Dr. Kazim Akyuzlu, Dr. Martin Guillot, Dr. Carsie Hall and Dr. Dongming Wei for serving on my committee.

Acknowledgements are also due to the Department of Energy and the Louisiana Board of Regents for their financial support. The award and funding from the ASME, International Gas Turbine Institute to support me to present my works in TurboExpo 2011 (Vancouver, Canada) is appreciated.

I am also thankful to my colleagues from the Energy Conversion and Conservation Center for helping me during my Ph.D. study. Jason Kent worked with me to build my preliminary test section. His "suction box" is used in the final test section and the laser movie works great. "Damon" Phuc Luong helped me to build my second test section and the heating unit. We went through an intense "summer lab camp" to put together most part of the second test section. Many discussions with Dr. Armin Silaen, Dr. Jobaidur Khan, Dr. Thirumalisai Dhanasekaran and many others are beneficial for my study and I am thankful for all of that.

Finally, I thank my family for their unconditional love and support. I can never thank them enough for that. They have been the backbone of my world.

TABLE OF CONTENTS

ABSTRACT

Film cooling is a cooling technique widely used in high-performance gas turbines to protect the turbine airfoils from being damaged by hot flue gases. Film injection holes are placed in the body of the airfoil to allow coolant to pass from the internal cavity to the external surface. The injection of coolant gas results in a layer or "film" of coolant gas flowing along the external surface of the airfoil.

In this study, a new cooling scheme, mist/air film cooling is investigated through experiments. A small amount of tiny water droplets with an average diameter about 7 μm (mist) is injected into the cooling air to enhance the cooling performance. A wind tunnel system and test facilities are built. A Phase Doppler Particle Analyzer (PDPA) system is employed to measure droplet size, velocity, and turbulence. Infrared camera and thermocouples are both used for temperature measurements.

Mist film cooling performance is evaluated and compared against air-only film cooling in terms of adiabatic film cooling effectiveness and film coverage. Experimental results show that for the blowing ratio M = 0.6, net enhancement in adiabatic cooling effectiveness can reach 190% locally and 128% overall along the centerline. The general pattern of adiabatic cooling effectiveness distribution of the mist case is similar to that of the air-only case with the peak at about the same location.

The concept of Film Decay Length (FDL) is proposed to quantitatively evaluate how well the coolant film covers the blade surface. Application of mist in the M = 0.6 condition is apparently superior to the M = 1.0 and 1.4 cases due to the higher overall cooling enhancement, the much longer FDL, and the wider and longer film cooling coverage area.

Based on the droplet measurements made through PDPA, a profile describing how the air-mist coolant jet flow spreads and eventually blends into the hot main flow is proposed. A sketch based on the proposed profile is provided. This profile is found to be well supported by the measurement results of the turbulent Reynolds stresses. The location where a higher magnitude of turbulent Reynolds stresses exist, which indicates a higher strength of the turbulent mixing effect, is found to be close to the edge of the coolant film envelope. Also, the separation between the mist droplet layer and the coolant air film is identified through the measurements: large droplets penetrate through the air coolant film layer and travel further into the main flow.

Based on the proposed air-mist film profile, the heat transfer results are re-examined. It is found that the location of optimum cooling effect is coincident with the point where the air-mist coolant starts to bend back towards the surface. Thus, the data suggests that the "bending back" film pattern is critical in keeping the mist droplets close to the surface, which improves the cooling effectiveness for mist cooling.

Key words: Gas Turbine, Heat Transfer, Film Cooling, Mist Cooling, Experimental Study, Droplet, Reynolds Stress, Film Decay Length, Phase Doppler Particle Analyzer

CHAPTER ONE
INTRODUCTION

In this chapter, the background information of gas turbine systems will be provided first, and the cooling technologies for turbine blades will then be introduced. After a broad introduction of different cooling technologies, the discussion will be focused on film cooling and mist cooling. The objectives and the specific tasks to be performed will be introduced at the end of this chapter.

1.1 Gas Turbine System

A gas turbine engine is essentially an energy conversion device that converts the energy in the fuel to useful mechanical energy in the form of rotational shaft power, compressed air, thrust, or any combination of these. Gas turbine engines are used to power aircraft, ships, power plant generators, tanks, etc. The term "gas" refers to the ambient air that is used as the working medium in the energy conversion process. Air is drawn into the compressor, mixed with fuel, and ignited in the combustor. The resulting hot gas from combustion is then directed into the turbine section. The energy is extracted through the hot gas expansion process at high velocity spinning the turbine airfoil which transforms the energy into output shaft power. The energy extracted in the turbine comes from the reduction in the temperature and pressure of the combustion gas. The residual thermal energy in the hot exhaust gas can be harnessed for a variety of industrial processes.

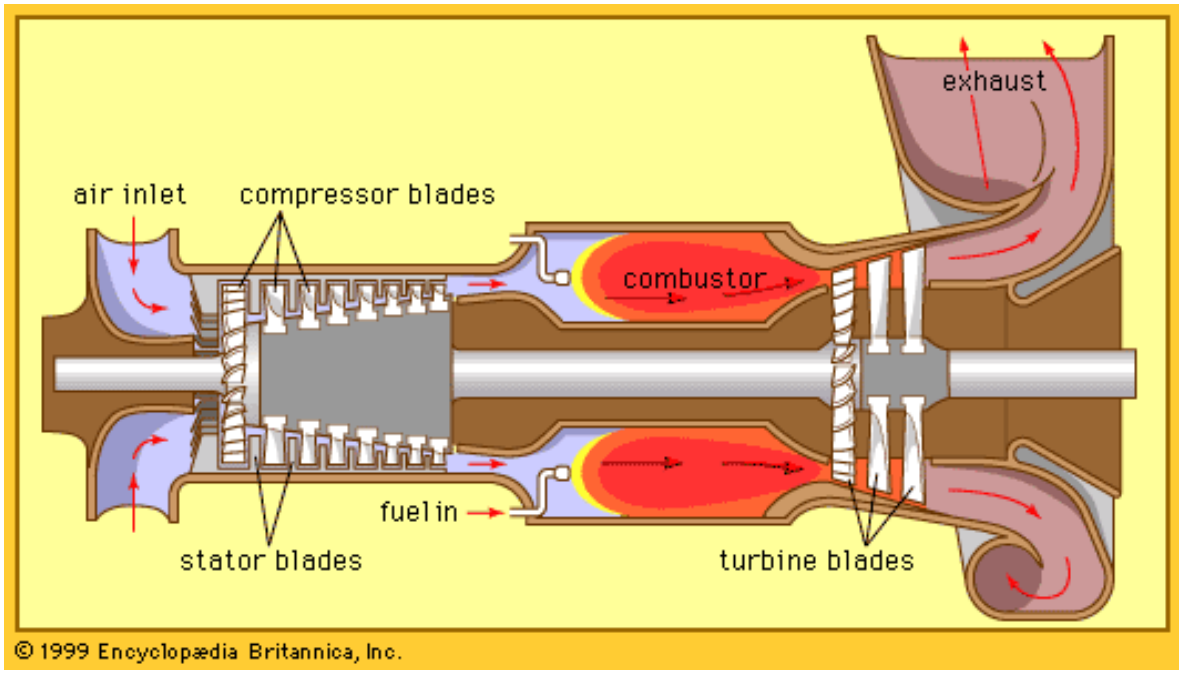

Figure 1.1 Schematic of a gas turbine (Source: Encyclopedia Britannica, Inc)

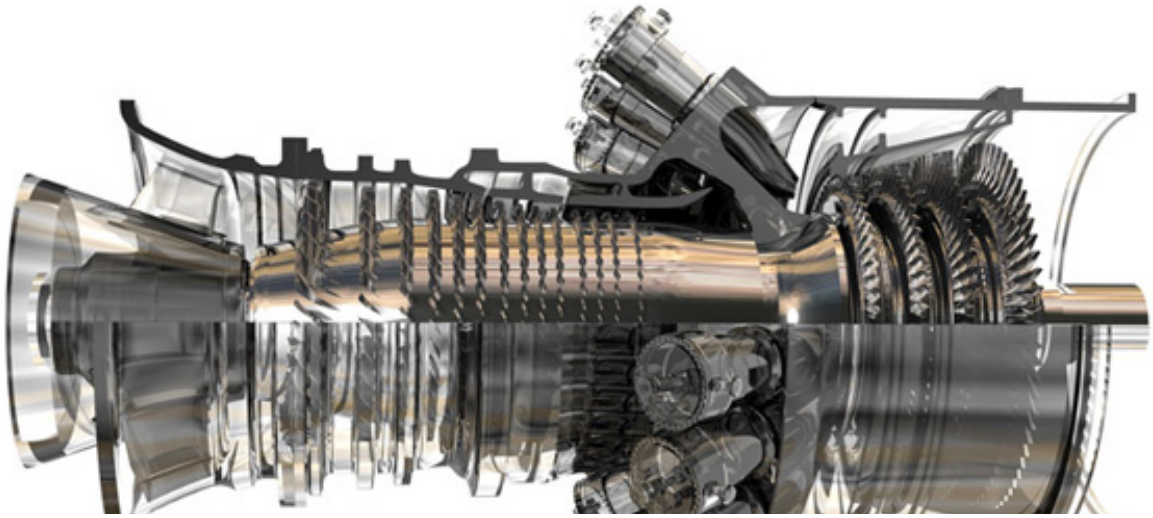

Figure 1.2 GE 9FB heavy duty gas turbine (source: GE energy)

Efficiency is one of the most important parameters in evaluating the performance of a gas turbine engine. With even a 1% efficiency increase, the operating costs can be substantially

reduced over the life of a typical power plant. GE estimates savings of $2 million per year over today's most efficient (57%-58%) combined-cycle plants (Power Technology, 2007). One of the most effective ways to improve the gas turbine system efficiency is to increase the turbine inlet temperature (TIT). A higher TIT leads to better system thermodynamic efficiency and, thus, is favorable. However, TIT is limited by the highest temperature that the material of the turbine blade can withstand. Therefore, technologies are needed to maintain the main flue gas hot while keeping the airfoil relatively cool.

Different approaches have been taken in the effort to increase TIT. One perspective is to enhance the material's ability to sustain higher temperatures. One example is the technology of single-crystal fabrication, which eliminates grain boundaries in the alloy and improves thermal fatigue and creep characteristics of the material. However, manufacturing of single-crystal airfoils is expensive and difficult and was previously limited to the first-stage vanes and blades of few models of GTs. Another approach is to find ways to protect the blade from the hot main flue gases. One effective way is to have a ceramic Thermal Barrier Coating (TBC) topcoat providing thermal resistance and a metal bond coat that provides oxidation resistance while bonding the topcoat to the substrate.

Another essential approach, which is the focus of this research, is using various cooling schemes to protect the turbine airfoils from the hot main flue gas.

1.2 Turbine Blade Cooling Technologies

The cooling technologies for turbine blades can be grouped in many ways, for example by the cooling medium--air, steam, water, mist cooling-- or by the location of the cooling--internal cooling or external cooling. Since a large number of technical or review papers associated with turbine blade cooling can be found in the open literature, only a general review and remarks for each cooling technology will be given, and then the discussion will be focused on the film cooling and mist cooling technologies.

Film Cooling

Film cooling is one of the earliest cooling technologies ever developed and is widely used in different types of turbine engines. It uses the compressed air extracted from certain

compressor stages as the coolant. Film injection holes are placed in the body of the airfoil to allow coolant to pass from the internal cavity to the external surface. The ejection of coolant gas results in a layer or "film" of coolant gas flowing along the external surface of the airfoil. Hence, the term "film cooling" is used to describe this cooling scheme.

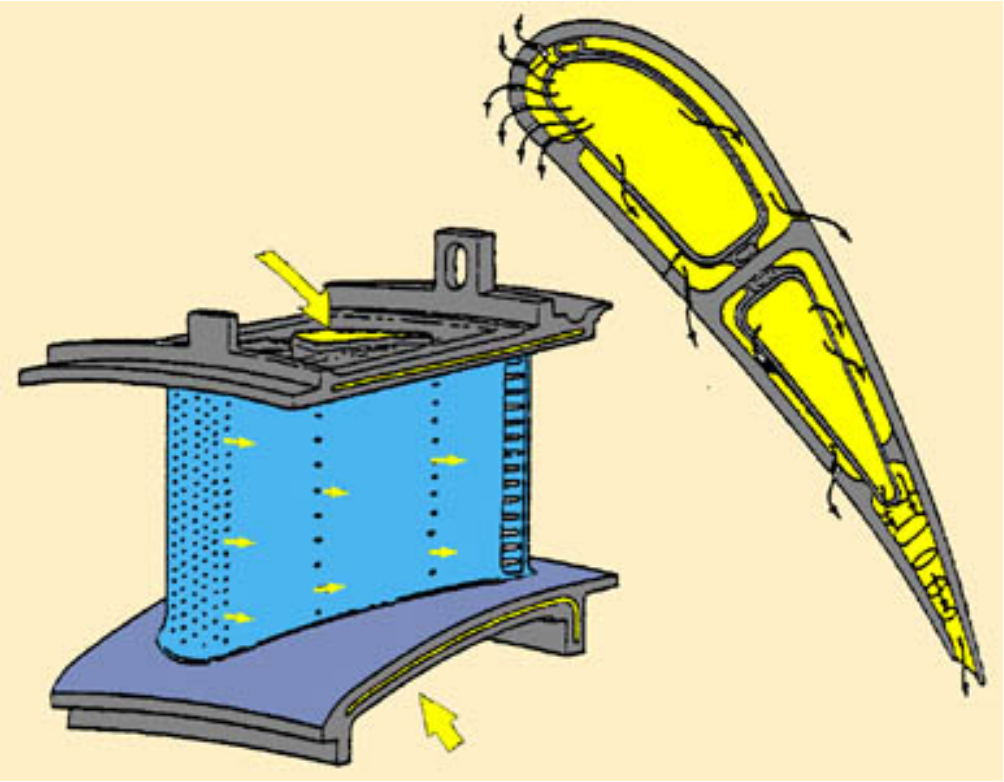

Figure 1.3 Schematic of film cooling (Source: DOE Gas Turbine Handbook, 2006)

Film cooling is a mature technology and various reliable design methodologies have already been developed and are continuously being improved. Some general comments for film cooling are the following:

- Compressed air used in film cooling essentially consumes a significant amount of the useful work generated by the turbine (to drive the compressor).
- For higher TIT, a large amount of compressed air is required. It is estimated that, under the Advanced Turbine System condition where TIT is over 1400 ^{o}C, over 35% of the overall compressor air will be used to cool the hot path components (Wenglarz, et al., 1994).

- When film cooling consumes a large amount of compressed air, less air enters the combustor and less hot gas is produced; as a result, the total power output is reduced.
- Since the cooling air must pass through roughened small internal cooling passages before it is ejected into main flow, the coolant needs to have a much higher pressure than the main flow to overcome the pressure lost. This essentially consumes an additional power to pressurize the coolant air.
- Film cooling has adverse effects on the cycle efficiency of the gas turbine system because, as the coolant jet interferes with the main flow field, it causes aerodynamic and thermal losses due to jet mixing and reduction of main flue gas's temperature (Little, et al., 1993; Bannister, et al., 1994).
- Film cooling induces unfavorable increase of local heat transfer on the blade due to strong mixing between film jet and main flow.
- Severe film cooling makes it very difficult to increase the gas turbine TIT to above 1400 ^{o}C. The highest possible temperature in a turbine system is the flame temperature in the combustor, which must be kept under 1500~1600 ^{o}C (2700~2900 ^{o}F) to maintain low NO_x emissions (Cook, 1993 and Farmer and Fulton, 1995). Due to the thermal mixing effects of film cooling, the gas turbine inlet temperature is always several hundred degrees lower than the flame temperature. As a result TIT is limited by this temperature drop between the flame temperature and TIT due to film cooling.
- Air coolant film blends into the main flow quickly; as a result, air film cooling is only effective for a short range. Consequently, in order to cover the entire blade surface, many rows of film holes are needed, which are detrimental to the blade integrity and mechanical strength.

Transpiration cooling

Transpiration cooling is similar to film cooling in that it creates a thin film of cooling air on the blade, but it is different in that the air passes through a porous wall rather than through injection holes to form the film. Transpiration-cooled blades generally consist of a rigid strut with a porous shell. Air flows through internal channels of the strut and then passes through the

porous shell to cool the blade (Flank, 2005, Boyce, 2006). One example of the porous wall structure for transpiration cooling is through sintered stainless steel walls, which usually have a pore diameter ranging between 10 and 50 μm and a wall thickness of about 1 mm.

The advantage of transpiration cooling is that the coolant coverage on the blade is more uniform than that of the discrete film cooling. Also, as the air passes through the porous wall, additional cooling effect is achieved within the blade. Thus, compared with film cooling under the same turbine operation conditions, less compressed air may be needed to achieve the same cooling effectiveness; and consequently more turbine output power can be generated.

Transpiration cooling has similar problems to film cooling--i.e., aerodynamics and thermal losses due to mixing effect between coolant and the hot main flow and extra power needed to pressurize the coolant to pass through the small passages. Moreover, the structural integrity of the porous wall under the thermal and mechanical stresses is a concern, especially when dealing with high temperatures, high pressures, and fast rotational speeds in a turbine engine. Another concern is the easy blockage of the porosity by air-borne impurities.

Effusion Cooling

If the number of holes increases considerably, the film cooling system is called an effusion cooling system. A number of studies [Andrew et al., 1985, Thole et al., 2006, Arcangeli et al., 2006] analyze the performance of such systems with hole diameters ranging between 640 and 8820 μm. One manufacturable effusion wall structure example is Poroform, which allows for manufactured components to have walls equipped with micro holes obtained by galvanic electroforming techniques (Battisti, 2002). Again, as in transpiration cooling, the mechanical strength and hole blockage are major concerns.

Water (Liquid) Cooling

Water cooling has an apparent advantage over film/air cooling, since water is a much better coolant than air. The specific heat of water is about four times larger than air, and its heat transfer coefficient is ten times higher. Most previous water cooling studies were focused on the internal convection cooling of the turbine blade, though some studies investigated the possibility of using external water spray cooling. However, all the previous work encountered some of the following problems (Bayley and Martin, 1971; Alff, et al., 1978; Johnson, 1978; Van Fossen and

Stepka, 1979):

- Severe corrosion in the gas turbine flow path due to water evaporation.
- Coolant flow instability and its induced vibration due to boiling phenomenon.
- Non-uniform blade overcooling.
- Coolant passage clogging.
- Unreliable coolant transporting and distributing system for the rotating blades.

Steam Cooling

Water vapor is used as the coolant medium in the steam cooling scheme, which was first proposed by Mukherjee and patented by BBC (Mukherjee, 1984). One example of the steam cooling application in industrial gas turbine is the GE "H" type combined cycle gas turbine system, in which internal steam cooling is employed to cool the first two turbine stages. Another example is the G-type industrial gas turbines manufactured by Siemens and Mitsubishi. The closed-loop steam cooling system is used for transition-piece and first-stage vane cooling. In a combined cycle turbine system, steam is readily available, and the energy of the returning coolant steam can be reused in the bottom steam cycle. Therefore, in the case of the combined cycle, the heat transfer performance of steam can be improved by increasing the steam flow rate without concern about bleeding valuable compressed air (Kirillov and Arsen'ev, 1986; Arsen'ev, et al., 1990).

The major advantage of the steam cooling scheme is that internal steam cooling alone can be sufficient for the necessary cooling load. In other words, film cooling is unnecessary because the heat transfer performance of the steam is greatly enhanced under a very high steam Reynolds number. This will greatly reduce the aerodynamics and thermal losses associated with the external film cooling.

Another advantage of using closed-loop steam cooling is that, without using film cooling, the turbine inlet temperature can be potentially increased much closer to the combustion flame temperature than it can be when using the film cooling scheme. As discussed before, open-loop film cooling reduces the fire temperature by hundreds of degrees; however, the difference between the flame temperature and TIT can be significantly reduced to be less than 100^{o}F. By eliminating external cooling, the TIT can be increased without elevating the flame temperature,

and NO_x emissions can be more readily controlled. (The fire temperature is not the same as TIT, so it must be used with caution.)

The disadvantage of steam cooling is that it is only economically applicable in systems where steam is readily available. Consequently, it limits the use of steam cooling to only large turbine systems--typically in combined cycles. Another problem with the steam cooling is that a very large quantity of steam--80 ~ 100% of all the steam in the bottom cycle--is needed (Mukherjee, 1984; Wenglarz, et al., 1994; Wang, et al., 1995).

Mist/Steam Cooling

Mist/Steam cooling, proposed by Guo and Wang (2000), utilized the mixture of steam and mist as the coolant medium, which cools the turbine blade internally. The steam-water mixture is generated by injecting very fine water droplets (5~30 μm) into the stream drawn from the bottom cycle in a plenum that is located outside the cooled gas turbine.

This cooling scheme has the following advantages:

- Compared with open loop film cooling, mist/steam cooling has all the advantages of the closed-loop steam cooling scheme.
- Compared with steam cooling, mist/steam cooling has a higher effective heat transfer coefficient than the single phase steam. Consequently, steam consumption can be reduced, and the power output of the bottom steam turbine will be increased accordingly. More about the benefits of mist cooling will be elaborated later.
- Compared with the water cooling application, mist/steam cooling can be applied in a well controlled manner to ensure that the cooling channel will not be flooded by the water droplets and that no severe over-cooled spots will occur. As a result, problems associated with liquid-water cooling such as overcooling, flow instability, and vibration caused by boiling can be avoided.

Similar to steam cooling, implementation of the mist/steam cooling scheme is limited to GT systems in combined cycles.

1.3 Theories of Film Cooling

As a good starting point toward understanding the mechanism of mist/air film cooling, the flow and heat transfer characteristics of film cooling will be examined in depth. It is believed that the fundamental concepts, methodologies, and approaches introduced in film cooling studies can provide guidance for the current investigation of mist/air film cooling. Thus a review of the film cooling literatures, with a focus on the fundamental concepts and methodologies, is conducted.

Fundamental Concepts of Film Cooling

Film cooling is one of the essential techniques to reduce the airfoil temperatures and thermal stresses which tend to increase and become exacerbated as the turbine inlet temperature is continuously raised to augment gas turbine performance. Air bled from the compressor flows into the airfoils for internal cooling and then is ejected through small holes to form a layer of cooling film that blankets and protects the airfoil's surface from the hot mainstream gases. The film cooling jets consume valuable compressed air; therefore, it is essential to continuously searching for new schemes to enhance film cooling performance and minimize the cooling mass flow through the jets.

The ultimate goal of introducing film cooling to turbine airfoils is to reduce the heat load on the blade--i.e., reduce the surface heat flux and/or lower the airfoil's temperature--so that the life of turbine airfoils can be significantly extended due to lower thermal stress and less spallation over thermal barrier coating. Thus, it is important to know how much heat flux or blade temperature can be actually reduced after film cooling is employed. However, due to the experimental difficulty in directly measuring the heat flux, the **Heat Flux Ratio (HFR)** q'' / q''_o is often evaluated indirectly through a theoretical relation developed by Mick and Mayle [1988] between two characteristic factors of film cooling heat transfer--adiabatic film effectiveness (η) and film heat transfer coefficients (h_{af} and h_o)--as

$$q'' / q''_o = (h_{af} / h_o) (1-\eta/\varphi) \qquad (1)$$

[NB: This equation is not exact and is to be revised later in this study.]

In the above equation, the **adiabatic film effectiveness** is defined as

$$\eta = (T_g - T_{aw}) / (T_g - T_j) , \qquad (2)$$

where T_g is the main flow hot gas temperature, T_j is the coolant temperature at the cooling jet hole exit, and T_{aw} is the adiabatic wall temperature. η is an excellent indicator of film cooling performance by comparing the insulated wall surface temperature (T_{aw}) with the would-be perfect wall temperature, T_j. If the film cooling were perfect, η =1 and the wall is protected as cold as the cooling jet temperature. The **adiabatic film heat transfer coefficient** is defined as:

$$h_{af} = q'' / (T_{aw} - T_w) , \qquad (3)$$

where T_w is the airfoil wall surface temperature that comes immediately into contact with the hot main gas flow. This definition is clear if the wall boundary condition is not adiabatic, which means that the actual wall heat flux would be driven by the potential adiabatic wall temperature T_{aw}.

In Eq. 1, the local heat flux without film cooling is given as

$$q''_o = h_o (T_g - T_w) . \qquad (4)$$

The **film cooling effectiveness**, φ, is defined as

$$\varphi = (T_g - T_w) / (T_g - T_j). \qquad (5)$$

The definition of φ is very similar to η except T_{aw} in Eq. 2 is replaced with T_w. To reduce complexity, T_j is assumed the same as internal coolant temperature, T_{ci}. Though η can be considered to be a special case of the more generically defined film cooling effectiveness (φ) when the wall is insulated, it is convenient to use both terms by designating φ for all non-adiabatic wall conditions and η only for the adiabatic wall condition. φ has also been termed the **non-dimensional metal temperature** (The Gas Turbine Handbook [2006]) or the **overall cooling effectiveness** in other literatures. Use of the former term is inconvenient and mind-boggling because a higher value of non-dimensional metal temperature actually means lower true wall temperature. Therefore, the latter is preferred and is used in this study. For a perfect film cooling performance, the film cooling effectiveness would have a value of unity (η or φ = 1.0)(i.e., T_{aw} equals the coolant temperature (T_j) at the exit of the jet injection hole), while a value of η or φ = 0 means that the film cooling has no effect in reducing the wall temperature, which is as hot as the mainstream gas.

Clarification of terminology is needed for HFR, since in some literatures it is referred to as Heat Flux Reduction originated from the study of Mick and Mayle [1988]. But from the

definition, it is actually the ratio of heat flux with film over without film cases, thus q'' / q''_o in Eq. 1 is more appropriately called Heat Flux Ratio, rather than Heat Flux Reduction. Meanwhile, Net Heat Flux Reduction (NHFR) is defined as $NHFR=1- q'' / q''_o=1- (h_{af}/ h_o) (1-\eta/\varphi)$. In this study, HFR is referred to as the Heat Flux Ratio and will be employed throughout this paper.

In a real gas turbine condition, the airfoils are cooled inside by internal coolant flow and part of the coolant is bled and utilized for film cooling. Therefore, the actual heat transfer path goes through a conjugate condition from hot main flow gas to the airfoil surface via convection and radiation, spreads over the airfoil via conduction, and then transfers to the internal cooling fluid via convection again. It needs to be emphasized that the ultimate energy source is the main flow of hot gases and the energy sinks are the internal flow and the film flow. Due to the complexity of this conjugate heat transfer condition, many film cooling experiments have been performed under simplified conditions, such as applying adiabatic wall condition or uniformly heated wall condition. Therefore, it has been always highly desired to know HFR through Eq. 1.

Adiabatic Wall Temperature

In the film cooling heat transfer analysis mentioned above, one of the core concepts is to deem the film cooled adiabatic wall temperature (T_{aw}) as the driving potential for the actual heat flux over the film-cooled surface, as proposed by R. J. Goldstein [1971]. This concept can be approached in two ways. First, T_{aw} can be simply treated as the highest temperature that the wall can possibly obtain when the wall is perfectly insulated. Hence, after the insulation is removed and the wall is subject to cooling underneath, the heat flux moves from the wall to the cooling flow underneath. This can be treated as being driven by the difference between T_{aw} and T_w. Second, theoretically the concept of treating the adiabatic wall temperature as the driving temperature potential is drawn from compressible flow when viscous dissipation becomes important and acts as a heat source to drive the heat flux; but, in conditions where viscous dissipation is negligible, which is common in film cooling experiments under laboratory conditions, the heat source is not coming from near the wall but rather from the main hot gas stream. It must be noted that the viscous dissipation phenomenon is fundamentally different from the physics in the film cooling condition. For flows in which viscous dissipation is crucial, dissipation is the actual energy source that converts the flow's kinetic energy to thermal energy near the wall, whereas the only energy source in the film-cooling flow is the hot gas stream

(assuming viscous dissipation is negligible in the film-cooling flow discussed in this study). Therefore, the highest temperature value T_{aw} in the viscously dissipative flow is related to how much the converted thermal energy can be recovered by the wall via the recovery factor. In the film-cooling flow, the highest temperature that T_{aw} can possibly reach is T_g. Thus, the use of the concept of recovery factor (r) or recovering temperature (T_r) in the film-cooling flow to explain T_{aw},as some researchers have done, seems artificial and shy of a support of flow physics if viscous dissipation is negligible. Lack of awareness of this difference has caused some confusion in explaining the film-cooling results. With this in mind, one of the objectives of this study is to examine whether the concept of treating adiabatic wall temperature as the driving potential in film cooling heat transfer is appropriate or not.

Harrison and Bogard [2000] studied the validity of using T_{aw} as the driving temperature via the approach of comparing the heat flux and wall temperature of a film cooled wall using computed values of T_{aw} and h_f/h_o with the result from a conjugate model. They used the relative thickness between the velocity boundary layer and the thermal boundary layer to explain that, if the thermal boundary layer is thinner than the velocity boundary layer, use of T_{aw} is acceptable, whereas, if both boundary layers are of similar thickness, then T_g is a more appropriate driving temperature than T_{aw} . Harrison and Bogard's observation and conclusion from the CFD results are not unexpected. Basically, their conclusion implies that T_{aw} is not always the driving temperature.

Considering that the passage of the heat flux in film cooling scenarios is from the only source (T_g) to the sink (coolant), it is reasonable to think that T_{aw} in the film-cooling flow represents not the energy source (a cause) that drives the heat flow but instead a "consequence" resulting from the thermal-flow fields. Since T_{aw} is just a result from the thermal-flow field, the other options can also be considered to determine the driving temperature by examining the near wall local temperature field. For example, an effective temperature located between the wall and the core of coolant can be designated as the driving temperature as $T_{eff}(x) = (T_g + f(x)T_j)/2$, where f(x) is a function that describes the coolant core temperature attenuation along the streamwise direction. In this approach, apparently f(x) is unknown and needs to be determined by experiments. However, a search for f(x) will further complicate the issue. This thought provokes the temptation to make it simple by just using the T_g as the driving temperature for all the film-cooling cases without trying to figure out what the effective local driving temperature

would be along the wall.

A sketch is shown in Fig. 1.4 to qualitatively illustrate the heat transfer scenarios including the temperature profiles at two locations: one near the jet injection hole with a possible reversed heat flow in the airfoil base metal and the other located further downstream from the injection hole region. The slopes of the temperature profiles are drawn to qualitatively reflect the heat flow directions.

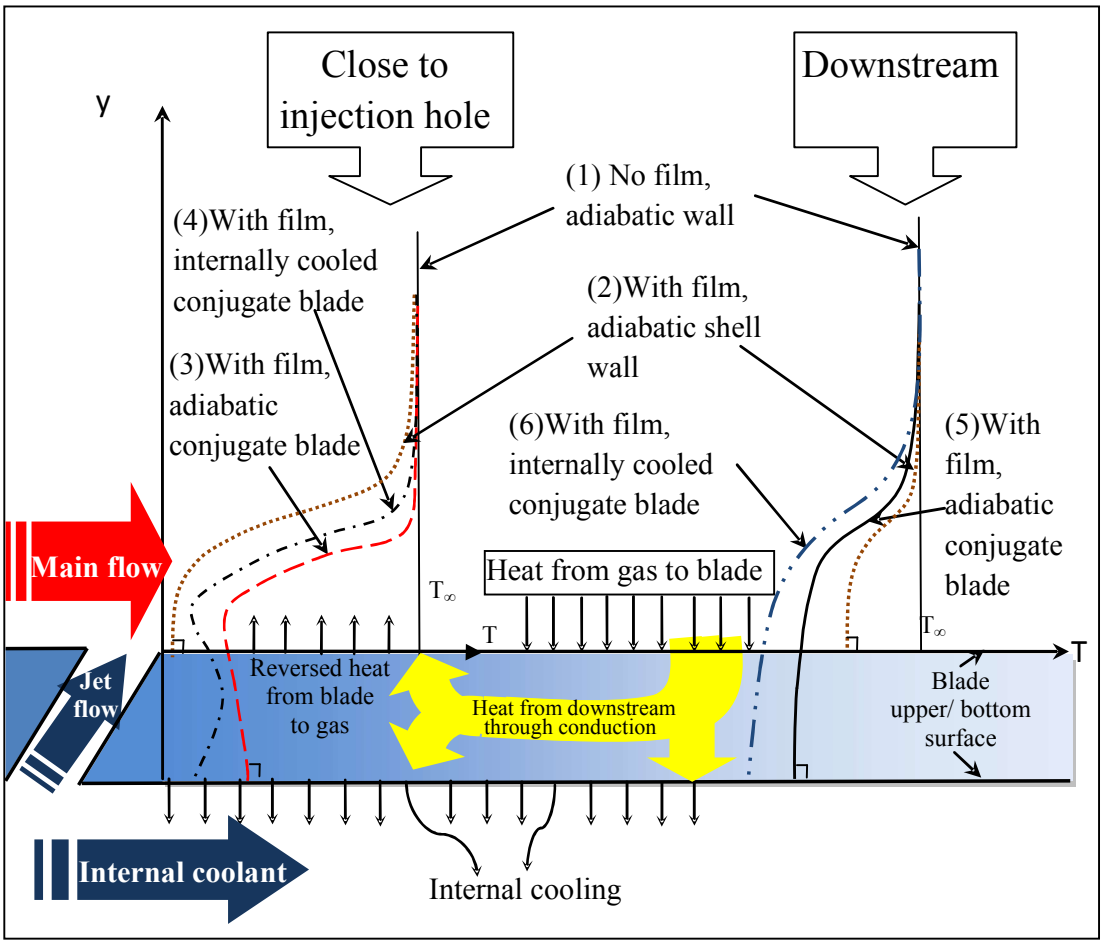

Figure 1.4 Qualitatively temperature profiles of a typical internally and film cooled blade at two locations: one near the injection hole region with potentially reversed heat transfer and the other located further downstream. The axial heat conduction transfer is small, and the size of reversed heat flux arrowhead is enlarged for illustration purpose.

Examining Fig. 1.4 raises another question: whether, theoretically, the T_{aw} used in Eq. 3 should be obtained with a perfect insulation of the surface. Will the conduction in the metal wall

(or conjugate wall) affect the true value of T_{aw}? If it does, what is the deviation from the true T_{aw} value? This question has not been answered or even raised in previous film cooling studies involved with conjugate walls, such as papers published by Bohn et al. [1995, 1999], Han et al. [2000], Rigbi et al. [1999], and Heidmann et al. [2001]. In summary, the conjugate wall effect on adiabatic wall temperatures has neither been noticed nor investigated in the previous studies.

Heat Flux Ratio

Eq.1 is mathematically derived, so it is supposed to be theoretically correct. In order to determine the value of q''/q_o'' through experiments, two tests need to be performed: one for the adiabatic case to acquire η and the other for the conjugate case (with and without film) for h_{af}/h_o. But how can φ be obtained? Based on the derivation by the original producers of this equation, Mick and Mayle [1988], φ is claimed to be typically about 0.6 for modern gas turbine components; however, no supporting material or data were provided in their paper to substantiate this value. This value of "0.6" has been widely used and cited since 1988, for example in the work of Sen et al. [1996] and Ou et al. [1991]. Examination of the φ definition in Eq. 5 unequivocally indicates that the value "0.6" implies the film cooling effectiveness is 0.6 under non-adiabatic conditions. It is understood that HFR calculated using a pre-assumed φ value could serve as an estimate for film cooling scheme applied in an assumed condition, but this practice brings about several issues of concern. The first issue is that this single constant value can hardly be valid for various cases of different conditions irrespective of the influence from parameters, such as jet temperature, blowing ratio, hole configurations, etc. The second issue is that film cooling effectiveness should actually be non-uniform along the surface; thus, applying a constant φ-value everywhere is questionable. The third issue is that a constant φ-value implies a constant wall surface temperature, which does not represent real film cooling conditions. The fourth issue is that since the value of 0.6 was assumed for real gas turbine environment, it is questionable that this same value is appropriate for use in low temperature laboratory conditions. Oh and Han [1991] and Lu et al. [2009] expanded the range of φ value from 0.6 to between 0.5 and 0.7, but no supporting material was found either for what φ value should be used under what conditions. Therefore, the practices of assigning or assuming a single value of φ are questionable and not convincing.

Furthermore, if Eq.1 is used to calculate q'', h_{af} will need to be calculated from Eq.3 by

measuring T_w distribution from an experiment. If T_w values are measured from the experiment, φ-values can be directly calculated through Eq.5 and then used in calculating HFR in Eq.1. Instead, many researchers employed an assumed single φ-value (0.6 or any other values) for calculating HFR despite the available φ-values in their specific study. The detailed investigation of this subject has been conducted in parallel with the experimental work of this study. The report is presented in Appendix A.

Heated Wall Practices

Isothermal (isoenergetic) film cooling is named for the condition where $T_j=T_g$--i.e., the jet is as hot as the gas stream. Conventionally, the h_{af} value is obtained by conducting an isothermal film experiment as performed by Burd et al. [2000] and Thurman et al. [2008]. Since h_{af} should include the effects from the film-disturbed flow field and the thermal field, an isothermal film experiment only provides the effect of the flow field, which actually helps enhance the heating of the surface instead of the cooling because the film jet promotes turbulence and augments surface heating. While the jet flow-induced mixing acts adversely toward the goal of reducing heat flux through film cooling, the lower coolant temperature serves to protect the surface by absorbing the heat from the main flow. These two mechanisms compete with each other, and it is therefore essential to distinguish the difference between the effects of disturbed flow field from the cooling effect of lower temperature on film cooling performance. Consequently, the overall performance of film cooling manifests a net wall heat flux reduction which takes into account the decreased gas temperature provided by the coolant film and the increased heat transfer coefficient due to the hydrodynamic mixing effect of coolant injection process.

In the isothermal film case, the actual heat transfer coefficient should be evaluated as $h = q''/(T_g-T_w)$; however, in order to fit the definition in Eq 1, h_{af} is calculated via Eq. 3 instead of h. In this practice, two issues are raised. First, the h_{af} so obtained does not include the effect of the actual jet coolant temperature, T_j; so **h_{af} is overvalued** because T_w should be lower if T_j's temperature effect is included. Second, in the isothermal film experiment, the wall heat flux needs to be measured. If q" can be measured, why not just use a lower-temperature coolant to perform the experiment and obtain the actual filmed-cooled heat flux without even bothering to use Eqs. 1 and 2 or run the adiabatic case? The reason is that an accurate measurement of heat flux is not easy under a conjugate condition, so most of the studies employ a uniformly heated

surface to simulate the isothermal film heat transfer study. Implicitly, the experiment reverses the heat path by transferring heat from the wall to the free-stream. This practice is acceptable with the above condition when $T_j=T_g$, but it leads to the next issue when $T_g>T_j$.

Conventionally, many film-cooling experiments and computational analyses have used a heated surface to simulate the actual film-cooling condition with a cooling jet and a hot main flow. One of the motivations of using this approach is to take advantage of the convenience of controlling the constant heat release without actually measuring the local heat flux or employing conjugate cooling below the surface. This practice is also based on the observation that the airfoil surface is usually hotter than the film temperature, so it seems appropriate and convenient to simplify the conjugate condition with a heated surface. Some examples of using the heated surface in the experiments are the studies of Jonsson et al. [2008] and Nicklas et al. [2001]. This simplified practice is seemingly fine, but a close examination of the physics leads to an unwelcome negative conclusion: a heated surface with a cooling jet and hot gas does not provide the correct physics of the heat flow under an actual film cooling condition; therefore, the results are questionable. This means that in the real film-cooled surface, the heat is transferred from the gas to the wall, which is the opposite of the heated flow experimental case where the heat transfers from the wall to the gas. It is easy to fall into the trap of thinking that the cooling film has a temperature lower than the wall, so the heat tends to transfer from the "hot" wall surface to the cooling air. The reality is that the cooling air, which mixes with the hot main stream gas, reduces the bulk temperature near the wall and hence reduces the heat transferred to the wall, but the mixture temperature is still higher than the wall temperature with an exception of the limited area where the wall temperature is higher than the near-wall gas due to heat conduction in the wall. This small region of reversed heat transfer has been reported by Mouzon et al. [2005] and Coulthard et al. [2007]. As has been emphasized, the only energy source in the actual film cooling condition is the main flow hot gas, so if there is a path for heat to transfer from the surface back to the gas flow, it must be the result of the natural course of the heat transfer. This means that the reason that the surface becomes hot must be due to accessible heat paths from the main gas flow to the surface. These heat paths can be attributed to turbulent eddies penetrating through the surface, secondary flows wrapping from the lateral direction, radiation, or pure diffusion of heat to the surface. Typically, the gas temperature adjacent to the wall would be higher than the wall surface temperature, and the chance for heat transferring back from the

surface to the gas must only be provided by the conduction inside the wall material that redistributes the heat from the hotter region to the colder region. This heat conduction path makes the wall surface temperature warmer than the adjacent gas temperature immediately away from the wall. Therefore, using a heated wall as the wall boundary condition is only valid for the limited area (usually near the film hole), where the wall temperature is hotter than the near-wall gas temperature.

On the other hand, the heated wall can be used as the correct boundary condition only if all the heat flow directions are consistently reversed--i.e., using a heating jet with a temperature higher than the main gas stream ($T_j > T_g$). Mick and Mayle [1] did just this by adopting a completely reversed heat flow condition in their study. The completely reversed system can also be found in some recent studies, for example in Burd at al. [2000] and Womack et al. [2007].

If the heated surface condition is employed for the purpose of obtaining h_{af} only, another concern is raised to the effect of variable properties since the temperature gradient is totally opposite from the real condition with the airfoil surface being cooled; the flow field, fluid properties, and heat transfer might be altered, especially in the near wall region. This concern can be investigated by examining h_{af}, obtained through both heated and cooled surface cases. The result is presented in Appendix A.

Film Cooling Performance Enhancement

There are numerous studies in the open literature discussing methods to improve the film cooling performance. The studies can be summarized in three different categories representing different perspectives to improve film cooling: coolant hole geometry and configuration, coolant/mainstream conditions, and airfoil geometry.

Coolant Hole Geometry and Configuration

In this category, the major factors affecting the film cooling performance are shape of the hole, hole orientations (injection angle, compound angle, etc.), length of the hole, hole spacing (p/d), number of rows, and row spacing. The first two factors are comparatively more significant in determining the film cooling performance. The key behind changing the coolant hole geometry and configurations is to modify the flow field to prevent the coolant jet from lifting up from the surface, reducing film penetration into the main flow.

The study of Goldstein et al. [1974] was generally accredited as the first to research the use of shaped coolant holes to improve film cooling performance. They tested a 10º spanwise-diffused hole and compared the performance with that of cylindrical holes. The shaped hole reduced the coolant momentum flux of the coolant jet. As a result, the coolant had less penetration into the mainstream compared to the cylindrical-hole cases, providing a better cooling effectiveness. Many studies followed their approach. Even today, after 37 years, there are still large numbers of ongoing researches focusing on discovering better hole shapes combined with most optimum orientation angles and other previously mentioned factors to improve film cooling performance. For example, Thole et al. [1996] measured the flow fields for three types of injection holes: a cylindrical hole, a laterally diffused hole, and a forward-laterally diffused hole. Their results showed that diffusing the injection hole reduces the coolant penetration into the mainstream and reduces the mixing intensity in the film and main flow shear regions when compared to cylindrical holes.

Cho et al. [2001] investigated the local heat, mass transfer characteristics and local film cooling effectiveness around a conical-shaped film cooling hole with compound angle orientations. Bell et al. [2000] found laterally diffused compound angle holes and forward diffused compound angle holes produce higher effectiveness over much wider ranges of blowing ratio and momentum flux ratio compared to the other three simple-angle configurations tested. Brittingham and Leylek [2002] concluded that the compound-angle shaped holes could be designed to eliminate cross flow line-of-sight between adjacent holes, thereby somewhat mimicking slot-jet performance.

To eliminate non-uniform cooling pattern inherent in the discrete injection holes, Wang et al. [2000] conducted experiments by embedding the discrete injection holes in a slot recessed beneath the surface. Premixing inside the slot makes the slot film cooling more uniform than discrete injection holes. Jia et al. [2003] studied the optimum inclination angle, and they found that the recirculation bubble downstream the jet vanishes when the angle is 30° or less.

Several researchers have focused on injection from a double row of cylindrical holes in order to approach a two dimensional film cooling situation. Jubran and Brown [1985], Jabbari et al. [1978], and Jubran and Maiteh [1999] have all shown that for the same injected mass flow rate per unit span, the double row provides better cooling protection than the single row. The

increased area ratio of the double row lowers the momentum of the coolant, which provides better lateral spreading of the coolant.

Spacing the holes closer together also increases the effectiveness in the lateral direction. Ligrani et al. [1996] showed that a compound angle orientation of the holes in the second row also increases the effectiveness. In addition, staggered rows of holes show better performance than inline rows of holes. The anti-vortex hole concept introduced by Heidmann and Ekkad [2008] is an alternative to the shaped holes using sibling holes to counteract the effect of vortex created by the main hole and, therefore, to increasethe film cooling effectiveness. This "anti-vortex" design is attractive in that it requires only easily machineable round holes, unlike shaped film-cooling holes.

An interesting study of Montomoli et al. [2010] investigated the impact of filleted edges variations on heat transfer. Their study is motivated by the fact that, in real gas turbines sharp edges will not exist or last because of manufacturing tolerances and/or material wear and tear occurring during operation. Their results showed that the effect of variation of fillet must be included in numerical simulations, especially for studies using LES and DNS.

Coolant/Mainstream Conditions

Since the mixing between the coolant and main flow is partially controlled by turbulence diffusion, the turbulence intensity of both the main flow and the coolant jet will affect the film cooling performance.

High mainstream turbulence levels degrade film cooling performance by increasing heat transfer coefficients and generally decreasing the film effectiveness. This is shown in the study of Bogard et al. [1996, 1998] simulating the large scale turbulence with levels of Tu = 10% to 17%, and an increase in heat transfer coefficient of 15% to 30% was found. Ekkad et al. (1995) also studied the effects of free-stream turbulence on the heat transfer into a film cooled turbine blade. In their study, it is concluded that high main flow turbulence results in an increased heat transfer coefficient and a slightly reduced film cooling effectiveness.

On the other hand, for coolant jet, Mayhew et al. [2004] showed that low inlet turbulence intensities keep the coolant close to the wall when the blowing ratio is low, while high inlet turbulence intensities help bring the coolant back to the wall when the blowing ratio is high. This result was adopted in the studies of Brittingham and Leylek [2002], Adami et al. [2002] in

their numerical studies. An inlet plenum, as well as the flow arrangement, was included in their simulation in order to consider the effect of upstream flow conditions for the coolant flow. It was concluded that an accurate prediction of coolant discharge and wall coverage of cooling film requires computation of flow field in the coolant air supply plenum and duct.

Airfoil Geometry Effect

Surface curvature is an important factor that affects film cooling performance. Turbine blade leading edge and suction side are featured by the convex curvature, while the pressure side is a concave surface. The curvature effect was extensively studied by Ito et al. [1978] and Schwarz et al. [1990]. It is summarized in their studies that, for typical operational blowing ratios, a convex surface will generate increased η, while decreased η is generally found for a concave surface, except at high momentum flux ratios. The surface curvature effect can be explained by the wall normal pressure gradients associated with wall curvature. When the momentum of the jet is less than that of the mainstream, the pressure gradients push the coolant jets towards the convex wall surfaces on the suction side. Also, the inward pressure has a positive effect of spreading the jet wider on the surface and keeping the jet attached to the wall for higher momentum flux ratios. Over concave surfaces, the opposite occurs. The coolant jets are pushed away from the wall, resulting in reduced film cooling effectiveness. Waye and Bogard [38] investigated the film cooling adiabatic effectiveness for axial and compound angle holes on the suction side of a simulated turbine vane. Some more examples studying the curvature effect on film cooling effectiveness can be found in the work of Zhang et al. [2009] and Ladisch et al. [2009].

Summary Comments for Film Cooling

Although the performance of conventional air film cooling has been continuously improved, the increased net benefits seem to be incremental, and it appears that they are approaching their limit. In view of the high contents of H_2 and CO in the coal or biomass derived synthetic fuels for next generation turbines, the increased flame temperatures and flame speeds from those of natural gas combustion will make gas turbine cooling more difficult and more important. Therefore, development of new cooling techniques is essential for surpassing current limits.

The benefits of improved film cooling can be evaluated from different aspects as follows.

- Less coolant air consumption – The turbine system efficiency will be improved if less compressor air is used for cooling, thus saving the compressor power consumption.
- Higher Turbine Inlet Temperature – With a higher cooling efficiency, a higher TIT can be expected, which implies higher system efficiency.
- Lower blade temperature – The blade life span can be extended longer with a lower blade temperature.
- Less coolant holes – The blade mechanical strength will be improved and the fabrication cost can be lowered.

It is noted that all the benefits may not be obtained for an improved cooling scheme . For example, the TIT of a turbine system can be increased due to better blade cooling scheme, but the blade temperature may still remain the same.

1.4 Mist/Air Film Cooling Concept

One of the new and potentially advantageous cooling techniques is mist cooling. The basic idea is to inject small amounts of tiny water droplets (mist) into the cooling air to enhance the cooling performance.

The key mechanisms of the enhanced cooling effectiveness of mist cooling are summarized below.

- Higher Cp values – Mist cooling can provide higher cooling effectiveness. The heat capacity of both water drops (liquid phase) and steam (gas phase) is higher than that of air. Thus, the sensible heat of the mist/steam and air mixture is higher than the single phase film consisting of air only. Due to the latent heat of evaporation, the water droplets serve as numerous heat sinks in the mist film flow. This also results in a higher effective specific heat for the mist film mixture. Consequently, the mean bulk temperature of the mist film flow will be lower than that of the corresponding single-phase air flow and gives better cooling effect for the blade surface.

- Evaporation thrust force – In the real gas turbine condition where the blade temperature is quite high (800^{o}C-1300^{o}C), instantaneous boiling will occur when mist droplets hit the blade surface. Due to the much lower density of steam compared with liquid droplets (1:950), a sudden volume expansion takes place at the contact surface, resulting in a "propulsive" force thrusting the water droplets away from the surface. This process will greatly enhance the flow mixing and heat transfer between the mist and the blade surface due to strong heat conduction and momentum interchange
- Increased flow speed – After liquid droplets evaporate to steam, the volume flow rate increases, resulting in a higher coolant flow rate and, consequently, an enhanced cooling.

Mist cooling has the following benefits:

- As a result of the higher cooling effectiveness of mist cooling, the amount of coolant air can be reduced and the corresponding turbine output power can be increased.
- Extended cooling coverage – Mist cooling can provide better blade coverage in both streamwise and lateral directions. Due to the high overall heat capacity of mist/steam and air mixture, it takes a longer time to heat up the mist film mixture when compared with the air-only flow. As a result, the mist/air coolant travels further downstream on the blade, covering a longer range of the blade before being heated up and blended into the main hot gas. Thus, mist cooling overcomes the short coverage problem of air film cooling.
- As a result of the better blade coverage of the mist cooling, the number of rows of coolant holes can be reduced. Consequently the blade mechanical integrity can be improved. Also, it provides the potential to reduce aerodynamics losses since less jet mixing is expected due to the reduced number of coolant holes needed.

Furthermore, mist/film cooling can take advantage of accumulated experiences and research results of the mature and extensively studied film cooling technology. Any benefit from the introduction of the mist is a bonus to the existing film cooling scheme. The similar cooling scheme of mist/steam cooling has already been proven to be effective through both experimental and simulation studies (Guo et al. 1999, Li et al. 2000, 2001, Dhanasekaran et al. 2010).

Mist has been used to enhance heat transfer in gas turbine systems in different ways. Gas turbine inlet air fog cooling (Chaker et al. [2002]) is a common application where the droplets evaporate to lower the compressor air inlet temperature until the relative humidity reaches 100%. In addition, fog overspray is used in industry to provide evaporative cooling inside the compressor. Petr [2003] reported the results of thermodynamic analysis of the gas turbine cycle with wet compression based on detailed simulation of a two-phase compression process. In 1998, Nirmalan et al. applied water/air mixture as the impingement coolant to cool gas turbine vanes. It is noted that this study actually employed spray-cooling, which utilized a much higher water volume rate than the proposed mist cooling in this study. To explore an innovative approach to cooling future high-temperature gas turbines, researchers (Guo et al., 2000, 2001, Li et al., 2003) have conducted a series of mist/steam cooling experimental studies by injecting 7 μm (average diameter) of water droplets into steam flow (NB: not air flow). For a straight tube as studied in Guo et al. 2000, the highest local heat transfer enhancement of 200% was achieved with 1~5% (weight) mist, and the average enhancement was 100%. In a mist/steam cooling experiment applied to a 180^{o} tube bend, Guo et al.(2001) showed that the overall cooling enhancement ranged from 40% to 300% with the maximum local cooling enhancement being over 800%, which occurred at about 45^{o} downstream of the inlet of the test section. For mist-air jet impingement cooling over a flat surface (Li et al., 2003), a 200% cooling enhancement was shown near the stagnation point by adding 1.5% (wt.) mist. Applying mist/air jet impingement on a concave surface as studied by Li et al., cooling enhancements of 30 to 200% were achieved within five-slot distance with 0.5% (wt.) mist.

The key difference between mist/steam cooling and the mist/air film cooling proposed in this study is that mist/steam cooling uses steam as the main carrying coolant while mist/air cooling employs air as the main coolant. In mist/steam cooling, the evaporation process is governed by the temperature and total pressure of the steam flow, whereas the evaporation process is governed by the water vapor partial pressure in mist/air cooling.

The above mist/steam cooling experiments were conducted for the application in closed-loop internal airfoil cooling such as used in G and H-type advanced gas turbines. The mist injected will serve as a portion of makeup steam and stay in the bottom steam turbine cycle. However, for air-cooled air foils, the mist is injected into the *air*-coolant stream (not in steam flow anymore) to provide the internal cooling. Eventually, the mist is injected through the film

cooling holes to provide the external airfoil's surface cooling. In 2005, Li and Wang conducted the first numerical simulations of air/mist film cooling. They showed that injecting a small amount of droplets (2% of the coolant flow rate) could enhance the cooling effectiveness about 30% ~ 50%. The cooling enhancement takes place more strongly in the downstream region, where the single-phase film cooling becomes less effective. Three different holes were used in their study, including a 2-D slot, a round hole, and a fan-shaped diffusion hole. They performed a comprehensive study on the effect of flue gas temperature, blowing angle, blowing ratio, mist injection rate, and droplet size on the cooling effectiveness. Analysis of droplet history (trajectory and size) was undertaken to interpret the mechanisms of droplet dynamics. Li and Wang [2005] further conducted a more fundamental study investigating the effect of various models on the computational results. The models they used included the turbulence models, dispersed-phase modeling, different forces models (Saffman, thermophoresis, and Brownian), trajectory tracking model, near-wall grid arrangement, and mist injection scheme. The effects of flow inlet boundary conditions (with/without the air supply plenum), inlet turbulence intensity, and the near-wall grid density on simulation results were also investigated. Using a 2-D slot film cooling simulation with a fixed blowing angle and blowing ratio, they showed that injecting mist of 2% coolant mass flow rate can increase the adiabatic cooling effectiveness about 45%. The RNG k-ε model, RSM and the standard k-ε turbulence model with the enhanced wall treatment produce consistent and reasonable results, while the turbulence dispersion has a significant effect on mist film cooling through the stochastic trajectory calculation. The thermophoretic force slightly increases the cooling effectiveness, but the effect of Brownian force and Saffman lift is imperceptible. The cooling performance is affected negatively by the plenum, which alters the velocity profile and turbulence intensity at the jet discharge plane.

Both of these studies were conducted at conditions of low Reynolds number, temperature, and pressure. Actually, most other studies discussed above were also conducted at low Reynolds number, temperature, and pressure conditions. As a continuous effort to develop a realistic mist film cooling scheme, Wang and Li (2006) examined the performance of mist film cooling under gas turbine operational conditions, featured by high pressure (15 atm), velocity (128 m/s), and temperature (1561k). The enhancement of the adiabatic cooling effectiveness was found less attractive than the cases with low pressure, velocity, and temperature conditions. However, due to high surface temperature under the GT operating condition, the additional wall temperature

reduction could achieve 60K even though the enhancement of adiabatic cooling effectiveness is only 5%. This temperature reduction can be critical to the airfoil life expectancy of gas turbines.

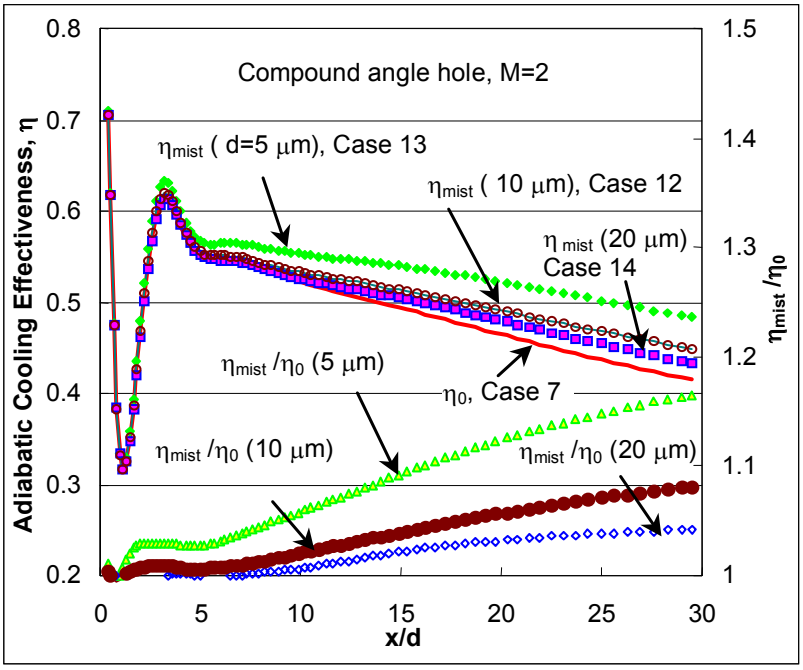

Figure 1.5 Effect of droplet size on mist cooling effectiveness (along the centerline of compound-angle hole cases 12 ~14) (Source: Li and Wang 2006)

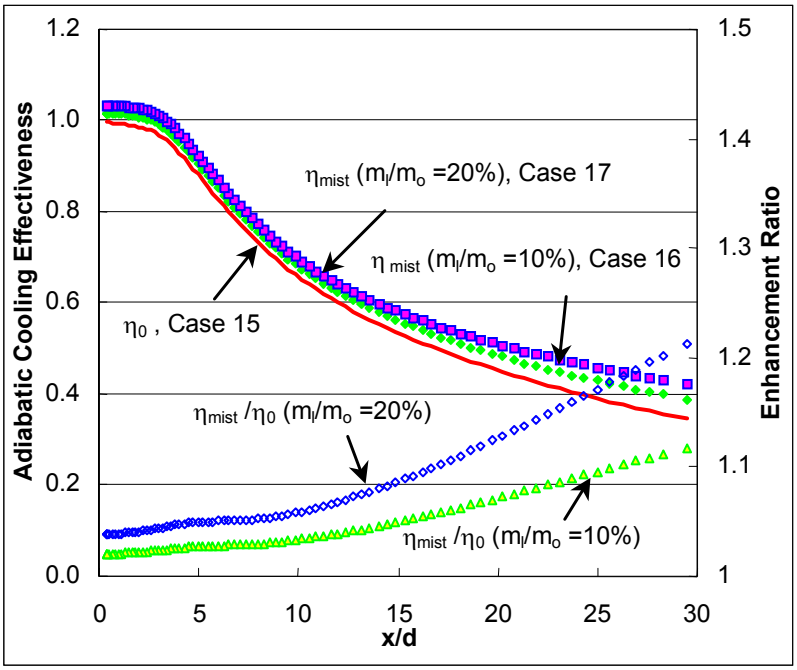

Figure 1.6 Effect of mist concentration on adiabatic cooling effectiveness (along the

centerline of the fan-shaped hole cases 15, 16, and 17 with the blowing ratio M=1) (Source: Li and Wang 2006)

Many challenges still exist and many questions need to be answered before the mist cooling is ready for applications in gas turbines. As has been reviewed, there are currently no experimental results studying the mist/air film cooling scheme for gas turbine blades. Even though the mist/air film cooling technology has been predicted to be effective through simulation studies, its validity is yet to be proven through experimental tests. Moreover, extensive investigations are needed to fully understand the heat transfer mechanism and droplet dynamics of the mist film flow (i.e., droplet/wall interaction, droplet/air interaction, effective droplet size distribution, etc.).

Due to the evaporation of the liquid droplets and the relative motion between the droplets and the air stream, there is momentum, heat, and mass transfer between the droplets and the air film. These interactions are expected to induce mixing and turbulence inside the main flow and the boundary layer. Two effects are produced: reduced wall temperature and enhanced heat transfer coefficient. The first effect is favorable, yielding higher cooling effectiveness, while the latter is detrimental to the purpose of reducing heat flux into the blade. Investigations are needed to clearly identify both effects for mist/film cooling.

Beside the need to better understand the mechanism of mist/film cooling, some practical questions need to be addressed in order to apply this technology in gas turbine engines, for example where to feed the mist into the gas turbine system and whether the mist can survive the journey from the mist injection location to the cooling holes under the high-temperature environment inside the gas turbines. Rather than develop the technology of transporting mist to the film cooling hold sites, the current strategy is to take the first step to conduct experiments under the laboratory conditions to prove the concept of mist/film cooling. During this concept-proving process, it is believed that some unforeseen problems or challenges may surface and be resolved. After convincingly proving the concept, with a better understanding of the mist cooling characteristics gained during the process, the practical issues related to mist transport will be studied and resolved in the second stage of this new technology development process.

1.5 Measurement Techniques for Mist/Film Cooling

Since film cooling has been studied for more than 60 years, numerous experimental instrumentations and techniques have been developed to investigate and evaluate the film cooling heat transfer performance. The key parameters to evaluate the cooling performance are the cooling effectiveness and heat transfer coefficient. The widely used surface temperature measurement techniques include thermocouples, thermal paints, infrared camera thermography, and liquid crystals. The measurement of the heat transfer coefficient is often more complicated as discussed in the film cooling review. An earlier work of Goldstein [1976] summarized the measurement instrumentations and techniques in a more general manner for heat transfer. A more recent work of Han et al. [2000] gave more descriptions for the measurement techniques specifically employed for film cooling.

Temperature mapping with thermocouples has been traditionally used. It is an accurate, robust, and reliable measurement method. However, since it is essentially a point measurement method, the spatial resolution is limited by the finite number of the thermocouple wires mounted on the surface. In order to improve the spatial resolution, more thermocouples on the test surface are needed. The addition of thermocouples to the test surface is time-consuming, costly, and can affect the original heat transfer characteristics of the surface. Examples of experiments using thermal couples are too numerous to be listed. One example is the earlier work of Goldstein et al. [1974] using thermocouples to determine the effects of coolant density and hole geometry on film cooling performance on a flat plate with an incline angle of 35°. In a more recent work, Piggush and Simon [2006]produced detailed flow temperature profiles using fine wire thermocouples measurement.

Thermocouples can give accurate temperature measurements for film cooling as proven in numerous studies; however, to overcome the problem of spatial resolution, the use of optical techniques has gained more popularity in recent studies. Optical techniques involve the use of cameras to capture changes of temperature on the surface. The advantage of these techniques is the ability to capture the heat transfer coefficient and film effectiveness distributions continuously over the whole test surface. Several optical techniques are described below.

A transient heat transfer method using a temperature sensitive paint (TSP) was first applied to a turbine internal cooling system by Clifford et al. (1983). TSP is a photo-luminescent paint which is thermally quenched. The intensity of the light emitted by the paint decreases as the temperature increases. The intensity of the light is captured by a camera and ,through a

calibration, can be converted to temperature. Since the early study of Clifford, numerous researches have adopted the technique. Baughn et al. (1989) compared the transient method to the uniform heat flux method. Liu et al. [2003] has demonstrated the calibration of TSP as well as the effects of lighting and viewing conditions. Lee et al. [2004] used TSP to capture surface temperatures on a flat plate-vortex generator. Some other transient method publications include Son et al. (2000), Azad et al. (2000), and Gillespie at al. (2000). The problem of irreversibility of this method limits its applications.

Infrared cameras can be used to measure adiabatic wall temperatures, thus the cooling effectiveness can be determined from a steady state experiment. The technique has been used by Dorignac & Vullierme (1993) and Gruber & Page (1993). Gritsch et al. [1998] used an IR technique to study the effects of hole geometry (expanded exits) on film cooling effectiveness. A transient IR technique similar to the method developed by Vedula and Metzger [1991] for liquid crystal has also been performed successfully by Ekkad et al. [2004]. In this technique, the film cooling effectiveness and heat transfer coefficient distributions were determined using a single experiment. Dhungel et al. [2007] have also used this transient IR technique to test the effect of anti-vortex holes on film cooling. The shortcoming of the infrared thermography is that if a foreign body is in between the infrared camera and surface to be measured, the thermal radiation released from the test body would be obstructed or at least altered, depending on the material of the obstruction. Even if the use of an observation window is feasible, which is not always the case, the material of the window can be costly. Comparisons of the possible materials that are infrared transitive are summarized in Appendix A. The pros, cons, and prices of all the materials are listed as well.

Finally, transient and steady-state thermochromic liquid crystals (TLC) schemes have been used recently by many researchers. The TLC schemes eliminate the surface resolution limitation and viewing-access problem. The TLC method assumes a one-dimensional heat conduction model within a semi-infinite wall, for which case a theoretical transient solution is available. With this method all three parameters, h, η and the local heat release q”, can be obtained simultaneously. Baughn (1995) reviewed methods of using narrow band and wide band TLCs for the measurement of local heat transfer coefficients for steady and transient states. Vedula and Metzger (1991) described an experimental method using a double TLCl approach for simultaneous determination of both local effectiveness and heat transfer information. Ekkad and

Han (1995) used two related transient tests to determine film cooling and heat transfer using a lTLC technique. TLCs have been used to obtain detailed heat transfer coefficient and adiabatic film cooling effectiveness distributions. Two common steady state liquid crystal experiments have been used: With both the yellow band tracking method as shown in the work of Hippensteele et al. [1983], Simonich and Moffat [1984], and the hue, saturation, intensity (HSI) method (Camci et al.,1992), external heat losses must be determined for the measurement of the detailed heat transfer coefficient distributions. To alleviate the concern of accurately determining external heat losses (while reducing the effect of lateral conduction) and to avoid the problem of the narrow band of effective temperature of a fixed mode of TLC, transient techniques were introduced as an alternative for acquiring detailed heat transfer coefficient and adiabatic film cooling effectiveness distributions. A transient HSI technique has been used in a similar data-acquisition and processing manner to the steady state HSI technique for various jet impingement heat transfer studies [Wang et al. 1995, 1996, Van Treuren et al. 1994]. A transient single color capturing technique has also been developed for acquisition of detailed heat transfer coefficient and adiabatic film cooling effectiveness distributions. Bunker and Metzger [1990], Ekkad and Han [1997], and Chen et al. [1998] have all made significant contributions to blade cooling using this technique. Vedula and Metzger [1991] made use of two closely related transient experiments to determine both the heat transfer coefficient and adiabatic film cooling effectiveness. This technique has been shown to match well with past results. To evaluate the validity of the 1-D assumption made in the TLC method, Lin and Wang [2002] conducted an experimental study using 3-D TLC method. Their results showed that many of 1-D transient TLC studies are not correct because the 1-D assumption does not hold for non-uniform surface temperature in which conduction in other directions has to be accounted for. The 3-D method is more appropriate in those situations.

Mass transfer experiments can also provide detailed heat transfer coefficient distributions by using the mass-heat transfer analogy. One advantage of using the mass transfer techniques is that conduction effects are eliminated. One type of mass transfer experiment uses naphthalene surfaces over which coolant air is blown to determine the amount of mass sublimed during the experiment. This lost mass is then related to heat flux and used to produce the heat transfer coefficients directly by accounting for material property differences and assuming that the boundary conditions and turbulent transport are similar in both the mass transfer and heat

transfer problems. Goldstein and Taylor [1982] conducted mass transfer experiments on a flat plat with inclined holes at 35° and were able to identify regions of decreased heat transfer and regions of enhanced heat transfer. Pedersen et al. [1977] also used a mass transfer technique to demonstrate the effect of density differences between the mainstream and coolant flows on film cooling. The mass-transfer techniques are not generally used to determine the adiabatic adiabatic film cooling effectiveness, although a novel technique has been demonstrated by Goldstein et al. [1995, 1999]. Another new mass transfer technique used to determine the adiabatic film cooling effectiveness uses the pressure sensitive paint (PSP) scheme. PSP relies on the photoluminescence of oxygen-quenched molecules illuminated by a light source, which reacts to the partial pressure of oxygen in contact with the paint surface. PSP was first utilized in the study of pressure distributions on the surfaces of structures in the aerospace industry. This paint can also be used to determine the adiabatic film cooling effectiveness based on a definition of effectiveness using the concentration of oxygen in the coolant and mainstream flow. Zhang et al. [1999] first used this technique to determine the adiabatic film cooling effectiveness on a vane end wall, and it was shown that the strength of this technique lies in the absence of conduction effects.

To evaluate the heat transfer performance of a cooling scheme, the blade heat load information is desirable for designers and researchers. One device to directly measure heat flux is the heat flux gauge. A detailed discussion of these gauges can be found in Diller (1993). Guo et al. (1996 and 1997) used thin-film gauges to study the heat transfer into a heavily film cooled inlet guide vane. Their measurements were performed in an annular cascade with attempts made to simulate realistic engine conditions. The heat transfer coefficient and adiabatic film cooling effectiveness profiles were determined. Popp et al. (1999) also used heat flux gauges in a transonic linear cascade to study the shower- head film cooling performance in the first stage turbine blades. Measurements were made using thin-film heat flux gauges of both the heat transfer coefficient and the adiabatic film cooling effectiveness at six locations along the blade suction side surface.

Through the review, it is noted that mist/film cooling is a rather new technology and not much previous work, especially none of the experimental studies, can be found. One key feature in understanding mist cooling is the ability to capture droplet information. Thus a combination of heat transfer measurement and particle measurement is essential and is needed in studying the

mist/film cooling performance and its fundamental multiphase flow physics. This motivates the present study.

1.6 Objectives

The **objective** of this research is to perform a fundamental experimental study to

(a) experimentally prove that the proposed concept of injecting mist into air can enhance film cooling performance,

(b) investigate the associated multiphase flow physics, and

(c) achieve better understanding of the connection between the droplet dynamics and the mist cooling heat transfer characteristics.

To reach these objectives, the following tasks will be performed:

1. Construct the mist film cooling test rig including a wind tunnel, a mist generation system, a chilling system, and a film-cooling test section.
2. Install the instrumentation and measuring systems including the Phase Doppler Particle Analyzer (PDPA), infrared temperature measuring system, thermocouple measuring system, and PDPA 3-D traversing system.
3. Conduct a heat transfer experiment for both film cooling and mist cooling to evaluate the cooling performance enhancement.
4. Perform particle information measurement to investigate the droplet behavior in conjunction with the thermal-flow fields.
5. Analyze the heat transfer results combined with the particle information to gain understanding of the mist cooling mechanism.

CHAPTER TWO

EXPERIMENTAL SETUP

2.1 Experimental Test Facility

A schematic of the overall experimental facility is shown in Figure 2.1. The experimental facility consists of the wind tunnel system providing main flow, the coolant film system providing the secondary cooling air, the atomizing system providing the water mist, and the test section where the film cooling holes and instrumented test wall are located and measurements of temperature and mist flow are taken. The details of each component of the test facility are presented in a dedicated section for each as follows.

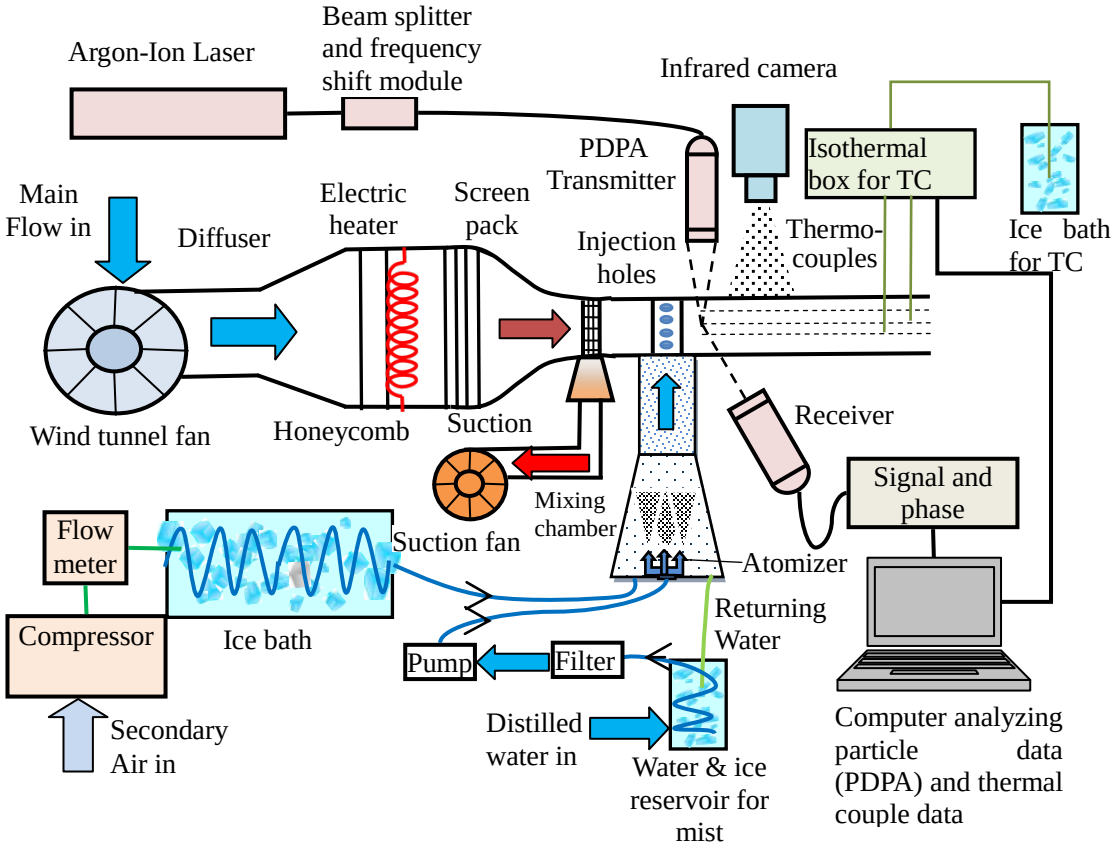

Figure 2.1 Schematic diagram of mist cooling experimental facility

2.1.1 Wind Tunnel System (Main Flow)

The wind tunnel system employed in this study is constructed and tested in the ECCC's (Energy Conversion and Conservation Center) laboratory in the University of New Orleans. The wind tunnel is an open-circuit, blowing type design, rated to provide 3000 CFM airflow. The room air is first heated by the heating unit installed inside the wind tunnel filter box and then is drawn into the fan inlet to pass through a diffuser to the flow straightening section, which includes a screen pack and a settling chamber. Two contraction sections are designed and constructed to connect the settling chamber to the test section, speeding up the flow and matching the dimensions of the test section inlet. With the current setup (two contractions installed), a maximum air speed of 39.8 m/s (130.58 ft/s or 89 mph) can be achieved in the test section. The detailed description of the wind tunnel components are provided as follows.

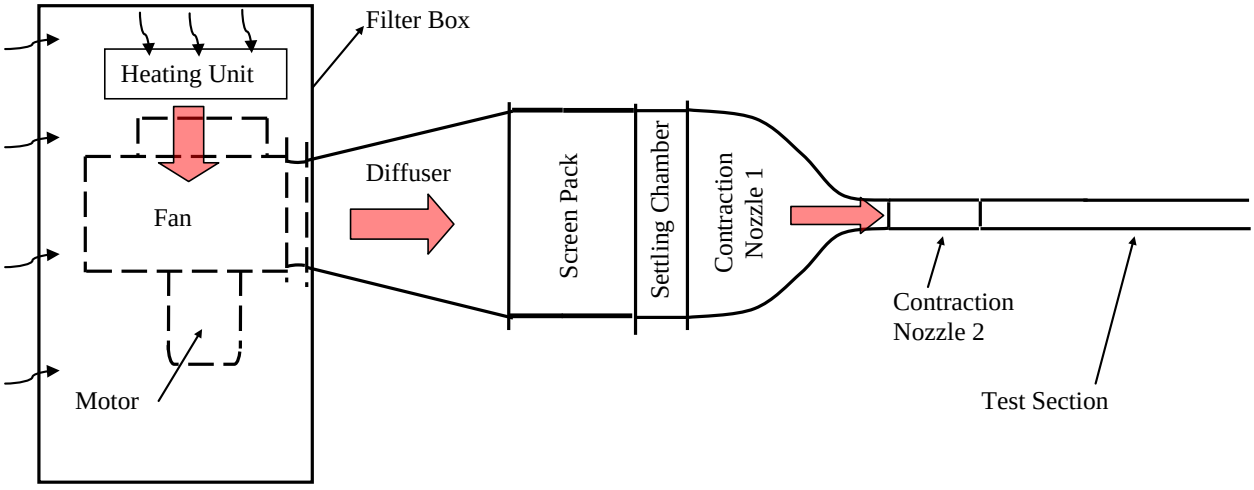

Figure 2.2 Plane view of the wind tunnel

Filter Box

To avoid the possibility of dust particles getting into the system, a filter box is constructed and the blower of the wind tunnel is enclosed in the filter box. The design goal of the filter box structure is to filter out particles larger than 5 μm, meanwhile minimizing the loss of pressure of the air going across the filter. A layer of polyester felt, manufactured by Buffalo Felt Products Corp., is used as the filtering material; and in order to reduce the large pressure drop across the thick felt, the filter box is specially designed to extend the felt surface area to the limit of the space available. Increasing

the surface area reduces the flow speed and consequently reduces the pressure drop across the felt.

The surface area of this box is about 10.22 m^2 (110 ft^2), and the flow speed across the felt at the maximum flow rate (3,000 CFM) is 0.15 m/s. The corresponding maximum pressure drop is approximately 5.08 mm (0.2 inch) H_2O. The box frame is constructed of 2″ x 2″ wooden bars covered with nominal 2-inch chicken wire to support the deforming force from the felt under suction force. A thin sheet of muslin cloth cover is placed over the felt to filter out the large-size dust particles. An observation window, constructed of Lexan glass, is installed so that the operator can visually check the heater condition inside the filter box.

Blower, Motor and Variable Speed Drive

The blower is an airfoil bladed fan by Cincinnati Fan powered by a 3-phase, 60 Hz, 230V, 3-hp motor directly driving the fan. At full load, the motor's speed is 1756 rpm. The operating point of the blower is at 3,000 CFM and 4 inches water column (static pressure). The blower is equipped with an inlet vane control, which offers a stable flow control at low speeds.

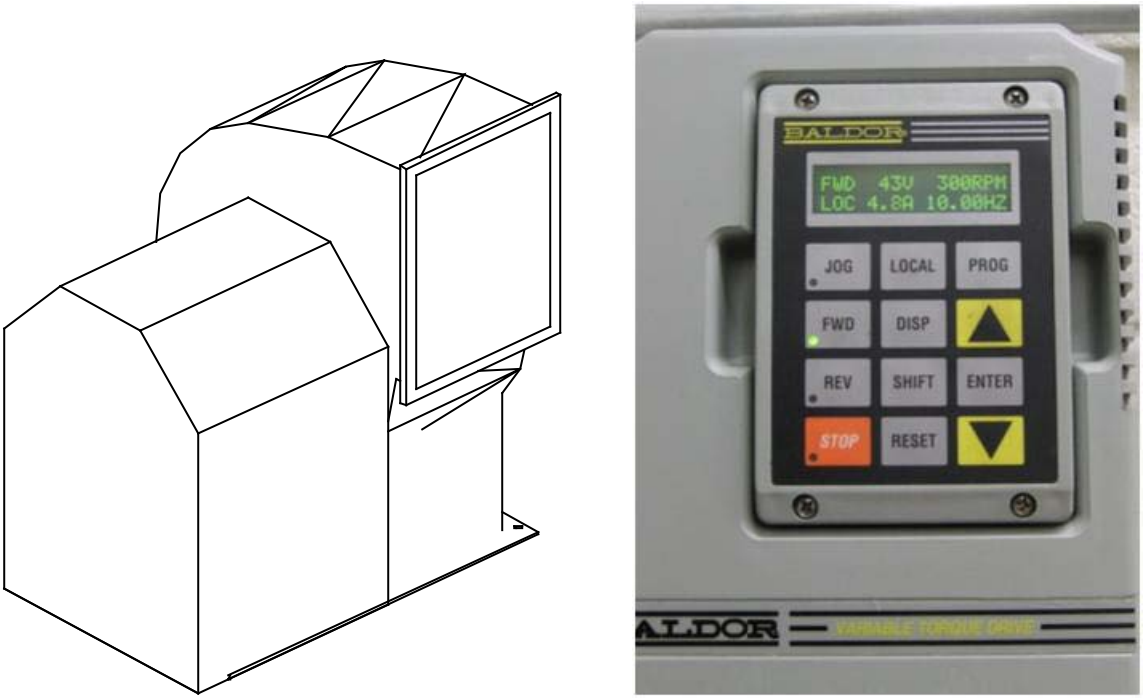

Figure 2.3 Fan, motor, inlet vane control and variable speed drive

A variable frequency, constant-torque motor controller (YASKAWA model GPD 506/P5)

shown in Fig. 2.3 is used to control the blower speed. It is a high performance AC motor drive modulated by sine-coded pulse width that generates an adjustable voltage/frequency three-phase output for complete speed control of the induction motor. The motor controller is equipped with automatic stall prevention with a voltage boost to prevent nuisance tripping during load or line side transient conditions.

Diffuser

The design considerations of the expansion section/diffuser are:

- Expansion angle less than 20° (limited by available space)
- Inlet inner area: 11-3/8" ×16-7/8"
- Outlet inner area: 2'×2'

The actual set up of the diffuser is shown in Fig. 2.4.

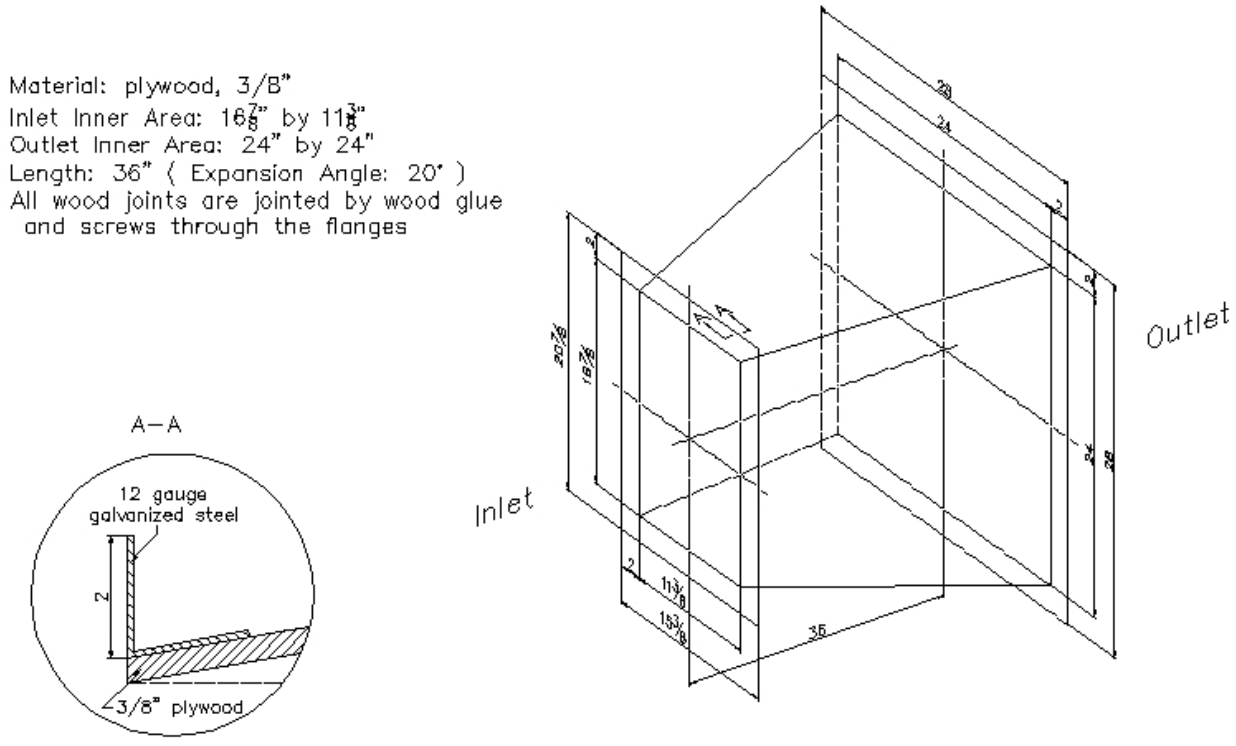

Figure 2.4 Diffuser design

Screen Pack

The screen pack serves as the flow straightener to break up the small eddies to make the

flow more uniform. The screen pack consists of four screen frames of three different mesh sizes. The screens are made of stainless steel wires and fastened with extruded aluminum frames. Their specifications are given in Table 2.1. The four screen frames are arranged in the order of 24, 30, 40, 40 meshes from upstream to downstream.

Table 2.1: Specifications of Wire Screen

Mesh Count	Wire	Mesh	Open Area Ratio
24	0.0090	0.0466	70.2
30	0.0075	0.0342	67.2
40	0.0065	0.0268	64.8

Extruded aluminum bars, 5 cm wide and 0.32 cm thick, are welded to form a rectangular frame with an inside dimension of 3 ft x 3 ft. Each screen is then riveted between two frames. The 7.62 cm wide U channel, formed by bending 0.16 mm (1/16 inch) thick aluminum plate, is spaced between each of two screens. The spacing between any two screens is 6 inches (15.24 mm), which is about 900-screen wire diameter long. This spacing allows enough distance for the wire-generated wakes to decay. A detailed drawing of the screen pack is also shown in Fig. 2.5.

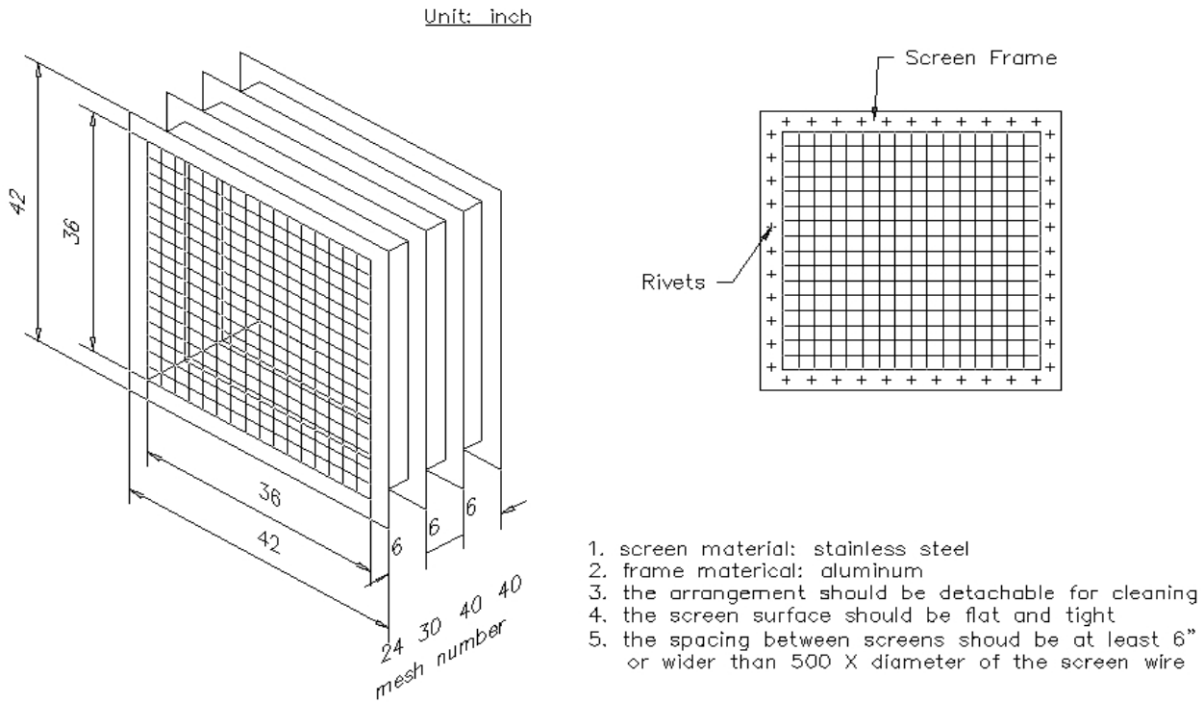

Figure 2.5 Screen pack

Contractions (Nozzles)

Contraction 1

This contraction is two dimensional with no convergence in vertical direction. The purpose of this first contraction is to convert the flow in a 2 ft x 2 ft cross-section to an almost two-dimensional plane flow with an aspect ratio of 6:1 and a cross-section of 0.6 ft x 2 ft. Its contour is designed by two cubic curves with inflection point (d^2y/dx^2 =0) at x/L=0.6. Here, L=22". The curvature of both inlet and outlet planes are zero and extended for 1". Contraction ratio is 24:1 with 2 feet in total length.

The curve is combined by two cubic polynomial curves:

$$Y_1 = a_1x^3 + a_2x^2 + a_3x + a_4 \quad (x<x_2)$$

$$Y_2 = a_5x^3 + a_6x^2 + a_7x + a_8 \quad (x>x_2)$$

The boundary conditions are,

$$Y_1(x_1) = Y_{01}$$

$$Y_2(x_3) = Y_{02}$$

$$dY_1(x_1)/dx = 0$$

$$dY_2(x_3)/dx = 0$$

$$dY_1^2(x_2)/dx = 0$$

$$dY_2^2(x_2)/dx = 0$$

$$Y_1(x_2) = Y_2(x_2)$$

$$dY_1(x_2)/dx = dY_2(x_2)/dx$$

Here, x is the axial distance from the inlet, x_1, x_2, x_3 are positions for the beginning of the first curve, the inflection, and the end of the second curve. Y_{01} and Y_{02} are the vertical distances from the axis to the beginning point of curve 1 and the end point of curve 2.

Matlab is used to solve these equations. The computer code and the results are listed in the Appendix.

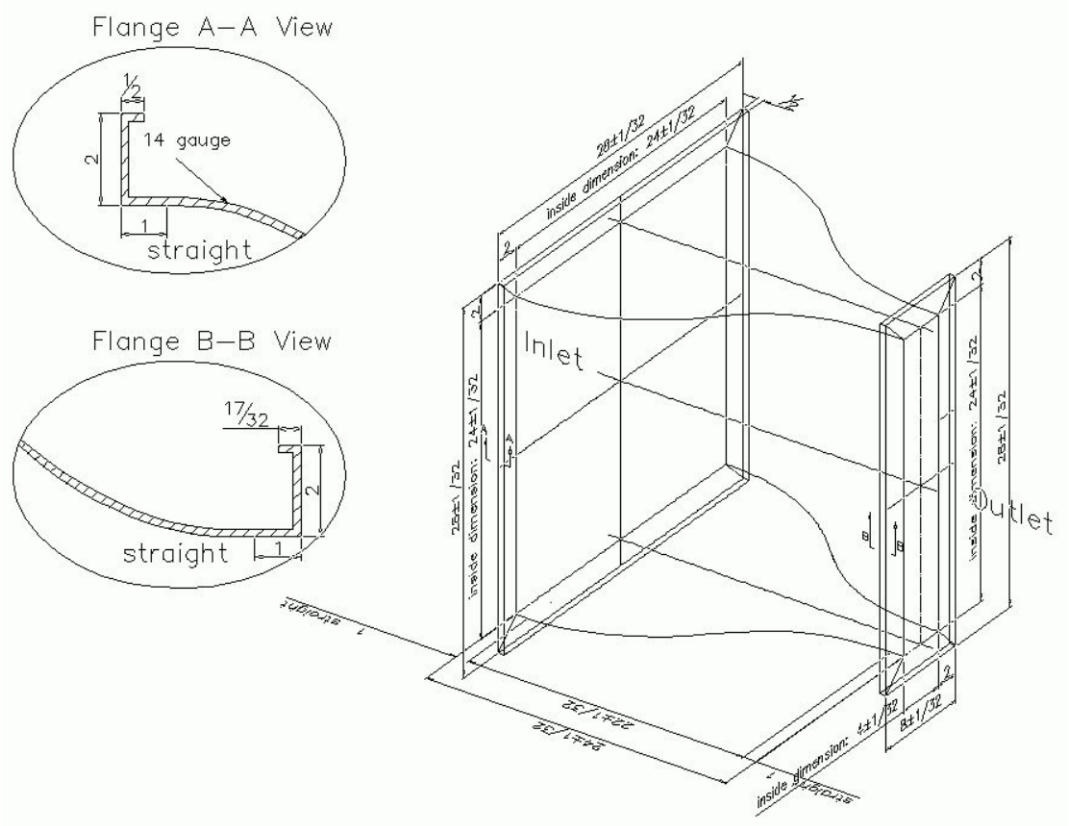

Figure 2.6 The first contraction design

Contraction 2

This contraction piece is also two dimensional, contracting in the vertical direction. The purpose of the second contraction is to convert the flow to the size of the test section. The design philosophy and procedures are the same as that of Contraction 1. The curvature and detailed coordinate are listed as following.

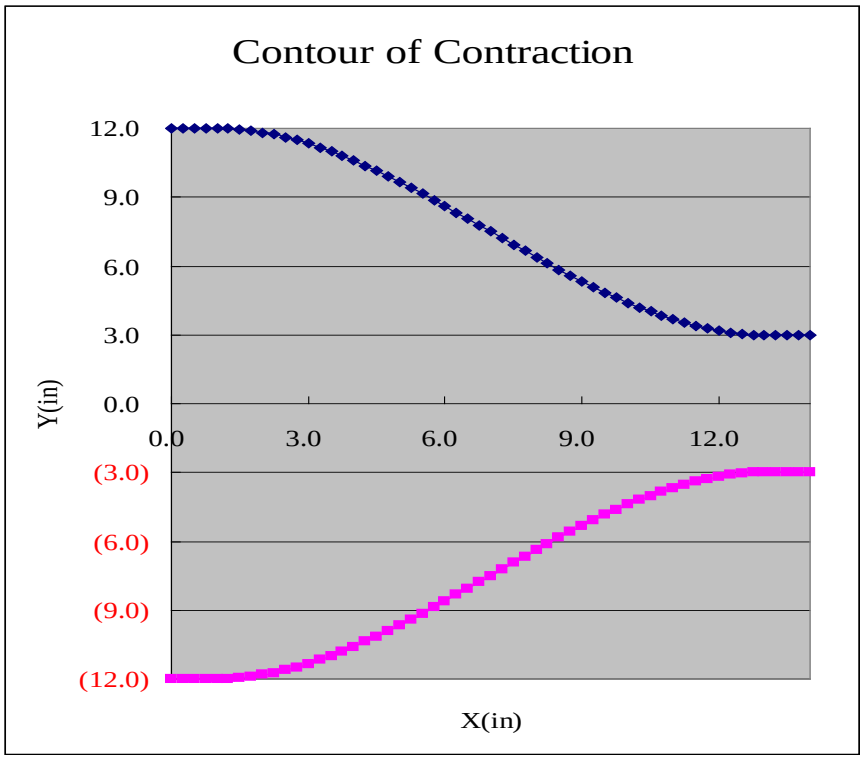

Figure 2.7 Contraction 2

Table 2.2 Coordinate of the 2D Contraction

(Function: $y=1/96\ x^3-3/16\ x^2+12$)

x(in)	y(in)
0.000	12.000
0.250	12.000
0.500	12.000
0.750	12.000
1.000	12.000
1.250	11.988
1.500	11.954
1.750	11.899
2.000	11.823
2.250	11.727
2.500	11.613
2.750	11.482
3.000	11.333
3.250	11.169
3.500	10.991
3.750	10.799
4.000	10.594
4.250	10.377
4.500	10.150
4.750	9.913
5.000	9.667
5.250	9.413
5.500	9.152
5.750	8.886
6.000	8.615
6.250	8.339
6.500	8.061
6.750	7.781
7.000	7.500

x(in)	y(in)
7.250	7.219
7.500	6.939
7.750	6.661
8.000	6.385
8.250	6.114
8.500	5.848
8.750	5.587
9.000	5.333
9.250	5.087
9.500	4.850
9.750	4.623
10.000	4.406
10.250	4.201
10.500	4.009
10.750	3.831
11.000	3.667
11.250	3.518
11.500	3.387
11.750	3.273
12.000	3.177
12.250	3.101
12.500	3.046
12.750	3.012
13.000	3.000
13.250	3.000
13.500	3.000
13.750	3.000
14.000	3.000

Suction Box

To remove the pre-established boundary layer in the expansion and contraction sections, a suction box is installed on the bottom of the test section inlet 2 inches upstream of the film injection holes. A perforated plate with holes of 1/8″ diameter and 3/16″ staggered center is installed on a 2” x 4” slot routed out from the test section. The plate is machined to flush with the test section surface to avoid tripping the boundary flow. The open area ratio of the perforated plated is 40%. Two layers of 18-mesh screen are installed in the suction box to improve the inlet

uniformity of the suction flow. A 24-inch flexible duct connects the suction box to a suction fan powered by a motor rated at 3/4 hp. The suction fan's operation condition is 324 CFM at 0.24 inch of water static pressure. Maximum suction flow rate can reach 20% of the main flow.

Heating Unit

As discussed in Chapter One, different experimental setups have been employed in simulating film cooling heat transfer scenarios, including heated surface, heated main flow, and heated secondary air. Through the investigation in the latter chapter, it is concluded in this study that the appropriate practice to set up the heat transfer experiment of film cooling is to have the main flow heated and secondary flow cooled, not the other way around. More detailed discussions can be found in Chapter Four.

A great deal of effort has been dedicated into generating a uniformly heated main flow. A first effort was made to inject heated air into the wind tunnel contraction section. The motivation for this practice is that it would be easy to accomplish without changing the wind tunnel setup. A settling box, made of aluminum sheet metal with heat guns mounted on the side walls, was inserted between the screen pack section and the contraction section. Heated air from the heat guns was injected into the chamber to mix with the main flow. However, the higher pressure of the main flow was dominant in such a way that the heated air from the heat guns could not be blown into the pressurized wind tunnel. As a result, the motor of the heat gun was overheated. Thus, this first effort was not successful.

A second effort was made using two units of duct heaters mounted inside the wind tunnel contraction section as shown in Fig. 2.8. Each unit had four heating strings, each rated 5kW at 240V. Both units were rewired to use 110V power source (from the wall plug). The total heat output was roughly 10kW. A 20 Amp circuit breaker for each heating string was used as the safety feature. The design consideration for this set up was that (a) mounting the heating unit inside the wind tunnel contraction could avoid modification of the upstream components including the fan, diffuser, honeycomb and screen pack sections; b) less heat is lost to the environment since only the contraction section is heated; c) avoiding potential hazards of melting the honeycomb made of plastic; d) avoiding wind tunnel bulk part expansion due to heating.

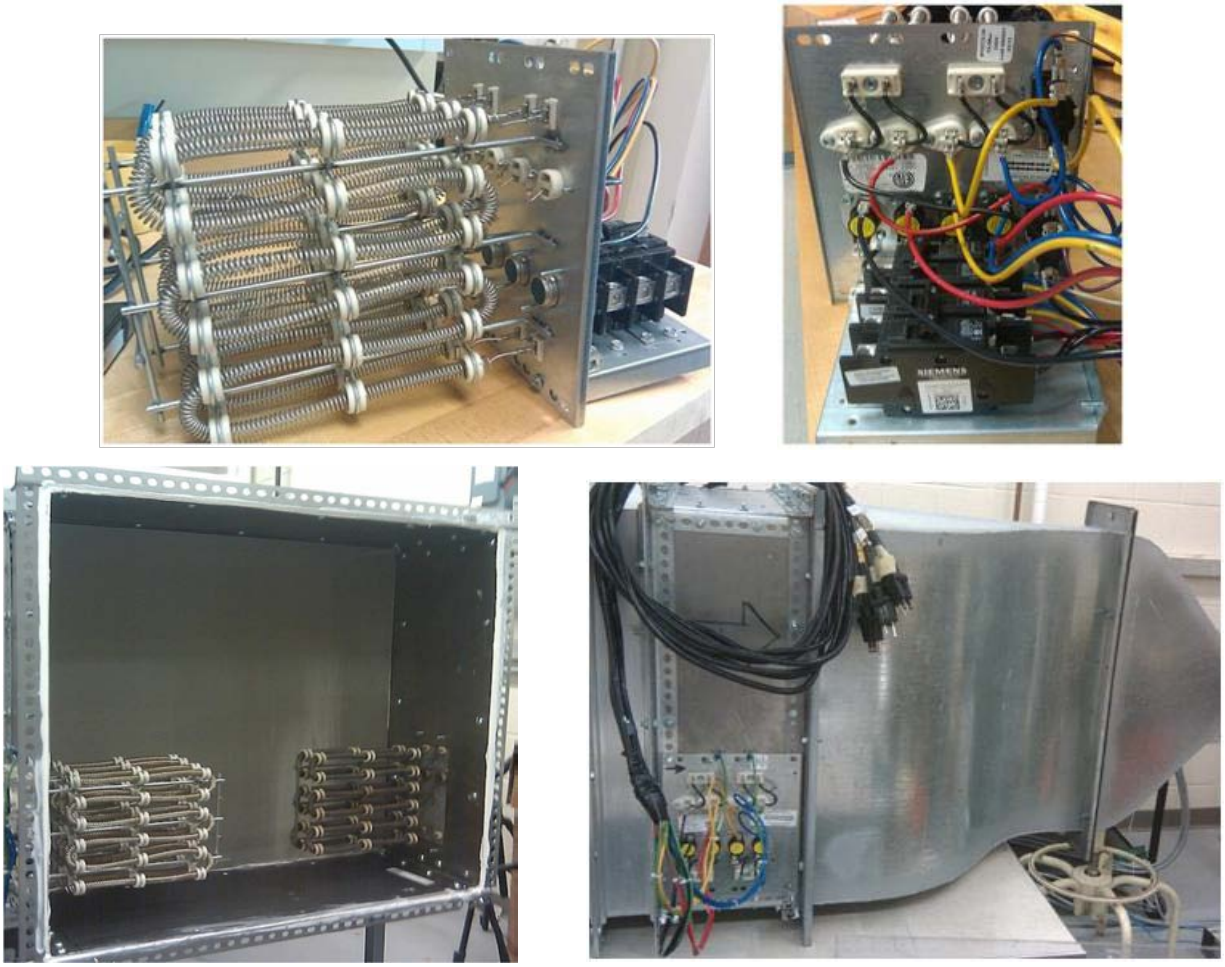

Figure 2.8 Preliminary heating elements and installation

However, there were two major problems associated with this approach. The first was that the inline heating elements generate disturbances to the flow field. This disturbance was especially noticeable near the bottom since there is always a gap between the heating unit and the bottom wall due to the installation requirement resulting in an accelerated flow in the region. The second problem was that the heat was not distributed uniformly in the main flow since only the air passing by the heating strings was heated. Also the contraction section was not long enough and had not been designed for the optimum mixing effect. As a result, the flow was not uniformly heated, and this effort was not successful either.

With the experience gained in those preliminary efforts, a heating unit consisting of 11 heat guns was placed in the filter box in front of the blower inlet. The advantages of this approach are:

- The rotating motion of the fan acts naturally as a good mixer, so that the air preheated by the heating unit can mix well with the main flow, generating a uniformly heated main flow.
- The suction effect at the fan inlet draws the hot air into the system naturally.
- Heating unit is mounted in the spacious filter box, thus the problem of confining the concentrated heat in a small space leading to overheating (as the potential safety concern in the practice two) can be avoided.
- Flow field is not disturbed since the heating unit is not inside the main flow passage.
- The main flow temperature uniformity is tested as $dT/dy<0.1\ ^{o}C$/inch, $dT/dz<0.04\ ^{o}C$/inch in the test section inlet.

2.1.2 Mist-Film Generation and Transportation

Compressed air from the building compressor is used as the secondary air. A spring-and-piston type flow meter (Omega FLMG-, Range 0-100 SCFM) is used to measure the secondary air flow rate (approximately 30 SCFM). A pressure gauge is installed between the flow control valve and the flow meter to monitor the inlet air pressure.

Compressed air is cooled in an ice chest (120 Quarts, 38¼" L x 17.38" W x 18.06" H) with a 2 inch thick insulation wall. Air passes through a copper coil (3/8” OD, 1/4” ID, and 6’ long) placed in the chest filled with ice and water mixture.

A pressure atomizing system, provided by Mee Industry Co, is adopted in this study to generate mist. The system consists of a water filter, a high pressure pump, and a nozzle. Filtered water is compressed to a pressure up to 1500 psi by a motor (Baldor Industrial Motors, 3/4 hp) and then goes through the nozzle to be atomized. The nozzle consists of a stainless steel body with ruby-orifice, impingement pin, and extended polypropylene filter to avoid trapping particles in the base of the nozzle. High-pressure water reaches the nozzle, shooting a fine liquid jet against an impingement pin resulting in atomization. Discussion of different atomizers can be found in the study of Guo and Wang (2001).

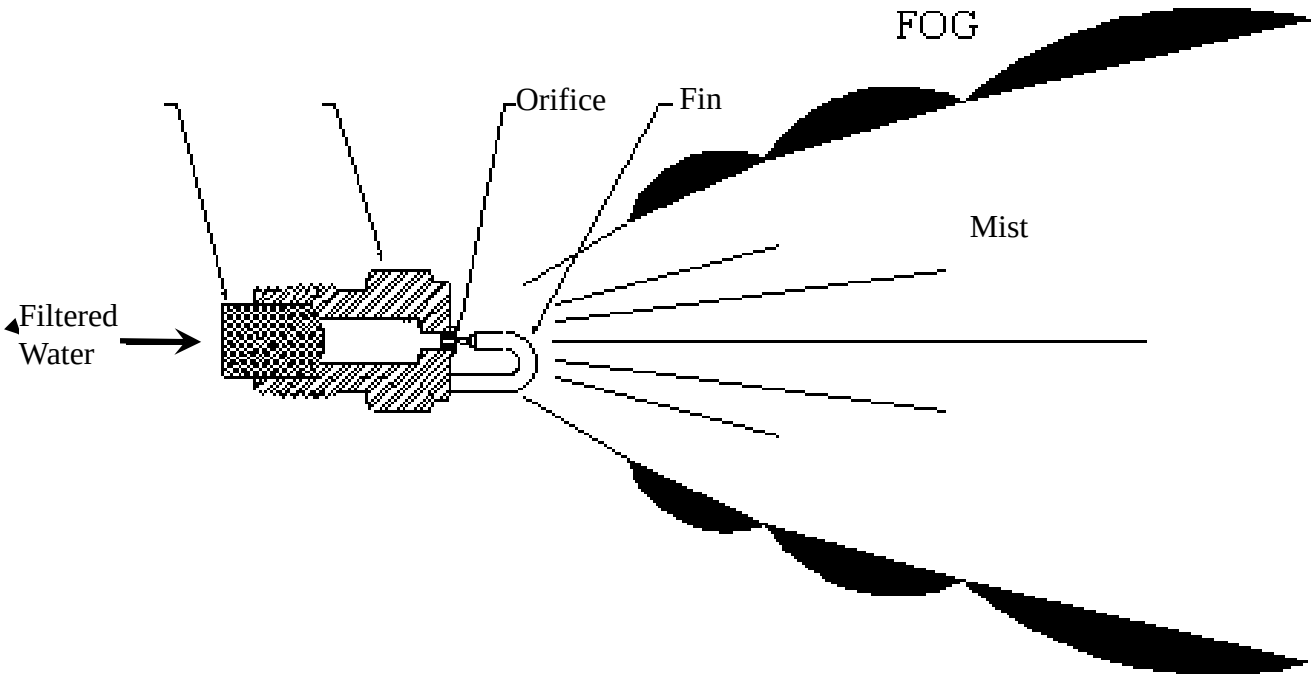

Figure 2.9 Atomizer (Mee Industry, Co.)

A mixing chamber is used to blend mist from the atomizer with the coolant air. Detailed design of the mixing chamber is shown in Figure 2.10. Both the compressed air injection and the mist-generating atomizer are located at the bottom of the mixing chamber. The top part of the mixing chamber serves as the blender. Excessive water condensate inside the mixing chamber is drained out and re-cycled for mist generation. The bottom of the mixing chamber is inclined toward the drainage hole to prevent water from accumulating at the bottom plate. Water congestion at the bottom plate needs to be avoided because it is detrimental to the mist size control. When the compressed air breaks up the water layer at the mixing chamber bottom (due to water jamming), the process is highly random. As a result, random sized mist particles are generated, which is hard to control.

One technical challenge identified through the preliminary tests is the droplet agglomeration problem. When the water mists land on a solid surface, if the air speed is not fast enough to blow them off quickly, mists will agglomerate and form big water drops or a water film on the surface. When the water drops reach certain size, they will be either be broken up into random sized water particles by the shear stress of the air passing by or be entrained into the film

injection hole and slowly creep out to the test section surface. As stated in the drainage hole design, the breaking up of the big water drops or water film will result in random sized water drops, which is hard to control. The creeping out water will eventually become water streaks moving on the test surface, which will disturb the temperature measurement. Both of these effects should be minimized.

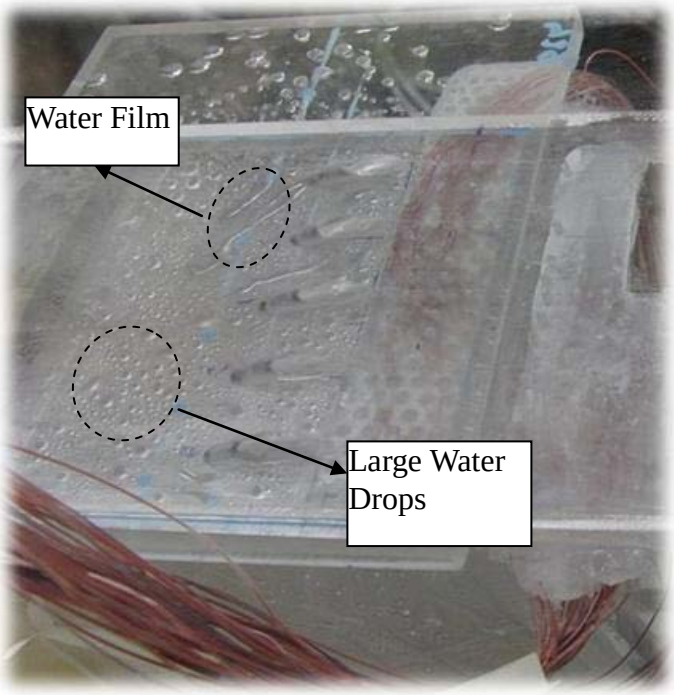

Figure 2.10 Test piece with agglomerated water drops and water film hanging on the bottom surface of the test section

Many different practices have been designed and tested to resolve the mist agglomeration problem. The design process is an art work in nature and requires a lot of trial and error. The principles for the design process are:

- preventing the air-mist flow from shooting directly at the film hole inlets;
- directing the flow to go over multiple flat surfaces so that agglomeration can take place before reaching the injection plate;
- directing the flow field near the injection plate so that, right before entering the film holes, the film/mist mixture has a velocity direction roughly parallel to the injection

hole internal surface.

In this way, mist agglomeration near the injection holes is found to be minimized.To accomplish the design goal of minimizing water drops and water film accumulating near the film hole inlet, three stages of inserts have been added into the mixing chamber.

The first stage is a perforated plate placed 2 inches on top of the atomizers. The purpose of the perforated plate is to

- block and deflect large water drops/clouds entrained by the strong air jet;
- divide the mixing chamber into sections, preventing recirculation of water drops;
- increase the pressure resistance so that the chamber is pressurized and so that the mist flow will be pressure driven and achieve better uniformity. Otherwise, the inertial driven flow would directly hit the film injection hole inlet from the bottom.

The second stage is the main flow blocker. The purpose is to channel the mist/film mixture to go over multiple surfaces so that mist agglomeration can occur in an earlier stage before reaching the film hole inlets. It is noted that a 1/4 inch gap is left purposely on the front and back side of the mixing chamber so that the water returning from the blocker can run down along the walls to the drainage to avoid being re-entrained by the jet (as shown in Fig. 2. 11). Also as shown in Fig. 2.11, looking from the bottom of the mixing chamber, the film injection holes are not visible. This means that the air water mixture is blocked and cannot shoot directly at the film holes which will cause the water film problem as occurred before installing the blocker piece.

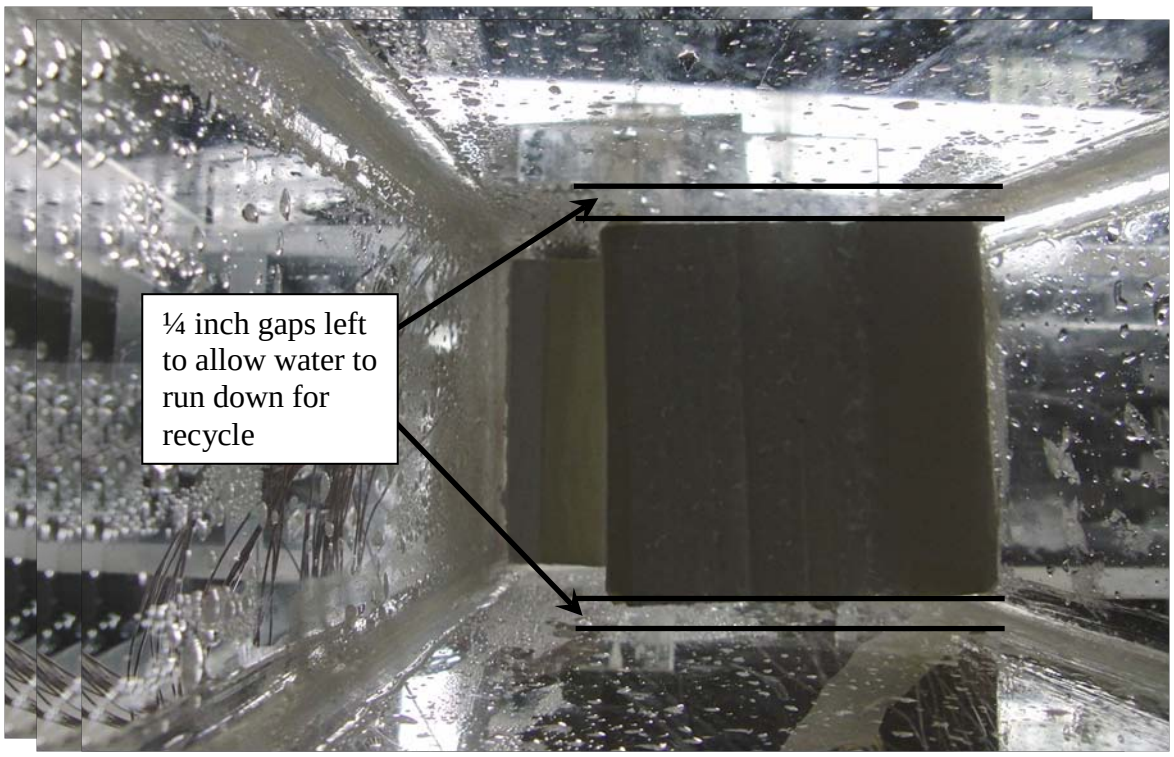

Figure 2.11 Bottom view of the mixing chamber (perforated plate is removed for clarity)

The third stage is the side blockers, serving as the flow guide and insulator. The flow is guided in line with the film hole direction before entering the holes. Also, the side blockers serve as insulators to insulate the film injection plate from the bottom.

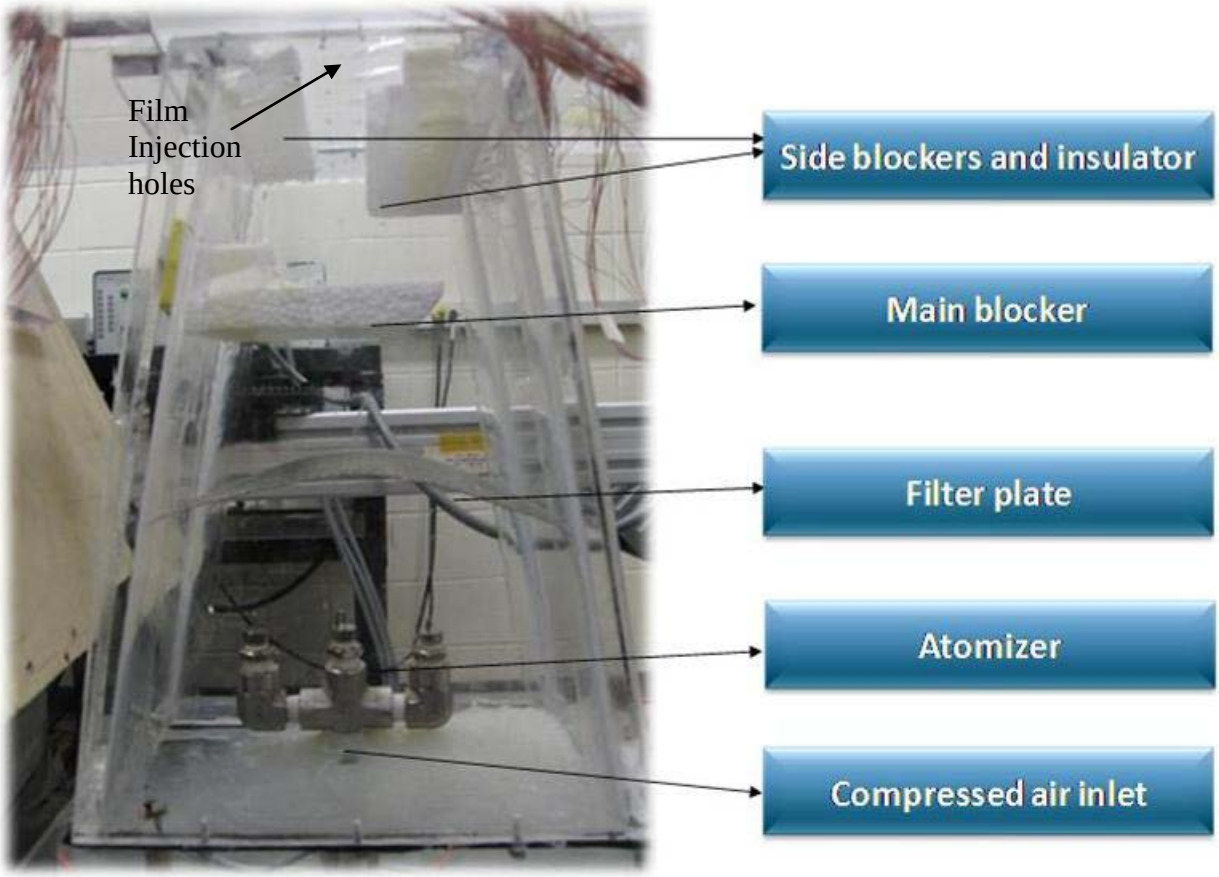

Figure 2.12 Structure of mixing chamber, Note that the top wall of the mixing chamber is the bottom of the test wall.

(Before) (After)

Figure 2.13 Effect of adding the 3-stage mixing chamber structure

2.1.3 Test Section

The test section is designed for studying the mist cooling scheme performance on a flat plate with cylindrical holes. Transparent acrylic sheet (manufactured by Piedmont Plastics Inc.) is used to construct the test section with the wall thickness of 0.354 inches (0.90 cm). The test section is a 4" (width) x 6" (height) x 24" (length) constant area channel. The bottom surface is the test surface where the thermocouples are mounted to measure the surface temperature. A special, partially open-top (4 inches x 12 inches) test section design is implemented to accommodate the use of an infrared camera to measure surface temperature and cooling effectiveness. The main purpose of this practice is to remove the issues associated with the infrared waves passing through window material for infrared camera measurement of test surface temperature. The wavelength range sensed by the infrared camera is 8-14 μm. Before making the decision of adopting the partially open-top practice, four materials which can pass the infrared wavelength are considered: Quartz, Zinc Sulfide, Zinc Selenide, and an

IR plastic film (material composition is not given) from Edmond Optics. The first three materials were too expensive and not adopted. The transmissivity of the Edmond IR plastic film (0.457 μm thick) varies from 0.4 to 0.6. It was used for about 6 months for conducting preliminary experiments. Due to its low transmissivity, the infrared signal's strength is weak, and the background noise is high, which leads to a low confidence level of the acquired temperature data. Therefore, it is decided that no material will be used for the window--i.e., the partially open-top practice is adopted.

However, to ensure that the open-top design does not adversely affect the main flow condition in the test section, an effort is made to compare the velocity profiles between the close-top and open-top conditions. The result indicates the main flow change is negligible. Actually, for the purpose of this study for comparing the result of air-only with air/mist cases, there is no need to compare the velocity profiles between close-top and open-top conditions as long as the velocity profiles are identical during the air-only and air/mist experiments. Nonetheless, the study of evaluating the open-top design effect on the flow field is documented in Appendix C.

Five cylindrical holes with an inclination angle of 30^o are employed to inject mist/air film. A special slide-in piece design is implemented to allow convenient interchanging of the test pieces with different film hole geometries without changing other setups. A 2-inch wide trench in the slide-in piece, covered with a metal sheet, is carefully manufactured to accommodate the proper mounting of the thermocouples without breaking the wires during the installation process. The trench is filled with silicon glue to glue the thermocouple junctions to the bottom of the trench wall.

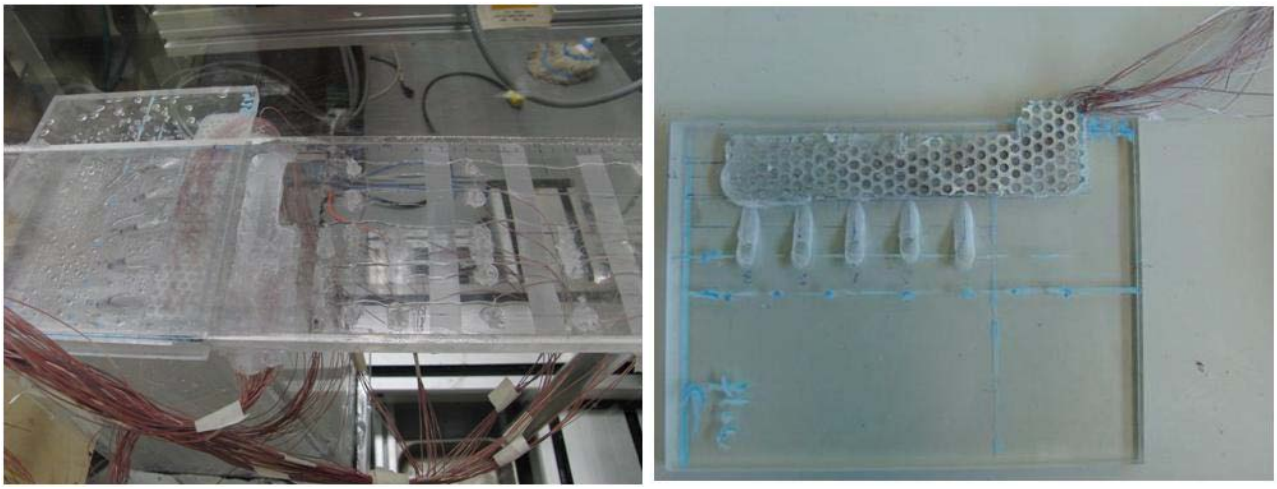

Figure 2.14 Test piece

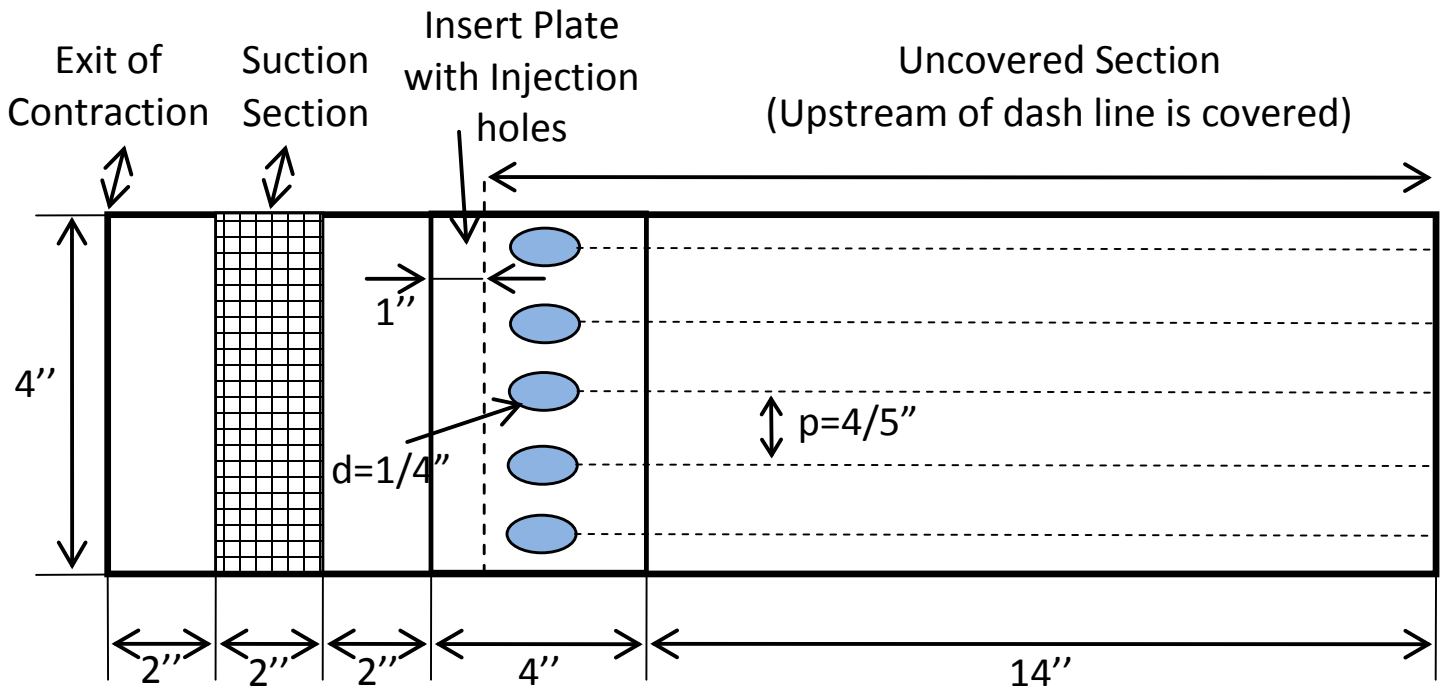

(a)

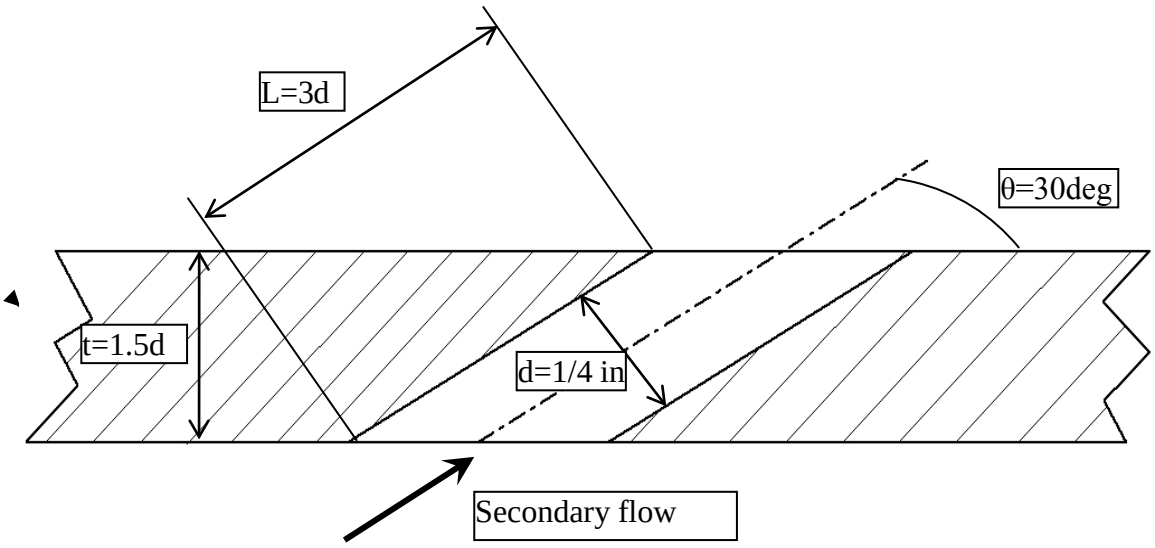

(b)

Figure 2.15 Test Section Setup (a) top view (b) film injection hole details

2.1.4 PDPA System

Particle (water droplets) sizing is an important part of this program since the particle sizes and their distribution play an essential role in determining mist film heat transfer and cooling effectiveness. A large number of particle sizing methods have been developed in the past (a review can be found in the paper by Swithenbank, 1991). A Phase Doppler Particle Analyzer (PDPA) system, invented by Bachalo in the 1980's (Bachalo, 1980; Bachalo and Houser, 1984), is used in this study.

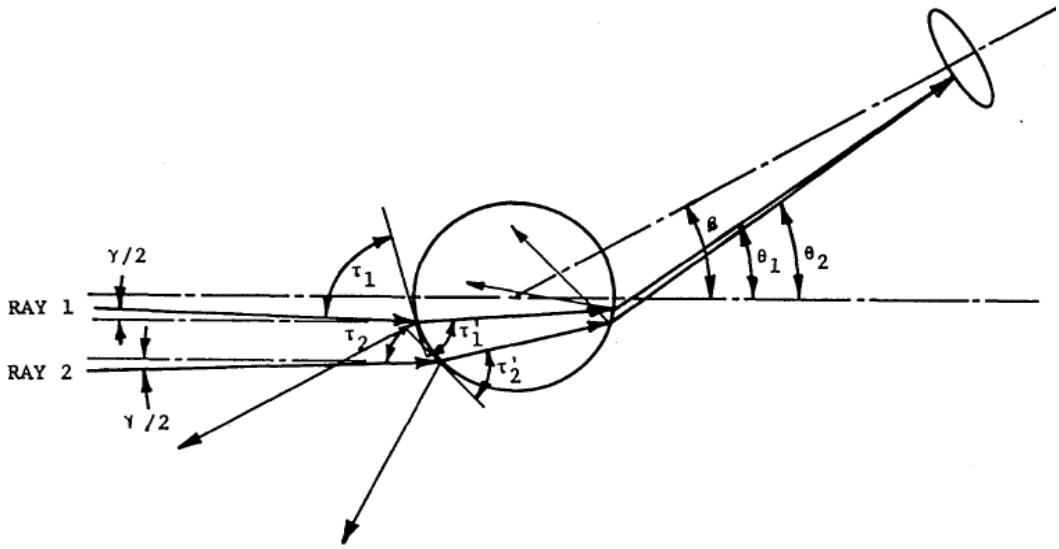

Figure 2.16 Film injection hole details

The Phase Doppler Method is based upon the principles of light scattering interferometry. Two collimated, monochromatic, and coherent laser beams are made to cross at a point (measurement point), where they interfere and generate light fringes. A particle moving across the fringes will reflect light, which is picked up by a receiving lens located at a certain off-axis collection angle. A set (usually 3) of detectors in the receiver is used to capture the signals. The temporal frequency of the signal is used to determine the particle velocity, and the spatial frequency can be used to calculate the particle size.

Based on geometric optics, the relative phase shift for any incidental light passing through a spherical droplet can be calculated by the following equation (Bachalo and Houser, 1984):

$\phi = 2\alpha \cdot (\sin\tau - m\sin\tau')$,where ϕ is the relative phase shift between any light passing through the droplet and a theoretical, reference light undergoing no phase shift; α is the non-dimensional size parameter, $\pi d/\lambda$, in which d is the droplet diameter, and λ is the wavelength of the incident light; τ is the angle formed by the incident light and the surface tangent of the droplet; τ' is the angle formed by the first refracted light and the surface tangent of the droplet; m is the relative (to air) index of refraction for the droplet.

The measurement volume is the body bounded by the ellipsoidal surface shown in Fig. 2.17, and it corresponds to the surface on which the light intensity of the fringes is $1/e^2$ of the maximum intensity, which occurs at the center of the measurement volume. This width definition

is also called the D86 width. If the light intensity profile follows a circular Gaussian profile, when it is integrated down to $1/e^2$ of its peak value, it contains 86% of its total power. Fringe spacing decreases with increasing angle κ.

NFR = number of fringes

V = volume of measurement volume

d_f = fringe spacing

d_m = diameter of the measurement volume

l_m = length of the measurement volume

f= focal length of the lens

λ= laser wavelength

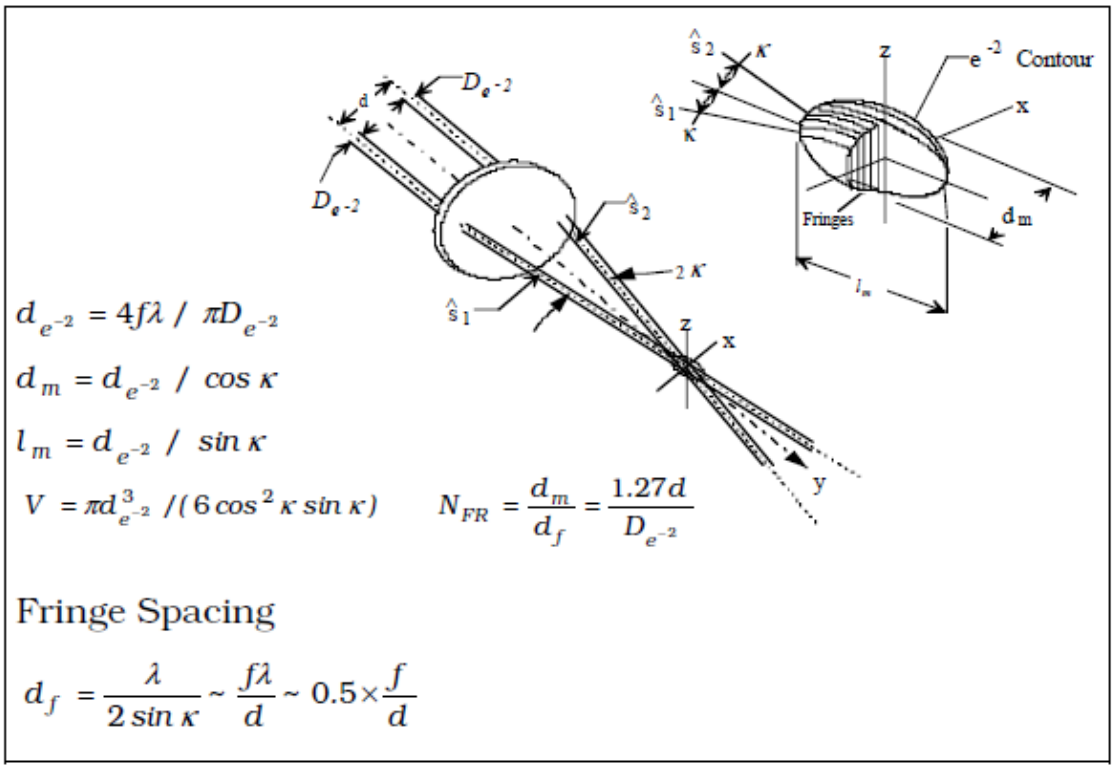

Figure 2.17 Film injection hole details

It is noted that one distinguished feature of Phase Doppler measurement, compared with conventional interferometric techniques such a Laser Doppler Anemometry (LDA), is that the change in phase is independent of the incident intensity or scattering amplitudes of light, but is directly proportional to the droplet diameter. PDPA measures the relative phase shift of the Doppler signal directly as a linear function of the droplet diameter. As such, PDPA measurements

are dependent on the wavelength of the scattered light, which is not easily affected by environmental conditions. This feature gives PDPA measurement a clear advantage over the conventional intensity based measurement method which is sensitive to background noise.

Another noted feature of the PDPA system is that its detector is commonly placed off the plane of the transmitting beams at an angle close to 30^{o}. This is because the intensity of the scattered light, which affects the Signal-to-Noise Ratio (SNR), can vary by several orders of magnitude depending on the receiving angle and the droplet concentration. Figure 2.18 shows the variation of the scattered light intensity as a function of receiver position for polarization perpendicular to the beams. The intensity values are obtained from the Mie scattering calculations. Generally, within the angle of 0^{o}-20^{o} off the transmitting axis, light is scattered primarily by **diffraction,** which contains no information for the PDPA process. At an angle between 20^{o}-90^{o}, which is called the forward-scattering region, the scattered light, mostly by **refraction** for non-opaque droplets, has the highest SNR, thus the size sensitivity is the best.

For some conditions, this forward-scattering configuration is difficult to traverse and the optical accessibility is poor because the transmitting and receiving optics are on the opposite side of the flow. For angles between 90^{o}-180^{o}, which is called the back-scattering region, most light will be scattered by **reflection**, which has an SNR higher than the forward-scattering. However, the optical accessibility and traversibility of the back-scattering configuration are better since all the optics are on one side of the measuring point, requiring only one window and providing easier traversing arrangement of the LDV system. In this case, the same lens is used for focusing the two beams and for collecting and collimating the scattered light. For PDPA application, the forward-scattering method must be used due to the special need to receive the strongest signal at about 30^{o} from light refraction caused by particle sizes.

The existing PDPA system has a fiberoptic probe with a focal length of 350 mm and a beam waist diameter of 115 μm. The beam spacing for the probe is 50 mm. The focal length of the receiver for the PDPA system is 500 mm. The laser system is an Argon-Ion type water cooled system with 4 watt maximum power output.

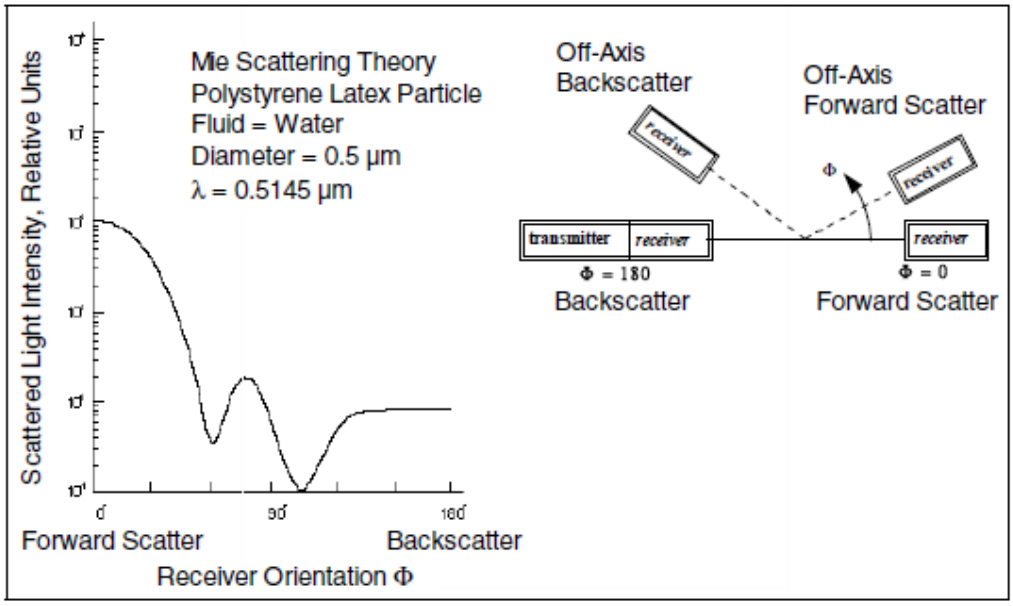

Figure 2.18 Film injection hole details

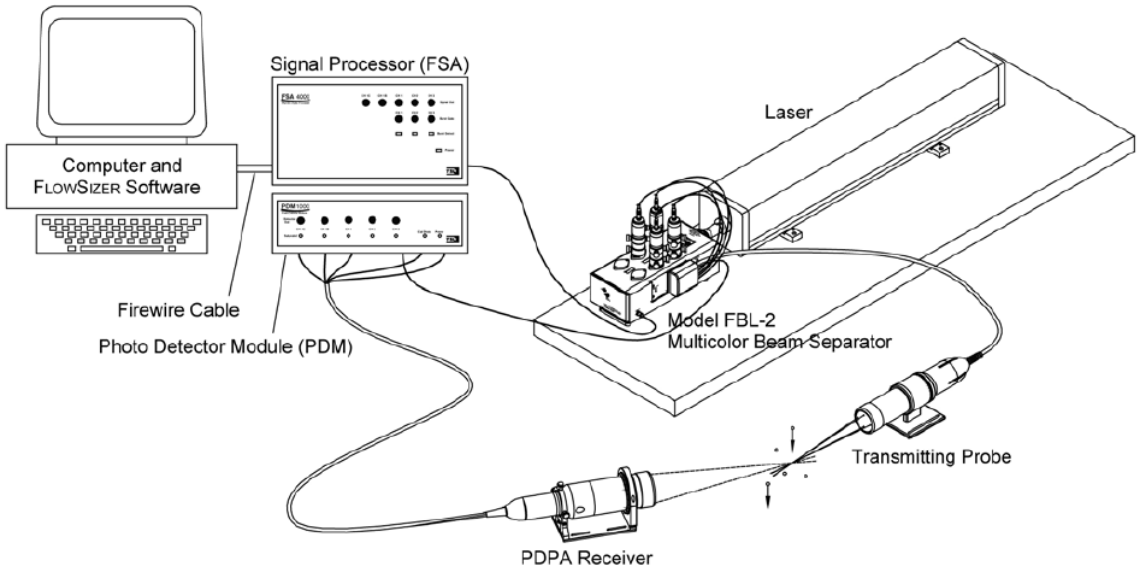

(a)

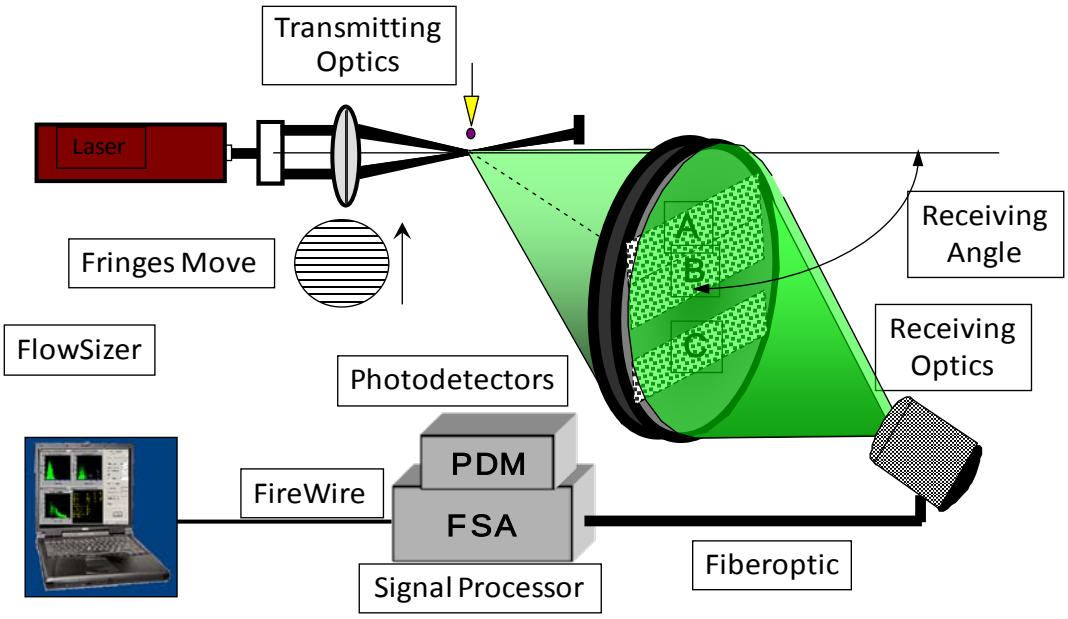

(b)

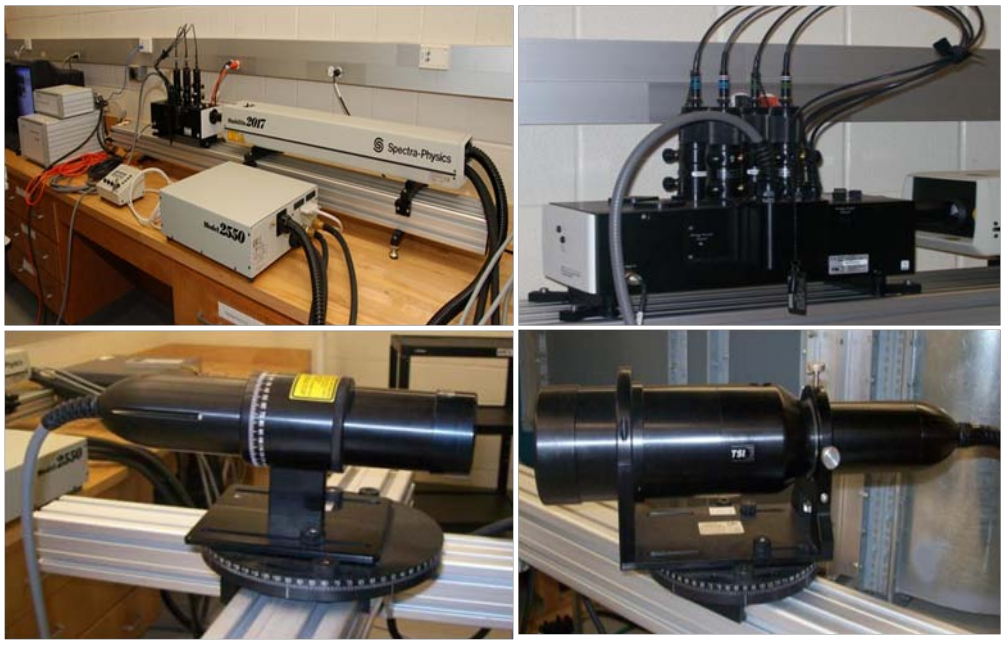

(c)

Figure 2.19 PDPA system overview (a) a schematic of complete PDPA system (b) a schematic of PDPA transimmitng and receiving layout (c) Photoes of the PDPA system for this study

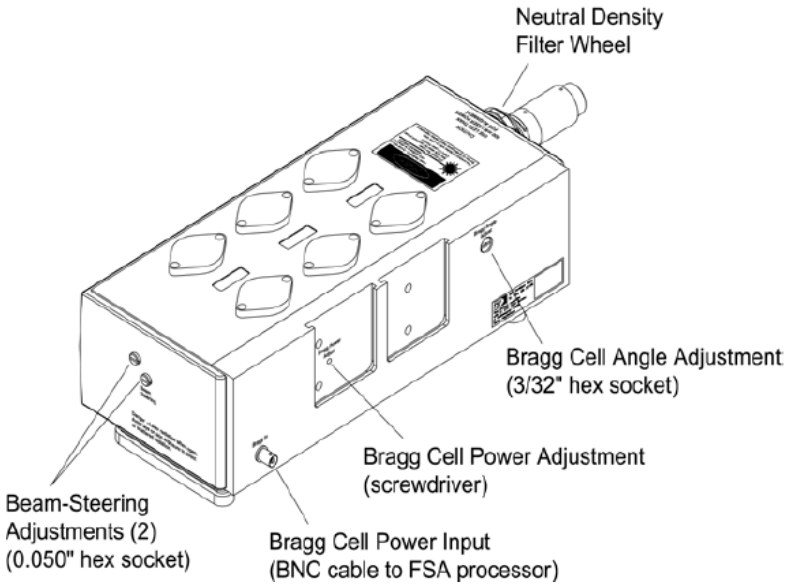

(a)

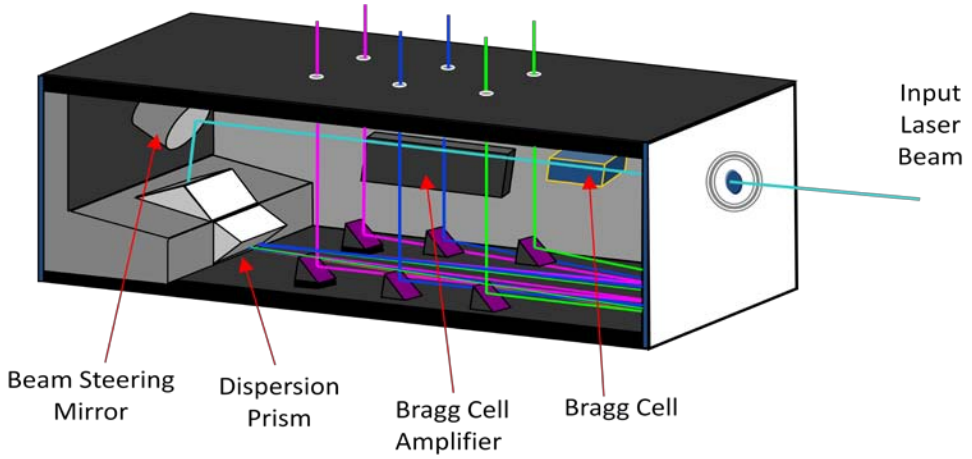

(b)

Figure 2.20 PDPA bragcell (a) Outisde look (b) Inside structure (TSI manual, 2007)

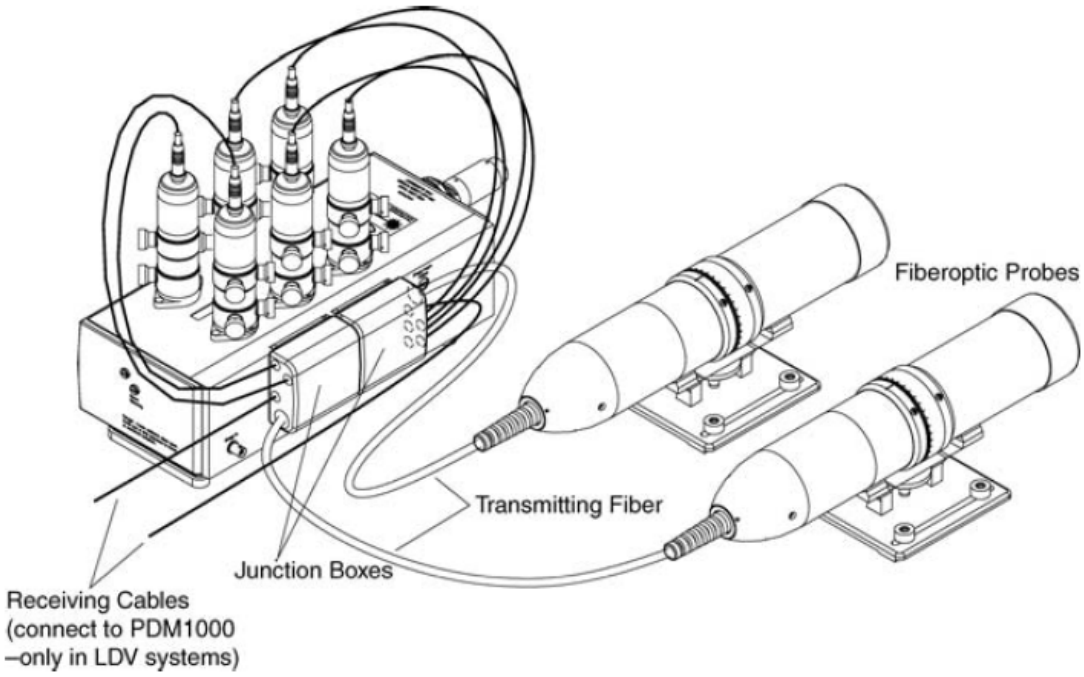

(a)

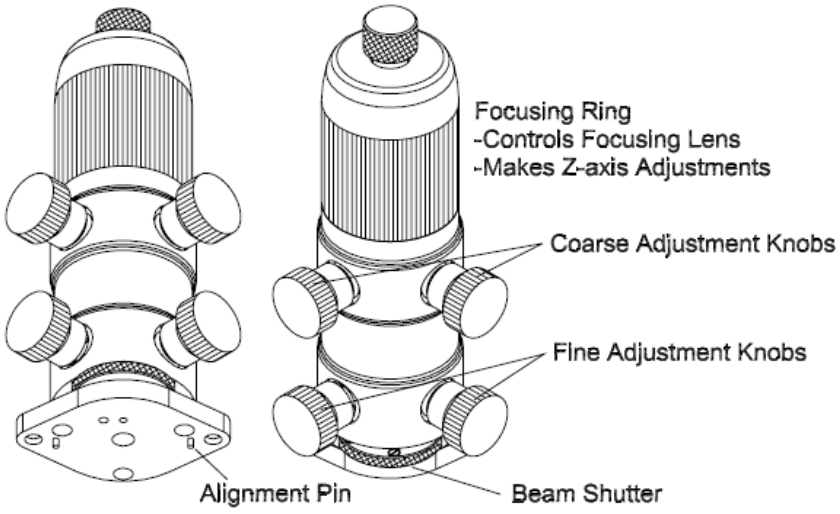

(b)

Figure 2.21 PDPA coupler (a) Connection with other parts (b) Adjusting knobs detail (TSI manual, 2007)

2.2 Instrumentation

This section includes the instrumentation for measurements of particles, temperature, flow,

and pressure.

2.2.1 Particle Measurement

Before taking the mist/air film heat transfer data, the PDPA system is verified against Polymer Latex particles (manufactured by Duke Scientific Corp.) of known-sizes. These particles, with moderately low standard deviations for a given size, are microspheres with a density of 1.05 x 10^3 kg/m^3 and a light refraction index of 1.59 at 590 nm. The verification process is performed by putting the Polymer Latex particles into a container made of the acrylic sheet with the same thickness as the test section wall. By doing so, the plastic window effect on the particle measurement as that would be included during the real test section measurement will be evaluated. The container is filled with water and the particles are suspended in the liquid. A small propeller driven by a mini-motor is immersed in the container. The purpose of the small propeller is to induce particle motion in the water so that a certain number of particles can be captured passing through the measurement volume to generate enough data rate in the PDPA measurement system to satisfy the requirement for statistical purposes. Three different particle sizes are used. Figure 2.18 shows the result of the PDPA measured particle sizes compared with the true particle sizes. It can be seen that in the size range of 2~40 microns, the measured particle sizes from PDPA agree well with the actual particle sizes. It is noted that the container wall (made of acrylic sheets) does not have a significant effect on particle size measurements.

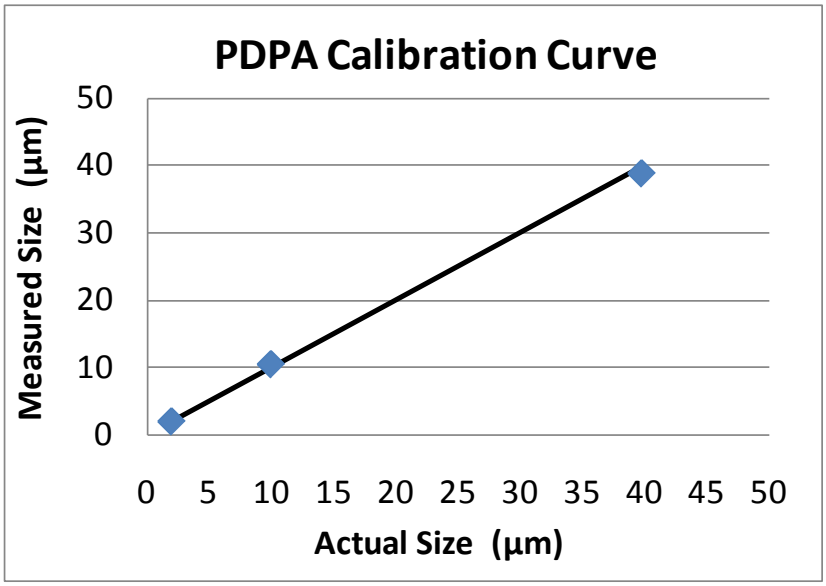

Figure 2.22 Calibration of the PDPA measurement with the mono-sized polymer latex

particles.

Droplet Size Measurement

PDPA is essentially a point measurement system. It measures the droplet size and velocity across the measuring volume during a certain period of time. To obtain the droplet size distribution, the PDPA system is traversed in the test section by means of a specially designed traverse system which synchronizes the movement of the transmitter and the receiver of the PDPA system. It is noted that, for this study, the droplet density is a function of both location and time. A great change in the particle density exists within the test section. As a result, the rate of particles being captured by the PDPA per unit time can vary from less than 10 Hz to more than 20,000 Hz. For different data rates, the set up of the PDPA operation parameters and signal filtering criteria need to be adjusted accordingly to correctly measure the particle sizes and velocities. A few rules of thumbs for adjustments based on the operator's experience are summarized below.

- It is always suggested to have a rough idea about the size distribution and velocity range of the particles to be measured, which provides necessary information to estimate the values of parameters to be used in the measurements.
- It is very important to check the laser light's alignment often. The data rate is quite sensitive to how well the laser light beams are aligned, and the alignment can be easily off even by the slightest vibration during traversing process (Fig. 2.19). When the data rate is really low or there is no data at all after adjusting the receiver location/angles, it is suggested to check the laser alignment as a possible culprit.

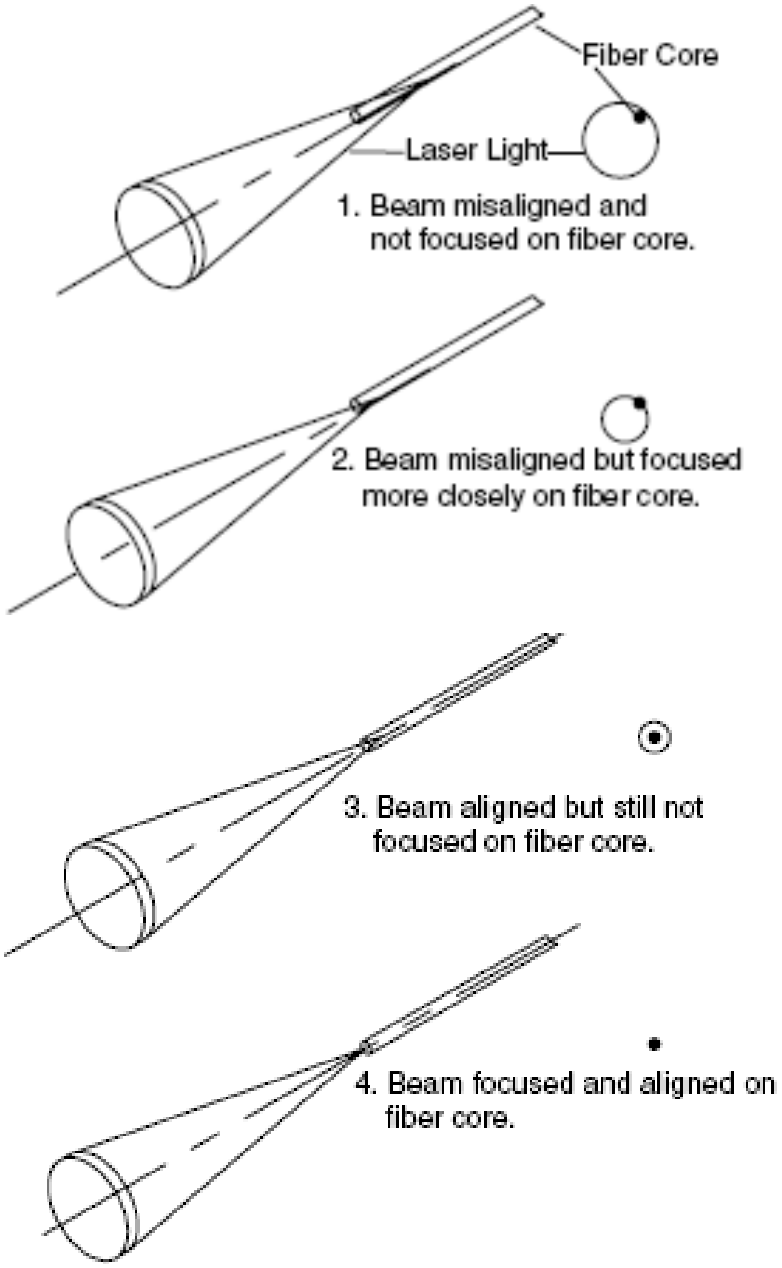

Figure 2.23 Laser beams alignment correction

- A reasonable combination of down-mixing frequency and signal filtering range is essential in getting correct velocity data. Checking the history plot for data frequency is helpful in identifying whether the setup is reasonable. Another tip is to check the data rate change corresponding to different setups. A sharp decrease in data rate usually suggests meaningful data has been filtered out incorrectly, and vice versa.

- Adjusting PMT voltage is often necessary based on the particle sizes. Higher PMT (600~1000 volts) is needed to capture particle less than 10μm but it will induce higher noise since reflection signals are amplified as well.
- High PMT voltage in some conditions will result in signal saturation (1000mv for the system used in this study) for big particles even though it captures the small particles better.

Mean Droplet Sizes

The most important parameter which represents the droplet characteristic is the mean diameter of the droplets. The mean droplet diameter can be evaluated in various ways. The most commonly used mean diameter is the Arithmetic Mean Diameter (d_{10}):

$$d_{10} = \frac{\sum_{i=1}^{n} d_i}{n}$$

Where n is the total number of droplets.

Other commonly used mean diameters are the Area Mean Diameter (d_{20}), Volume Mean Diameter (d_{30}), and the Sauter Mean Diameter (d_{32}) which represents the ratio of volume to area:

$$d_{20} = \sqrt{\frac{\sum_{i=1}^{n} d_i^2}{n}} \qquad d_{30} = \sqrt[3]{\frac{\sum_{i=1}^{n} d_i^3}{n}}$$

$$d_{32} = \frac{\sum_{i=1}^{n} d_i^3}{\sum_{i=1}^{n} d_i^2}$$

Obviously, if all the droplets are of the same sizes, then $d_{10} = d_{20} = d_{30} = d_{32} = d$. For droplets with different sizes, d_{10}, among all the mean diameters, has the smallest value, while d_{32} has the largest. Generally, d_{10} represents the diameters of most droplets; d_{32} represents the diameters of large droplets. For example, if we have 10 spherical droplets with 9 of them having diameters of 1, and 1 having a diameter of 10, then $d_{10} = 1.9$, $d_{20} = 3.3$, $d_{30} = 4.7$, and $d_{32} = 9.3$.

2.2.2 Temperature Measurement

Two methods of temperature measurements are utilized in this study: thermocouple measurements and infrared thermograph measurement. Generally, a thermocouple has a more accurate measurement capability and yields less uncertainty than the infrared thermograph measurement. However, a thermocouple measurement is essentially a point measurement. The space resolution is limited by the necessity of keeping the surface condition and heat transfer path intact, as well as being limited by the capacity of the thermocouple instrumentation. Also, a great deal of effort is required to install the thermocouples underneath the test piece, especially when the bottom of the test piece is not easily accessible. On the other hand, infrared measurement is easier to accomplish. Moreover, it gives the information of the complete surface (within the view angle) which enables one to generate useful contour plots. This information is essential in evaluating a continuous cooling coverage on the surface. However, infrared measurement suffers from lower accuracy (smallest detectable temperature variation is about 0.1 ^{o}C) and high uncertainties because of the varying values of the surface emissivity condition due to uneven surface properties, surface oxidation, and non-uniform surface temperature. In this study, the emissivity changes abruptly if the surface is wet with traveling liquid droplets. A combination of both measurement methods used in this study enables one to conduct a more informative analysis. Since an accurate infrared measurement is more sensitive to the variation of surface emissivity, the thermocouple measurements also serve as the in-situ calibration standard for the infrared measurements.

The overview of the temperature measurement system is shown in Fig. 2.20. All of the temperatures are measured by using E-type (chromel-constantan) 36 gauge (0.01 inch) thermocouples, manufactured by Omega's Fine Duplex Insulated Thermocouple Wire (TT-E-36-1000). The maximum measuring temperature of this kind of thermocouple is 480 ^{0}C. The measured temperatures are monitored by a FLUKE data logger (Model 2250).

Two Keithley model 2700 multimeter/data acquisition systems shown in Fig.2.21 are used to measure the thermocouple voltage readings. The Model 2700 Multimeter/Data Acquisition System is a high-performance, half-rack instrument that combines the functionality and high channel count of a data logger with the accuracy, convenience, and stability of 6-1/2-digit Digital Multimeter. The Model 2700 provides 80 channels or 40 differential channels of multiplexed measurement and control. The two multimeters give a total of 160 channels or 80 differential

channels. The Model 2700 reads as low as 0.1 μV and provides a digitizing capability with the equivalent of 22-bit A/D resolution. The highest scanning rate is 65 channels/second, and the highest sampling speed is 2000/sec, which is more than sufficient for thermocouple measurements.

The boundary layer flow is important in determining the cooling effectiveness. In order not to disturb the boundary layer flow, the thermocouples are mounted from underneath the test surface (not penetrating). Holes (d=1/32") are drilled from the bottom of the test plate penetrating 9mm deep, leaving a thickness of 0.5mm from the top surface (Fig. 2.22). In order to minimize the uncertainty of the temperature measurement, the thermocouples are carefully mounted in a consistent manner. Since the plate is transparent and also the clearance thickness (between the hole tip and the top surface) is thin, visual examination is conducted to make sure the tips of thermocouple joints have securely contacted with the surface by showing a noticeable black dot that can be clearly seen from the top surface. Silicon glue is then used to fill the hole to ensure that the thermocouple junctions are well protected and fixed in place.

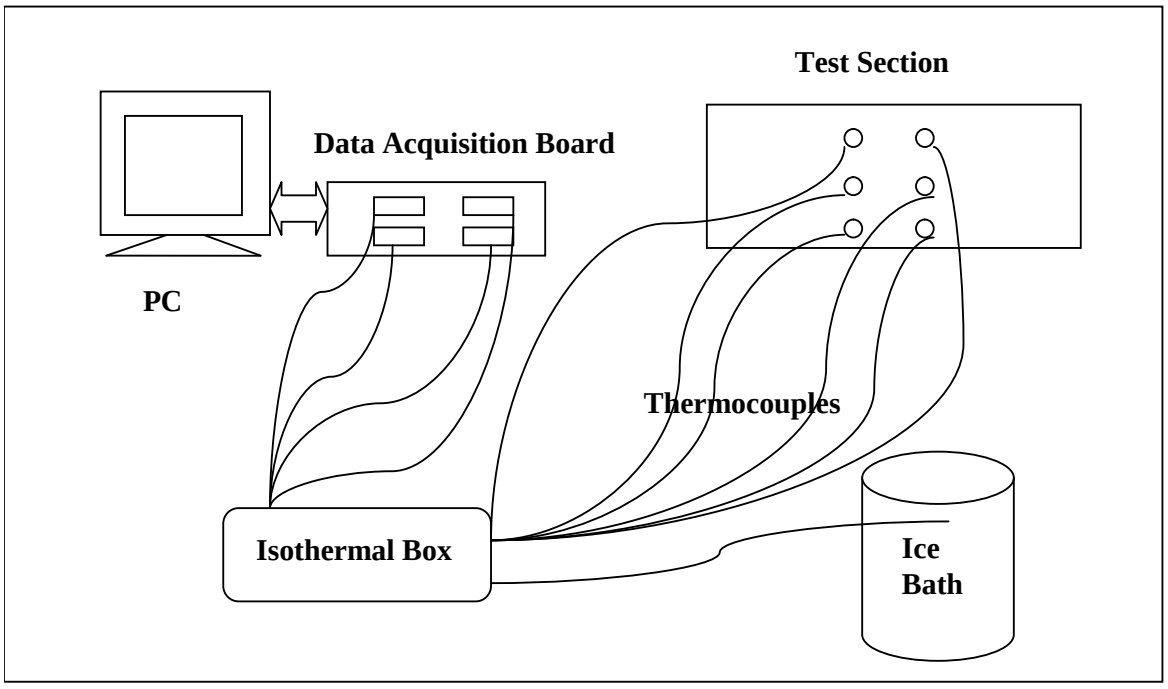

Figure 2.24 Overview of temperature measurement system

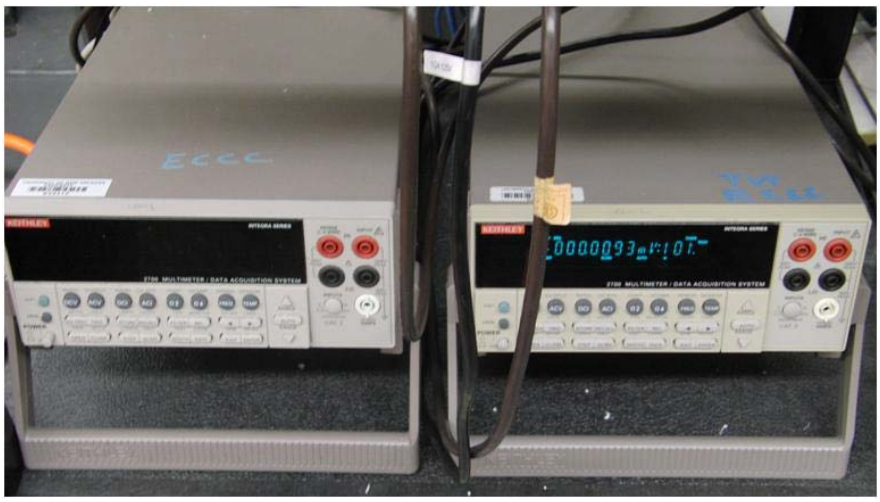

Figure 2.25 Keithley model 2700-multimeter/data acquisition systems with 48 channels of differential ports.

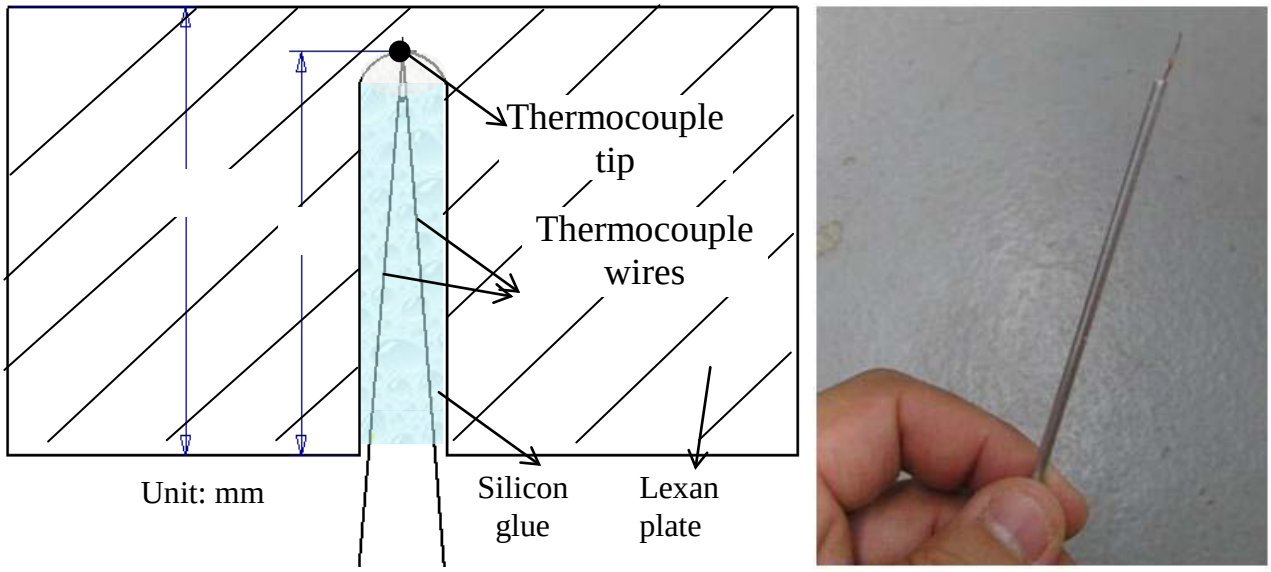

Figure 2.26 Thermocouples instrumentation and the temperature probe

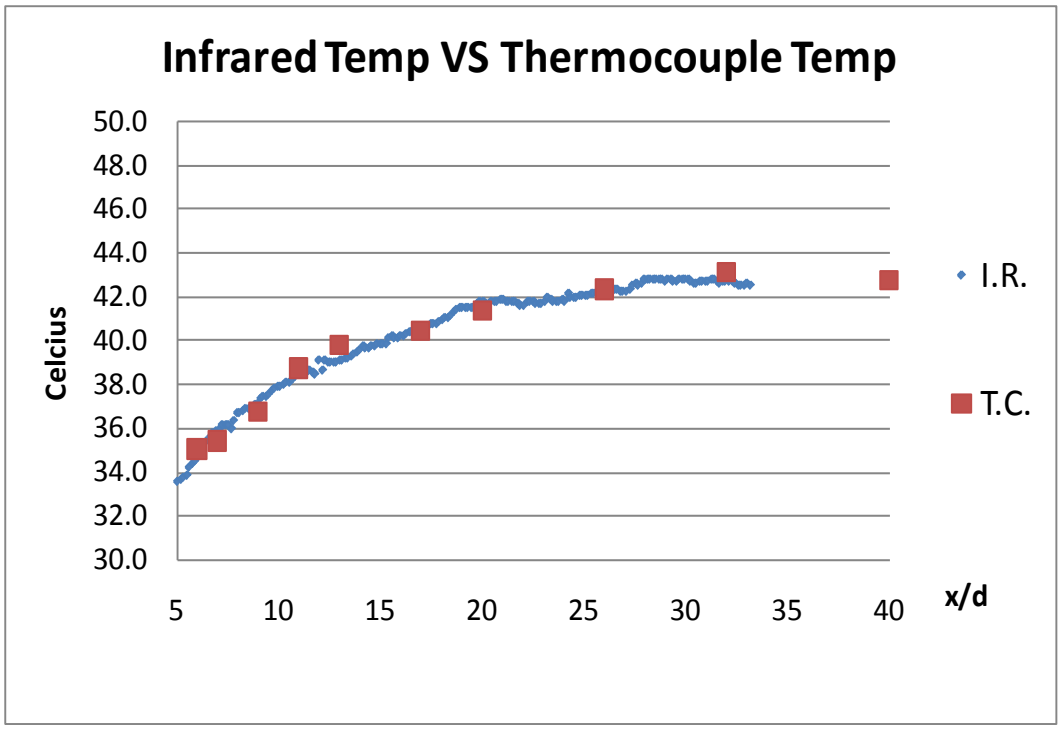

Figure 2.27 Comparison between thermocouple measurements and infrared camera measurements

Infrared data acquired from the camera is not readily available for direct data analysis. The procedures needed to produce cooling performance data based on infrared camera picture are the following:

1. Indentify the border of test section in the infrared picture using "infrared marks" by placing pre-cooled metal sticks at known locations.
2. Adjust the emissivity of the material by matching the temperature data with the thermocouple data.
3. Export the X (pixel), Y (pixel) and temperature (Celsius) data into Excel for data processing.
4. Convert X and Y into X/D and Y/D using the information from step 3.
5. Convert temperature data into cooling effectiveness (η) based on main flow temperature and coolant jet temperature.
6. Format the data and import them into Tecplot for contour plotting.

Infrared marks are objects that are detectable by the infrared camera. A thin metal stick

pre-cooled in a freezer is placed on the test section surface at X/D=0 with hot main flow running. The temperature difference makes the stick detectable in the infrared picture and provides a good reference to locate the actual location of each pixel in an infrared image.

The temperatures measured by the infrared camera are compared with the temperature measured by the thermocouples as shown in Fig. 2.23. The thermocouple measurements agree fairly well with the infrared camera measurement (± 0.2^{o}C). During the experiment, the thermocouple readings serve as in-situ calibration for the infrared measurement.

The temperature measurement system uses an in-house designed isothermal box, which is fabricated by 1-inch thick aluminum blocks (Fig. 2.24). The isothermal box provides a massive body to isolate the thermocouple-copper junctions inside the isothermal box from the ambient temperature fluctuations, thereby reducing the unsteadiness uncertainty of the experiment. The constant ice melting temperature of the ice bath (0^{o}C) is used as a reference temperature. The readings from the data acquisition system indicate the relative temperature difference between the thermocouple measurement location and the isothermal box temperature. To determine the absolute temperature at the thermocouple junction, the temperature difference between the isothermal box and ice bath is added on the data acquisition readings. Therefore, the actual temperature of the isothermal box is not important; rather the uniformity and steadiness of the isothermal box temperature provide a system that renders a good quality temperature measurement. Another function of the isothermal box is to avoid potential errors caused by the third material involved in the thermo"couple" circuits. In this case, the copper wire and copper connecting junctions of the multimeter would introduce the third material to the thermocouple circuits if the isothermal box is not used. A test has been conducted to verify the uniformity, as well as the steadiness, of the isothermal box temperature. Two measurements at both the center of the box and edge of the box within a 45-minute period have been taken. As shown in the plot in Fig. 2.25, the temperature inside the isothermal box is very uniform (dT<0.03 ^{o}C from center to corner) and the steadiness is estimated as dT/dt=0.002 ^{o}C/minute. Six pairs of thermocouples are calibrated at ice-melting point with an average deviation of 0.001mv from the manufacture supplied table. Since the thermocouple wires were delivered in the same spool, it is assumed that all of them have the same property. The average ice-point offset of 0.001mV has been applied to all the rest of thermocouples.

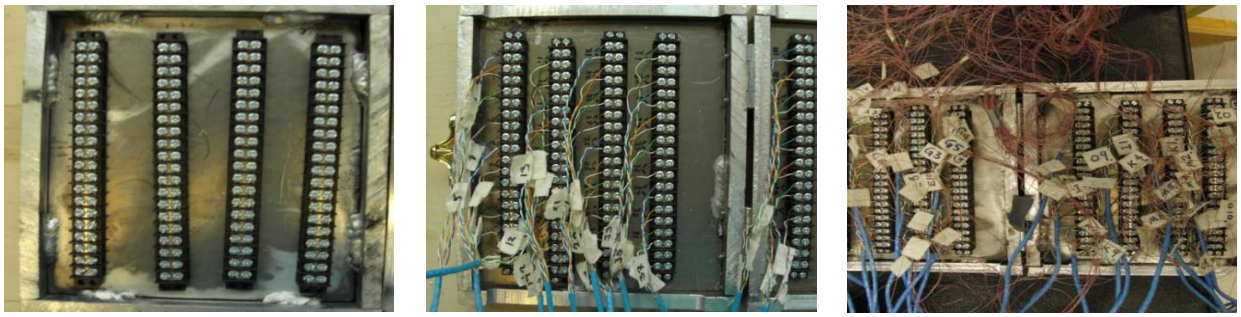

(a) **(b)** **(c)**

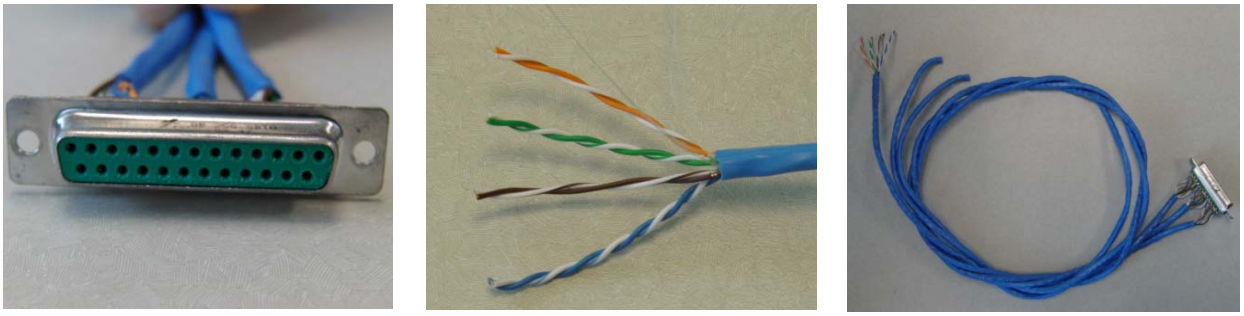

(d) **(e)** **(f)**

(g) **(h)** **(i)**

Figure 2.28 Components used in the thermocouple measurement (a), (b), and (c) are internal views of isothermal box setting up steps; (d), (e), and (f) are copper wires and RS232 connectors used to connect isothermal box and data acquisition board; (g), (h), and (i) are data acquisition board and its connectors.

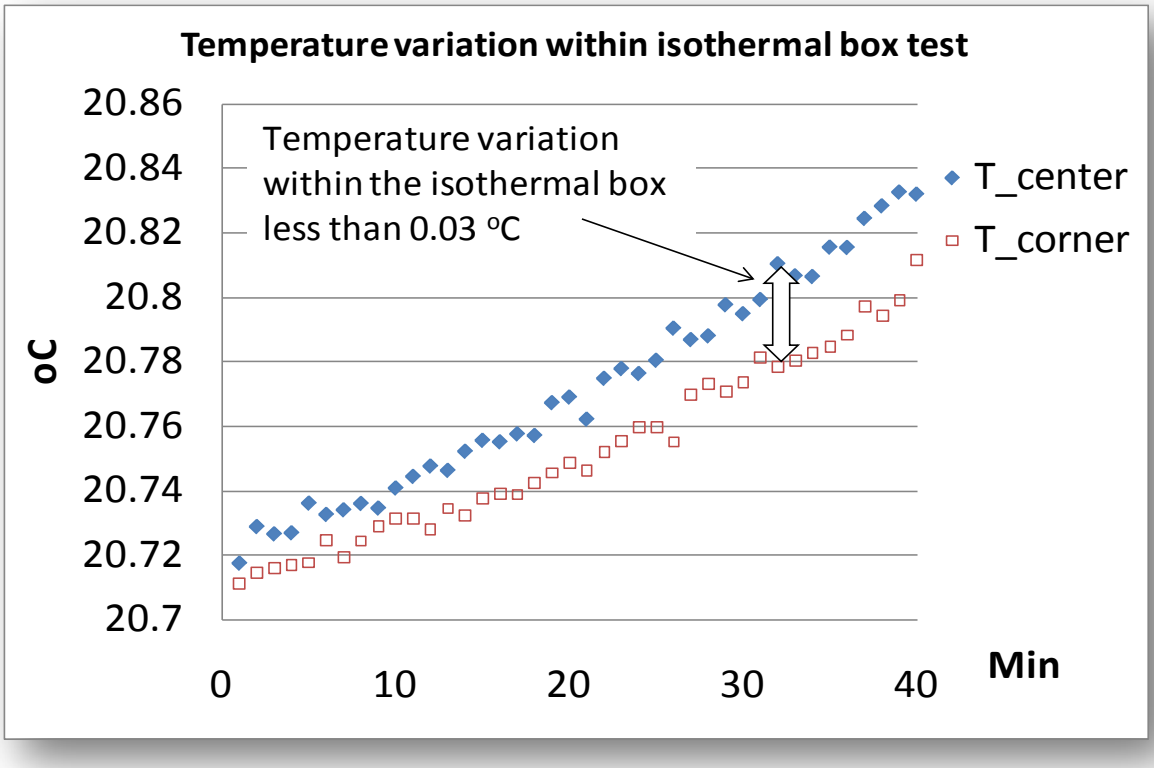

Figure 2.29 Temperature variation inside the isothermal box

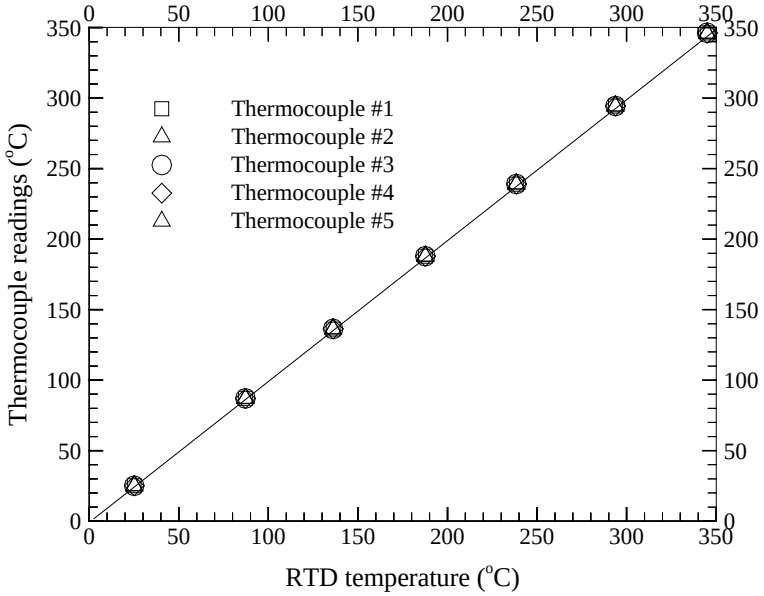

Figure 2.30 Thermocouple calibration

A total number of 91 thermal couples are used in this study. The location and number of

thermal couples are listed in Table 2.3. X is the streamwise direction and Z is the lateral direction. D is the injection hole diameter (1/4 inch, 0.635cm). x/d=0 is the center line of the middle hole and x/d=3.2, 6.4, -3.2, -6.4 are the other four hole center lines. A top view of the test section is shown in Fig. 2.31 marked with the thermal couple locations and corresponding numbers.

Table 2.3 Thermal Couple Map

x/d	y/d	T.C. Num	x/d	y/d	T.C. Num	x/d	y/d	T.C. Num
0	1	5	1.6	9	54	6.4	28	85
0	2	14	1.6	11	59	6.4	36	91
0	3	23	1.6	13	66	-0.8	1	4
0	5	31	1.6	16	71	-0.8	2	13
0	6	40	1.6	22	78	-0.8	3	22
0	7	47	1.6	28	83	-0.8	5	31
0	9	52	1.6	36	89	-0.8	6	39
0	11	57	3.2	1	8	-0.8	7	46
0	13	64	3.2	2	17	-1.6	1	3
0	16	69	3.2	3	26	-1.6	2	12
0	22	76	3.2	5	34	-1.6	3	21
0	28	81	3.2	6	43	-1.6	5	30
0	36	88	3.2	7	50	-1.6	6	38
0.8	1	6	3.2	9	55	-1.6	7	45
0.8	2	15	3.2	11	60	-3.2	1	2
0.8	3	24	3.2	13	67	-3.2	2	11
0.8	5	32	3.2	16	72	-3.2	3	20
0.8	6	41	3.2	22	79	-3.2	5	29
0.8	7	48	3.2	28	84	-3.2	13	63
0.8	9	53	3.2	36	90	-3.2	22	75
0.8	11	58	6.4	1	9	-3.2	36	87
0.8	13	65	6.4	2	18	-6.4	1	1
0.8	16	70	6.4	3	27	-6.4	2	10
0.8	22	77	6.4	5	36	-6.4	3	19
0.8	28	82	6.4	6	44	-6.4	5	28
1.6	1	7	6.4	7	51	-6.4	13	62
1.6	2	16	6.4	9	56	-6.4	22	74
1.6	3	25	6.4	11	61	-6.4	36	86
1.6	5	33	6.4	13	68			
1.6	6	42	6.4	16	73			
1.6	7	49	6.4	22	80			

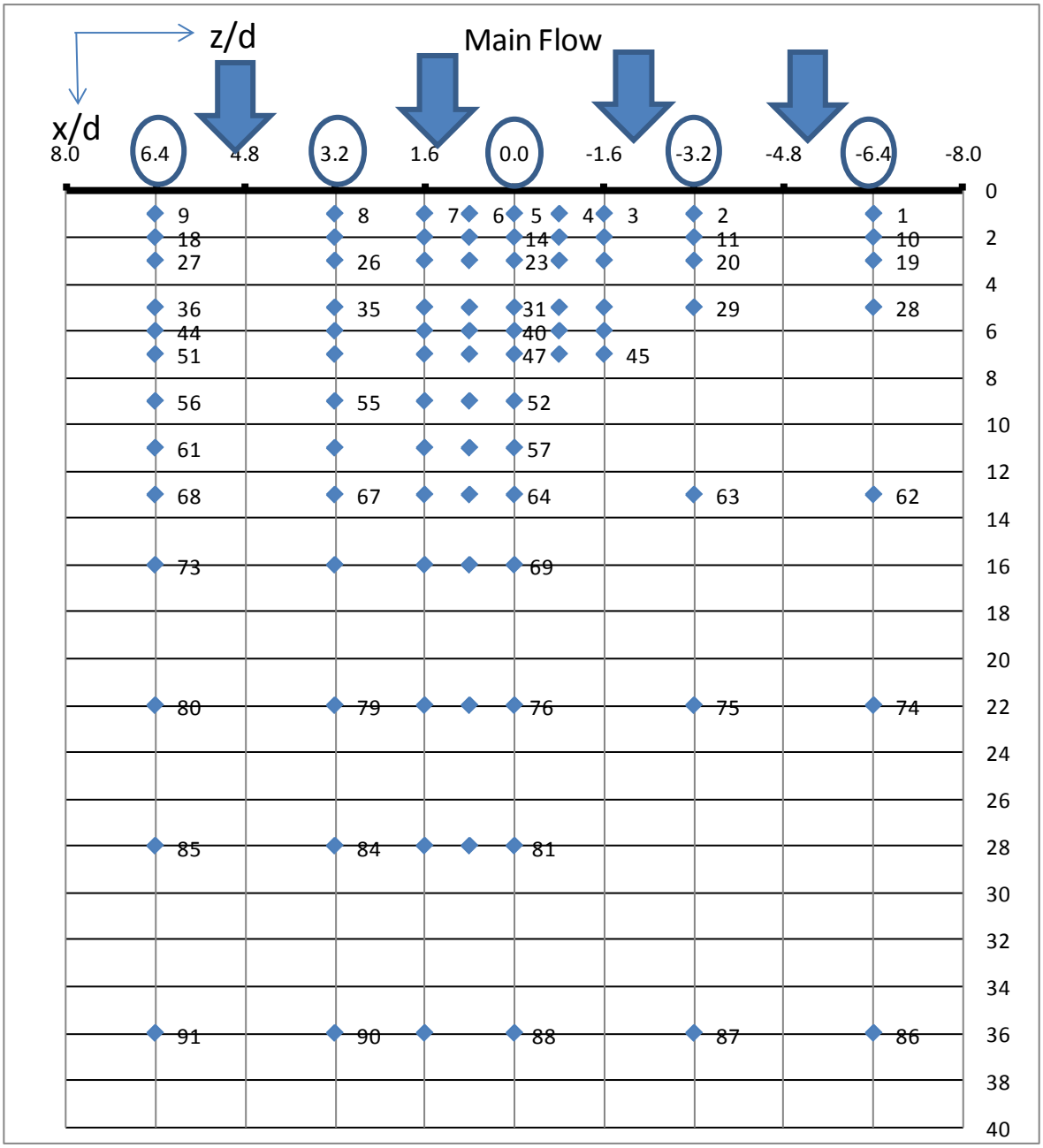

Figure 2.31 Top view of the test section with thermal couple marks

2.2.3 Flow Measurement

Secondary Air Flow Rate

Compressed air from the building compressor is used as the secondary cooling air. A

spring-and-piston type flow meter (Omega FLMG-, Range 0-100 SCFM) is used to measure the secondary air flow rate (approximately 30 SCFM). A pressure gauge is installed between the flow control valve and the flow meter to monitor the inlet air pressure. The flow rate is cross checked with the velocity measurement at the jet exit using a pitot-static tube. Uncertainty of the coolant flow rate is estimated at 5% with a typical flow rate of 25 SCFM.

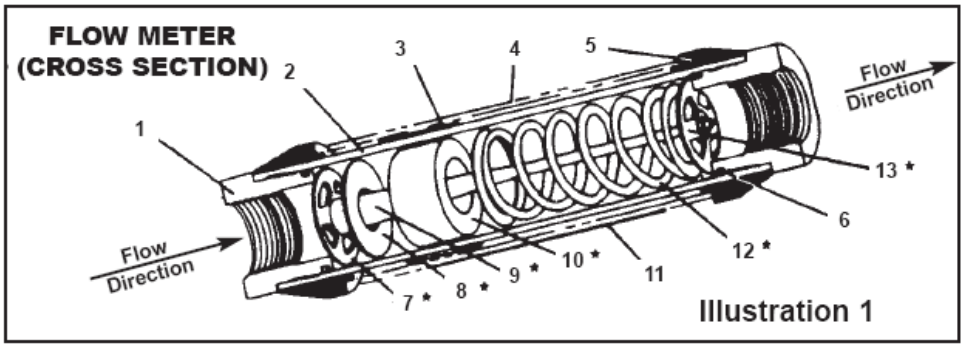

1. End Porting
2. Body Casing
3. Magnet Follower
4. Window Tube
5. Window Seal
6. Seal Assembly
7. Pilot Disk
8. Flowing Sharp-Edged Orifice Disk
9. Tapered Center Shaft
10. Transfer Magnet
11. Scale
12. Return Spring
13. Retainer Ring

Figure 2.32 Pressure gauge and flow meter

Mist Mass Flow Rate

The mist flow rate is acquired by measuring the difference between the water flow rate coming into the atomizer and that returning to the reservoir. Both flow rates are measured in-situ by using the catch-and-weigh method. The uncertainty of the mist flow rate is estimated at 7% to 10% of a typical flow rate of 0.3 gallon/hour depending on the coolant film flow rate. The relative high uncertainty is attributed to the nature of droplets agglomeration related unsteadiness inside the mixing chamber.

Main Flow Velocity and Pressure Measurements

A Pitot-tube combined with a pressure transducer is used in this study to measure the main flow velocity. A pressure transducer converts a measured pressure into an analog electrical signal. Although there are various types of pressure transducers, one of the most common ones is the strain-gage base transducer. The conversion of pressure into an electrical signal is achieved by the physical deformation of strain gages that are bonded into the diaphragm of the pressure transducer and wired into a Wheatstone bridge configuration. Pressure applied to the pressure transducer produces a deflection of the diaphragm which introduces strain to the gages. The strain will produce an electrical resistance change proportional to the pressure. The electrical signal is then transferred to a signal conditioner.

Signal conditioners are the nucleus of any test measurement system. They receive output from the transducer, carry out basic processing of the signal, and pass the signal on to the display, storage, and analysis components. Signal conditioners may also supply an excitation voltage to power the transducer. In a typical measurement system, signal conditioning equipment is located between the transducer and the display. It conditions the transducer signal into a form the display can use. Some transducers have the signal conditioning electronics built into the body. This type of transducer can provide a high-level, low-impedance output signal that is immune to noise contamination caused by radio frequency interference or electromagnetic interference. The disadvantages include a limited temperature environment, resulting from the electronic components and the large size of the transducer. Relatively simple in design, analog signal conditioners, which employ a series of operational amplifiers for signal amplifications, have been in use for decades. . An analog signal conditioner's output is calibrated to a scale by adjusting zero and span potentiometers. These potentiometers can be interactive and require the repetition of calibration steps to obtain optimum scale accuracy. Analog signal conditioners are dependable devices with a low failure rate. Their operation is easily understood with little training required for their use. A drawback to analog signal conditioners is the intrinsic drift of potentiometers used for signal adjustment. This can lead to output drift over time. Potentiometers can also be awkward to adjust, complicating a calibration process.

A fluid flowing through a confined area exerts pressure consisting of two distinct components. These components are distinguished as the static pressure and the dynamic pressure. The static pressure does not cause any velocity change within the flow. The static pressure is

usually measured by drilling a porthole through the container wall and connecting the porthole to a manometer. The drilled porthole must be perpendicular to the flow to ensure only the desired static pressure is attained. The dynamic pressure is due to the movement of the fluid. The static and dynamic pressures together make up the total or stagnation pressure. The stagnation pressure is measured by placing a pitot-static tube (Fig.2.28) directly parallel to the flow and connecting the pitot-static tube to a manometer.

A pitot-static tube combines the static and stagnation pressure measurements into one device. It consists of a tube within a tube. The configuration is then placed in the duct facing upstream parallel to the flow of the fluid. The pressure tap facing upstream gives the stagnation pressure, while the tap which is perpendicular to the flow gives the static pressure. When the pitot-static tube is in the fluid flow, the pressure difference between the stagnation and static pressure can be measured using a manometer connected to each port. Applying Bernoulli's equation between the two pressure ports yields

$$\frac{p_{stg} g_c}{\rho_{air} g} + \frac{V_{stg}^2}{2g} + z_{stg} = \frac{p_{st} g_c}{\rho_{air} g} + \frac{V_{st}^2}{2g} + z_{st} \qquad \text{(Eq.2.1)}$$

p_x = pressure
g_c = gravitational constant
g = local gravity
V_x = velocity
ρ_x = density
z_x = elevation from datum

where the subscripts "stg" represents the stagnation component and "st" represents the static component. The elevation difference between the stagnation and static port can be neglected in the present study. In addition, the velocity where the stagnation pressure is measured is zero. As a result, Bernoulli's equation reduces to the following

$$\frac{p_{stg} g_c}{\rho_{air}} = \frac{p_{st} g_c}{\rho_{air}} + \frac{V_{st}^2}{2} \qquad \text{(Eq.2.2)}$$

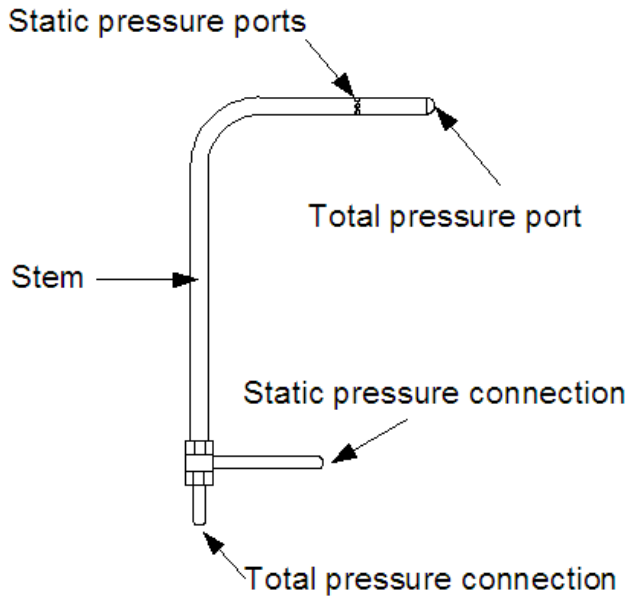

Figure 2.33 Pitot-Static tube

After rearranging the following equation and solving for the velocity,

$$V = \sqrt{\frac{2g_c}{\rho_{air}}\left(p_{stg} - p_{st}\right)} \quad . \qquad \text{(Eq. 2.3)}$$

The subscript "st" is dropped to show the velocity at the static port is the same as the velocity of the airstream approaching the pitot-static tube. The gravitational constant is required if English units are being utilized, particularly if the unit of mass of the density is given in pound-mass (lbm). However, if SI units are being used the gravitational constant will be absent from the equation, thereby reducing to

$$V = \sqrt{\frac{2\left(p_{stg} - p_{st}\right)}{\rho_{air}}} \quad . \qquad \text{(Eq. 2.4)}$$

A manometer with the attached microtector connected to the pitot-static tube is used to acquire the pressure difference between the stagnation point and the static port by measuring the height of the water column.

Figure 2.34 Dwyer model 1430 microtector

By applying the hydrostatic equation, the pressure difference is derived in the following manner

$$p_{stg} + \frac{\rho_{air} g}{g_c} x + \frac{\rho_{air} g}{g_c} \Delta h = p_{st} + \frac{\rho_{air} g}{g_c} x + \frac{\rho_{water} g}{g_c} \Delta h \quad , \qquad \text{(Eq. 2.5)}$$

where Δh is the height of the water column. The vertical measurement x is measured from the centerline of the pitot-static tube to the immediate water interface in either leg of the manometer. For instance, if the manometer is located above the pitot-static tube, x is measured from the centerline to the lowest water interface. However, if the manometer is located above the pitot-static tube, x is measured from the centerline to the highest water interface. In either case, the terms containing x cancel each other, which shows that x is arbitrary. After the x terms are canceled out the equation becomes

$$\Delta P = p_{stg} - p_{st} = \Delta h(\rho_{water} - \rho_{air})g \quad . \qquad \text{(Eq. 2.6)}$$

In the preceding equation $\rho_{water} \gg \rho_{air}$; therefore, ρ_{air} can be neglected, thereby reducing the equation to

$$\Delta P = p_{stg} - p_{st} = \Delta h \rho_{water} g \quad . \qquad \text{(Eq.2.7)}$$

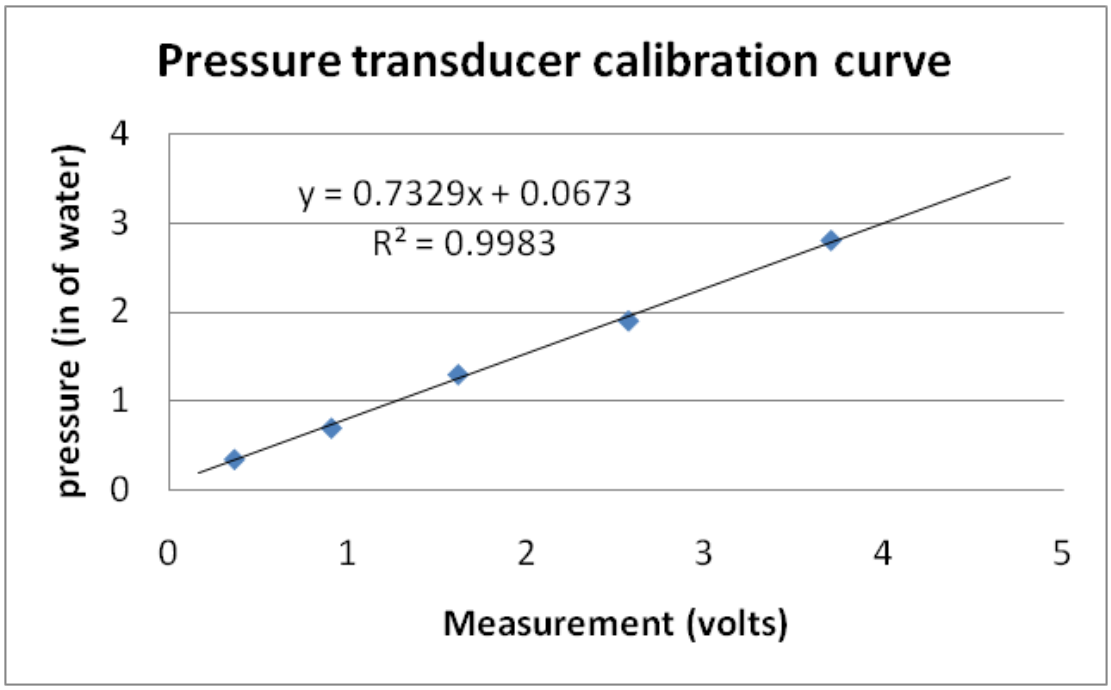

Figure 2.35 Calibration curve of the pressure transducer

2.3 Experiment Repeatability

To make sure the measurement data is taken at a comparable steady-state condition, repeated measurements are taken. Since one scanning cycle of all thermocouples takes approximate 30 seconds, the room temperature changes within this time frame are negligible (less than 1°C in an hour, as documented in Fig. 2.36). The data taken before the steady state is reached are not used for data analysis, but they are kept as reference to observe the tendency of data changes. The typical time needed to reach the steady state is summarized below:

- Main flow: 1.5 hours after turning on the heater.
- Film Flow: 45min to reach steady temperature after being turned on
- Within the test plate, without film: 45min (without preheating)
- Within the test plate, with film: 40min
- Within the test plate, with mist: more than 30min

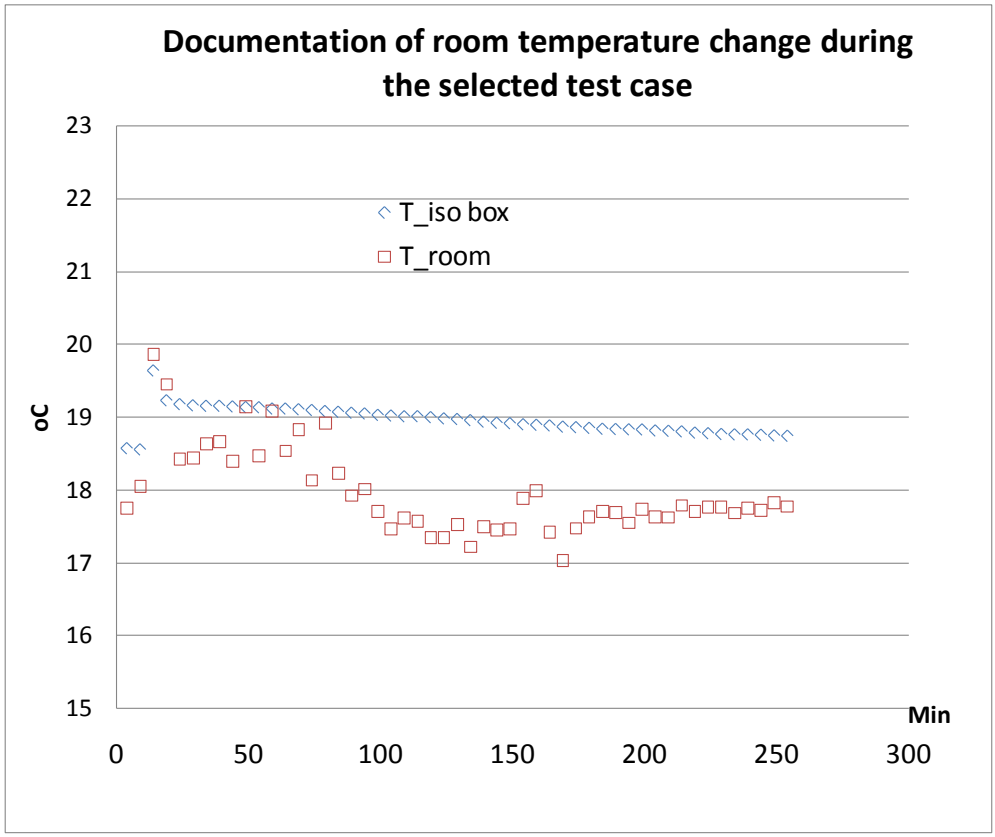

Figure 2.36 Room temperature fluctuations within 5 hours

2.4 Uncertainty Analysis

An uncertainty analysis is performed to assist in identifying large uncertainty sources and planning for experimental procedure. The method used in this study for the uncertainty analysis is based on the theories of Kline (1985) and Moffat (1985) and closely follows the method used by Wang and Simon (1989) and will not be detailed here. The results of the uncertainty analysis are summarized below.

The first step of the uncertainty analysis is to identify the independent primary measurement variables for the data reduction process. For this study, three temperatures are used to evaluate cooling effectiveness: main flow temperature, wall temperature, and coolant temperature.

The second step is to calculate the sensitivity coefficient (∂XR / ∂Xi) of each component--i.e., the influence of each independent variable on the final result (the heat transfer coefficient in this study) due to a small variation of each independent variable. An Excel spreadsheet is developed based on the data reduction process. The sensitivity coefficient is obtained by subjecting each independent variable to a certain perturbation ($\pm$1%) from its nominal value and recomputing the output.

The third step is to choose a nominal value (Xi) and an uncertainty value (δX_i) for each independent variable with a 95% confidence level, and the fourth step is to calculate the composite or total uncertainty using the following equation:

$$\delta X_R = \left\{ \sum_i \left[\left(\frac{\partial X_R}{\partial X_i} \right) \delta X_i \right]^2 \right\}^{1/2} , \qquad \text{(Eq. 2.8)}$$

where X_i is the i-th independent variable and X_R is the resultant.

The results of the uncertainty analysis vary with the level of replication on which the analysis is based. Zeroth-order (Moffat, 1985) and pretest uncertainty (Wang and Simon, 1989) analyses have been performed during the development stage of the experimental system. The first-order and Nth-order uncertainty analyses have been performed during the data-gathering stage. The zeroth-order analysis is made in the early stage of the experiment when no hardware existed. The zeroth-order analysis is helpful in making decisions about the precision required for purchasing new equipment or the adequacy of using the existing equipment. At this stage, the only uncertainties recognized are those associated with the interpolation or round-off error of the proposed instrumentation. For this analysis, the uncertainty value, δX_i, is taken to be one-half of the smallest scale division for analog instruments and one-half of the value of an increment of the least significant digit for digital instruments. All calibrations are presumed to be accurate, and the facility and instrumentation are assumed to be steady and free of bias errors.

In the pretest analysis, the instrument imprecision uncertainty discussed earlier and labeled as the zeroth-order contribution is combined with the best estimate of the calibration uncertainties. These calibration uncertainties are estimated based on previous experience, including knowledge of the calibration capability of the laboratory and the best estimate of uncertainties associated with the removal of known bias errors in the calibration.

The first-order analysis is performed after the construction of the experimental system is

completed. Basically, the effect of unsteadiness is considered in the first-order analysis in combination with the zeroth-order analysis. The Nth-order uncertainty analysis includes the uncertainties caused by imprecision, unsteadiness, calibration error, and errors in the correction models incorporated to minimize all known bias errors. The Nth-order analysis is calculated by the following equation:

$$\delta X_{i,n} = \left[(\delta X_{i,0})^2 + (\delta X_{i,u})^2 + (\delta X_{i,c})^2 \right]^{1/2} . \qquad \text{(Eq.2.9)}$$

Results for the zeroth-order and pretest uncertainty analyses for the heat transfer coefficient are documented in Table 2.3, and the first-order and Nth-order uncertainty analyses for the heat transfer coefficient are documented in Table 2.4.

Table 2.3 Uncertainty Analysis: Zeroth-Order and Pretest Uncertainties

Independent variable	Nominal Value	dx_r/dx_i	Uncertainty of Imprecision	Uncertainty of Calibration	Uncertainty of Unsteadiness (film only)	Uncertainty of Unsteadiness (with mist)	Zeroth Order magnitude	Zeroth Order (%)	Pretest uncertainty magnitude	Pretest uncertainty (%)
T_{aw} wall temperature (^oC)	40.00	0.02	0.02	0.20	0.03	0.20	0.00	0.17	0.20	2.01
T_g main flow temperature (^oC)	50.00	0.02	0.02	0.20	0.02	0.02	0.00	0.12	0.20	1.47
T_j jet temperature (^oC)	10.00	0.01	0.02	0.20	0.03	0.10	0.00	0.04	0.20	0.50
Total Uncertainty of η (%)								0.21		2.54

Table 2.4 Uncertainty Analysis: First Order and Nth Order Uncertainties

Independent variable	First order uncertainty magnitude (film only)	First order uncertainty-film only (%)	First order uncertainty magnitude (mist/film)	First order uncertainty-mist/film (%)	Nth order uncertainty magnitude (film only)	Nth order uncertainty (%) (film only)	Nth order uncertainty magnitude (mist/film)	Nth order uncertainty (%) (mist/film)
T_{aw} wall temperature (^oC)	0.03	0.34	0.20	2.01	0.20	2.03	0.28	2.83
T_g main flow temperature (^oC)	0.03	0.19	0.03	0.19	0.20	1.48	0.20	1.48
T_j jet temperature (^oC)	0.03	0.09	0.10	0.25	0.20	0.51	0.22	0.56
Total Uncertainty of η (%)		0.40		2.03		2.56		3.24

CHAPTER THREE
EXPERIMENTAL RESULTS AND DISCUSSION

In this chapter, the experimental results for mist cooling are presented and discussed. **The strategy of the current study** is to first to obtain the knowledge of: 1) overall heat transfer performance through measurement and 2) droplet behavior through the analysis conducted based on the droplet information measurements; then combine the information of both the overall heat transfer results and the particle behavior measurements to reach the goal of an in-depth understanding of mist cooling. **Investigation of the particle behavior and finding its impact on overall heat transfer performance are highlights of the analysis.**

3.1 Flow Conditions

The main flow mean velocity at the inlet is 20.13 m/s with the turbulence intensity of the streamwise component at 3.47%. The mean velocity is measured by a Pitot-static tube and the turbulence intensity is based on the PDPA velocity measurements of water drops sized between 12μm and 20μm at an elevation of 22mm above the test section bottom surface. Even though smaller droplets would serve better for turbulence measurements, they are not present at the prescribed height for meaningful mean flow measurement because of evaporation due to the heated main flow. *Note that, in this study, the main flow is not seeded: the water droplets (mist) injected from the film holes are used as particle seeds for velocity measurements. Only large droplets can possess sufficient momentum residence time and thermal residence time (the duration before the droplet completely vaporizes) to travel further away from the injection hole to reach the main flow.* The turbulence intensity value is expected to be undervalued due to the relaxation time and slip velocity of the relatively large droplets, which results in differences between flow velocity and droplet velocity.

In order to measure main flow temperature distribution at the inlet, a thermocouple probe is inserted into the test section perpendicular to the bottom plate at X/D = -2. This temperature probe is made of a small stainless steel tube of 1/8 inch in external diameter. An array of four thermocouples uniformly spaced 2 inches apart are attached to this probe. The bottom thermocouple is 2 inches (Y/D=8) elevated away from the plate. A measurement is taken every

10 seconds over a total duration of two minutes. The results are documented in Table 3.1. Based on the results, the temperature variation in the Y direction is estimated as 0.12 ^{o}C per inch. And the temperature variation in time (unsteadiness) is estimated as $\pm$0.2 ^{o}C per minute. Similar measurements are repeatedly taken by traversing the probes in the X- and Z-directions (lateral direction) and the temperature gradient is estimated less than $\pm$0.15 ^{o}C per inch in Z-direction and 0.14 per inch in X-direction.

Table 3.1 Main flow temperature(°C) measurement

t (s)	T,°C (Y/D=8)	T,°C (Y/D=16)	T,°C (Y/D=24)	T,°C (Y/D=32)	Space Averaged
0	55.16	54.81	54.82	55.08	54.96±0.18
10	54.88	55.31	54.70	54.78	54.92±0.27
20	54.65	55.20	54.71	54.71	54.81±0.25
30	55.15	54.62	54.48	54.44	54.67±0.33
40	55.03	55.14	54.73	54.53	54.86±0.28
50	54.99	54.72	54.89	55.32	54.98±0.25
60	55.22	54.62	55.05	55.22	55.03±0.28
70	54.69	54.96	54.63	54.49	54.69±0.19
80	55.04	54.97	55.20	54.78	55.00±0.18
90	54.80	54.91	54.67	54.45	54.70±0.20
100	55.09	54.63	55.07	55.18	54.99±0.25
110	54.89	54.93	54.94	55.07	54.96±0.08
120	55.05	54.67	54.93	54.84	54.87±0.16
Time Averaged	54.97±0.18	54.88±0.23	54.83±0.20	54.81±0.31	54.88±0.24

The approaching boundary layer thickness in this study is estimated using PDPA velocity measurement data of small water droplets (< 5μm) at X/D = 0.5. The measurements are compromised due to a few constrains:

1. Small droplets, which follow the flow better (i.e. lower slip velocity and less momentum relaxation time), serve better in measuring air flow velocity. However, as explained earlier, they are injected from the film cooling holes and do not have enough momentum to travel to higher elevations away from the plate surface. Thus, droplets smaller than 5 μm are not present for measurements beyond certain elevation levels (for example Y > 12mm at X/D=0).

2. Bigger droplets have enough momentum to travel to higher elevations, but they do not follow the flow well, generating much higher uncertainties in velocity measurements.
3. Ideally, the stream-wise location for approaching boundary layer thickness would be at X/D = -2, which is upstream of the film injection holes. However, there are no water droplets present in this area.

Despite the constraints mentioned above, an effort is made to give the best estimation of the approaching boundary layer thickness. With the velocity profile as shown in Fig. 3.1, the displacement thickness, which is defined as:

$$\delta = \int_0^\infty \frac{u}{U} dy$$

is measured as 1.936mm. The momentum thickness, defined as:

$$\theta = \int_0^\infty \frac{u}{U}(1 - \frac{u}{U})dy$$

where u is the local velocity, and U is the free stream velocity, is calculated as 1.047mm. The shape factor (δ/θ) is 1.849 based on the measurements.

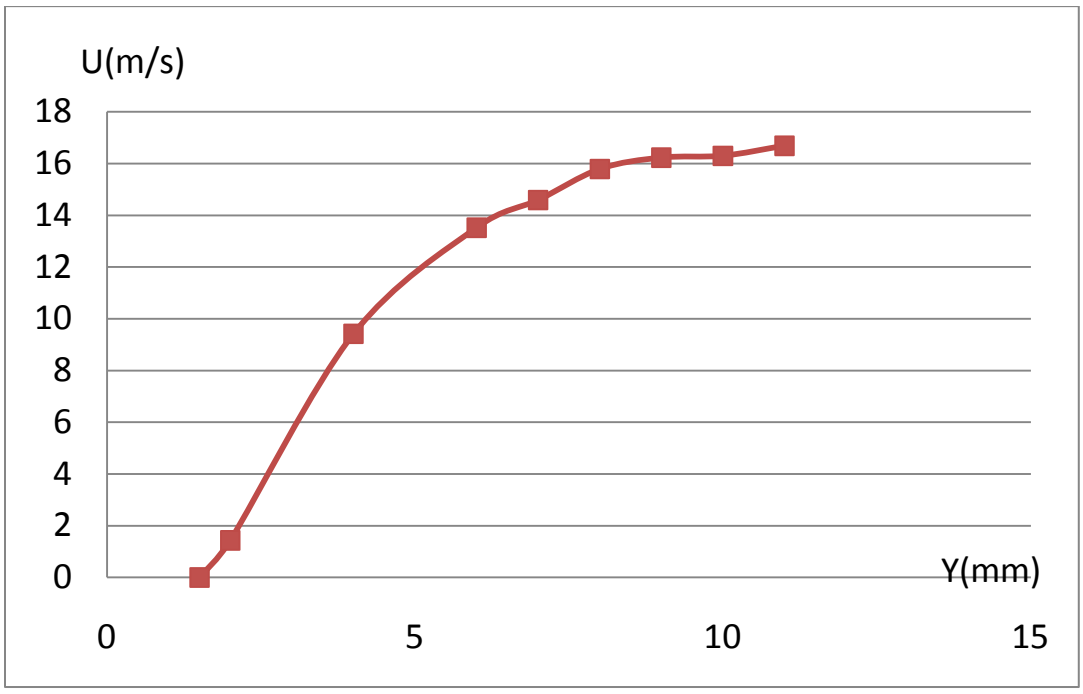

Figure 3.1 Velocity profile measured from droplets 5 μm or less at X/D=0.5

The flow conditions together with the uncertainties are documented in Table 3.2. Uncertainties of the flow conditions based on both the measurements and the educated estimate of some errors is also given in the table shown as delta with the confidence level of 95%. Three blowing ratios are employed in this study: 0.6, 1.0 and 1.4. Those are typical values employed in gas turbine film cooling applications. Efforts have been made to reduce the uncertainties of the measurements, including reducing the effect of environmental condition variations, main flow speed fluctuations, main flow temperature non-uniformity, and jet flow speed and mist mass flow fluctuations. The major source of the experimental uncertainty arises from the unsteadiness feature of the mist flow rate. In order to acquire good-quality mist, which would suspend in the air, filters and blockers are employed in the mixing chamber. Mist agglomeration and the actions of water droplets breaking up processes that may occur on the surface of mixing chamber structures are transient and unsteady in nature. As a result, the unsteadiness of mist flow is identified as the main contribution to wall temperature uncertainty.

Table 3.2 Summary of Flow Conditions

Main flow	U(Δ) (m/s)	Tu (Δ) (%)	Re_L	Re_d	T∞ (Δ) (oC)
	20.23 (0.22)	3.47 (0.08)	206,756	8,615	54.88 (0.28)
Secondary flow ---------- M=(ρV)j/(ρV)∞	M	V (m/s)	Tj (Δ) (oC)	Density Ratio	Mist ratio (Δ) (%)
	1.4	25.04	10.25 (0.32)	1.16	8.15 (0.52)
	1	18.24	12.16 (0.22)	1.15	7.39 (0.47)
	0.6	11.58	15.35 (0.20)	1.14	7.14 (0.44)

3.2 Heat Transfer Results

A list of the cases studied is presented in Table 3.3. In order to evaluate the validity of mist/air film cooling performance, two groups of heat transfer experiments are carried out. The first group is the air film only case. In this group of experiments, only the air is injected as the

coolant. The wall temperature is measured after steady state is reached. The second group of cases is the air/mist film case, in which mist is added into the air film and injected into the main flow channel. Again, temperature measurements at the same location as in the air-only case are taken after steady state is reached. The temperature measurements are then processed to produce the cooling effectiveness by incorporating both the main flow temperature and the jet temperature for each case. Comparisons are then conducted to evaluate the performance of the proposed mist/air film cooling as opposed to traditional air film cooling. Evaluation is made based on the following criteria: local cooling performance, lateral averaged cooling performance, overall cooling performance (integral over the whole surface), and the cooling effect coverage in both the lateral direction and the stream-wise direction.

Table 3.3 List of Cases

Case Number	Film	Blowing Ratio
Case 1	Air only	0.6
Case 2	Air/Mist	0.6
Case 3	Air only	1
Case 4	Air/Mist	1
Case 5	Air only	1.4
Case 6	Air/Mist	1.4

Two methods of temperature measurement are utilized in this study: thermocouple measurement and infrared thermograph measurement. Generally, a thermocouple has a more accurate measurement capability and yields less uncertainty than the infrared thermograph measurement. However, a thermocouple measurement is essentially a point measurement. The space resolution is limited by the necessity of keeping the surface condition and heat transfer path intact as well as the capacity of the thermocouple instrumentations. Also, as shown in the previous chapter, a great deal of effort was required to install the thermocouples underneath the test piece, especially when the bottom of the test piece is not easily accessible. On the other hand, infrared measurement is easier to accomplish. Moreover, it gives the information of the complete surface (within the view angle), which enables one to generate useful contour plots. This information is essential in evaluating a continuous cooling coverage on the surface. However, infrared measurement suffers from lower accuracy (smallest detectable temperature

variation is about 0.1 ^{o}C) and high uncertainties due to the varying values of the surface emissivity condition due to uneven surface properties, surface oxidation, and non-uniform surface temperature. In this study, the emissivity changes abruptly if the surface is wet with traveling liquid droplets. A combination of both measurement methods used in this study enables one to conduct more informative analysis. Since an accurate infrared measurement is more inclined to the variation of surface emissivity, the thermocouple measurements also serve as the in-situ calibration standard for the infrared measurements.

3.2.1 Case 1 and Case 2 (Air film vs. mist film with B=0.6)

The cooling effectiveness contour for Case 1 and Case 2 are shown in Fig. 3.2 (a) and (b), respectively. The contour plots are produced based on the infrared camera image following the procedures described above. The adiabatic cooling effectiveness is defined as:

$$\eta = (T_{aw}-T_g)/(T_j-T_g)$$

where T_g is the main flow hot gas temperature, T_j is the coolant temperature at the cooling jet hole exit, and T_{aw} is the adiabatic wall temperature. η is an excellent indicator of film cooling performance by comparing the insulated wall surface temperature (T_{aw}) with the would-be perfect wall temperature, T_j. If the film cooling were perfect, $\eta = 1$ and the wall is protected as cold as the cooling jet temperature. $\eta = 0$ implies that film is not effective at all: the adiabatic wall temperature is as hot as the main flow temperature. With the definition of cooling effectiveness explained, the blue color in the contour plots indicates low cooling effectiveness, meaning that the blade surface is not protected well against the hot main flow with a high adiabatic wall temperature. On the other hand, the red color indicates that the cooling scheme is effective, resulting in a lower surface temperature.

Two hole pitches are shown in Fig 3.2. This figure gives a straightforward and more quantitative idea of the cooling effectiveness distribution. A symmetric and periodic pattern of cooling effectiveness distribution is generally followed. The imperfection of symmetry between the two coolant injections is due to the coolant holes' machining defects. From Fig. 3.2 (a), the cooling effectiveness decays smoothly as X/D increases. The trace of the coolant coverage is clearly identifiable up to X/D about 25 ($\eta = 0.15$). In-between the coolant hole, the surface is not covered well by the coolant, leaving a low cooling effectiveness in the area. Also it is noticed

that there is no significant interaction between the injections. The two injections traces seem to be separated from each other.

After mist is added, as shown in Fig. 3.2 (b), the cooling effectiveness is noticeably higher. Moreover, the coolant coverage is much better in both the stream-wise direction and the lateral direction. Looking at the stream-wise direction, the cooling clearly covers up to a distance of X/D beyond 35 ($\eta = 0.3$). Also, it is noticed that the cooling coverage in-between holes is much better. The uncovered area is much smaller compared with the air film only case. This implies that the coolant spreading is enhanced as mist is added into the coolant. However, a small, uncovered area still exists for this case ($1< X/D <8$). The coolant does not have a mechanism to reach that area. Also from this figure, it seems that the two injections merge at around $X/D = 13$, generating a uniformly cooled area in-between the coolant holes for $X/D > 13$.

There are two key aspects through which the film cooling performance is evaluated: the cooling effectiveness and the film coverage. Film cooling effectiveness has always been evaluated in a quantitative manner using variables like adiabatic cooling effectiveness, heat transfer coefficients, or net heat flux reduction. However, through the literature studies of film cooling, there is no clearly defined variable to quantitatively evaluate the cooling effect coverage enhancement. It is recommended in this study to set a benchmark value and measure the stream-wise location (X/D) where the cooling effectiveness decays to this value. The benchmark value is set to certain percentage of the peak value. The length that it takes for the film cooling effectiveness to decay to this value is called the **Film Decay Length (FDL).** For example, 50% of the peak value is used as the benchmark value in this study. The length from $X/D = 0$ to the location where the centerline effectiveness decays to one-half of the benchmark value is called **50% FDL**. The purpose of identifying this length is to quantitatively evaluate how well the coolant film covers the blade surface in the stream-wise direction. Moreover, this length indicates how fast the coolant dissipates and mixes with the main flow.

For the air-only case (Case 1), the **FDL (50%)** is 14.6, i.e. the cooling effectiveness decays to 50% of the peak value at $X/D = 14.6$. While, for the mist/air case, the FDL (50%) is $X/D = 24.2$. Thus, it is estimated that adding mist to the air film increases the FDL (50%) by 83% for cases with a blowing ratio of 0.6. It should be noted that this number may change when other percentages, instead of 50% FDL, are employed.

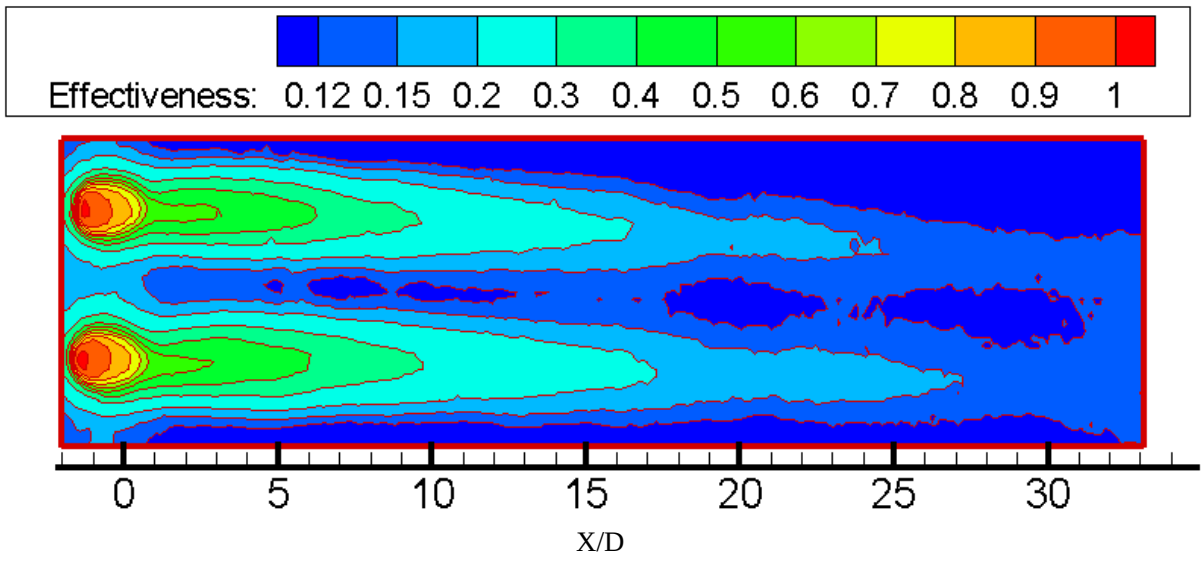

(a)

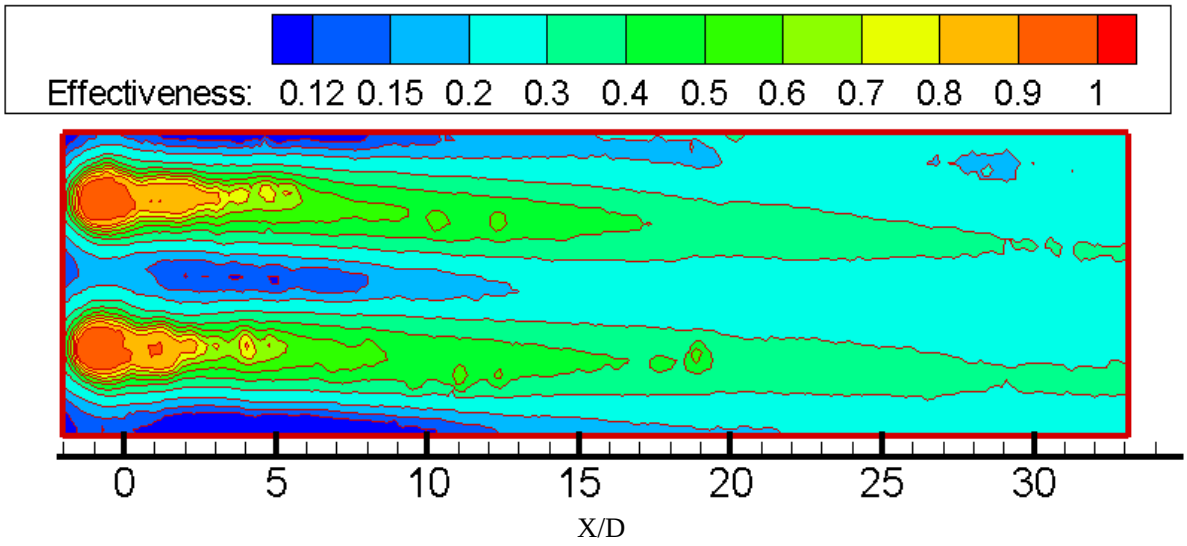

(b)

Figure 3.2 Contour of cooling effectiveness for (a) Case 1, M=0.6, air-only film (b) Case 2, M=0.6, mist/air film

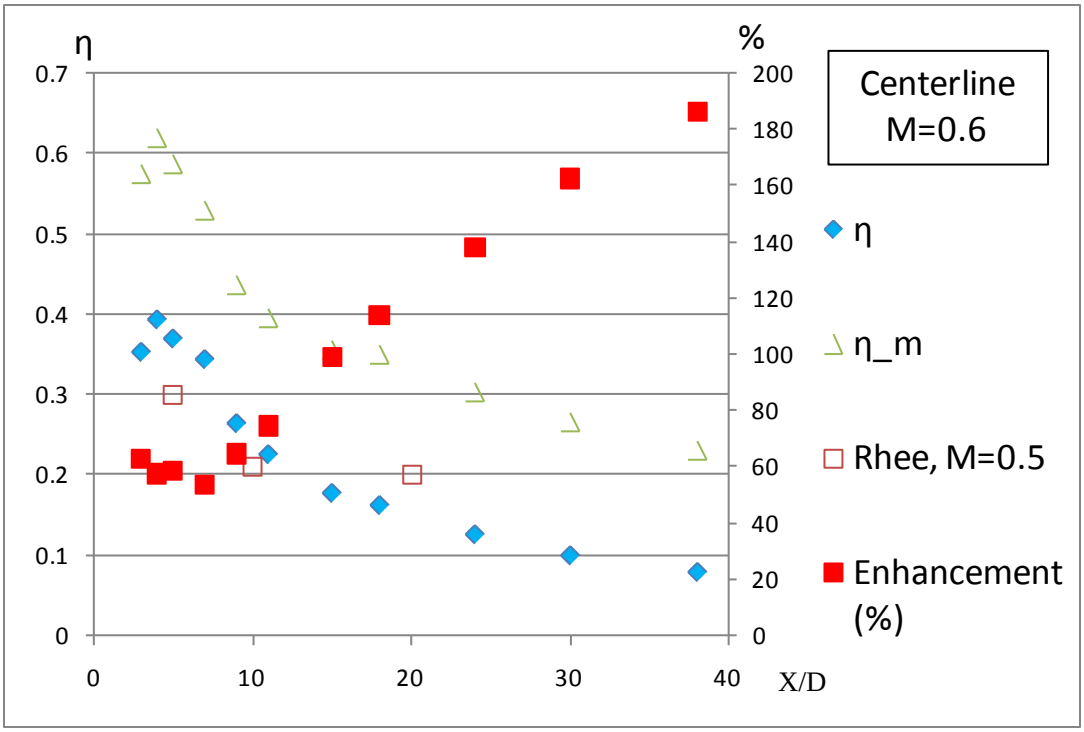

(a)

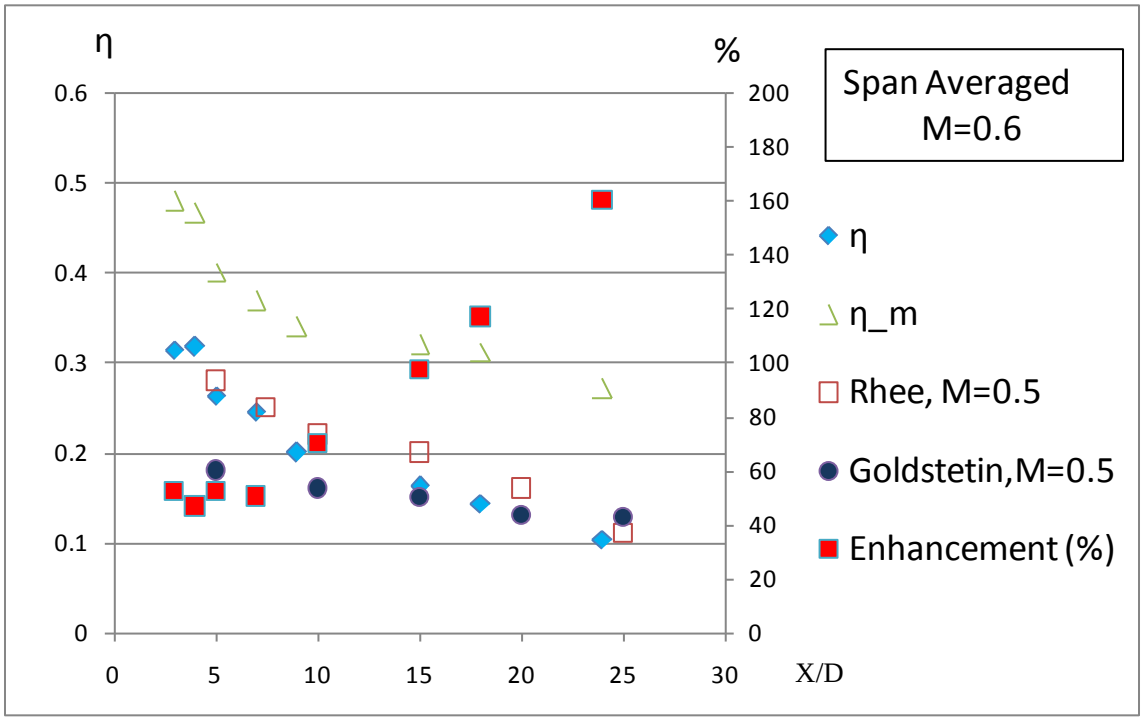

(b)

Figure 3.3 Cooling effectiveness (plotted on y coordinate on the left) and net enhancement (plotted on secondary y coordinate on the right). Compared with the experimental data from Goldstein et al. and Rhee et al. (a) M=1.4, centerline data (b) M=1.4, spanwise averaged data

The cooling effectiveness at the injection hole centerline and spanwise averaged result for the M = 0.6 cases (Case 1 and Case 2) are shown in Fig. 3.3 (a) and (b), respectively. The plots are produced based on the thermocouple measurements. The cooling effectiveness is defined the same as it was in the previous section. To evaluate the cooling enhancement of adding mist into the air film, the net enhancement is plotted on the secondary y-axis on the right-hand side. The net enhancement is defined as follows:

$$\text{Net Enhancement} = (\eta_m - \eta)/\eta$$

The subscript "m" means mist is added. Without any subscript, it means air-only film is used. From the definition, net enhancement is zero if the mist cooling effectiveness is the same as the air-only cooling effectiveness. In order to verify the current experimental results, the experimental data from the studies of Goldstein et al. and Rhee et al. are also plotted in the same figure for comparison. It is noted that the running conditions are slightly different from the current study, but still in a comparable range. For example, the blowing ratio in both Rhee and Goldstein's study is 0.5 while a value of 0.6 is adopted in the current study. Also, the inclination angle of the film injection holes for Rhee's experiment is 35^o corresponding to the 30^o holes used in the current study. Looking at the spanwise averaged data, results show that Rhee's data is reasonably close to that of the current study in both the changing trend and the values of the adiabatic film effectiveness, η. The largest η difference is less than 11% at x/L = 15. In the center line data for the air-only case, a peak value of $\eta = 0.62$ is found at around X/D = 4. The reason for the peak is attributed to the blowing off and reattachment flow patterns of the coolant jet flow. Within the blowing off area (X/D < 4), the hot main flow wraps from the side, resulting in a hotter surface temperature and a correspondingly low cooling effectiveness. The cooling effectiveness decays from the peak value of 0.62 at around X/D = 4 to about 0.1 at X/D = 30.

Also for the centerline data, after mist is added, the cooling effectiveness, η_m, is higher than that of the air-only case. The general pattern of the cooling effectiveness distribution of the mist case is similar to that of the air-only case with the peak at about the same location. This implies that adding mist in the air film does not change the general cooling pattern drastically, so that knowledge acquired through film cooling can generally be applied into mist cooling. However, the cooling effectiveness is changed greatly, and so is the coolant coverage. Furthermore, the decaying rate of η for the mist case is slower than that of the air-only case.

This is especially noticeable in the area X/D > 15. In other words, the effectiveness of mist/air film lasts longer than the air-only film. This feature is very favorable in considering applying mist cooling in gas turbines because:

1. the well-accumulated knowledge of air film cooling is still applicable in mist/air film cooling;
2. cooling effectiveness is enhanced without changing the cooling pattern, so that cooling hole geometry and arrangement can be kept the same;
3. the liquid droplets in the film provides a more extended film cooling coverage effect than the air film cooling.

Mist/air film cooling keeps all the merits of air film cooling while being more effective. Therefore, retrofitting the old air film cooling systems with mist cooling seems attractive.

It is observed that the centerline net cooling effectiveness enhancement, plotted on the right hand side y-axis of Fig. 3.3 (a), keeps approximately a constant value of 50% between X/D = 3 and X/D = 7, and then increases to 190% as X/D increases to 40. This result is supported by the observation that the decaying rate of cooling effectiveness is much slower than that of the air-only case. The integral net increase over the whole surface is 128% (centerline). A similar curve of net enhancement is found for the spanwise averaged plots. It is noted that the net enhancement is slightly lower (9% - 15%) than the centerline plot. This results from the fact that the cooling effectiveness enhancement is higher in the centerline and lower in-between injections.

The distribution pattern of the net cooling effectiveness enhancement reveals an attractive feature of mist cooling. As noticed in Fig. 3.3 (a) and (b), the net enhancement of mist cooling is increasing as X/D increases. As discussed in the previous introduction section, one of the key drawbacks of air film cooling is that the cooling effectiveness decays quickly as the air coolant film progresses downstream and mixes with the hot main flow, and, thus, loses its cooling effectiveness. However, after mist is added, the cooling enhancement actually increases as X/D increases. This implies that adding mist in the air film not only increases the cooling effectiveness, but also the liquid droplets takes some time to evaporate and extends the cooling

coverage longer downstream. Furthermore, mist generates a more uniform surface temperature distribution which is critical for reducing wall thermal stresses.

3.2.2 Case 3 and Case 4

Contours of cooling effectiveness for Case 3 and Case 4 are plotted in Fig. 3.4 (a) and (b), respectively. Comparing with the plots for Case 1 and Case 2, where the blowing ratio was set to 0.6, the cooling effectiveness of Case 3 and Case 4 is apparently lower for both with and without mist cases. Also, the coolant film coverage seems to be worse than Cases 1 and 2 in both the stream-wise and lateral directions. The un-cooled area between injections is bigger than the M = 0.6 cases. Injections from the adjacent holes are further separated from each other resulting in a bigger un-cooled gap. Moreover, it is noticed that the cooling effectiveness of the M = 1.0 cases decays more quickly than the M = 0.6 cases.

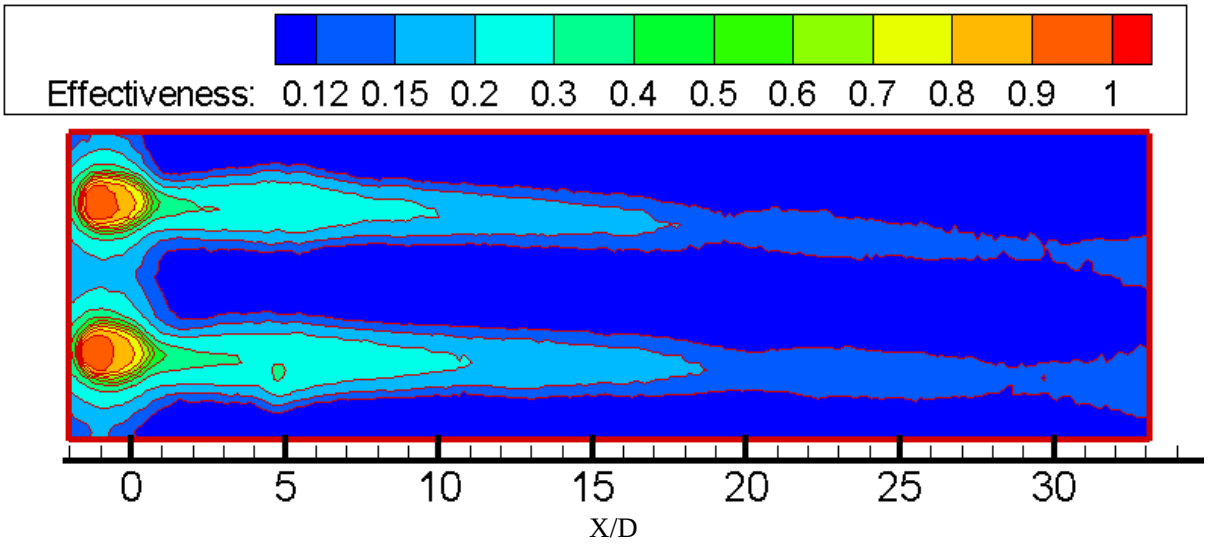

(a)

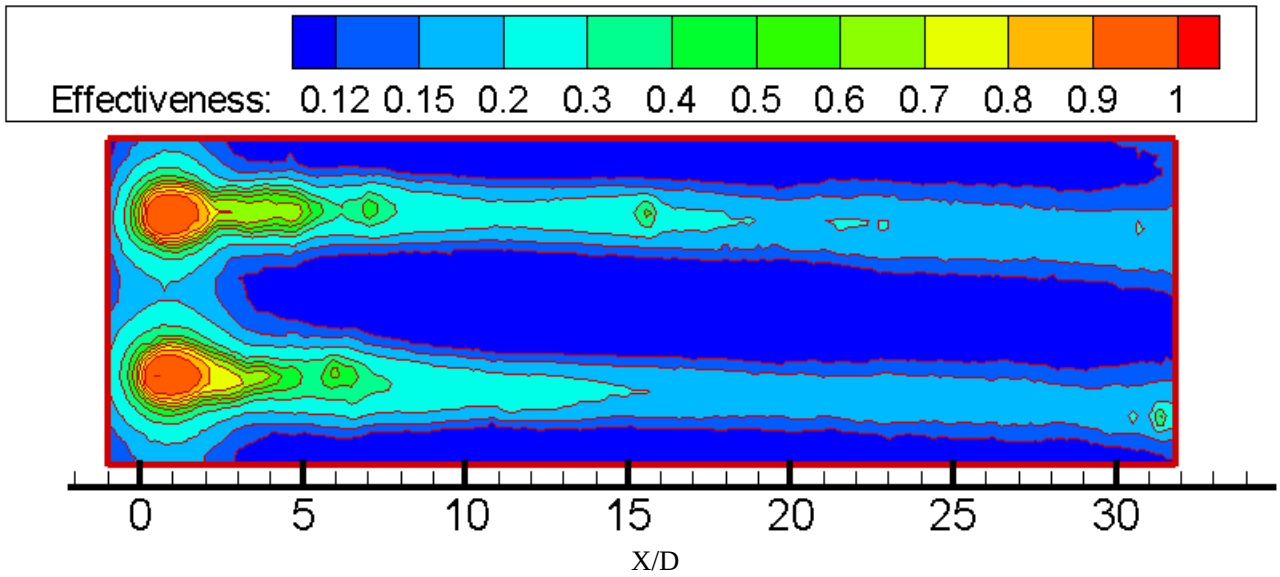

(b)

Figure 3.4 Contour of cooling effectiveness (a) Case 3, M=1.0, air-only film (b) Case 4, M=1.0, mist/air film

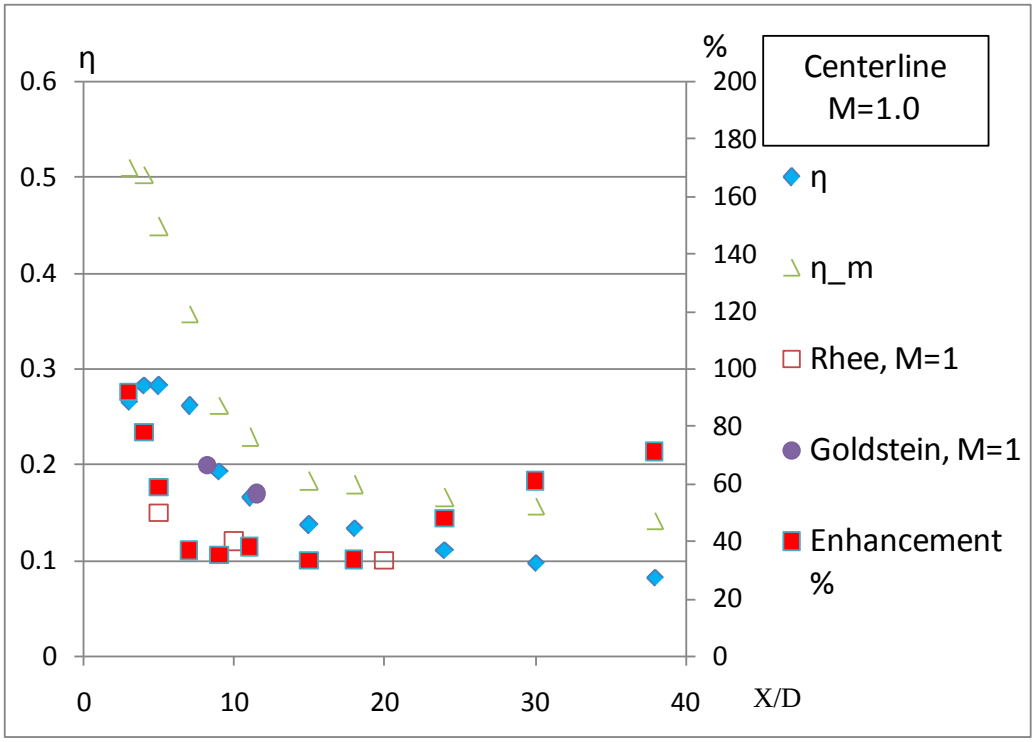

(a)

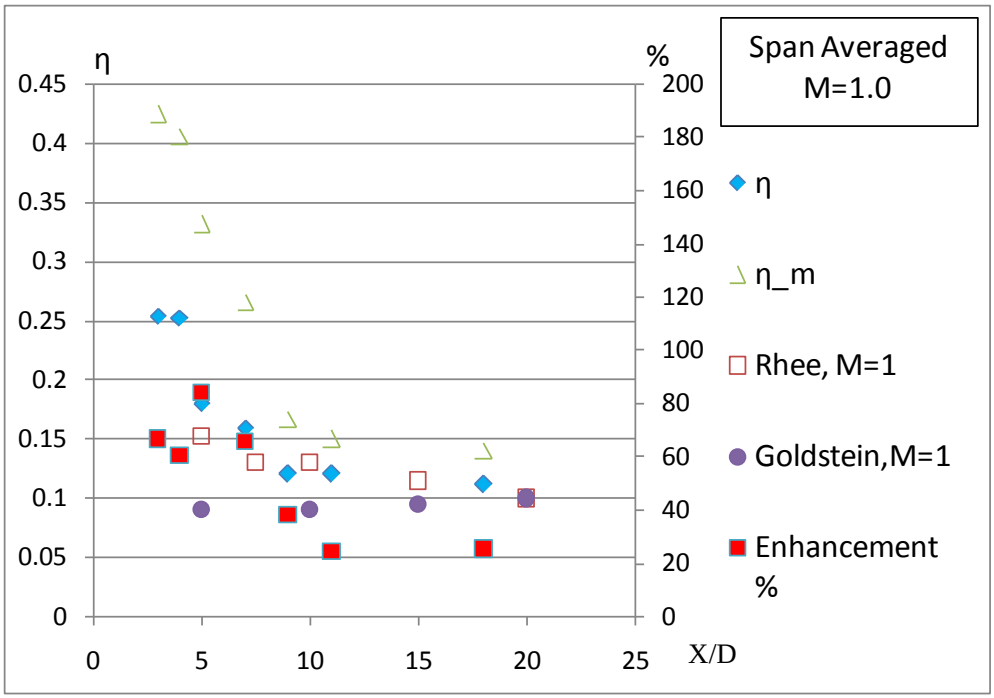

(b)

Figure 3.5 Cooling effectiveness (y-coordinate on the left) and net enhancement (y-coordinate on the right) compared with experimental data from Goldstein et al and Rhee et al (a) M=1.0, centerline data (b) M=1.0, spanwise averaged data

After mist is added, as shown in Fig. 3.4 (b), again, significant cooling enhancement is found, especially at the area close to the injection hole. The mist cooling effectiveness is higher, and the effective cooling coverage area is wider in lateral direction in this area than without mist. However, the large cooling enhancement is limited to a relatively small area where X/D < 7. The cooling enhancement is much lower downstream. It is noted that the gap between injections remains almost the same as without adding mist for the area with X/D > 7, indicating that mist in this case with M= 1 is not as effective as the previous case with M = 0.6.

The cooling effectiveness at the injection hole centerline and spanwise averaged result for the M = 1.0 cases (Case 3 and Case 4) are shown in Fig. 3.5 (a) and (b), respectively. Again, the experimental results of Goldstein et al. and Rhee et al. are plotted in the same figure for comparison.

Looking at the centerline cooling effectiveness in Fig. 3.5 (a) for Case 3 (air-only film), a peak value of 0.28 is found around X/D = 5. Cooling effectiveness dips a littlenear the injection point with only one data measurement point available for X/D < 5. This peak value is lower than the corresponding peak value of 0.39 for Case 1 in Fig. 3.3a. The cooling effectiveness decays quickly in the area 5 < X/D < 15, from 0.39 to 0.17, and levels out slowly downstream of X/D = 15, eventually dropping to 0.083 at X/D = 38. In general, the pattern of cooling effectiveness distribution for Case 3 is similar to that of Case 1, only that the cooling effectiveness values are lower in Case 3. Again, utilizing the concept of **50% Film Decay Length** introduced in the previous cases, Case 3's **FDL (50%)** occurs at X/D = 13.2. Comparing this value with that of Case 1 (FDL(50%) of X/D = 14.6), the difference is not significant (10% difference), which again indicates that the decaying rate of cooling effectiveness is similar between Case 1 and Case 3. This is understandable because the fundamental mechanism of cooling is the same for both cases with air only. The **FDL (50%)** for Case 4 (mist/air film) is 10.2, which is unexpectedly smaller than Case 3 (air film). This reveals that the decaying of cooling performance is faster when mist is added. It should be noted noted that the cooling effectiveness is still enhanced after mist is added in Case 4 compared to Case 3 for all locations. Comparing the **FDL (50%)** of Case 4 (10.2) to that of Case 2 (24.2), Case 4 yields a significantly shorter **FDL**. In contrast, the **FDL** of Case 3 is similar to that of Case 1. From the perspective of application in gas turbine blade cooling, a longer **FDL** is always favorable because it implies that the cooling performance decays slower: a longer stream-wise range on the blade surface can be covered by film cooling,

and thus, less stream-wise temperature gradient is generated, resulting in lower thermal stresses.

To look at this phenomenon from another perspective, the net enhancement plot in Fig. 3.5 (a) is examined. The net enhancement drops from 92% at X/D = 3 to 35% at X/D = 7, and levels out for 7 < X/D < 18 at about 35%. Then, the net enhancement goes up again from 34% to 71% in the region 18 < X/D < 36. This change in trend of net enhancement, decreasing and then increasing, is also very different from that of the M = 0.6 case. Again, recall that in the M = 0.6 cases, the net enhancement is roughly constant at about 58% in the region of X/D < 7, and increases sharply downstream from X/D = 7 reaching 186% at X/D = 36.

The obvious difference is that the M = 0.6 cases generally produced apparently higher cooling performance enhancement after mist is added. But, in the region very close to the injection area (X/D < 5), the net enhancement of the M = 1.0 cases can reach as high as 92%, which is higher than that of the M = 0.6 case at 62%. Combined with the findings in the previous **FDL** analysis, the highest cooling enhancement for the M = 1 cases appears near the cooling hole and decays more quickly than the M = 0.6 cases. More concentrated cooling in the M = 1 cases may induce more thermal stress. Application of mist under the M = 0.6 condition is apparently superior to doing so for the M = 1.0 condition due to both the higher overall cooling enhancement and the much longer **FDL.**

In the far downstream regions where X/D > 18, the cooling enhancement of M = 1.0 cases and M = 0.6 cases have a similar changing trend, both increasing monotonously. But the M = 0.6 cases produced significantly higher net cooling performance enhancement. The centerline integral net enhancement for the M = 1.0 cases is 53% compared to the value of 128% for the M = 0.6 cases.

3.2.3 Case 5 and Case 6

The contour of cooling effectiveness for Case 5 (M = 1.4, air-only film) and Case 6 (M = 1.4, air/mist film) are shown in Fig. 3.6 (a) and (b), respectively. Comparing this with the corresponding plots for Cases 1-4, it is first noticed that the film coverage is clearly significantly smaller. The un-cooled gap between injections is bigger, indicating poor film coverage. Similar to the M = 1.0 cases, cooling effectiveness is enhanced in the region close to injection hole area (X/D < 7). Figure 3.6 (a) is expected because, from the experience of air film cooling studies, with a blowing ratio of 1.4 under the current study's hole geometry, the coolant film will have

enough momentum to be detached from the blade surface, resulting in low cooling effectiveness and poor cooling coverage. Fig. 3.6 (b) shows that adding mist will not provide much benefit in improving cooling effectiveness and coverage, especially in the downstream area away from the coolant injection holes.

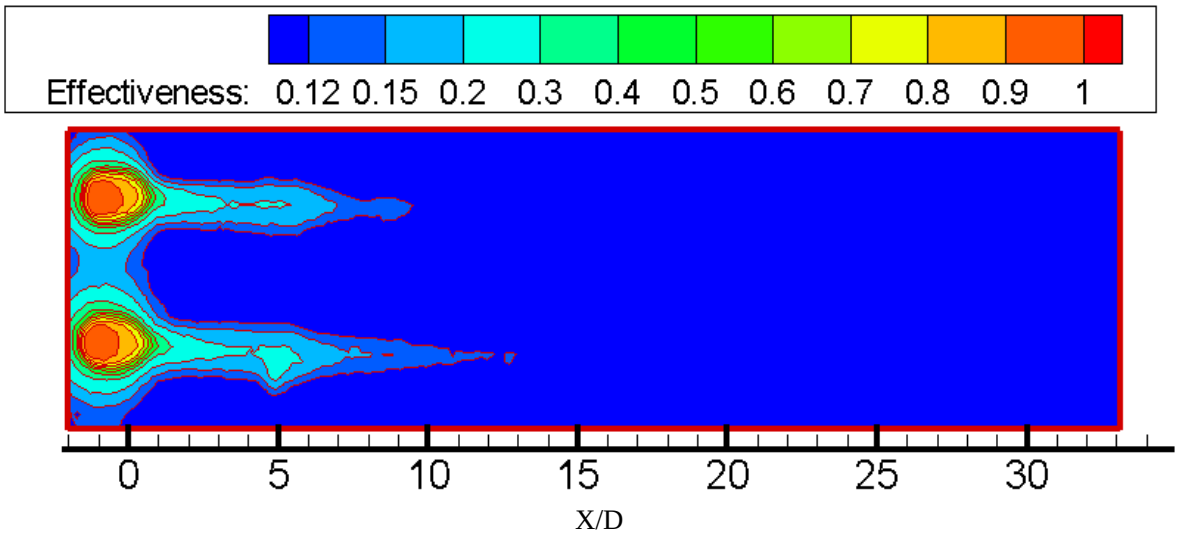

(a)

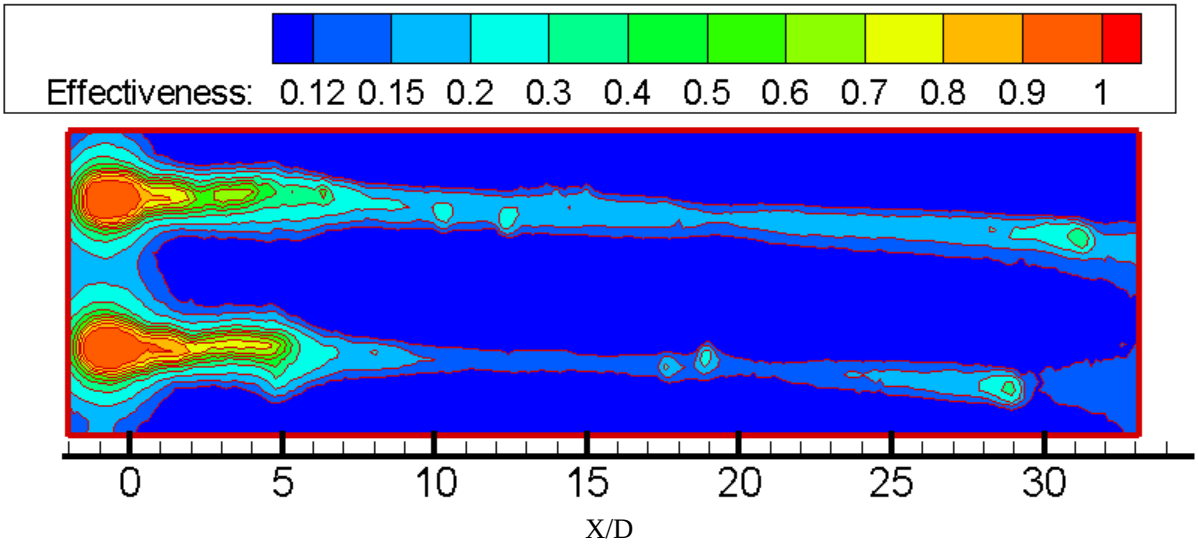

(b)

Figure 3.6 Contour of cooling effectiveness (a) Case 5, M=1.4, air film only (b) Case 6, M=1.4, mist/air film

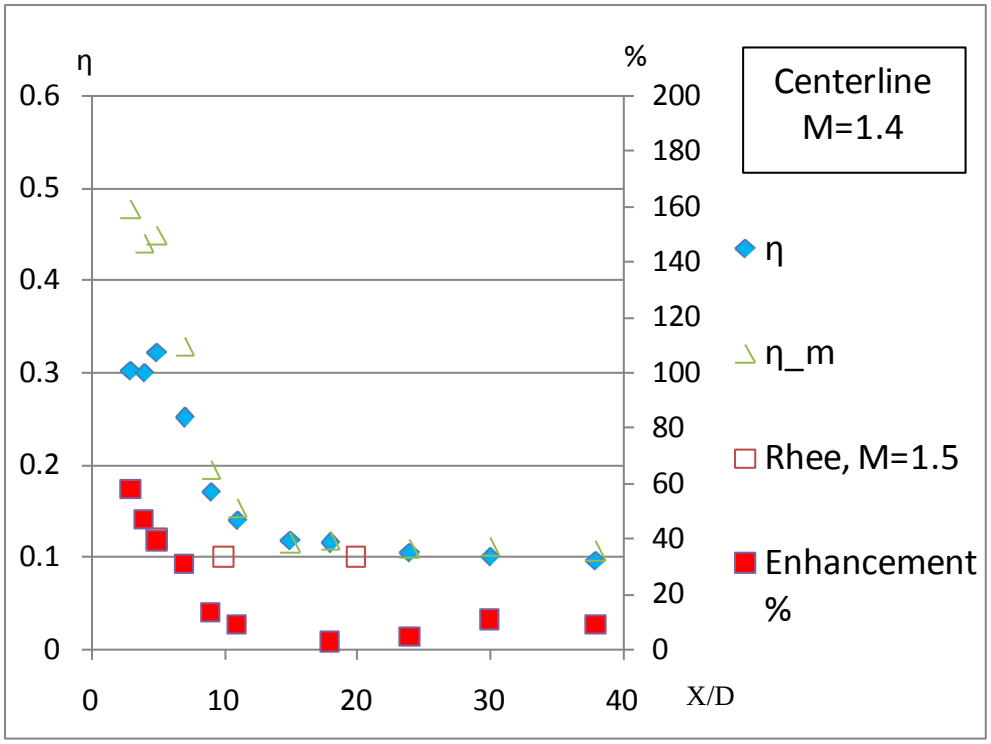

(a)

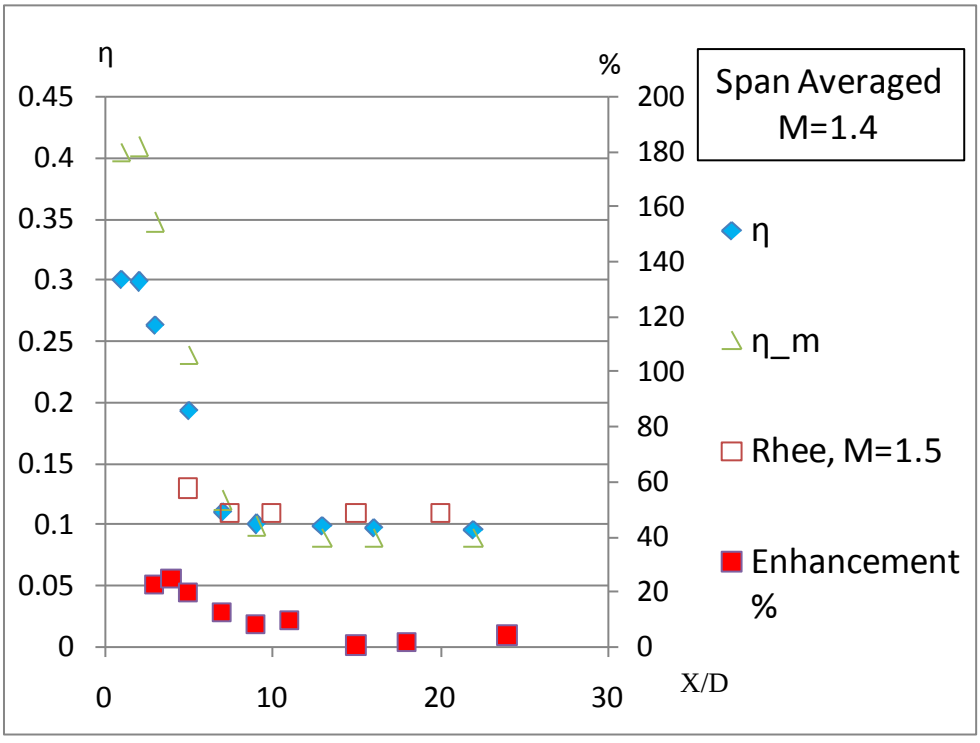

(b)

Figure 3.7 Cooling effectiveness (y-coordinate on the left) and net enhancement (y-coordinate on the right) compared with the experimental data from Goldstein et al and Rhee et al (a) M=0.6, centerline data (b) M=0.6, spanwise averaged data

The cooling effectiveness at the injection hole centerline and the spanwise averaged result for the M = 1.4 cases (Case 5 and Case 6) are shown in Fig. 3.7 (a) and (b), respectively. The experimental results of Rhee et al. are plotted in the same figure for comparison.

The **FDL (50%)** for Case 5 and Case 6 is 10.2 and 8.3, respectively. Again, comparing the **FDL** of Case 5 and Case 6 shows that adding mist does not provide improved stream-wise film coverage, which is similar to that of the M = 1.0 cases. The **FDL (50%)** of Case 5 is slightly smaller compared to that of Case 1 and Case 3, implying that, as the blowing ratio increases from 0.5 to 1.4, film coverage actually decreases in the centerline of the stream-wise direction. This is understandable since, as the blowing ratio increases, the coolant film has more momentum to be lifted further away from the surface and mix with the hot main flow. As a result, the film coverage over the surface is worse than the lower blowing ratio cases even though more mass flow of coolant is injected into the flow channel. Among these three blowing ratios, Case 2 with M = 0.6 is clearly the most superior in the sense that it has the highest **FDL** and broadest film cooling coverage areas provided. Also, when the coolant film is not detached from the surface, adding mist will significantly improve both the cooling effectiveness and also the film coverage. However, in the blowing off cases, adding mist does not improve the cooling performance in either the effectiveness or the coverage. Therefore, it is important to bear in mind that when applying mist cooling, choose the low blowing ratios to keep the coolant film attached to the surface to exploit the full benefits of mist cooling.

Looking at the centerline cooling effectiveness for both Case 5 (η) and Case 6 (η_m), it is noticed that η_m is apparently higher than η only in a limited area close to the injection holes (X/D < 9). In the downstream area of X/D > 11, the cooling effectiveness with mist is almost identical to that of the air-only case. This is also supported by the net enhancement data. The net enhancement of cooling effectiveness is first decreasing from the peak value of 60% in the region close to the injection hole (X/D < 11), then becomes almost constant at a value close to zero in the area of 11 < X/D < 24, and slightly increases to about 10% at X/D = 38. The pattern of the net enhancement curvature is very similar to that of the M = 1.0 cases, only that the values are lower for the M = 1.4 cases. Both the M = 1.0 and M = 1.4 cases produce very different net enhancement curves from the M = 0.6 cases, indicating the different mechanism of cooling performance enhancement between those cases.

The centerline integral net enhancement for Cases 5 and 6 is 11.4% which is the lowest

for all three groups of cases. Adding mist is ineffective, especially in the area of 11 < X/D < 24, with the net enhancement almost zero in this area.

3.3 Particle Measurement Results

To understand the mist cooling heat transfer results presented in the previous section, an understanding of the droplets behavior and their interactions with the flow field and temperature field is essential. Thus, particle measurement is an integral part of this experimental study of mist cooling. The PDPA system, as described in Chapter Two, is employed in this study to measure the particle information. The particle information that is of interest to the current study includes droplet size distribution, velocity, and droplet density. The particle velocity includes the instantaneous velocity and the averaged velocity in both the streamwise and vertical (perpendicular to the wall) directions.

It must be noted that there are some features associated with the particle data that requires special attention.

1. The PDPA measurement is essentially a point measurement method. It documents the particle that passes by the specific point of measurement. Traversing of the laser beams is needed to map out the information in a plane or space to give a more general picture of the whole field. This requires a lot of time and effort to accomplish, and as a result, the spatial resolution is limited to the number of measurement points.
2. The particle signal is random in nature. A certain number of samplings are needed to give meaningful measurements. As a result, all of the measurement data needs to be treated in a statistical manner. Interpretation of the data also requires an understanding of the random nature of the data. For example, the Fourier Transform for the random data is very different from that of a continuous measurement. Some assumptions need to be made to perform the Fourier Transform analysis over scattered and non-periodic data.

3.3.1 Droplet Size Distribution Plots

The distribution of droplet sizes for the case where M = 0.6 is shown in Figs. 3.8- 3.11 at different stream-wise locations. Within each figure, the particle size distribution at different elevations (Y-axis) from the surface is plotted. The X-axis is the particle size and the Y-axis is

the particle data rate. Those figures are intended to give the information of the particle size distribution over the flow field. Particle size information is critical in understanding the droplets' behavior and the evaporation process in mist cooling. It has close interactions with the thermal-flow field. Also, the variation of droplet size reveals the heat transfer characteristic of mist cooling.

The particle data rate is the number of particles that are captured and counted per unit time at the measurement location. It is noted that not all of the particle signals are counted in the measurement: only the signals that meet certain threshold criteria.. For example, the intensity of the light that is reflected by a particle is theoretically proportional to its size, i.e. bigger particles reflect higher intensity light while smaller particles reflect lower intensity light. Thus, if a particle's signal bears very low light intensity, but still appears quite large in size based on the frequency measurement, the signal will be dropped because it is very likely that the light signal is from wall reflection or is simply noise.

The particle data rate is determined by a combination of two factors: particle velocity and particle density. As particle velocity increases, more particles pass the measurement volume per unit time, and, as a result, the particle data rate is higher. Similarly, if the particle distribution is dense in the area, more particles will be captured per unit time, also resulting in higher data rates.

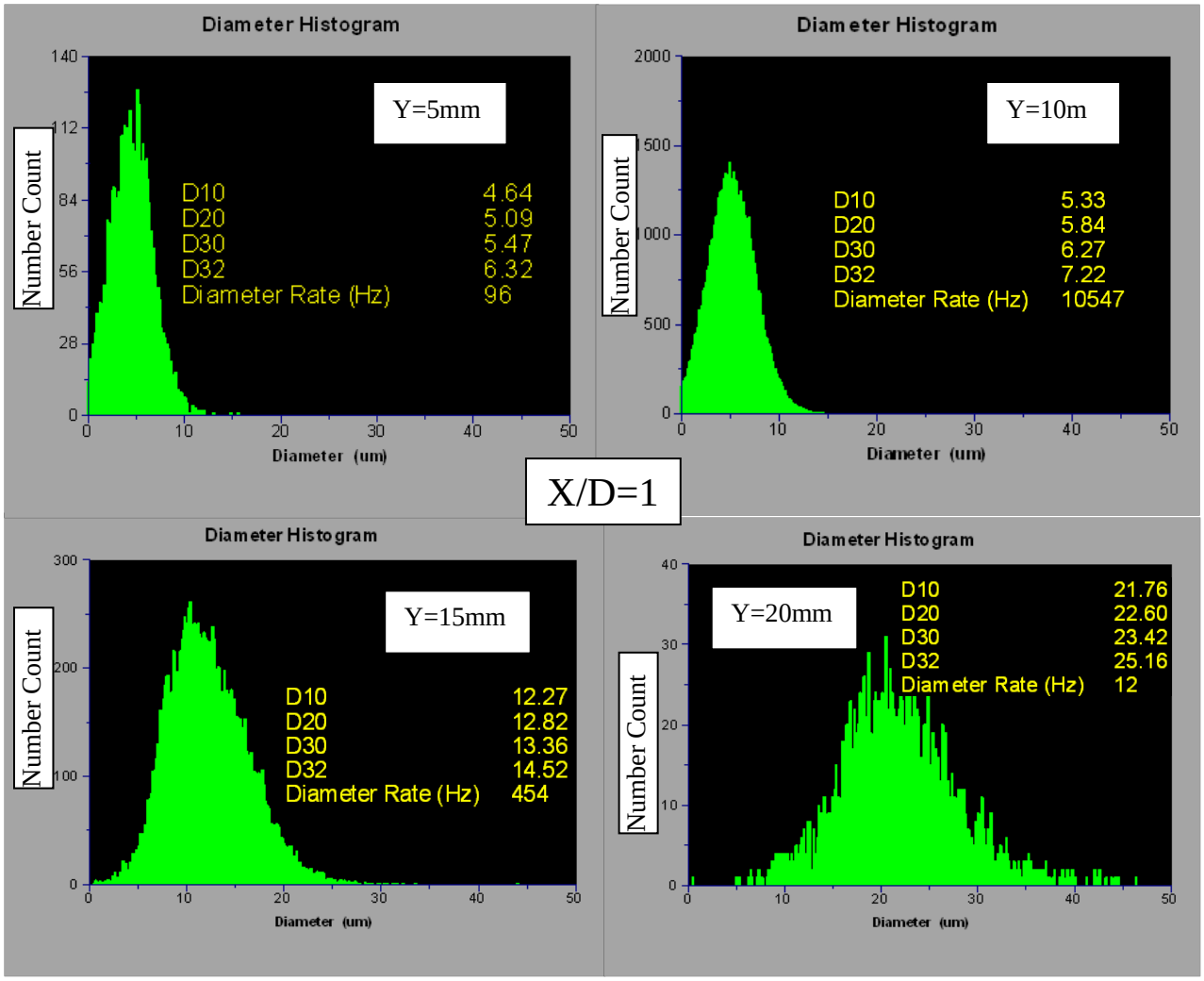

Figure 3.8 Droplet size distribution of various y locations at X/D=1, M=0.66

In the area very close to injection hole, X/D = 1, as shown in Fig. 3.8, the droplet distribution of different y-elevations is plotted. Notice that the droplet distribution patterns at y = 5mm and 10mm are quite similar. The droplet size distribution is centered at about 5μm and the biggest droplets are sized at 15μm. The difference is that the droplet data rate at y = 10mm is one scale higher than that of y = 5mm. As a result, the curve of y = 10mm looks smoother than that of y = 5mm. As the measurement elevates to y = 15mm, the droplet distribution changes greatly with the most frequently captured droplet size increasing to about 12μm with the largest droplets sized at 30μm. Droplets that are smaller than 10μm only account for less than 5% of the total droplet population. It is noted that the particle number counts (within the same time

interval) shown on the Y-axis reduce to about the same level as y = 5mm. As the Y-coordinate further increases to 20mm, the most frequently captured size increases to 21μm and the biggest droplet can be as large as 40μm or larger. Meanwhile the droplets smaller than 10μm almost disappear at this elevation level. It is noted that the droplet data rate is very low too.

In summary, at an area very close to the injection hole, X/D = 1, the particle size distribution moves towards larger sizes away from the surface. The particle data rate increases first from 5mm to 10mm away from the surface, and then decreases to zero at higher Y-elevations.

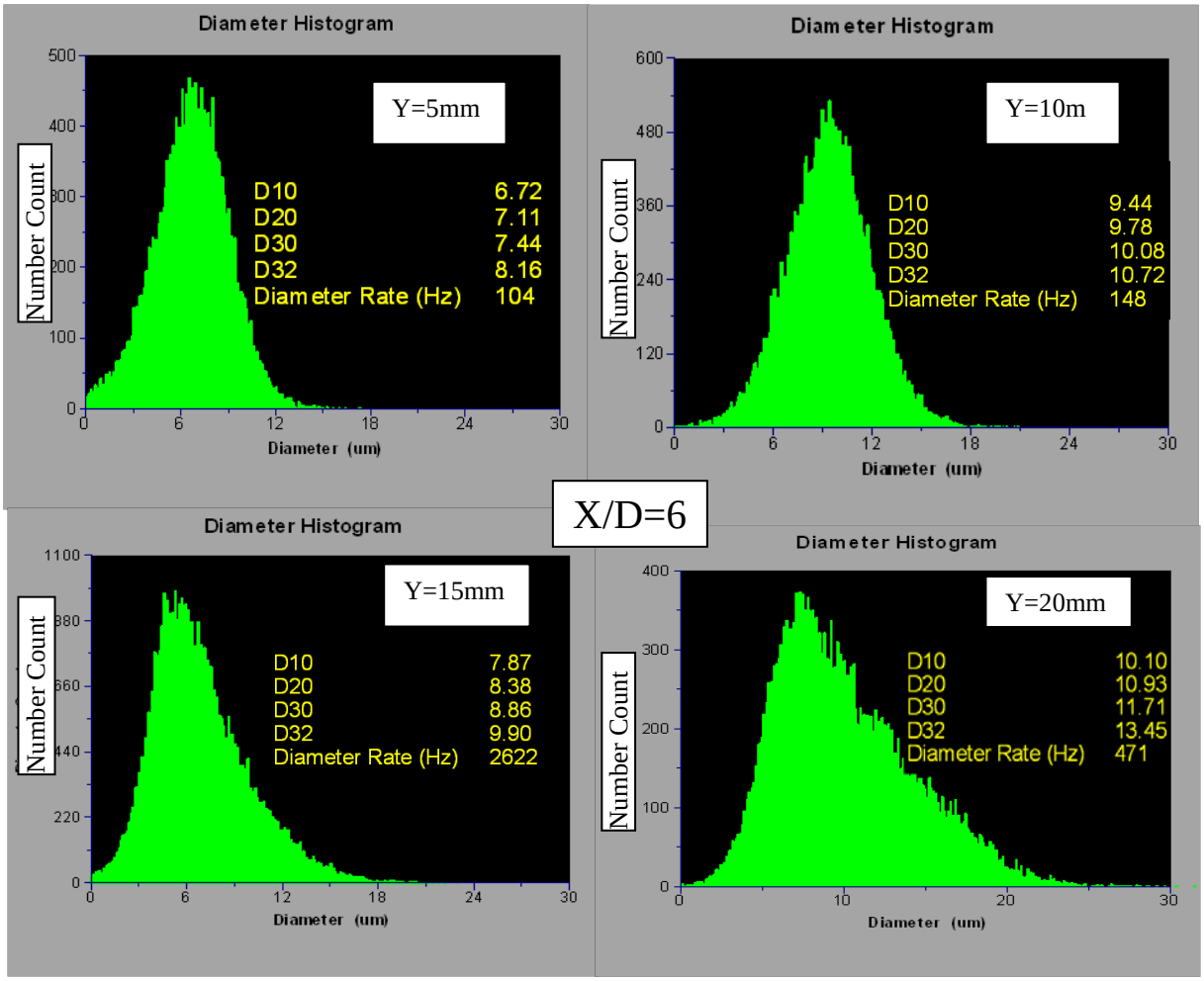

Figure 3.9 Droplet size distribution of various y locations at X/D=6, M=0.66

As X/D further increases (i.e. moving downstream), the particle size distributions at the same elevations at X/D = 6 are plotted in Fig. 3.9. At Y = 5mm, compared to the same plot at

X/D = 1, the size distribution leans towards bigger sizes, with the most frequently captured size being 7μm (compared to 5μm for X/D = 1 at 5mm). Correspondingly, the largest size reaches 17μm. The smaller particles make up a smaller portion of the total particle population. At Y = 10mm, the size distribution leans towards bigger sizes compared to those at Y = 5mm with the most frequently captured size at 10μm.. An interesting observation is noticed when the comparison is made between the distributions at Y = 10mm and 15mm. The center of the droplet size distribution moves towards smaller droplets, decreasing from 10μm to about 6μm. This is opposite to the trend found for X/D = 1. At Y = 20mm, the droplet size increases again. So looking from bottom to top, the droplet size first increases, then decreases slightly, and eventually increases again. This is one of the interesting characteristics of droplet distribution pattern involving film jet flow with particles. It is a combined effect of the droplet interactions within the flow and temperature fields. Detailed investigation and interpretation of these phenomena and their effects on surface heat transfer will be discussed after more information about the particles is presented.

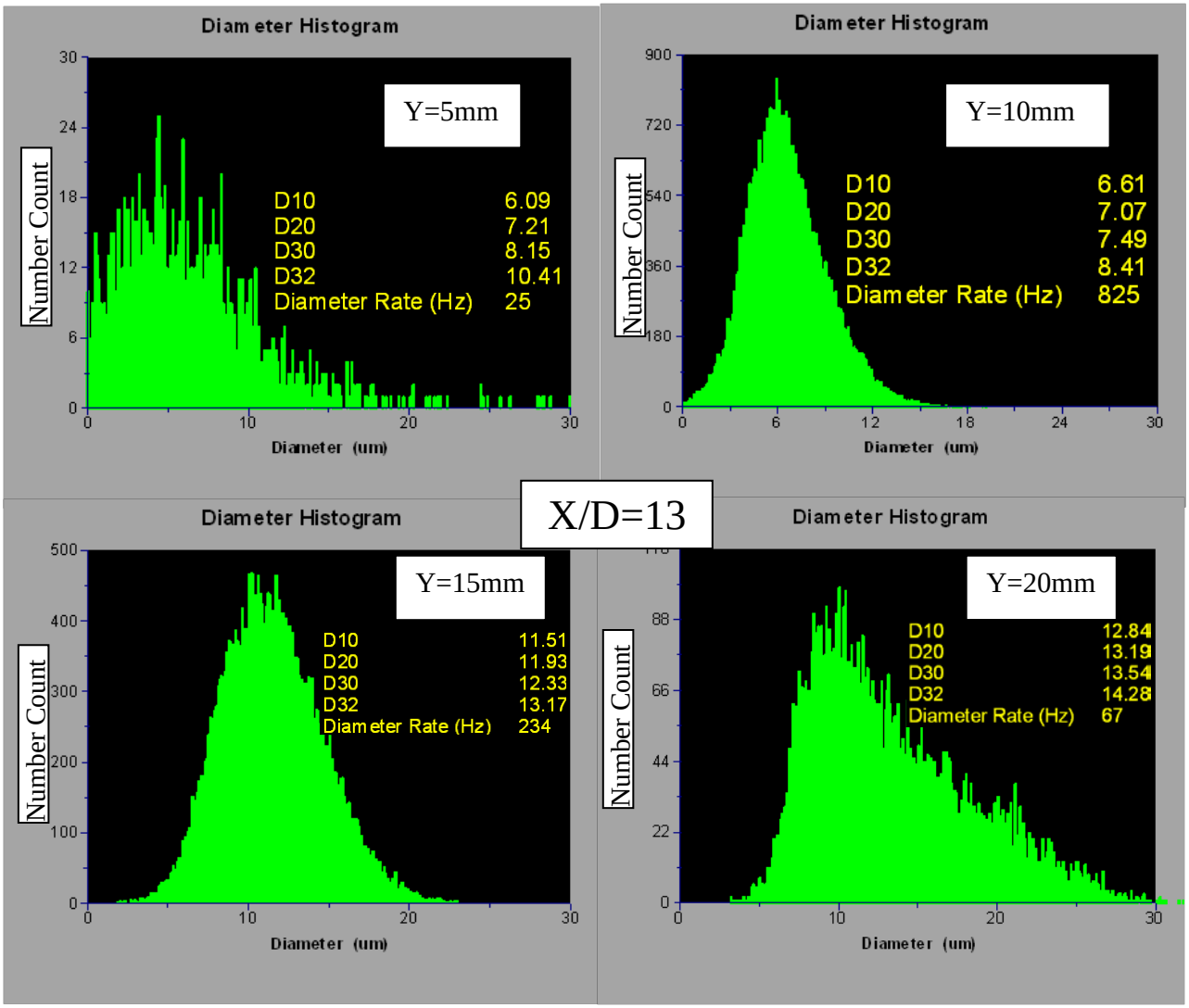

Figure 3.10 Droplet size distribution of various Y locations at X/D=13, M=0.66

As X/D further increases to 13, it is found in Fig. 3.10 that at Y = 5mm, the data rate is very low and the size distribution curve is rugged due to the small amount of sampling data. The data rate increases significantly at Y = 10mm showing a smooth, symmetric distribution curve centered with the 7μm droplets as the most frequently captured size and ending with the biggest size at about 18μm. At Y = 20mm, the droplet size distribution leans towards bigger droplets and the data rate is very low, while the size distribution is no longer symmetric as in the lower elevation levels. This means that bigger droplets are more frequently present at this measurement point.

In the region far away from the injection hole, X/D=28, shown in Fig. 3.11, the particle

size distributions at Y = 5mm and 10mm are both almost symmetric with the average size at Y = 10mm being bigger than at Y = 5mm. This distribution is quite similar to that of the upstream locations. One interesting finding is that at elevations Y = 20mm and higher (i.e. the Y = 20mm, 25mm, and 30mm), the size distribution is almost identical. The plots have similar shape, the average size is about the same, and the droplet size distribution leans towards bigger particles. It is also noticed that the particle data rates are similar. Assuming that this height is outside the boundary layer and inside the core of the main flow (which proved to be true later), the speed of the droplets is almost the same. Since the data rate is determined by the particle density and speed, it is concluded that the droplet density is also similar in this region. Thus, this information shows that beyond a certain height away from the surface, the droplets have a similar size distribution, density, and speed. This is interpreted to mean that, at the elevations beyond Y = 20mm, the droplet distribution is not a function of elevation any more.

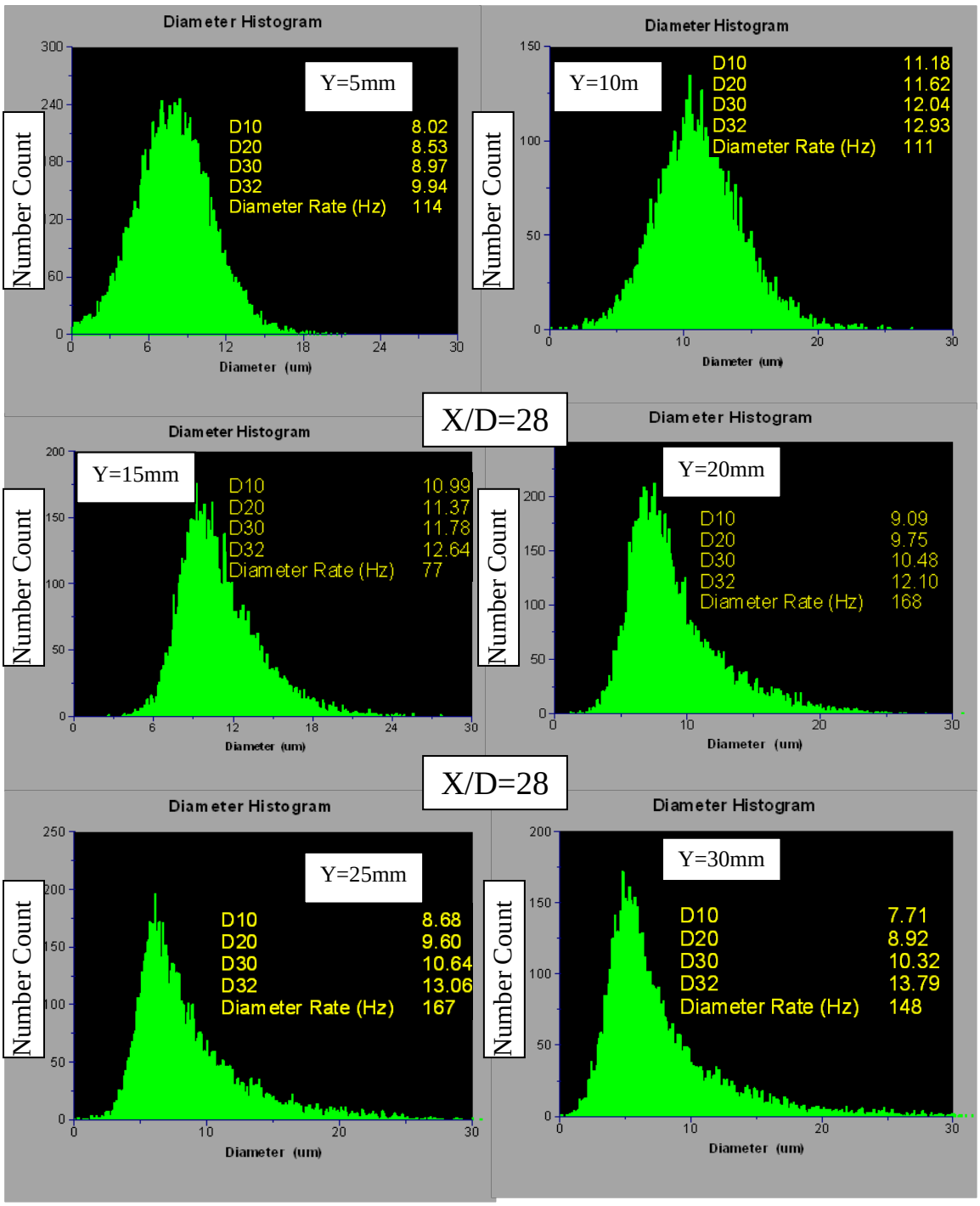

Figure 3.11 Droplet size distribution of various Y locations at X/D=28, M=0.66

3.3.2 Size Distribution with Particle Data Rate Plots

In order to give more detailed information about the droplet behavior, the average droplet size distribution is plotted together with the droplet data rates in Fig. 3.12. By putting them together in the same plot, some correlation patterns are expected to be discovered.

The average droplet size as a function of the vertical distance from the surface is plotted in Fig. 3.12 for different stream-wise locations. On the chart, the X-axis is the vertical distance (Y) from the plate surface and the Y-axis on the left is the average droplet size. Four stream-wise locations, X/D = 1, 6, 13 and 28 are plotted in Fig. 3.12 (a), (b), (c), and (d), respectively. The data rates are plotted on the secondary Y-axis on the right.

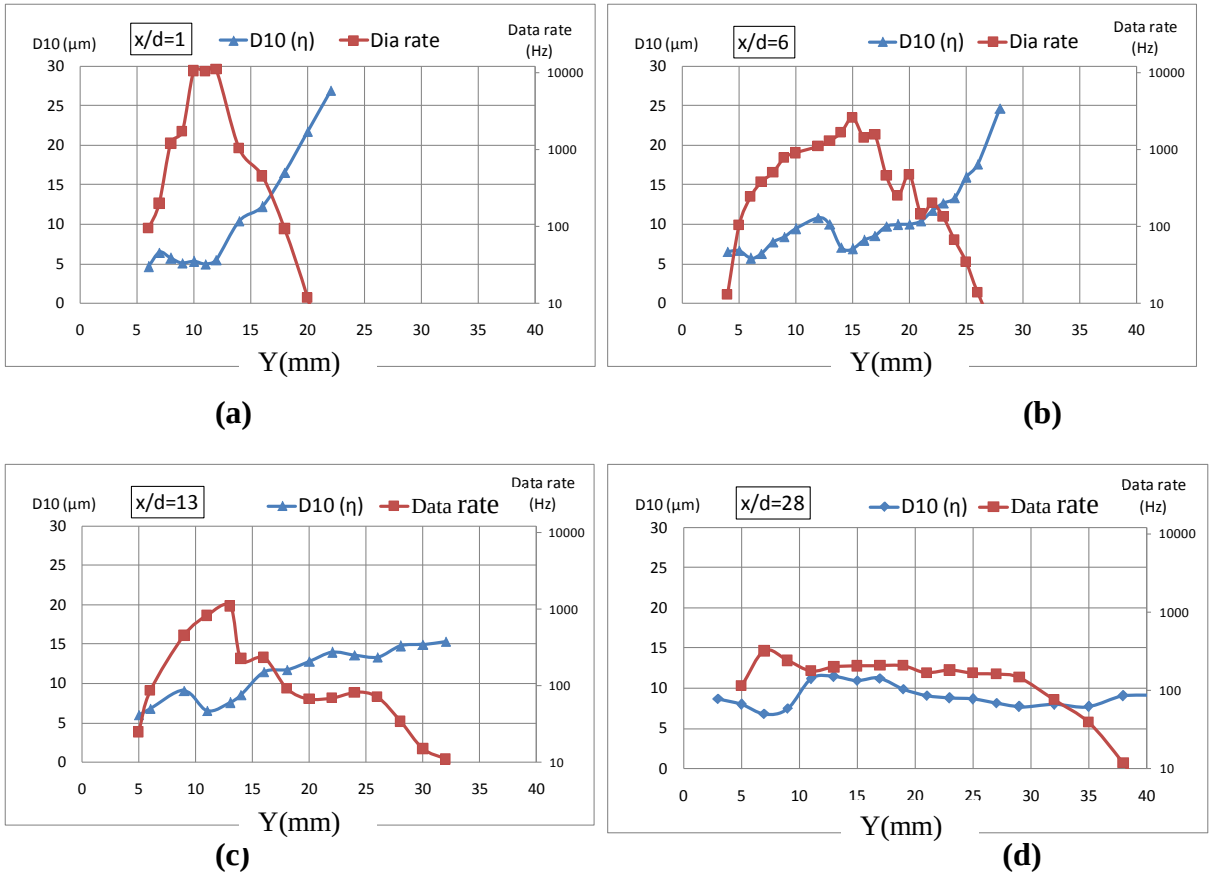

Figure 3.12 Case 2 (M=0.6) particle size distribution (plotted on Y coordinate on the left) and particle data rate distribution (plotted on Y coordinate on the right) as a function of Y locations at (a) X/D=1 (b) X/D=6 (c) X/D=13 (d)X/D=28

Looking at the averaged droplets size (D10) distribution for X/D = 1, the first measurement point is 6mm away from the surface. It is noted that below this point, the data rate

is too low to produce a meaningful measurement. This means that there is a very minimal number of droplets present under a certain elevation from the surface. From a real physics point of view, this result shows that the droplets are actually lifted away from the surface at the area very close to the injection hole (X/D=1). This is understandable because mist droplets are carried into the main flow chamber by the coolant. With the help of the initial coolant jet's injection momentum, droplets will be lifted off. The average droplet size is almost constant (5μm) from 6mm to 12mm away from the surface. The average droplet size suddenly starts to increase from Y = 12mm to reach 27μm at Y = 22mm. Again, it is noted that beyond Y = 22mm, the data rate is too low for any meaningful measurements. This indicates that the droplets are almost absent beyond Y = 22mm. This is also understandable from the physics point of view that the momentum of the droplets acquired from the coolant jet is not strong enough to shoot the droplets this high. Also, the particle distribution information rules out the possibility that the absence of droplets higher than Y = 22 mm is caused by complete evaporation at this height, because the trend of the droplets size is actually increasing below this point. Therefore, the reason for the low droplet count beyond a certain height is mainly caused by the fluid mechanics, not the heat transfer. It can be concluded that **fluid mechanics is the dominant factor that determines the droplet size distribution.**

At X/D = 1, it is noticed that there is a small “hump” (local maximum) in the droplet size distribution curve at around Y = 7mm. Due to the measurement uncertainty, which is estimated as high as 5%, it is not clear whether this “hump” is real or not from this figure alone.

Examining the Fig. 3.12 (b) at X/D = 6, the general pattern of D_{10} increasing as Y increases is followed. But, this figure shows many other interesting patterns that can be more clearly seen by comparing it with the D_{10} distribution in Fig. 3.12 (a). The results of comparison are summarized as follows:

1. In the region of Y < 6mm at X/D = 6, the average droplet size is relatively small at about 6μm. Similar to the size distribution at X/D = 1, the droplet size is almost constant within this area, but slightly bigger than the corresponding size distribution at X/D = 1.
2. In the next region of 6mm < Y < 15mm, a “hump” is seen in the D_{10} distribution at Y = 12mm. Within the “hump”, the average droplet size first increases to about 11μm at Y = 12mm and then decreases to about 7μm at Y = 15mm.

3. It is noted that the slope of the left side of the “hump” is smaller than that on the right side. This means that the droplet size increases slowly toward the peak as Y increases and then decreases quickly away from the surface.
4. In the region beyond Y = 15mm, the droplet size continues increasing to reach about 24μm at Y = 25mm.

In summary, the size distribution can be roughly characterized in three sections: the flat curve section with Y < 6mm, the “hump” section with 6mm < Y < 15mm, and the outside “hump” section with Y > 15mm.

Now looking at Fig. 3.12 (c) at X/D = 13, the D_{10} distribution pattern is similar to that of Fig. 3.12 (b). But the differences are:

a) The flat curve section is not obvious.
b) The location of the “hump” moves closer to the wall for 5mm < Y < 12mm.
c) The “hump” is smaller compared to X/D = 6 with the peak value of D_{10} about 9μm.
d) The droplet size outside the “hump” is smaller compared to the size within the same region (outside of hump, not necessarily the same Y values) of the X/D = 6 case. The largest D_{10} is 15μm compared to the 24μm of the X/D = 6 case.

The size (D_{10}) distribution at X/D = 28 is quite different from the previous cases. The “hump” pattern is not recognizable. Droplet size slightly decreases from Y = 2.5mm to Y = 7mm and then sharply increases starting above Y = 7mm. In the region higher than Y = 20mm, the average size changes only slightly.

Physical interpretation of those distribution patterns is very important in understanding the mist cooling mechanisms. Before making any judgment or conclusion based on the size distribution plots, the particle data rate distribution will be examined as well, which is expected to help in the interpretation of the data.

Again, the particle data rate is the number of particles that are captured and accounted per unit time at the measurement location. Since the particle data rate is affected by both the particle velocity and the density, in order to simplify the analysis, it is first assumed that the droplet velocity does not significantly affect the particle data rate. The validity of this assumption will be re-examined later in this chapter. With this assumption made, the particle data rate can now be interpreted to be directly proportional to the droplet's density.

The particle data rate is plotted on the Y-axis on the right in Fig. 3.12 (a), (b), (c), and (d) for different X/D locations of 1, 6, 13, and 28, respectively. The X-axis is the vertical distance from the plate surface. The data rate, due to its high variation in scales, is plotted on a log coordinate. Examining Fig. 3.12 for data rate plot for different X/D locations, it is found that a roughly "cone" shape is observed in all four plots. The "cone" shape is not as obvious for the X/D = 28 case as it is in the other three cases, but it is still recognizable. In general, the particle data rate increases first and then decreases, with some exceptions, locally in small scales. In a nutshell, there exists an "envelope" of air containing the droplets within the flow. All droplets are distributed only within the "envelope," which is characterized by an apex showing the highest droplet density and bounded by upper and lower elevations. Outside this envelope, the droplet density quickly drops to almost zero. A first impression is that this envelope might represent the trace of the film jet's width. This is not correct: if the "envelope" were the jet film, many patterns of the droplet size distribution could not be explained.

One important observation by considering both the size distribution and the data rate together, is that the peak location of the particle data rate is always in the close neighborhood of the location where the droplet size starts to increase "on the right side of the hump"--- a local minimum. In other words, the location of the peak of the data rate "envelope" is always close to the right boundary of the "hump." The values of the locations acquired corresponding to the peak of the data rate curve and the "hump" right boundary of the droplet size curve are summarized in Table. 3.3. As shown in the table, the Y-locations corresponding to the peak in the data rate curve and the right side of the "hump" in the droplet size curve are almost identical except for a slight difference at X/D = 13.

Table 3.3 Comparison of the Y location for coolant film upper boundary acquired from the data rate curve and the size curve (Case 2, M=0.6)

X/D	size curve (mm)	data rate (mm)
1	11.0	11.0
6	15.0	15.0
13	11.0	13.0
28	7.0	7.0

3.4 The Proposed Coolant Air/Droplet Spreading Profile in the Cooling Film

The physics of the aforementioned observations is summarized below:

1. The coolant film, mixed with the mist droplets, keeps its own identity traveling in the main flow channel in the area of $1 < X/D < 13$ in the stream-wise direction. The coolant film with mist travels as a layer with finite thickness, which is discernable through the combined information of both the size curve and the data rate curve.
2. The right side of the "hump" in the droplet size curve indicates the upper boundary of the coolant jet layer. This upper boundary can also be identified by the location of the peak value from the data rate curve.
3. The bottom boundary of the film cannot be identified as clearly as the upper boundary. However, the bottom boundary can be roughly estimated by the location where the data rate is lower than 50 Hz on the left side of the "hump". The difference between the two is not significant and the shapes of the curves are similar, which will be shown later in this section.
4. The size of the "envelope", as shown by the data rate curve, is the range where the droplets can reach. It is noted that this envelope size is larger than the film layer width. However, the width of the "hump" corresponds to the width of the jet film.

Based on the proposed profile of coolant air film, another important observation is made that there is a separation between the coolant air film (mixture of air and droplets) and the droplet layer (within which droplets reside). The two layers do not coincide. In other words, large droplets penetrate through the air coolant film layer and travel further into the main flow. This phenomenon was observed in CFD simulations as well and was reported by the studies of Li and Wang (2007, 2008).

3.4.1 Supporting Data for the Proposed Coolant Air/Droplet Spreading Profile

It is noted that after the peak value in the data rate curve, the data rate decreases sharply for all cases in Fig. 3.12. Based on the assumption that the data rate is positively proportional to the droplet density, this implies that the droplet density decreases sharply after the peak. From the previous assumption for easier analysis, the coolant film still keeps its identity and travels in a layer of spreading finite thickness. Also, the peak of the data rate curve is right on the boundary of the coolant film layer. Thus, the right side of the peak of the data rate curve is

actually outside the span of the coolant film. Noting that the mist is injected into the main flow channel carried by the coolant film, it makes sense that number of droplets decrease sharply outside the coolant film layer. The data rate decreases quickly outside the coolant film carrying the most mist. Water droplets, with a higher density than air, tend to shoot higher than the air coolant film. Thus, the droplet population density is higher toward the top boundary of the coolant jet. Another minor reason for the data rate going higher toward the top boundary is that the air flow speed is slightly higher on the top of the film and approaches the main flow speed, so more droplets pass the measurement location during the observation time, resulting in a higher data rate. Overall, (1) inside the film layer, the data rate goes higher because of the fluid mechanics determined distribution and (2) the data rate starts to decrease at the film's top boundary. Thus, the peak can only exist at the top of the boundary as a natural result of 1 and 2.

On the other hand, if the droplets can travel outside of the coolant film layer, they must possess momentum that is high enough to break through the coolant film layer. Due to the long distance that the droplets have traveled through in the mixing chamber, it is believed that the droplets have reached their terminal speed (i.e. the droplets maintain a constant slip velocity with the coolant air.) before entering the film hole. As a result, bigger droplets will have higher initial momentum shooting into the main chamber because the droplets are accelerated though the film hole channel from the coolant supply plenum. Bigger droplets have higher mass, and, thus, higher momentum. Therefore, the droplets that are able to acquire enough momentum to break through the coolant film must be “big” droplets. Now, from the series of analyses conducted above, it is concluded that this feature of bigger droplets existing outside the coolant film stream should be reflected in the size distribution curve. It is actually shown clearly in the size curve. As discussed previously, outside the “hump”, the average droplet size increases with the elevation. Thus, combining the information from the size curve and the data rate curve, the particle and flow physics, it is concluded that **the location where the data rate starts to decrease is exactly where the droplet size begins to increase as the upper boundary of the film stream.**

As discussed in the previous section, the initial droplet size distribution is determined mainly by fluid mechanics rather than heat transfer. The bigger the droplets are, the higher their momentums are, and, in turn, the further up those big droplets can travel to. This explains why the droplet size increases as Y elevates. And, due to those big droplets, which are able to break

through the coolant film layer, the size (width) of the “envelope” in the data rate curve is bigger than the size (width) of the “hump”.

As for the bottom boundary of the coolant film layer, it cannot be easily measured due to the fact that the gap between the coolant film and the test surface is in the scale of millimeters. The droplet density in this area is very low and not enough measurement points are available. As a result, there is no significant pattern from either the droplet size curve or the data rate curve that can clearly identify the jet stream lower boundary. However, rough estimates could be made by extrapolating the data rate curve to the location where zero data rate would occur or by identifying the left boundary of the “hump” in the droplet size curve. Both estimates are very rough and uncertain. The locations of the lower boundary of the jet stream obtained by using these two rough approaches, are presented in Table 3.4.

Table 3.4 Comparison of the Y-location for coolant film lower boundary acquired from the data rate curve and the size curve (Case 2, M=0.6)

X/D	size curve (mm)	data rate (mm)
1	6.0	3.0
6	6.0	4.5
13	5.0	4.0
28	2.0	2.5

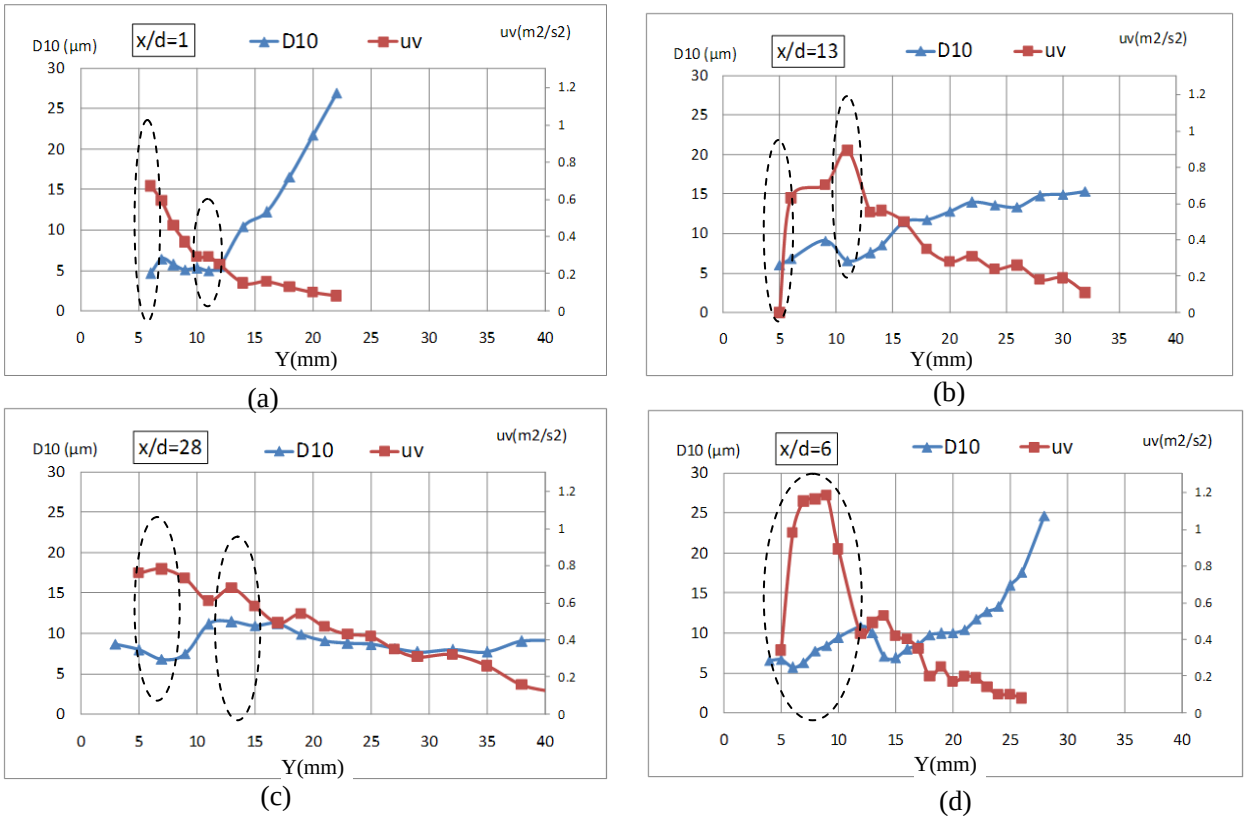

Figure 3.13 (Case 2, M=0.6) Droplet size distribution (plotted on Y-coordinate on the left) and Reynolds Stress distribution (plotted on Y-coordinate on the right) as a function of Y-locations at (a) X/D=1 (b) X/D=6 (c) X/D=13 (d)X/D=28

In order to further investigate the relationship between the droplet size distribution and coolant stream boundaries, the Turbulence Reynolds Stress (uv) is plotted on the secondary Y-axis in the same figure of the size distribution curve in Fig. 3.13.

The Turbulence Reynolds Stress is expected to be higher in the shear layer between the coolant film layer and the main flow. Looking at Fig. 3.13, quite surprisingly, the locations of the peak of the Reynolds Stress shows reasonable agreement with the left and right boundary of the "hump". The corresponding patterns are circled in each figure. Even though some of the patterns are not clearly identifiable, the corresponding patterns are still discernable in most of the cases. Therefore, based on the droplet's data count and the maximum Reynolds shear stress, the edges of the hump of the droplet size curve coincides with the upper and lower boundary of the jet's width.

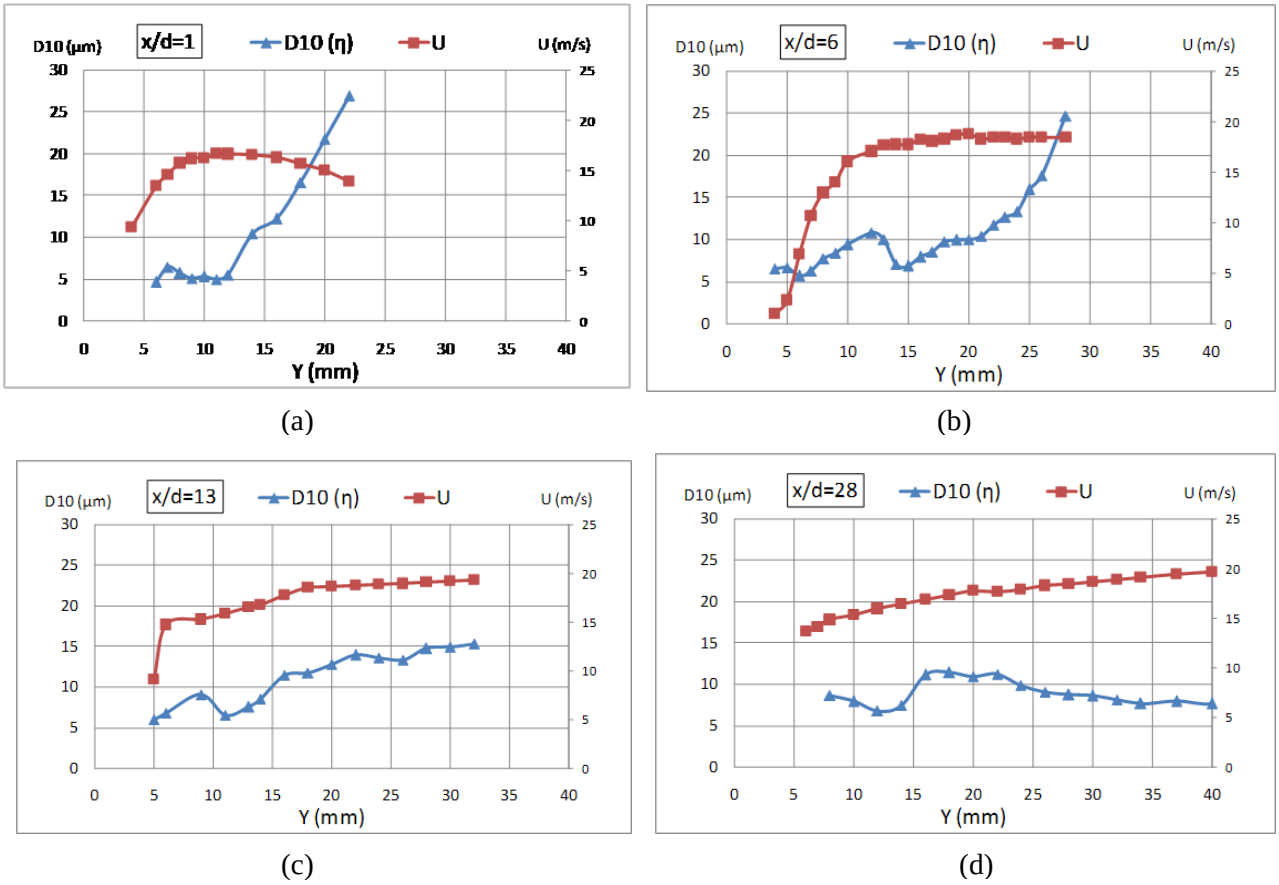

Figure 3.14 Particle size distribution (plotted on Y-coordinate on the left) and the droplets mean velocity (plotted on Y-coordinate on the right) as a function of Y locations at (a) X/D=1 (b) X/D=6 (c) X/D=13 (d)X/D=28

Now the assumption that the droplet velocity will not affect the data rate needs to be examined. The average particle velocity (U) is plotted on the secondary Y-axis in the same figure of the size distribution curve in Fig. 3.14.

3.4.2 Further Explanation of Droplet Distribution

According to the previous analysis from a fluid mechanics point of view, the right end of the "hump" of the droplet size curve is the upper boundary of the coolant jet film and the left end of the "hump" is approximately the lower surface of the film layer. In other words, the width of the "hump" is roughly corresponding to the width of the coolant jet film. The profile of the "hump" indicates that the biggest droplets are in the middle of the film layer and the droplet sizes decrease from the center towards both sides of the film layer. This can be explained that heat

transfer becomes high near the jet stream boundaries, so the droplet sizes diminish towards the boundaries. On the upper boundary, the droplets are directly exposed to the hot main stream flow, and on the lower boundary, the droplets are also exposed to a relatively hot flow which results from the 3-D flow wrapping the main flow around the sides via the lateral vorticities. Thus, the droplet size becomes smaller as it approaches the surface.

Combining the explanation for both the upper and bottom surface boundaries of the air/mist film, there is a cold core inside the film. The droplet sizes are bigger inside this cold core due to the less severe heat transfer, thus slower evaporation of the mist droplets.

It is observed previously in Fig. 3.12 that for the X/D = 6 case, the slope of the droplet size curve is different on both sides of the "hump." Droplet sizes decrease faster towards the upper boundary and decay slower towards the lower boundary. As a result, the peak size inside the film skews towards the upper boundary. This implies that the heat transfer rate from the upper surface into the coolant jet is stronger than that from the lower boundary.

Looking at the droplet size distribution curve at X/D = 1 and X/D = 6 in Fig. 3.12, inside the film layer, i.e. the "hump," the sizes for the X/D = 1 cases are around 5μm. However, the size for the X/D = 6 case reaches as high as 10μm. This posits a tough question for the proposed profile to answer. If the mist droplets are contained in the mist/air film, as they travels from X/D = 1 to X/D = 6, they should absorb heat from the surrounding hot main flow, evaporate gradually, and become smaller. But, the data shows that the opposite occurs. What is the reason? Is there something that is missing in the proposed profile? The answer can be found in the detailed droplet size distribution plots presented previously in Fig. 3.8 and 3.9.

As observed in Fig. 3.8 for the plot at Y = 10mm, big droplets do exist as well as the small droplets and the average of the droplet size is about 5μm, which is consistent with the plot in Fig. 3.12 (a). It is noted that the peak of the data rate is about 1500 Hz. Now looking downstream at the location X/D = 6 in Fig. 3.9 for the plot at the same Y at 10mm, the small droplets that are less than 5μm takes only a minor portion of the total droplets population. Also, it is noticed that the maximum data rate drops to about 500 Hz. This means that the smallest droplets dry out faster than the bigger droplets, and, as a result, the total number of droplets decreases and the average droplet size weights more towards the bigger droplets. This explains why the average droplet sizes inside the film increase as it travels downstream. However, this phenomenon only occurs in the early part of the mist's journey ($0 < X/D < 6$). Downstream from

X/D = 6, the droplet sizes and data rates continuously decrease.

Now examining the droplet behavior outside the coolant film: for example, looking at the maximum droplet size at Y = 20mm, the droplet size is observed decreasing from X/D = 1 to X/D = 6, which is opposite to that at Y = 10mm (shown in Fig. 3.14). This is also reasonable, because, based on the proposed profile, those droplets are outside the mist/air film layer and only big droplets can reach above the film layer. Therefore, no small droplets are available to begin with, so the droplet sizes only follow a diminishing trend.

The maximum D_{10} for each X/D location is plotted in Fig. 3.15 and the highest elevations where measurements of droplets are feasible are also plotted in the same figure on the secondary Y-axis on the right hand side. It is found that the maximum size of droplets is getting smaller as the droplet moves downstream. Meanwhile, the maximum height that the droplets can reach increases as X/D increases.

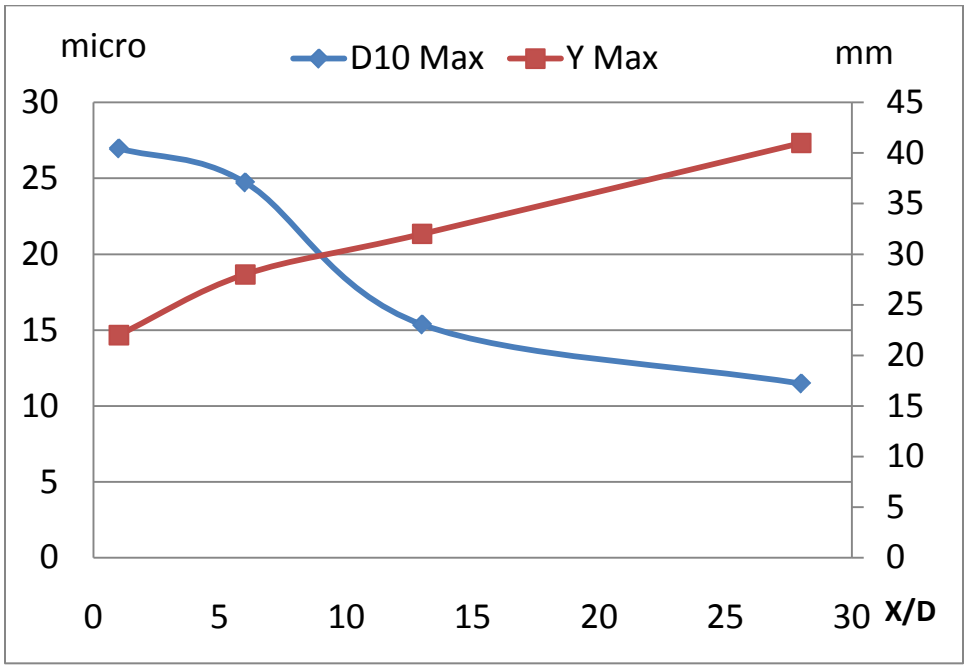

Figure 3.15 Centerline droplet size distribution for Case 2, M=0.6, at X/D=1, Y=10mm, 20mm and at X/D=6, Y=10mm, 20mm

Based on the description of the thermal-flow physics, the droplet size distribution curves, the droplet data rate distribution curves, and the previous discussion, an illustration of the particle distribution patterns at different locations are drawn in Fig. 3.16.

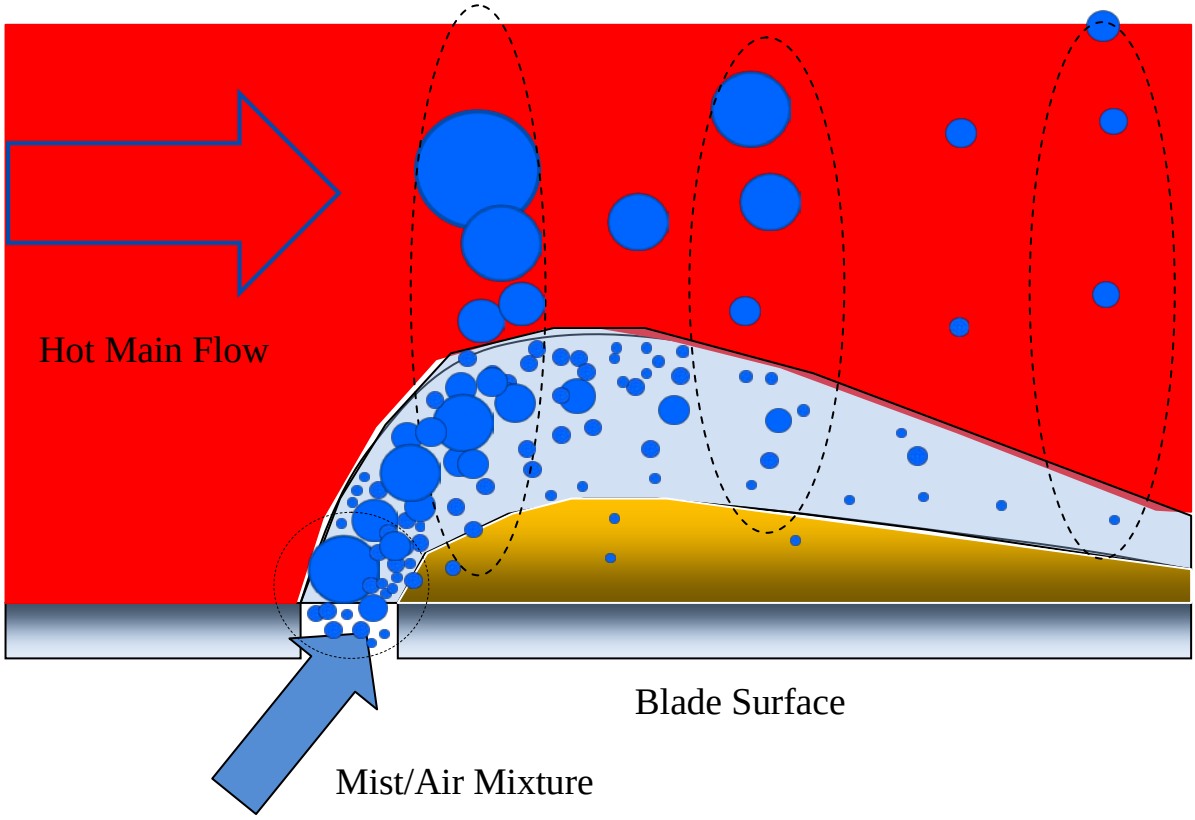

Figure 3.16 Illustration for droplet distribution profile for low blowing ratio (M=0.6) mist film cooling

3.5 Linking the Particle Data with the Heat Transfer Data

Now that the droplet physics has been well examined and is successful in explaining the particle data measurements, efforts will be dedicated to using the knowledge gained for detailed particle behavior to understand the overall heat transfer results. The goal is to find the connection between the droplets behavior and the heat transfer pattern of mist cooling.

Based on the previous analysis, the shape of the coolant film layer is outlined in Fig. 3.17 by plotting the upper and lower boundaries of the film layer. It is noted that the plot actually represents the 2-D film layer's center-plane on which the measurements were made. In the experiment, this film layer is actually three dimensional rather than the two dimensional plot as shown. The lower boundary is plotted according to the data rate curve. The X-axis is the stream-wise location in terms of X/D while the Y-axis is the elevation from the plate surface.

As shown in Fig. 3.16, a “bending back” pattern for the mist/air coolant film layer is

apparently found at X/D = 7 on the upper boundary of the film. The initial momentum for the jet flow enables the coolant mixture to shoot into the main flow chamber but is bent by the main flow at a certain inclined angle. Since the injection momentum for this case M = 0.6 is not strong enough for the film to be completely lifted off from the surface, the film of air and mist mixture is bent back towards the surface again. The turning point for the film layer is at around X/D = 7 as shown in Fig. 3.17.

It must be noted here that this detailed description of the film layer shape is only made available with the help of the particle measurement data.

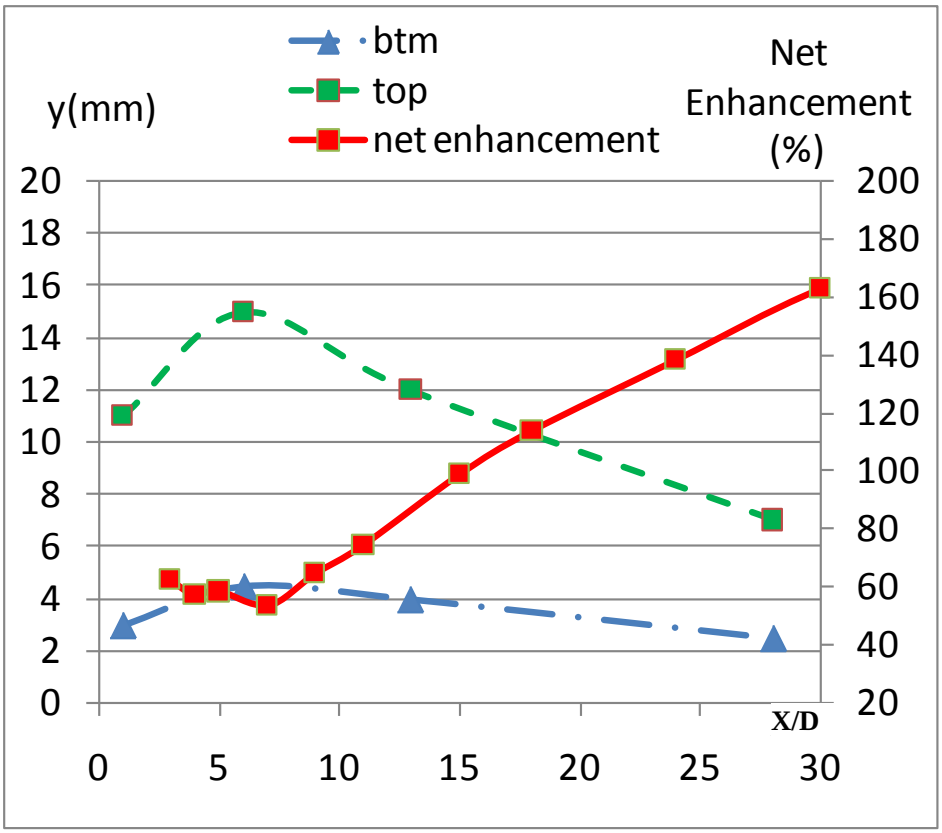

Figure 3.17 The mid-plane shape of the mist/air coolant film layer for M=0.6 Case at the hole centerline with the Net Enhancement of Cooling Effectiveness plotted on the secondary Y-axis

Motivated by the goal of finding the link between the particle behavior and the mist cooling heat transfer, the net enhancement of cooling effectiveness for this case is also plotted in the same figure of the mist/air coolant film sketch in Fig. 3.17. It is immediately noticed that the

starting point of the sudden increase in net enhancement is in the close neighborhood of the "bending back" location of the mist/air film.

This implies that as the mist/air film is bent back and approaches the surface again, the enhancement of cooling effectiveness increases. This "bending back" film pattern is critical in keeping the mist droplets close to the surface, thus improving the cooling effectiveness. It is most important to make sure that the film does not "blow off" in order to have a high cooling enhancement from mist cooling.

CHAPTER FOUR
CONCLUSIONS

In this study, an experimental investigation of mist cooling under laboratory conditions is conducted. Mist cooling is evaluated and compared against air film cooling in terms of adiabatic film cooling effectiveness and film coverage.

It is found that the general pattern of the adiabatic cooling effectiveness distribution of the mist case is similar to that of the air-only case with the peak at about the same location. This implies that adding mist in the air film does not change the general cooling pattern drastically, so that knowledge acquired through film cooling can generally be applied to mist cooling.

For the 0.6 blowing ratio case, the cooling effectiveness is greatly enhanced. The net enhancement of adiabatic cooling effectiveness compared to the air film case can reach 190% locally and 128% overall at the centerline.

Noticing that there is no clearly defined parameter to quantitatively describe the film cooling coverage in literatures, the concept of **Film Decay Length (FDL)** is proposed in this study. It is a measure of the streamwise length (X/D) where the cooling effectiveness decays to a benchmark value, say 50% or 63% ($1 - e^{-1}$) of the maximum value. The purpose of identifying this length is to quantitatively evaluate how well the coolant film covers the blade surface in the streamwise direction. Moreover, this length indicates how fast the coolant dissipates and mixes with the main flow.

It is found for the M = 0.6 case, the FDL(50%) of the mist case (X/D = 24.2) is 165% longer than the air only case (X/D = 14). It indicates that the decaying rate of adiabatic cooling effectiveness, η, for the mist case is much slower than that of the air-only case. In other words, the effectiveness of the mist film lasts longer than the air-only film. And, the mist cooling generates a much more uniform surface temperature, which is critical for reducing wall thermal stresses.

The **FDL (63%)** for Case 4 (M = 1.0, mist/air film) is 10.2, which is unexpectedly shorter than that of Case 3 (M = 1.0, air film). This reveals that the decaying of cooling performance is faster when mist is added, although it is noted that the cooling effectiveness is

still enhanced for all the locations. The centerline integral of net cooling enhancement for all M = 1.0 cases is 53% compared with the value of 128% for the M = 0.6 cases.

The effect of the mist in the M = 0.6 condition is apparently greater than that of the M = 1.0 cases due to the higher overall cooling enhancement, the much longer **FDL,** and the wider film cooling coverage area. It is also noted for the high blowing ratio cases with coolant lift-off condition that mist cooling makes the streamwise surface temperature gradient steeper, which may raise a concern for increased thermal stresses. Therefore, it is more beneficial to choose a relatively low blowing ratio to keep the coolant film attached to the surface when applying the mist cooling. The centerline integral of net enhancement for M = 1.4 is only 11.4%, which is the lowest for all three of the blowing ratios tested.

Through the examination of droplet size, data rate, velocity, and turbulent Reynolds stresses plots, the process of mist interactions with the coolant film is described, and the profile of the coolant film mixture spreading shape is proposed. Characteristics of droplet distribution due to the interaction with both the flow field and temperature field are analyzed. The key points of the physical model are summarized as follows:

1. The coolant air film layer (mixture of coolant air and droplets) does not always coincide with the "droplet layer" (within which droplets reside). The droplets are discovered traveling outside the coolant air film.
2. The coolant air film, mixed with the mist droplets, keeps its own identity with distinguishably high Reynolds stresses at the boundaries and also large gradients in the particle size distribution
3. The initial droplet path and distribution are determined mainly by fluid mechanics rather than heat transfer.
4. There is a cold core inside the film layer. The droplet size is bigger within the core and smaller towards both the upper and lower boundaries of the cold core layer.
5. The droplet size decreases faster from the core towards the upper boundary and decays slower towards the lower boundary. As a result, the droplet size population density inside the film skews towards the upper boundary.
6. The droplet population density is higher towards the upper boundary inside the coolant film, but starts to decrease outside the film.
7. Droplets outside the film layer (farther away from the wall) are of larger sizes due to

the coolant injecting inertia and a subsequent penetration through the air film layer.

8. The profile of the upper boundary of the air coolant film can be clearly identified from the data rate and droplet size curves. The bottom boundary of the film can be roughly estimated by the location where the data rate is almost below 50Hz.

Based on the above behaviors observed from the experimental measurements, a profile of the "bending back" pattern for the air/mist coolant film is drawn. The bending back location of the mist film layer is at around X/D = 7.

A further cross-examination of both the overall heat transfer data and the particle measurements shows that the starting point of the sudden increase in net cooling enhancement is close to the "bending back" location of the mist film. This implies that, as the mist film is bent back and approaches the surface again, the enhancement of cooling effectiveness increases. This "bending back" film pattern is critical in keeping the mist droplets close to the surface, thus improving the cooling effectiveness. It is wise to avoid too strong a blowing ratio so that the film will not lift off or separate from the surface in order to take full advantage of the higher mist cooling enhancement.

REFERENCES

1. Adami, P., Martelli, F., Montomoli, F., and Saumweber, C., 2002, “Numerical Investigation of Internal Crossflow Film Cooling,” ASME Turbo Expo 02, 3A, pp. 51-63.
2. Baughn, J.W. (1995) "Liquid Crystal Methods for Studying Turbulent Heat Transfer", International Journal of Heat and fluidflow, Vol. 16, No. 5, pp.365-375
3. Bell, C. M., Hamakawa1, H., and Ligrani, P. M., 2000, “Film Cooling From Shaped Holes,” ASME J. Heat Transfer, 122, pp. 224-232.
4. Bohn, D., Becker, V., Kusterer, K, Otsuki, Y., Sugimoto, T., Tanaka, R., “3-D Internal and Conjugate Calculations of a Convective Cooled Turbine Blade with Serpentine-shaped and Ribbed Channels,” IGTI paper 99-GT-220, 1999.
5. Bohn, D., Bonhoff, B., Schonenborn, H., “Combined Aerodynamic and Thermal Analysis of a Turbine Nozzle Guide Vane,” IGTC-paper-108, Proc. Of the 1995 Yokohama Int. Gas Turbine Congress, 1995c
6. Bohn, D., Bonhoff, B., Schonenborn, H., Wilhelmi, H., “Prediction of the Film-cooling Effectiveness of Gas Turbine Blades Using a Numerical Model for the Coupled Simulation of Fluid Flow and Diabatic Walls,” AIAA paper 95-7105, 1995b
7. Boyce, Meherwan P. (2006). "Chapter 9: Axial Flow Turbines and Chapter 11: Materials". Gas Turbine Engineering Handbook (3rd ed.). Oxford: Elsevier. ISBN 9780750678469.
8. Brittingham, R.A. and Leylek, J. H, 2002, “A Detailed Analysis of Film Cooling Physics: Part IV—Compound-Angle Injection with Shaped Holes,” ASME J. Turbomachinery, 122, pp. 133-145.
9. Bunker, R.S., and Metzger, D.E., 1990. “Local Heat Transfer In Internally Cooled Turbine Airfoil Leading Edge Regions. Part 1: Impingement Cooling Without Film Extraction,” ASME J. Turbomachinery, Vol. 112, pp. 451-458.
10. Camci, C., Kim, K., and Hippensteele, S.A., 1992. “A New Hue Capturing Technique for the Quantitative Interpretation Of Liquid Crystal Images Used in Convective Heat TransferStudies,” ASME J. Turbomachinery, Vol. 114, pp. 765-775.
11. Chen, P.H., Ai, D., and Lee, S.H., 1998. “Effect of Compound Angle Injection of Flat-Plate Film Cooling Through a Row of Conical Holes,” ASME Paper No. 98-GT- 459.

12. Cho, H. Rhee, D., Kim, B., “Enhancement of film Cooling performance using a shaped film cooling hole With compound angle injection,” JSME International Journal, 44, pp. 99-110, 2001.
13. Cho, H.H., Rhee, D.H., and Kim, B.G., 2001, “Enhancement of Film Cooling Performance Using a Shaped Film Cooling Hole with Compound Angle Injection,” JSME International Journal, Series B, 44, No. 1, pp. 99-110.
14. Clifford, R.J., Jones T.V and Dunne, S. D. 1983, "Techniques for obtaining detailed heat Transfer coefficient measurements within gas turbine blade and vane cooling passages," ASME paper 83-GT-58.
15. Dhungel, A., Lu, Y., Phillips, W., Ekkad, S. V., Heidmann, J., 2007. “Film Cooling from a Row of Holes Supplemented With Anti Vortex Holes,” ASME Paper No. GT2007-27419.
16. Diller, T. E., 1993, “Advances in Heat Flux Measurement”, Advances in Heat Transfer, Vol. 23, Eds. J. P. Hartnett et al., Academic Press, Boston, pp. 279-368.
17. Dorignac, E. & Vullierme, J.-J. (1993) "Wall Heat Transfer Modelisation on a Heated Plate in Subsonic Flow with Injection", Proc. Eurotherm 32, pp.22-24
18. Ekkad, S. V., Ou, S., Rivir, R. B., 2004 “A Transient Infrared Thermography Method for Simultaneous Film Cooling Effectiveness and Heat Transfer Coefficient Measurements From a Single Test,” ASME J. Turbomachinery, Vol. 126, pp. 597-603.
19. Ekkad, S.V., and Han, J.C., 1997. “Detailed Heat Transfer Distributions in Two-Pass Square Channels with Rib Turbulators,” International J. Heat and Mass Transfer, Vol. 40, No. 11, pp. 2525-2537.
20. Ekkad, S.V., Hui Du, and Je-chin Han, 1995, "Local Heat Transfer Coefficient and Film Effectiveness Distributions on a Cylindrical Leading Edge Model Using a Transient Liquid Crystal Image Method," ASME 95-WA/HT-3.
21. Eriksen, V.L. and Goldstein, R. J., 1974, “Heat Transfer and Film Cooling Following Injection Through Inclined Tubes,” ASME J. Heat Transfer, 96, pp. 239–245.
22. Flack, Ronald D. (2005). "Chapter 8: Axial Flow Turbines". Fundamentals of Jet Propulsion with Applications. Cambridge Aerospace Series. New York, NY: Cambridge University Press. ISBN 9780521819831.
23. Fluent Manual, Version 6.2.16, Fluent, Inc. 2005.

24. Goldstein, R. J., Eckert, E. R. G., and Burggraf, F., 1974, “Effects of Hole Geometry and Density on Three-Dimensional Film Cooling,” Int. J. Heat Mass Transfer, 17, pp. 595–607.
25. Goldstein, R. J., Jin, P., and Olson, R. L., 1999. "Film Cooling Effectiveness And Mass/Heat Transfer Coefficient Downstream of One Row of Discrete Holes." Asme joumal ofturbomachinery, vol. 121, Pp. 225-232.
26. Goldstein, R.J., Measurements in Heat Transfer, Hemisphere Pub. Corp., 1976.
27. Gritsch, M., Schultz, A., and Wittig, S., 1998. “Adiabatic Wall Effectiveness Measurements of Film Cooling Holes With Expanded Exits,” ASME J. Turbomachinery, Vol. 120, Pp. 549-556.
28. Gruber, T.C. & Page, R.H. (1993) "Infrared Technique: Heat Transfer Measurement", SPIE, Vol. 2005, pp.228-236
29. Guo, S.M., Jones, T.V., University of Oxford, and Lock, G.D., University of Bath, 1996, "Gas Turbine Heat Transfer Measurements with Engine Simulated Film Cooling," 2nd European Conference on Turbomachinery Fluid Dynamics and Thermodynamics, Technological Institute, Section on Aeronautics.
30. Guo, S.M., Lai, C.C., Jeong, J.H., Jones, T.V., and Oldfield, M.L.G., University of Oxford, 1997, "Use of Liquid Crystal Techniques to Measure Film Cooling Heat Transfer and Effectiveness," 90th Symposium of the Propulsion and Energetics Panel, AGARD 20-24.
31. Guo, T., Wang, T., and Gaddis, J. L., 2000, “Mist/Steam Cooling in a Heated Horizontal Tube, Part 1: Experimental System, Part 2: Results and Modeling,” ASME J. Turbomachinery, 122, pp. 360–374.
32. Guo, T., Wang, T., and Gaddis, J.L., 2001, “Mist/Steam Cooling in a 180o Tube Bend,” ASME J. Heat Transfer, 122, pp. 749-756.
33. Han, Z., Dennis, B., Dulikravich, G., “Simultaneous Prediction of External Flow-Field and Temperature in Internally Cooled 3-D Turbine Blade Material,” IGTI paper 2000-GT-253, 2000.
34. Heidmann, J. D., Rigby, D. L. And Ameri, A. A., 2000, “A Three-Dimensional Coupled Internal/External Simulation of a Film-Cooled Turbine Vane,” ASME J. Turbomachinery, 122, pp. 348-359.

35. Hippensteele, S.A., Russell, L.M., and Stepka, F.S., 1983. “Evaluation of a Method for Heat Transfer Measurements And Thermal Visualization Using a Composite of a Heater Element and Liquid Crystals,” ASME J. Heat Transfer, Vol. 105, pp. 184-189.
36. Jabbari, M. Y., and Goldstein, R. J., 1978, “Adiabatic Wall Temperature and Heat Transfer Downstream of Injection Through Two Rows of Holes,” ASME J. Eng. Power, 100, pp. 303–307.
37. Jabbari, M. Y., and Goldstein, R. J., 1978, “Adiabatic Wall Temperature and Heat Transfer Downstream of Injection Through Two Rows of Holes,” ASME J. Eng. Power, 100, pp. 303–307.
38. Jia, R., Sunden, B., Miron, P., and Leger, B., 2003, “Numerical and Experimental Study of the Slot Film Cooling Jet with Various Angles,” Proceedings of the ASME Summer Heat Transfer Conference, pp. 845-856.
39. Jubran, B. A., and Maiteh, B. Y., 1999, “Film Cooling and Heat Transfer From a Combination of Two Rows of Simple and/or Compound Angle Holes in Inline and/or Staggered Configurations,” International. J. Heat and Mass Transfer, 34, pp. 495–502.
40. Jubran, B., and Brown, A., 1985, “Film Cooling From Two Rows of Holes Inclined in the Streamwise and Spanwise Directions,” ASME J. Eng. Gas Turbines Power, 107, pp. 84–91.
41. Kuo, K. Y., 1986, Principles of Combustion, John Wiley and Sons, New York.
42. Kwak, J. S. And Han, J. C., 2003, “Heat Transfer Coefficients and Film-Cooling Effectiveness on a Gas Turbine Blade Tip,” ASME J. Heat Transfer, 125, pp. 494-502.
43. Lee, J.J., Dutton, J.C., Jacobi, A.M., 2007. “Application of Temperature-Sensitive Paint for Surface Temperature Measurement in Heat Transfer Enhancement Applications,” J. Mechanical Science and Technology, Vol. 21, pp. 1253- 1262.
44. Li, A. And Ahmadi, G., 1992, “Dispersion and Deposition of Spherical Particles from Point Sources in a Turbulent Channel Flow,” Aerosol Science and Technology, 16, pp. 209-226.
45. Li, X and Wang, T., 2005, “Simulation of Film Cooling Enhancement with Mist Injection,” ASME Turbo Expo 2005, Nevada, USA, June 6-9.
46. Li, X, Gaddis, J. L., and Wang, T, “ Mist/Steam Heat Transfer with Jet Impingement onto a Concave Surface,” ASME J. Heat Transfer, vol. 125, pp. 438-446
47. Li, X., Gaddis, J. L., and Wang, T., 2003, “Mist/Steam Cooling by a Row of Impinging Jets,” Int. J. Heat Mass Transfer, 46, pp. 2279-2290.

48. Ligrani, P. And Lee, J., 1996, “Film Cooling from a Single Row of Compound Angle Holes at High Blowing Ratios,” International Journal of Rotating machinery, 2, Pp.259-267.
49. Ligrani, P. M., Wigle, J. M., Ciriello, S., and Jackson, S. M., 1994, ‘‘Film Cooling From Holes With Compound Angle Orientations: Part1: Results Downstream of Two Staggered Rows of Holes With 3D Spanwise Spacing,” International. J. Heat and Mass Transfer, 116, pp. 341– 352.
50. Liu, Q., Kapat, J.S., Douglass, C.J., and Qiu, L., 2003. “Applicability of Temperature Sensitive Paints for Measurement of Surface Temperature Distribution,” ASME Paper No. GT2003-38591.
51. Mayhew, J. E., Baughn, J. W., and Byerley, A. R., 2004, “
52. Nirmalan, N. V., Weaver, J. A., and Hylton, L. D., 1998, “An Experimental Study of Turbine Vane Heat Transfer with Water–Air Cooling,” ASME J. Turbomachinery, 120, No. 1, pp. 50–62.
53. Pedersen, D. R., Eckert, E. R. G., Goldstein, R. J., 1977. “Film Cooling with Large Density Differences Between the Mainstream and the Secondary Fluid Measured by the Heat- Mass Transfer Analogy,” ASME J. Heat Transfer Vol. 99, Pp. 620-627.
54. Piggush, J.D., Simon, T.W., 2006, “Adiabatic Effectiveness Measurements in a First Stage Nozzle Cascade Having Endwall Contouring, Leakage and Assembly Features”, ASME GT2006-90576.
55. Piggush, J.D.; Simon, T.W., 2006, “Heat Transfer Measurements in a First Stage Nozzle Cascade Having Endwall Contouring: Misalignment and Leakage Studies”, ASME GT2006-90575.
56. Popp, O., Smith, D., Bubb, J., Grabowski, H., Diller, T., Schetz, J., Ng, W., 1999, “Steady and Unsteady Heat Transfer in a Film cooled Transonic Turbine Cascade,” ASME 99-GT-259.
57. Ranz, W. E. And Marshall, W. R. Jr., 1952, “Evaporation from Drops, Part I,” Chem. Eng. Prog., 48, pp. 141-146.
58. Ranz, W. E. And Marshall, W. R. Jr., 1952, “Evaporation from Drops, Part II,” Chem. Eng. Prog., 48, pp. 173-180.

59. Rhee, D. H., Lee, Y. S. And Cho, H. H, 2002, “Film Cooling Effectiveness and Heat Transfer of Rectangular-shaped Film Cooling Holes,” ASME Turbo Expo, 3, pp. 21-32.
60. Simonich, J.C., and Moffat, R.J., 1984. “Liquid Crystal Visualization of Surface Heat Transfer on a Concavely Curved Turbulent Boundary Layer,” ASME J. Engineering For Gas Turbines and Power, Vol. 106, pp. 619-627.
61. Steven W. Burd, Cynthia J. Satterness, and Terrence W. Simon, “Effects of slot bleed injection over a contoured end wall on nozzle Guide vane cooling performance: part ii - thermal measurements”, Proceedings of ASME TURBOEXPO 2000 May 8-11, 2000, Munich Germany 2000-GT-200
62. Talbot, L. Cheng, R. K., Schefer, R. W., and Willis, D. R., 1980, “Thermophoresis of Particles in a Heated Boundary Layer,” J. Fluid Mech., 101, pp.737-758.
63. The Gas Turbine Handbook, Office of Fossil Energy, National Energy Technology Laboratory, U.S. Department of Energy, 2006, PP. 310-318.
64. Thole, K. A., M.Gritsch, Schulz, A., and Witting, S., 1997, “Effect of a Crossflow at the Entrance to a Film- Cooling Hole”, Journal of Fluid Engineering, 119, Pp.533-540.
65. Thole, K., Gritsch, M., Schulz, A., and Wittig, S., 1996, ‘‘Flowfield Measurements For Film Cooling Holes With Expanded Exits,’’ IGTI Turbo Expo, Birmingham, UK, Paper 96-GT-174.
66. Tyagi, Mayank, and Acharya, Sumanta, 2003, “Large Eddy Simulation of Film Cooling Flow from an Inclined Cylindrical Jet,” ASME J. Turbomachinery, 125, n. 4, pp. 734-742.
67. Van Treuren, K.W., Wang, Z., Ireland, P.T., and Jones, T.V., 1994. “Detailed Measurements of Local Heat Transfer Coefficient and Adiabatic Wall Temperature Beneath an Array of Impingement Jets,” ASME J. Turbomachinery, Vol. 116, pp. 369-374.
68. Vedula, R.J. & Metzger, D.E. (1991) "A Method for the Simultaneous Determination of Local Effectiveness and Heat Transfer Distributions in Three-Temperature Convection Situations", ASME Paper presented at the International Gas Turbine and Aeroengine Congress and Exposition, Orlando, Florida- June 3-6, ASME 91-GT-345
69. Vedula, R.J., and Metzger, D.E., 1991. “A Method of the Simultaneous Determination of Local Effectiveness and Heat Transfer Distributions in Three-Temperature Convection Situations,” ASME Paper No. 91-GT-345.

70. W.J. Mick, R.E. Mayle, Stagnation film cooling and heat transfer, including its effect within the hole pattern, ASME J. Of Turbomachinery 110 (1988) 66-72.
71. Wang, M. J. And Mayinger, F., 1995, “Post-dryout Dispersed Flow in Circular Bends,” Int. J. Multiphase Flow, 21, n. 3, pp. 437-454.
72. Wang, T., Chintalapati, S., Bunker, R. S., and Lee, C. P., 2000, “Jet Mixing in a Slot,” Experimental Thermal and Fluid Science, 22, n. 1, pp. 1-17.
73. Wang, Z., Ireland, P.T., and Jones, T.V., 1995. “An Advanced Method of Processing Liquid Crystal Video Signals from Transient Heat Transfer Experiments.” ASME J. Turbomachinery, Vol. 117, pp. 184-189.
74. Wang, Z., Ireland, P.T., and Jones, T.V., and Davenport, R., 1996. “A Color Image Processing System for Transient Liquid Crystal Heat Transfer Experiments.” ASME J. Turbomachinery, Vol. 118, pp 421-427.
75. Wilcox, D.C., 1998, Turbulence Modeling for CFD, DCW Industries, Inc., La Canada, California.
76. Wolfstein, M., 1969, “The Velocity and Temperature Distribution of One-Dimensional Flow with Turbulence Augmentation and Pressure Gradient,” Int. J. Heat Mass Transfer, 12, pp. 301-318.
77. Wright, L.M., Gao, Z., Varvel, T.A., and Han, J.C., 2005, “Assessment of Steady State PSP, TSP, and IR Measurement Techniques for Flat Plate Film Cooling,” ASME Paper No. HT2005-72363.
78. Zhang, L.J. and Jaiswal, R.S., 2001, “Turbine Nozzle Endwall Film Cooling Study Using Pressure-Sensitive Paint,” ASME J. Turbomachinery, Vol. 123, pp. 730-735.
79. Zhang, L.J. and Moon, H.K., 2003, “Turbine Nozzle Endwall Inlet Film Cooling – The Effect of a Backward Facing Step,” ASME Paper No. GT2003-38319.
80. Zhao, L. and Wang, T. An Investigation of Adiabatic Wall Temperature as the Driving Temperature in Film Cooling Studies, GT2011-46012, manuscript submitted to ASME Turbo Expo2011, Vancouver, Canada, June 6-10, 2011
81. Zhao, L. and Wang, T., Discussion on the Practice of Using Heated Surface in Film Cooling Studies, GT2011-46614, manuscript submitted to ASME Turbo Expo2011, Vancouver, Canada, June 6-10, 2011

APPENDIX A
EXPERIMENTAL TEST SECTION DESIGN AND MANUFACTUREING

Consideration of Options for Infrared Camera Observation Window:

Zinc Sulfide

Manufacturer and brand name: TECHSPEC® Zinc Sulfide Cleartran™)

Transmission range: 0.4 - 12μm

Comment: Material is clear in both the visible and infrared. It will be pricy if a large window is to be built. Only circular lenses are commercially available.

Fig. A1 Zinc Sulfide Lens

Transmittance as shown in the following figure.

Cost: $450 for a round lens with diameter 50mm. Customization cost depends.

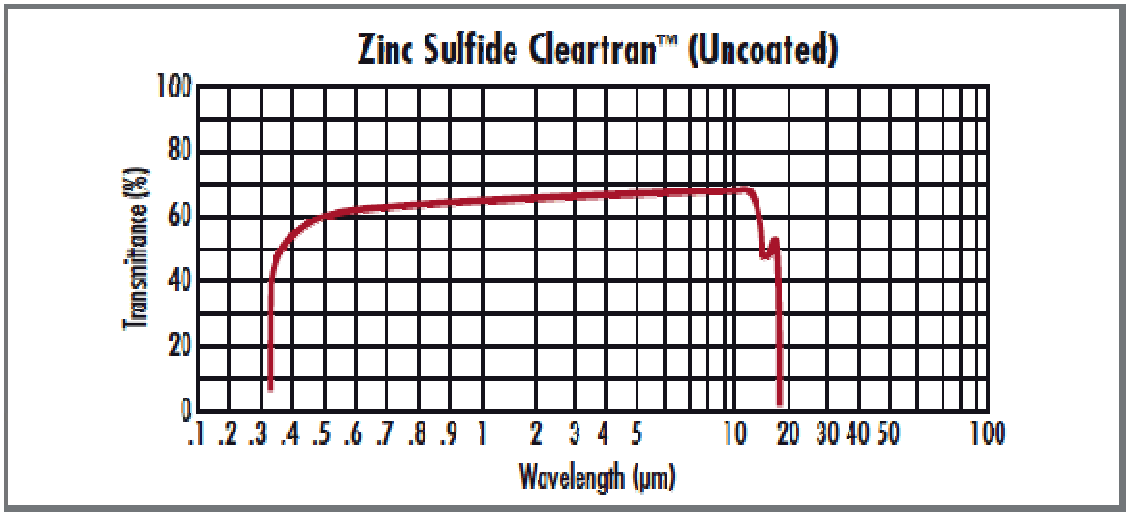

Fig. A2 Zinc Sulfide Transmittance

Zinc Selenide (ZnSe)

Transmission range of 3 - 12µm

Comments: Material is colored. It offers higher transmittance, but is relatively soft and scratches easily.

Transmittance as shown in the following figure.

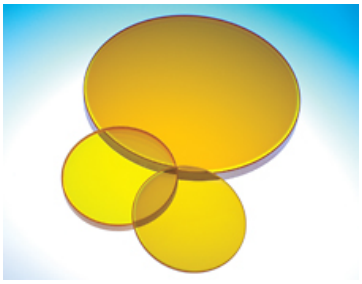

Fig. A3 Zinc Selenide Lens

Cost: $530 for a round lens with diameter 50mm. Customization cost depends.

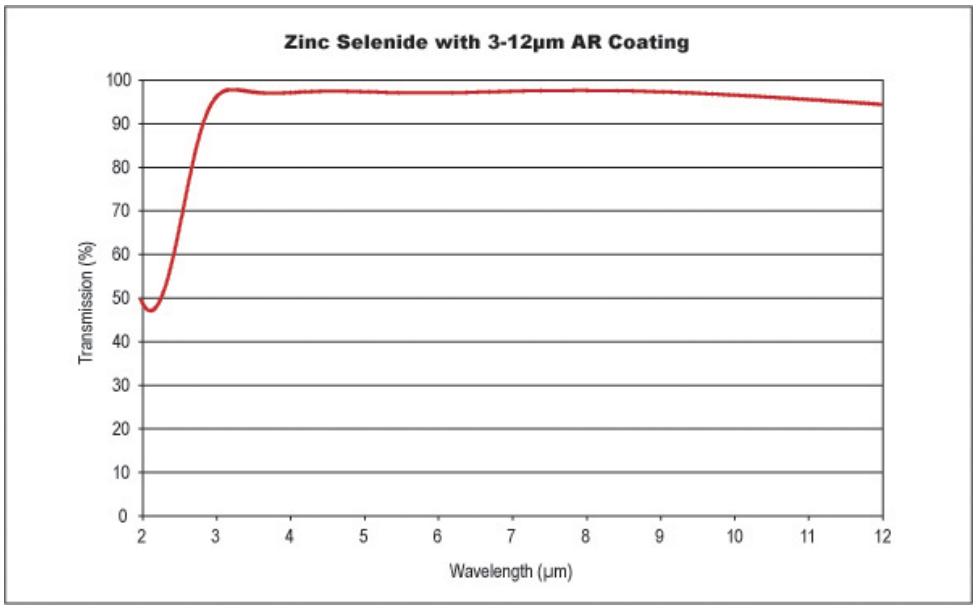

Fig. A4 Zinc Selenide Transmittance

IR Polystyrene Film:

Material: plastic (no detailed information disclosed by the supplier)

Supplier: Edmund Optics.

Transmission range: 8 - 14µm

Comment: Transmittance is not ideal.

Transmittance as shown in the following figure.

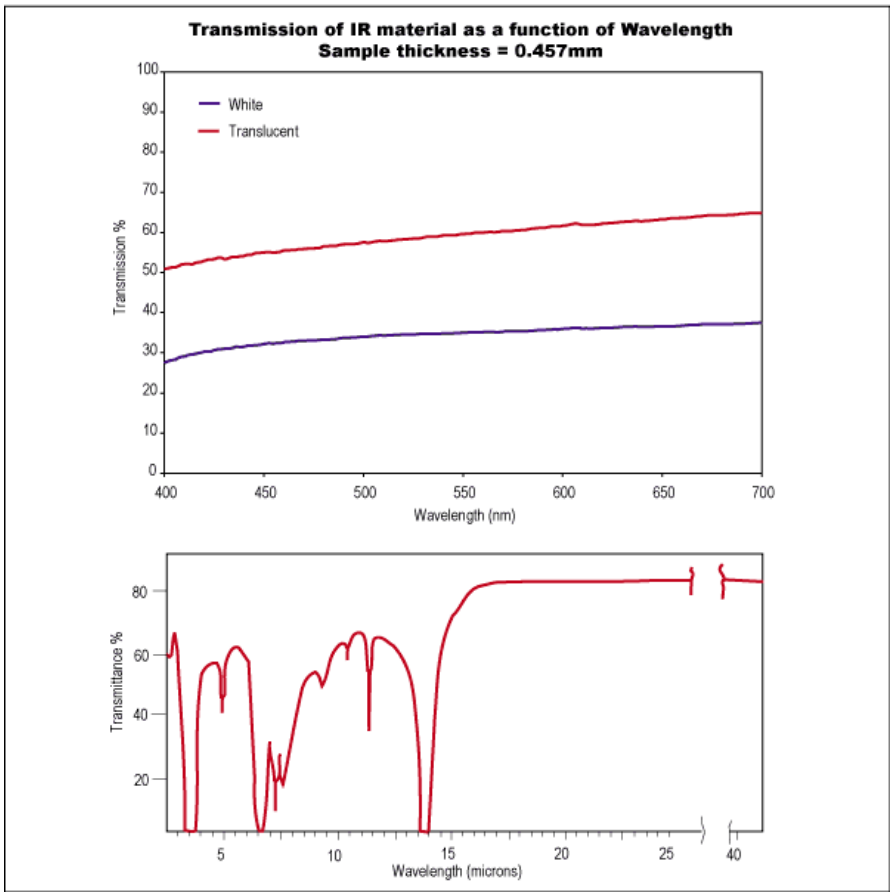

Fig. A5 Polystyrene Transmittance

Test Section Fabrication Plan

The test section is a 24" (length) x 4" (width) x 6" (height) channel made of Lexan. The optimum observation window is a 4.75"x6.25" rectangle plate which offers the capability of covering X/D= 0~25. (The size can be reduced for compromised observation area.)
The four film injection holes are cylindrical, angled at 30^{o} to the main flow direction. The holes have a uniform diameter of 1/4 inches, spaced at 4/5 inches away from each other.

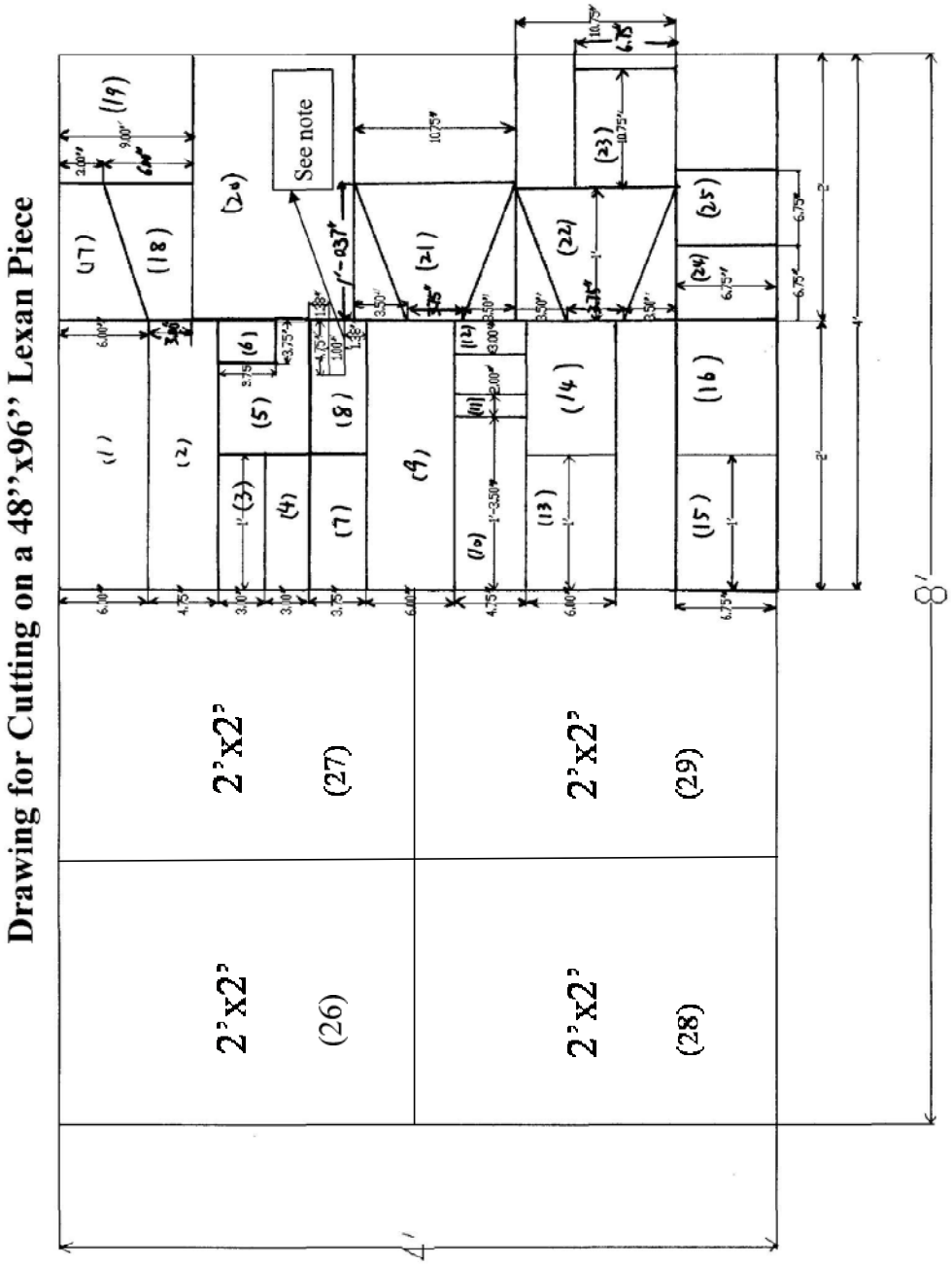

Fig. A6 Cutting on a 48x98 sheet

Note: The noted piece should look like the fork-shaped piece as shown below.

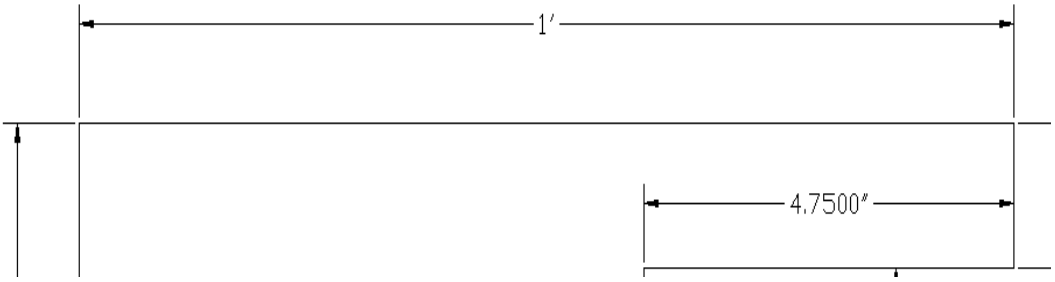

Fig. A7 Fork shaped piece of test section fabrication

Table A1 List of parts of the original test section

Part #	Width	Length	
1	6.000	24.000	
2	4.750	24.000	
3	3.000	12.000	
4	3.000	12.000	
5	Omit		
6	3.750	3.750	
7	3.750	12.000	
8	3.750	12.000	with cut out
9	6.000	24.000	
10	4.750	15.500	
11	2.000	4.750	
12	3.000	4.750	
13	6.000	12.000	
14	6.000	12.000	
15	6.750	12.000	
16	6.750	12.000	
17	6.000	12.000	with angle out
18	6.000	12.000	with angle out
19	9.000	12.000	
20	Omit		
21	10.750	12.370	with angle out
22	10.750	12.000	with angle out
23	6.750	10.750	
24	6.750	6.750	
25	6.750	6.750	
26	24.000	24.000	
27	24.000	24.000	
28	24.000	24.000	
29	24.000	24.000	

Preliminary Test Section Design

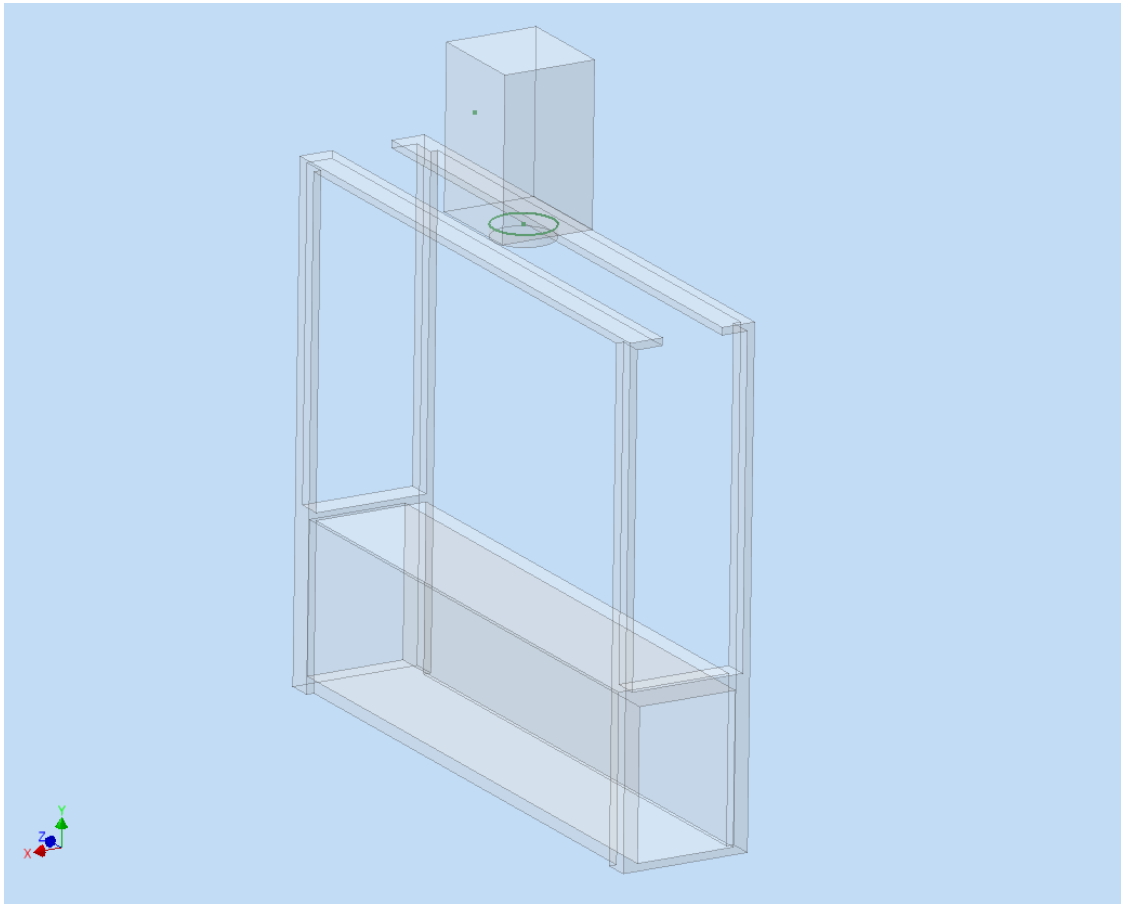

Fig. A8 Drawing of I.R. camera stand for preliminary test section

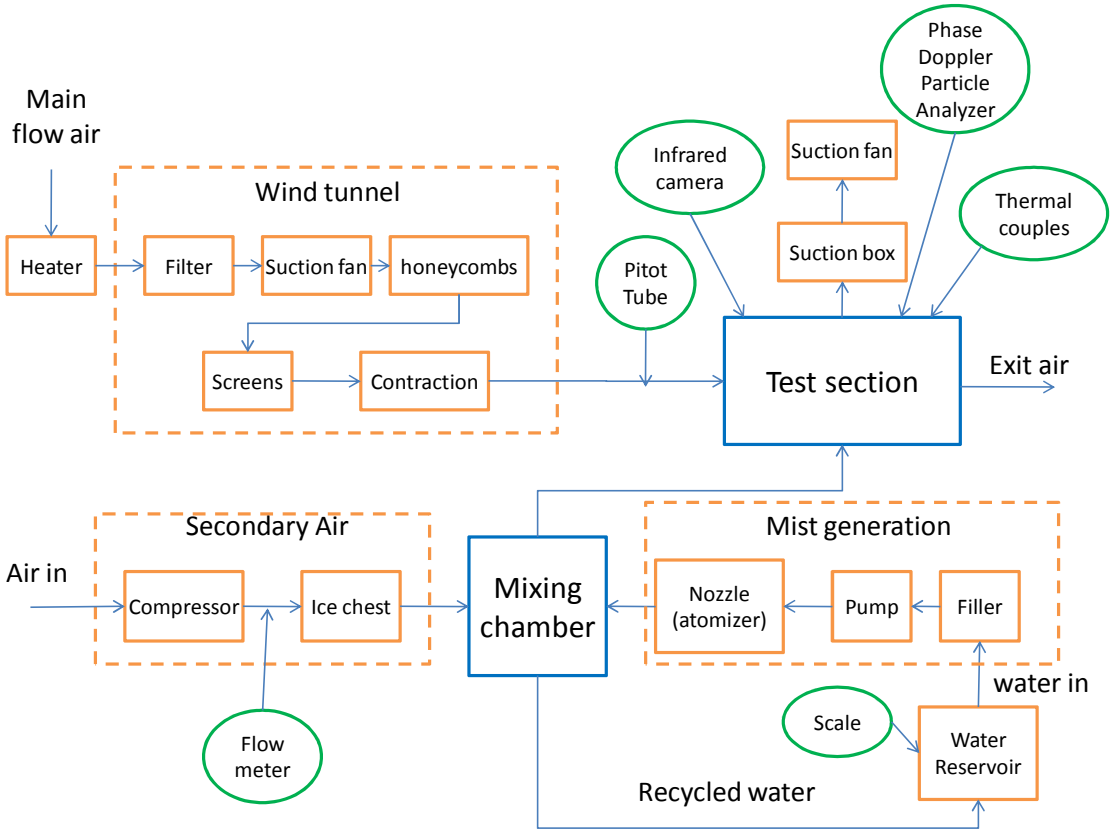

Fig. A9 Schematic of the preliminary test system

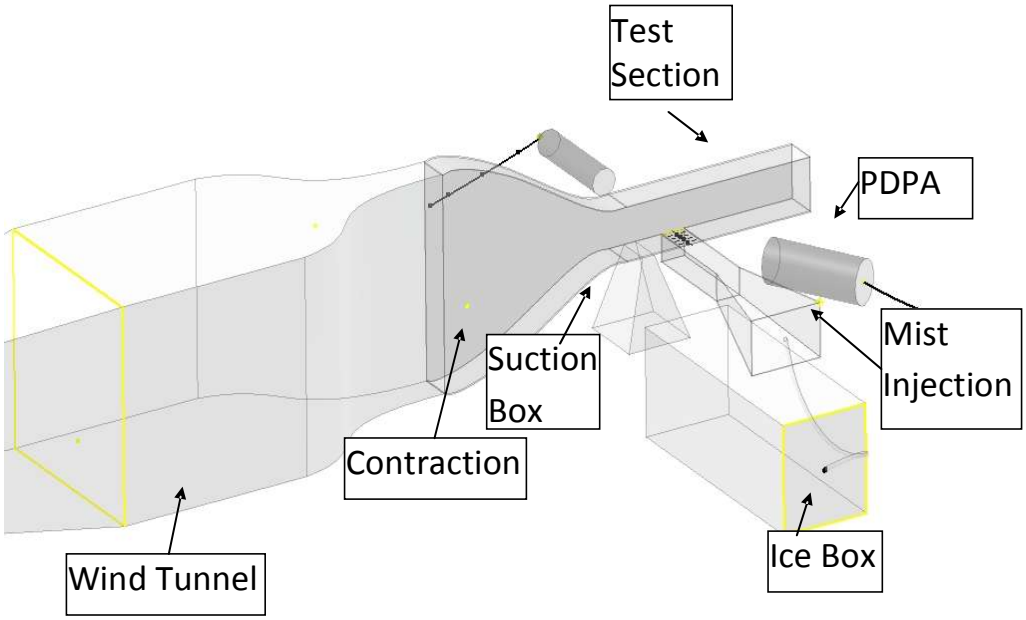

Fig. A10 Cad drawing for the preliminary test section

APPENDIX B

DISCUSSIONS OF SOME MYTHS AND CONCERNED PRACTICES OF FILM COOLING RESEARCH

ABSTRACT

This Appendix focuses on discussing four myths and concerned conventional practices of film cooling research guided by a series of computational simulations. The issues that have been discussed include (a) The film cooling effectiveness (φ) is given a constant number 0.6 to calculate the Heat Flux Ratio (HFR = q''/q''_o) between film-cooled and no-film cases; (b) Adiabatic wall temperature is the driving temperature of film cooling; (c) The adiabatic film heat transfer coefficient can be obtained from an isoenergic film experiment ($T_j = T_g$); (d) Using a heated surface can provide a simplified approach to simulate the film-cooling condition. The result shows that adiabatic film temperature is not always the driving temperature (i.e. T_{aw} is not always larger than T_w), but T_{aw} does act well as the reference temperature in correctly predicting the heat flux direction. Using a constant value for φ is questionable and may lead to un-realistic or false HFR. The conventional equation of HFR was not theoretically exact and can lead to a 20% error. A revised HFR equation is provided in this paper. The dominant energy passage in turbine airfoil film cooling is always from hot combustion gas flows into the airfoil; therefore, employing a heated wall as a boundary condition with hotter main stream flow and cold film injection to simulate the actual film cooling condition is found to be fundamentally questionable. A conjugate simulation that includes wall heat transfer and internal flow cooling shows that reversed heat transfer from blade to gas that gives a minus HFR is possible, due to the heat conduction from the downstream hotter region into the near film hole cooler region.

NOMENCLATURE

b	coolant injection slot width (mm)
h_{af}	adiabatic film heat transfer coefficient ($h_{af} = q'' / (T_{aw}-T_w)$) ($W/m^2K$)
HFR	heat flux ratio (q'' / q''_o)
l	chord length (mm)
M	blowing ratio, $(\rho u)_j/(\rho u)_g$
Nu_x	Nusselt number, hx/λ
NHFR	net heat flux reduction ($1- q'' / q''_o$)

q" heat flux (W/m^2), positive value for heat flowing from gas into the wall

Re_l Reynolds number based on chord length, ul/ν

T_{aw} adiabatic wall temperature (K)

T_w wall surface temperature in contact with gas (K)

T_g main gas flow temperature (K)

T_j coolant temperature at the cooling jet hole exit (K)

T_{ci} internal coolant temperature (K)

Greek Letters

α thermal diffusivity (m^2/s)

η adiabatic film cooling effectiveness, $(T_g-T_{aw})/(T_g-T_j)$

φ film cooling effectiveness, $\varphi = (T_g-T_w) / (T_g-T_j)$ (or non-dimensional metal temperature)

Subscript

aw adiabatic wall

ci internal cooling

conj conjugate blade

f with film cooling

g main flow of hot gas/air

j coolant or jet flow

o without film

w wall

KEY WORDS: Film cooling, heat flux reduction, film cooling effectiveness, conjugate heat transfer, film heat transfer coefficient

INTRODUCTION

Film cooling has been widely used in high-performance gas turbines to protect turbine airfoils from being damaged by hot flue gases. Film injection holes are placed in the body of the airfoil to allow coolant to pass from the internal cavity to the external surface. The ejection of coolant gas results in a layer or "film" of coolant gas flowing along the external surface of the airfoil. Hence, the term "film cooling" is used to describe the cooling technique.

The ultimate goal of introducing film cooling to turbine airfoils is to reduce the heat load on the blade, i.e. reduce surface heat flux and/or lower airfoil's temperature, so the life of turbine airfoils can be

significantly extended due to lower thermal stress within the material and less spallation over thermal barrier coating under lower thermal load. Thus it is always desired to know how much heat flux or blade temperature can be actually reduced after film cooling is employed. However, due to the experimental difficulty in directly measuring the heat flux, the **Heat Flux Ratio (HFR)** q'' / q''_o is often evaluated indirectly through a theoretical relation developed by Mick and Mayle [1] between two characteristic factors of film cooling heat transfer: adiabatic film effectiveness (η) and film heat transfer coefficients (h_{af} and h_o), as:

$$q'' / q''_o = (h_{af} / h_o)\,(1-\eta/\varphi) \qquad (1)$$

In which, the **adiabatic film effectiveness** is defined as:

$$\eta = (T_g - T_{aw}) / (T_g - T_j) \qquad (2)$$

Where T_g is the main flow hot gas temperature, T_j is the coolant temperature at the cooling jet hole exit, and T_{aw} is the adiabatic wall temperature. η is an excellent indicator of film cooling performance by comparing the insulated wall surface temperature (T_{aw}) with the would-be perfect wall temperature, T_j. If the film cooling were perfect, η =1 and the wall is protected as cold as the cooling jet temperature. The **adiabatic film heat transfer coefficient** is defined as:

$$h_{af} = q'' / (T_{aw} - T_w) \qquad (3)$$

where T_w is the airfoil wall surface temperature that comes immediately in contact with the hot main gas flow. This definition is clear if the wall boundary condition is not adiabatic, which means that the actual wall heat flux would be driven by the potential adiabatic wall temperature T_{aw}.

In Eq. 1, the local heat flux without film cooling is given as:

$$q''_o = h_o\,(T_g - T_w) \qquad (4)$$

the **film cooling effectiveness**, φ, is defined as:

$$\varphi = (T_g - T_w) / (T_g - T_j) \qquad (5)$$

The definition of φ is very similar to η except T_{aw} in Eq. 2 is replaced with T_w. To reduce complexity, T_j is assumed the same as internal coolant temperature, T_{ci}. Although we can say that η is a special case of the more generically defined film cooling effectiveness (φ) when the wall is insulated, it is convenient to use both terms by designating φ for all non-adiabatic wall conditions and η only for the adiabatic wall condition. φ has also been named as **non-dimensional metal temperature** (The Gas Turbine Handbook [2]) or the **overall cooling effectiveness** in other literatures.

For a perfect film cooling performance, the film cooling effectiveness would have a value of unity (η or φ = 1.0), i.e. T_{aw} equals to the coolant temperature (T_j) at the exit of the jet injection hole; while a value of η or φ = 0 means that the film cooling has no effect in reducing the wall temperature, which is as hot as the mainstream gas.

Clarification of terminology is needed for HFR, since in some literatures it is referred to as Heat Flux Reduction originated from the study of Mick and Mayle [1]. But from the definition, it is actually the ratio of heat flux with film over without film cases, thus q'' / q''_o in Eq. 1 is more appropriately called Heat Flux Ratio, rather than Heat Flux Reduction. Meanwhile, Net Heat Flux Reduction (NHFR) is defined as $NHFR=1- q'' / q''_o=1- (h_{af} / h_o) (1-\eta/\varphi)$. In this study, HFR is referred to as the Heat Flux Ratio and will be employed throughout this paper.

In a real gas turbine condition, the airfoils are cooled inside by internal coolant flow and part of the coolant is bled and utilized for film cooling. Therefore, the actual heat transfer path goes through a conjugate condition from hot main flow gas to the airfoil surface via convection and radiation, spreads over the airfoil via conduction, and then transfers to the internal cooling fluid via convection again. The ultimate energy source is the main flow of hot gases and the energy sinks are the internal flow and film flow. Due to the complexity of this conjugate heat transfer condition, many film cooling experiments have been performed under simplified conditions such as applying adiabatic wall condition or uniformly heated wall condition. Therefore, it has been always highly desired to know HFR through Eq. 1.

Myth 1: The φ in Eq. 1 is given a constant value of 0.6.

Eq.1 is mathematically derived, so it is theoretically correct. To determine the value of q''/q_o''through experiments, two tests need to be performed: one for the adiabatic case to acquire η and the other for the conjugate case (with and without film) for h_{af} / h_o. But how can φ be obtained? Based on the derivation by the original producers of this equation Mick and Mayle [1] φ is claimed to be typically about 0.6 for modern gas turbine components; however, no supporting material or data were provided in their paper to substantiate this value. This value of "0.6" has been widely used and cited since 1988, for example in [3] and [4]. Examination of the φ definition in Eq. 5 unequivocally indicates that the value "0.6" implies the film cooling effectiveness is 0.6 under non-adiabatic conditions. It is understood that HFR calculated using a pre-assumed φ value could serve as an estimate for film cooling scheme applied in an assumed condition, but this practice brings about many concerned issues. The first issue is that it is difficult to understand that this single constant value can be valid for various cases under the influences of different conditions i such as jet temperature, blowing ratio, hole configurations, etc. The second issue is that film cooling effectiveness should be non-uniform along the surface, thus applying a constant φ-value everywhere is questionable. The third issue is that a constant φ-value implies a constant wall surface temperature, which is not true under real film cooling conditions. The fourth issue is that the value of 0.6 was given at real gas turbine environment, it is questionable this same value is appropriate to be used for low temperature laboratory condition. Although Oh and Han [4] and Lu et al. [5] expanded the range of φ value from 0.6 to

between 0.5 and 0.7, they did so without any supporting material either. Therefore, the practices of assigning or assuming a single value of φ is questionable and not convincing.

Furthermore, if Eq.1 is used to calculate q", h_{af} will need to be calculated from Eq.3 by measuring T_w distribution from an experiment. If T_w-values are measured from the experiment, φ-values can be directly calculated through Eq.5 and then used in calculating HFR. Instead, many researchers employ an assumed single φ-value (0.6 or any other value) for HFR calculation in despite of the available φ-values that already obtained in their specific studies. In other words,
it is not clear why not just insert the actual φ-value calculated by Eq. 5 into Eq.1 at each location rather than use a single φ-value (0.6 or any other value) for each location.

Myth 2: T_{aw} is the driving temperature of wall heat flux.

Equation 3 is generated by employing the concept of deeming adiabatic wall temperature as the driving potential for the actual heat flux over the film-cooled surface as proposed by Goldstein [6] in 1971. Theoretically, the concept of adiabatic wall temperature is drawn from the phenomenon that occurs in a compressible flow over a cooled wall when viscous dissipation becomes important near the wall and produces a thermal field that generates higher temperature in the overriding gas than the wall temperature. The concept of recovery temperature is used to describe the elevated temperature due to heating from both viscous dissipation and compression. Under this condition, the heat flux received by the wall is more appropriately evaluated by using the temperature difference of T_{aw}-T_w.

This practice also provides the result that h_{af} will always be a positive value even for the situation when the wall temperature is higher than the free stream flow temperature (T_g), under which the h-value defined by the traditional approach, $h = q"/ (T_g-T_w)$ may become negative because the heat is transferred to the wall even when T_w is higher than T_g. The sign convention in this study is that a positive q" means heat flux moves into the wall from the gas stream. However, this viscous dissipation phenomenon is fundamentally different from the physics in the film cooling condition. In flows that viscous dissipation is crucial, dissipation is the actual energy source which converts the flow's kinetic energy to thermal energy near the wall; whereas in the film-cooling flow the only energy source is the hot gas stream (assuming viscous dissipation is negligible in the film-cooling flow discussed in this paper.) Therefore, the highest temperature value T_{aw} in the viscously dissipative flow is related to how much the converted thermal energy can be recovered by the wall via the recovery factor; whereas, in the film-cooling flow, the highest temperature that T_{aw} can possibly reach is T_g. Thus, using the concept of recovery factor (r) or recovering temperature (T_r) in the film-cooling flow to explain T_{aw} by some researchers seems artificial and shy of a support of flow physics if viscous dissipation is negligible. Lack of awareness of this difference has caused some confusion in explaining the film-cooling results.

Harrison and Bogard [7] studied the validity of using T_{aw} as the driving temperature via the approach of comparing the heat flux and wall temperature of a film cooled wall using computed values of T_{aw} and h_f/h_o with the result from a conjugate model. They used the relative thickness between the velocity boundary layer and the thermal boundary layer to explain that if the thermal boundary layer is thinner than the velocity boundary layer, use of T_{aw} is acceptable; whereas if both boundary layers are of the similar thickness, then T_g instead of T_{aw} is more appropriate driving temperature. Their observation and conclusion from the CFD results are not unexpected. Basically, their conclusion implies that T_{aw} is not always the driving temperature.

Considering what has been emphasized earlier in this paper that the passage of the heat is from the only source (T_g) to the sink (coolant), it is reasonable to think that T_{aw} in the film-cooling flow doesn't represent the energy source (a cause) that drive the heat flow but a "consequence" resulting from the thermal-flow fields. Since T_{aw} is just a result of thermal-flow field, the other options can be chosen to determine the driving temperature. For example, an effective temperature located between the wall and the core of coolant can be designated as the driving temperature as $T_{eff}(x) = (T_g + f(x)T_j)/2$, where f(x) is a function that describes the coolant core temperature attenuation along the streamwise direction. Apparently, f(x) is unknown and needs to be determined by experiments, but a search for f(x) will further complicate the issue. This thought provokes the temptation to make it simple by just using the T_g as the driving temperature for all the film-cooling cases without trying to figure out what the effective local driving temperature would be along the wall.

Myth 3: h_{af} in Eq.3 can be obtained from isoenergetic film experiments

Isoenergetic film cooling is named for the condition where $T_j=T_g$, i.e., the jet is as hot as the gas stream. Conventionally, the h_{af} value is obtained by conducting an isothermal film experiment. Since h_{af} should include the effects from film-disturbed flow field and thermal field, an isothermal film experiment only provides the effect of flow field, which actually helps enhance heating of the surface instead of cooling of the surface because the film jet promotes turbulence and augments surface heating.

While the jet flow-induced mixing, which changes the film distribution and concentration, acts adversely to the goal of reducing heat flux through film cooling, the lower coolant temperature serves to protect surface by absorbing the heat from the main flow. These two mechanisms compete with each other, and it is therefore essential to distinguish the difference between the effects of flow field from the effect of lower temperature on film cooling performance. Consequently the overall performance of film cooling manifests a net wall heat flux reduction which takes into account decreased gas temperature provided by the coolant film and the increased heat transfer coefficient due to the hydrodynamic effect of coolant injection process.

In the isoenergetic film case, the actual heat transfer coefficient should be evaluated as $h = q''/(T_g-T_w)$; however, in order to fit the definition in Eq 1, h_{af} is calculated via Eq. 3 instead of h. In this practice, two issues are raised. First, the h_{af} so obtained does not include the effect of actual jet coolant temperature, T_j, so **h_{af} is overvalued** because T_w should be lower if the T_j's temperature effect is included. Second, in the isoenergetic film experiment, the wall heat flux needs to be measured. If q" can be measured, why not just use a lower-temperature coolant to perform the experiment and obtain the actual filmed-cooled heat flux without even bothering to use Eqs. 1 and 2 or to run the adiabatic case? The reason is that an accurate measurement of heat flux is not easy in a conjugate condition, so most of the studies employing a uniformly heated surface to simulate the isoenergetic film heat transfer study. Implicitly, the experiment reverses the heat path by transferring heat from the wall to the free-stream. This practice is acceptable with the above condition when $T_j=T_g$, but it leads to the next Myth when $T_g>T_j$.

Myth 4: Using a heated surface can provide a simplified approach to simulate the actual film-cooling condition

Conventionally, many film-cooling experiments and computational analyses have used a heated surface to simulate the actual film-cooling condition with a cooling jet and a hot main flow. This practice is based on the observation that the airfoil surface is usually hotter than the film temperature, so it is appropriate to simplify the conjugate condition with a heated surface. This simplified practice is seemingly fine, but a close examination of the physics leads to an unwelcome negative conclusion: heated surface with cooling jet and hot gas does not provide the correct physics of the heat flow under an actual film cooling condition and therefore the results are questionable! This means that in the real film-cooling surface, the heat transfers from the gas to the wall which is opposite to the heated flow experimental case where the heat transfers from the wall to the gas. It is easy to fall into the trap of thinking that the cooling film has a temperature lower than the wall, so the heat tends to transfer from the "hot" wall surface to the cooling air. The reality is that the cooling air, which mixes with the hot main stream gas, reduces the bulk temperature near the wall and hence reduces the heat transfers to the wall, but the mixture temperature is still higher than the wall temperature with an exception of limited area where the wall temperature is higher than the near-wall gas due to heat conduction in the wall. The small region of reversed heat transfer has been reported by Mozon et al. [8] and Coulthard et al. [9] and will be discussed and simulated by CFD later.

As having been emphasized before, the only energy source in the actual film cooling condition is the main flow hot gas, so if there is a path for heat transferring from the surface back to the gas flow, it must be the result of the natural course of the heat transfer. This means that the reason that the surface becomes hot must be due to accessible heat paths from the main gas flow to the surface. These heat paths can be contributed by turbulent eddies penetration to the surface, secondary flow wrapping from the lateral

direction, radiation, or purely diffusion of heat to the surface. Typically the gas temperature adjacent to the wall would be higher than the wall surface temperature and the chance for heat transferring back from the surface to the gas must only be provided by the conduction inside the wall material that redistributes the heat from the hotter region to the colder region. This heat conduction path makes the wall surface temperature warmer than the adjacent gas temperature immediately away from the wall. Therefore, using a heated wall as the wall boundary condition is only valid for the limited area (usually near the film hole) where the wall temperature is hotter than the near-wall gas temperature.

The heated wall can be used as the corrected boundary condition only if all the heat flow direction is consistently reversed, i.e. using a heating jet with a temperature higher than the main gas stream ($T_j > T_g$). Mick and Mayle [1] did just this by adopting a completely reversed heat flow condition in their study.

There is another concern related to the effect of variable properties when using heated surface condition to measure h_{af}, since the temperature gradient is totally opposite from the real condition with the airfoil surface being cooled. , This concern can be investigated by examining h_{af} obtained through both heated and cooled surface cases in this study.

A sketch is shown in Fig. 1 to qualitatively illustrate the heat transfer scenario including the temperature profiles at two locations: one near the jet injection hole with a possible reversed heat flow and the other located further downstream from the injection hole region. The slopes of the temperature profiles are drawn to qualitatively reflect the heat flow direction.

The objective of this paper is to systematically investigate the above myths and associated issues guided by CFD simulations.

MODELING AND METHODOLOGY

The investigation in this paper is guided by a series of computational fluid dynamic (CFD) simulations. Although the actual numerical values of CFD are often subject to large uncertainties from different turbulence models, discretization resolution, and grid quality, the global heat transfer and flow physics can be captured relatively trustfully. Since the focus of this study is on illustrating thermal-flow physics and relative comparisons of different cases, any bias generated by CFD scheme is generally not so critical in the comparative nature of the analysis conducted in this paper.

Considering film cooling studies using low temperature and low heat flux laboratory conditions having been more commonly seen in open literatures than those employing real engine conditions, in this study the issues will be discussed based on simulations of lab conditions. While quite obviously in real engine conditions, which are characterized by elevated pressure, temperature, heat flux, and flow speed conditions, the properties of airfoil wall material and fluid flow will differ from in the lab conditions. But since the

discussions are based on normalized value of φ and η and focused on methodology of practices, using data in lab conditions should not change physics and issues extensively discussed in this paper. The elevated conditions will only affect the quantitative values of η and φ, but not the fundamental physics and methodology investigated in this paper. For example, in certain real engine condition, the φ-value could change from 0.6 to another value and the area of reversed heat transfer may expand a bit larger, but the issues and conclusions would not be affected. A supporting simulation case with real engine condition is shown in Appendix to avoid distraction from the continuous presentation of the cases simulated under laboratory conditions.

Geometrical Configuration

To make analysis easier, 2-D conditions with various changing parameters are simulated. In 2-D cases, a slot is selected; its configuration and the main dimensions are shown in Fig. 2.
The slot width (b) is 4 mm. The injection angle is 35^o, which is considered as the optimal value by Bell et al. [10] and Brittingham et al. [11]. The length of the film slot is 3b from coolant supply plenum to the surface. The computational domain has a length of 80b and a height of 20b. The slot jet is set to 20b from the entrance of the mainstream. In the conjugate cases arrangement, the solid metal wall (Nickel) with a uniform thickness of 1.72b is included in the computational domain and an internal cooling channel flow is imposed below the base wall bottom surface, with an internal heat transfer coefficient h_i and a coolant flow temperature T_{ci} as shown in Fig. 2. It is understood that coolant plenum and film injection hole wall cooling conditions have important effects on film cooling performance. To simplify the analysis and focus on the HFR issues, plenum is not included and adiabatic wall is assumed within the film injection wall.

Governing Equations

The 2-D, time-averaged, steady-state Navier-Stokes equations as well as equations for mass, energy and species transport are solved. The governing equations for conservation of mass, momentum, and energy are given as:

$$\frac{\partial}{\partial x_i}(\rho u_i) = S_m \tag{6}$$

$$\frac{\partial}{\partial x_i}(\rho u_i u_j) = \rho \vec{g}_j - \frac{\partial P}{\partial x_j} + \frac{\partial}{\partial x_i}\left(\tau_{ij} - \rho\overline{u'_i u'_j}\right) + F_j \tag{7}$$

$$\frac{\partial}{\partial x_i}(\rho c_p u_i T) = \frac{\partial}{\partial x_i}\left(\lambda \frac{\partial T}{\partial x_i} - \rho c_p \overline{u'_i T'}\right) + \mu\Phi + S_h \tag{8}$$

where τ_{ij} is the symmetric stress tensor defined as

$$\tau_{ij} = \mu\left(\frac{\partial u_j}{\partial x_i} + \frac{\partial u_i}{\partial x_j} - \frac{2}{3}\delta_{ij}\frac{\partial u_k}{\partial x_k}\right). \qquad (9)$$

$\mu\Phi$ is the viscous dissipation and λ is the heat conductivity.

Notice the terms of $\rho\overline{u_i' u_j'}$, and $c_p\overline{u_i' T'}$ represent the Reynolds stresses and turbulent heat fluxes, which should be modeled properly for a turbulent flow. The Reynolds number of the main flow (based on the duct height and the inlet condition specified later) is about 21,000 in this study. Therefore, a turbulence model needs to be included.

Turbulence Models

Standard k-ε Model – The standard k-ε model with enhanced wall function is employed in the CFD calculation.

The constants in the k-ε equations are assigned with the recommended values by Launder and Spalding [12]. The turbulence Prandtl number, Pr_t, is set to 0.85, and the turbulence Schmidt number, Sc_t, is set to 0.7.

In the enhanced wall treatment, the two-layer model is combined with the wall functions. The whole domain is separated into a viscosity-affected region and a fully turbulent region by defining a turbulent Reynolds number, Re_y,

$$Re_y = yk^{1/2}/\nu \qquad (10)$$

where k is the turbulence kinetic energy and y is the distance from the wall. The standard k-ε model is used in the fully turbulent region where $Re_y > 200$, and the one-equation model of Wolfstein [13] is used in the viscosity-affected region with $Re_y < 200$. The turbulent viscosities calculated from these two regions are blended with a blending function (θ) to smoothen the transition.

$$\mu_{t,enhanced} = \theta\mu_t + (1-\theta)\mu_{t,l} \qquad (11)$$

where μ_t is the viscosity from the k-ε model of high Reynolds number, and $\mu_{t,l}$ is the viscosity from the near-wall one-equation model. The blending function is defined so it is equal to 0 at the wall and 1 in the fully turbulent region. The linear (laminar) and logarithmic (turbulent) laws of the wall are also blended to make the wall functions applicable throughout the entire near-wall region.

Boundary Conditions

All walls have a non-slip velocity boundary condition in this study. Flow conditions with low temperature, pressure, and velocity for typical laboratory experiments are employed. For the 2-D conjugate cases, the solid wall is assumed to be Nickel (Ni) with a density of 8,900 kg/m^3, a heat conductivity of 91.74 W/m-K, and a specific heat of 460 J/kg-K. A heat transfer coefficient of h_i = 100 W/m^2-K and coolant flow temperature T_{ci} = 300K are assigned to the internal cooling flow, which is located at the bottom of Figure 2.

Variable properties effect has been included in the simulation. Air is modeled as an incompressible ideal gas with the density varying with temperature and the heat capacity is modeled as a piecewise polynomial function of temperature with two temperature sub-ranges of 100K-1000K and 1000K to 2000K, respectively. Inlet and outlet conditions, wall thermal boundary conditions for different cases are summarized in Table. 1. Details of the cases set-up will be shown later in this section.

Table 1 Summary of Boundary Conditions

		2-D hole	
Operational pressure	P (atm)	1	
Main stream inlet	T_g (K)	400	400K=260.6°F
	u_g(m/s)	10	Uniform
	Tu (%)	3	Turbulence Intensity
	$Re_l x10^{-6}$	0.21	l=0.32m
Jet inlet	T_j(K)	300	300 K = 80.6°F
	u_j (m/s)	10	Uniform
	Tu (%)	3	Turbulence intensity
	$Re_d x10^{-3}$	2.67	d=4mm
$M=(\rho u)_j/(\rho u)_g$	M	1.3	blowing rato
Outlet	P (atm)	1	Constant pressure
Conjugate cooling wall	T_{ci} (K)	300	
	h_i (W/m^2-K)	100	
Constant temperature wall	T_w (K)	325	φ=0.75
	T_w (K)	375	φ=0.25
Elevated main flow temperature	T_g (K)	1400	
Uniformly cooled wall	q" (W/m^2)	-3000	Constant heat flux
	q" (W/m^2)	-6000	
Uniformly heatd wall	q" (W/m^2)	3000	Constant heat flux

Numerical Method

The commercial software code Fluent (version 6.2.16) from Ansys, Inc. is adopted in this study. The simulation uses the segregated solver, which employs an implicit pressure-correction scheme [14]. The SIMPLE algorithm is used to couple the pressure and velocity. Second order upwind scheme is selected for spatial discretization of the convective terms and species.

As shown in Fig. 3, structured but non-uniform grids are constructed in this study. The grids near the jet wall and the bottom wall of the main domain are denser than the other area. Grid independence study is conducted by comparing adiabatic film effectiveness of simulations based on two different meshes of 80,000 and 48,000 cells respectively. The results are almost identical. The grid adopted in this study is of 400 meshes in the x-direction and 120 in the y-direction for 2D studies.

Converged results are obtained after the specified residuals are met. A converged result renders mass residual of 10^{-5}, energy residual of 10^{-7}, and momentum and turbulence kinetic energy residuals of 10^{-6}. These residuals are the summation of the imbalance for each cell, scaled by a representative of the flow rate. Typically, 1000 to 2000 iterations are needed to obtain a converged result, which takes about 1~2 hours on

a parallel computer cluster consisting of eight nodes of 2.53 GHz Pentium dual-core personal computers.

Y+ values from qualification case are shown in Fig. 4. Y+ values is below 0.8 for most X locations

CFD Model Qualification and Uncertainty Estimate

Effect of turbulence models using the same 2D mesh has been investigated in previous study by Li and Wang [15]. The CFD results are compared with the experimental result of Rhee et al. [16], as shown in Fig. 5. Since the standard k- ε model is one of the three turbulence models that are relatively close to the experimental data and is faster than the RNG and RSM to achieve convergence, it has been adopted in this study.

The uncertainty from the key factors are estimated as: 10% for 3 different turbulence models, 5% for turbulence length scales, 3% for resolution of second order central and upwind methods, 1% for convergence resolution, 3% for the effect of grid size, and 3% for the near-wall grid effect. The overall uncertainty for cooling effectiveness is estimated to be 12% with root-mean-square method. The above uncertainty is estimated from the computational results under low temperature and pressure conditions. Therefore, the estimated uncertainty is not centered with the true value; rather it represents the uncertainty excursion of the results that are attributed by the computational model and scheme. Again it needs to be mentioned that this paper is focused on the methodology and global thermal-flow physics. The actual quantitative data, even with some bias, will not change the fundamental physics to be presented and discussed in this paper.

Methodology and Cases Set-up

The conjugate heat transfer scenario of an operational turbine airfoil film cooling system includes a main flow of hot gas with known conditions overrides on the airfoil's upper surface, while internal coolant flow moves underneath the airfoil's bottom surface and part of the coolant is injected through the coolant holes over the airfoil surface. The airfoil wall temperature and heat flux are determined by those conditions. The most appropriate simulation of this film-cooling system is to set up the main flow, internal flow and film injection conditions as boundary conditions while leaving the airfoil's wall thickness as part of the conjugate calculation. Also to evaluate heat flux reduction on the airfoil, heat transfer of the same system running without film injection needs to be simulated. The conjugated cases described above are set as the baseline cases of this study and named as:

Case 1.1 Without-film Internally Cooled Conjugate Case

Case 1.2 With-film Internally Cooled Conjugate Case. (**Baseline Case**)

The Heat Flux Ratio calculated based on the simulation results of the two cases is thus the "real" HFR of a system, opposing to HFR acquired through mathematical manipulation and calculations as in Eq. 1,

which requires additional information of h_{af}, h_o, and η.

To evaluate Eq. 1 for HFR calculation, simulation of the adiabatic case is needed to acquire η. Considering the conjugated airfoil condition, two approaches can be taken to simulate the adiabatic boundary condition: (1) adiabatic wall condition is directly imposed on the wall surface in contact with gas and the airfoil's wall thickness is not considered(**shell wall**) (2) The adiabatic condition is applied to the inner (or bottom) surface of the airfoil and the airfoil's thickness is included in the calculation (**finite wall**). Option 1 is the ideal case for achieving the adiabatic condition. The T_{aw} obtained from Option 1 is what is supposed to be used in Eqs. 2 and 3. Option 2, in turn, is the common practice in experiments due to the necessity of installing a wall with a finite thickness and the convenience of directly applying insulation on the test section's outer surface. It would be interesting to use CFD to find out the difference of T_{aw} obtained from these two different approaches. Option 2 is used for Cases 1.1 and 1.2

Case 2. Film-cooled adiabatic finite wall case

Case 3. Film-cooled adiabatic shell wall case

With the results of Cases 1.1, 1.2, 2 and 3, parameters to evaluate Eq. 1 can be acquired and the following issues can be examined.

1. Whether the adiabatic wall temperature is the driving temperature --- The guiding criterion to judge whether T_{aw} behaves as the driving temperature is to determine whether the heat flux direction can be accurately predicted by applying the CFD results to Eq. 3. Ideally if the driving temperature is higher than the wall temperature, heat should be transferred into the wall and vice versa.
2. The effect of the wall thickness on T_{aw}.
3. Heat Reduction Prediction Using Eq. 1--- All the parameters needed to calculate HFR using Eq. 1 can be readily acquired through Case 1.1 (h_o), Case 1.2 (h_{af}), and Case 2/Case 3 (η). Three values for φ, 0.4 0.6 and 0.9 are adopted for calculation of HFR. The values of φ=0.4 and 0.6 are popular values used in many film cooling literatures and they are employed to demonstrate HFR results using constant φ values in Eq. 1. The value of φ=0.9 is chosen to show that values other than the commonly assumed φ value (0.4~0.6) could give more reasonable result in some cases. In addition, T_w obtained from Case 1.2 via CFD is also employed to calculate the corresponding HFR using Eq. 1. Calculations using Eq. 1 are then compared with the HFR obtained from the CFD simulations. Evaluation of Eq. 1 is then conducted through a thorough discussion.

Since the experiments have been commonly conducted with uniformly heated/cooled wall condition or constant wall temperature condition, Case 4.1-8.2 are simulated to shed light into the appropriateness of employing these wall boundary conditions. All simulated cases are summarized in Table 2 and Fig. 6.

Table 2 Summary of Cases Set-up

Case #	Film Existence	Thermal Boundary Condition
Case 1.1	without film	internal cooling, conjugated
Case 1.2	with film	internal cooling, conjugated
Case 2	with film	adiabatic, conjugated
Case 3	with film	adibatic, shell wall
Case 4.1	without film	constant T_w=375K, φ=0.25
Case 4.2	with film	constant T_w=375K, φ=0.25
Case 5.1	without film	constant T_w=325K, φ=0.75
Case 5.2	with film	constant T_w=325K, φ=0.75
Case 6.1	without film	uniformly cooled wall, q''=-3kW/m^2
Case 6.2	with film	uniformly cooled wall, q''=-3kW/m^2
Case 7.1	without film	uniformly cooled wall, q''=-6kW/m^2
Case 7.2	with film	uniformly cooled wall, q''=-6kW/m^2
Case 8.1	without film	uniformly heated wall, q''=+3kW/m^2
Case 8.2	with film	uniformly heated wall, q''=+3kW/m^2

RESULTS AND DISSCUSSIONS

Heat Flux Calculation of an Internally Cooled Conjugate Airfoil

The wall temperature distributions from Cases 1.1, 1.2 (baseline case), 2 and 3 are shown in Fig. 7. For an easier comparison of temperature and heat flux correlations, wall heat flux of Case 1.1 and Case 1.2 are also plotted in the same figure on the secondary y-axis. Subscripts "f" and "o" indicated with and without film presence, respectively.

Adiabatic Film Temperature as the Driving Temperature

As discussed in the Introduction section, using adiabatic film temperature as the driving temperature potential is the center concept of calculating the Heat Flux Ratio using Eq. 1. To evaluate the appropriateness of this concept, comparison of wall temperature (T_w) from Case 1.2 (with conjugate wall) and adiabatic wall temperatures (T_{aw}) from Cases 2 and 3 (adiabatic wall) are examined and then the consistency of their heat flux directions from Case 1.2 is compared. Again, Case 3 is the ideal condition where wall thickness is not considered and adiabatic condition is directly applied on the surface in contact with gas, whereas Case 2 is the real condition where wall thickness is included and adiabatic condition is applied on the bottom wall .

In Fig. 7, first look at the baseline (Case 1.2) temperature distribution, then compare it with the adiabatic Cases 2 and 3. It can be seen that Case 2 has a more uniformly distributed temperature profile than

Case 1, indicating the "smearing" effect of the wall through conduction in Case 2 when conjugate wall is included in the computational domain. In most part, T_{aw} of Cases 2 and 3 is higher than T_w of Case 1.2, so if T_{aw} is the driving temperature, the heat should flow from the gas into the wall. Examining of the heat flux curve in Fig. 7 does show the heat flux of Case 1.2 is positive. It is further noticed that the heat flux flips to the negative direction (i.e. moving from wall to the gas) at x< 6D near the crossing point of T_w of Cases 1.2 and 3. In this case, the heat flux direction is consistent with the sign of T_{aw}-T_w : when T_{aw}>T_w, positive heat flux is found (heat moves from the gas to the wall) and when T_{aw}<T_w, the heat flux is negative, moving from wall to gas. This reversed heat transfer direction (T_w >T_{aw}) indicate T_{aw} is not always the driving temperature, although T_{aw} still serves an important role as the reference temperature to determine the heat flux direction.

Usually, T_w should be always lower than T_{aw} if the wall thickness were negligibly thin. Since the wall thickness and the accompanied heat conduction are not negligible in the conjugate case, heat flows from downstream hotter region to the near-hole colder region and heats the wall temperature to a level higher than T_{aw}. Therefore, theoretically, it seems the concept of treating T_{aw} as the driving temperature still holds if the wall conduction is negligible.

If the wall conduction is the culprit which has caused $T_w > T_{aw}$, what would happen if the wall is included in the adiabatic wall simulation? This is done in Case 2 by applying the adiabatic condition on the bottom wall. Figure 7 shows T_{aw} of Case 2 is higher than T_w of Case 1.2 throughout the entire region downstream of the film. In this condition, no heat flux direction change should occur if T_{aw} from Case 2 is the driving temperature, but as discussed earlier, heat flux of Case 1.2 changes sign at x/d=5.6 in Fig. 7, indicating using T_{aw} as a driving temperature in Case 2 does not always work out. Thus it is concluded that T_{aw} from the case with adiabatic condition imposed on the upper wall surface is more appropriate in acting as the driving temperature.

The wall temperature and heat flux of no-film case (Case 1.1) are also shown in Fig. 7. Comparison with the film-cooled cases clearly shows reductions on both the wall temperature and heat load, attributed to film cooling.

In summary, T_{aw} is an important reference temperature that provides correct information to determine the heat flux direction. "Reference temperature" means it serves as the "reference" that is compared with T_w to determine the heat flux direction. For example, $T_{aw} > T_w$ resultsin heat flux moving from the gas to the wall and vice versaSince T_{aw} is not always higher than T_w, the more precise way to credit the contribution of T_{aw} is that T_{aw} is an excellent reference temperature.

Effect of Conjugate Wall

Previous results show that T_{aw} without including the wall thickness is a more appropriate selection as

the driving temperature than the T_{aw} obtained with the conjugate wall. In reality, however, the airfoil wall has always been included in the adiabatic wall temperature measurement in experiments because in actual film-cooling experiments, the test walls always have a finite thickness. Due to the finite wall thickness and the good conductivity of metal, heat transfer inside the wall from the hotter downstream region to upstream cooler region is not negligible, so the overall wall temperature distribution of Case 2 is "smeared" to become more uniform than Case 3 with higher temperature in the near-hole region and lower temperature in the downstream area. T_w curves of Cases 2 and 3 cross over at around x/d=30. The bottom wall temperature of Case 2 is only about 1^oC cooler than the top surface due to the thin thickness of the wall. For this specific case, the wall thickness of 1.72d yields about 12 percentage point increase of maximum η near the film hole and a reduced η of about 5 percentage point in far downstream (x/d > 50).

To further investigate the wall heat conduction effect, a low thermal conductivity wood is used to replace the metal wall. The CFD result shows T_w of the wood wall is very close to Case 3's shell wall approach. This proves the importance of including metal wall in both the experimental and computational analysis of film cooling study.

Evaluation of Heat Reduction Prediction Using Eq. 1

From the real system operating point of view, one of the desires of evaluating the performance of a film cooling scheme is to find out how much heat flux or wall temperature will actually be reduced after film is added into a system. As explained earlier, Eq. 1 has been widely used to evaluate the heat flux reduction by employing film cooling. Examining derivation process of Eq. 1 reveals that a hidden assumption of $T_{w,o}=T_{w,f}$ has been implicitly introduced implying that the wall surface temperature of the system without-film is assumed to be the same as that would occur with film-cooled condition.

To verify the validity of HFR calculation using Eq. 1, heat flux directly obtained from CFD simulations of Case 1.1 and 1.2 are shown as $(q"/q"_o)_{CFD}$ in Fig. 8. Note that there is no mathematical manipulation involved in this HFR value obtained from the CFD simulations. Calculations using Eq. 1 are then performed with three φ-values, 0.4, 0.6, and 0.9, respectively. Also, calculation using varying local wall temperature from Case 1.2 is shown as $(q"/q"_o)_{vari}$. Observations of Fig. 8 are discussed below.

The CFD predicted heat flux ratio $(q"/q"_o)_{CFD}$ monotonously increases from a negative value (-0.2) immediately downstream of the film hole to 0.56 at the end of the computational domain, meaning the film performance downgrades downstream away from the film hole. A negative value of HFR means reversed heat transfer from the wall to the main flow. This is possible as explained previously due to the heat conduction from the downstream hotter region into the near film hole cooler region, resulting in a higher wall surface temperature than the near-wall gas temperature. Thus, heat is transferred back into the film flow in the limited local area close to the film hole within the region x/d <6.

The calculated HFR using Eq. 1 is way off from the CFD predicted conjugate case (Case 1.2) for using either φ=0.4 or 0.6 case. Negative values of HFR are resulted in most of the streamwise locations. As shown in Eqs. 1 and 3, a negative HFR is caused by $T_{aw}<T_w$, so the heat flow is reversed by moving from the wall to the mean flow. Usually, reversed heat flux is only possible in limited region near the film hole where heat conduction from downstream in the metal wall is significant such as within x/d < 6 in Fig. 7. But in these two cases (φ =0.4 and 0.6), the negative heat flux prevails in the entire surface. This implies that the wall temperature corresponding to φ =0.4 or 0.6 (T_w = 360K and 340K) are higher than T_{aw} or, in other words, η is higher than φ, as can be seen Fig. 9a & b, so q" or HFR becomes negative from Eq. 3 or Eq. 1, respectively. This also implies that selection of φ =0.4 or 0.6 is artificial and does not adequately represent the physics of the currently simulated cases. Note, cases of φ = 0.4 and 0.6 correspond to T_w = 360K and 340K, respectively. Their values (not shown) can be easily represented by horizontal lines and compared with T_{aw} and η in Fig. 9a &b.

Furthermore, these data have another big issue: it is unrealistic to have any heat reduction more than 100%. For any part of the data where the HFR value dipped below -1**(shoul it be 0?)** implies that film cooling actually feeds heat into the main flow with the thermal energy generated not from the main hot gas but from an artificially added source or sink! (HFR larger than 1 means film is not protecting the surface but rather it increased the surface heat transfer.)This is because a constant φ-value corresponds to a constant T_w condition, which serves as either an energy source or a sink depending whether T_w is hotter or cooler than T_{aw}.

Among the three constant φ cases, φ=0.9 yields the closest results to the baseline case, but it over-predicts the heat flux reduction by more than 25% and the accuracy in predicting HFR is not as good as the case using variable φ values.

Since using a single φ-value is not appropriate, it will be interesting to see how the calculated HFR results fare in Fig. 8 if the correct local φ-values obtained from CFD (Fig. 9b) are substituted into in Eq. 1. The comparison in Fig. 8 shows the case using varying φ-values achieves a much better agreement to the conjugate baseline case predicted by CFD (Case 1.2). However, it is noticed that in the further downstream region, varying wall temperature calculation over-predicts heat reduction (i.e. a lower HFR value) by as much as 20% of the CFD predicted HFR. It is not clear why there is a 20% deviation because Eq. 1 is supposed to be theoretically exact and the deviation should be within the precision (not accuracy) of the CFD results. This 20% deviation prompts a re-examination of the accuracy of Eq. 1 as detailed below.

From the original derivation of HFR, it is implicitly implied that the wall temperature without film being the same as with the film, i.e. T_w in Eq. 3 is the same as in Eq. 4. In a real operation, adding coolant film will result in a change of blade temperature. The original derivation in Mick and Mayle's paper [1] was

ambiguous in this issue and planted the seed for confusions and errors when Eq. 1 was used later on. If the wall temperature change is taken into account between film-cooled and without film cases, Eq. 1 can be re-derived as

$$\begin{aligned}
\frac{q''}{q''_o} &= \frac{h_{af}}{h_o}\frac{T_{\mathrm{aw}}-T_w}{T_g-T_{wo}} = \frac{h_{af}}{h_o}\left(1-\frac{T_g-T_{aw}}{T_g-T_{wo}}+\frac{T_{\mathrm{wo}}-T_w}{T_g-T_{wo}}\right) \\
&= \frac{h_{af}}{h_o}\left(1-\frac{(T_g-T_{aw})/(T_g-T_j)}{(T_g-T_{wo})/(T_g-T_j)}\right)+\frac{h_{af}}{h_o}\frac{(T_{\mathrm{wo}}-T_w)/(T_g-T_j)}{(T_g-T_{wo})/(T_g-T_j)} \\
&= \frac{h_{af}}{h_o}\left(1-\frac{\eta}{\varphi_o}\right)+\frac{h_{af}}{h_o}\frac{(T_{\mathrm{wo}}-T_w)/(T_g-T_j)}{\varphi_o} \\
&= \frac{h_{af}}{h_o}\left(1-\frac{\eta}{\varphi_o}\right)+\frac{h_{af}}{h_o}\frac{(T_{\mathrm{g}}-T_w)/(T_g-T_j)-(T_{\mathrm{g}}-T_{wo})/(T_g-T_j)}{\varphi_o} \\
&= \frac{h_{af}}{h_o}\left(1-\frac{\eta}{\varphi_o}\right)+\frac{h_{af}}{h_o}\frac{\varphi-\varphi_o}{\varphi_o}
\end{aligned} \tag{12}$$

The difference between Eqs. 1 and 12 is:

$$\begin{aligned}
\left(\frac{q''}{q''_o}\right)_{eq12}-\left(\frac{q''}{q''_o}\right)_{eq1} &= \frac{h_{af}}{h_o}\left(1-\frac{\eta}{\varphi_o}\right)+\frac{h_{af}}{h_o}\frac{\varphi-\varphi_o}{\varphi_o}-\frac{h_{af}}{h_o}\left(1-\frac{\eta}{\varphi}\right) \\
&= \frac{h_{af}}{h_o}\left(\frac{\eta}{\varphi}-\frac{\eta}{\varphi_o}+\frac{\varphi-\varphi_o}{\varphi_o}\right) = \frac{h_{af}}{h_o}\left(\frac{\eta\varphi_o-\eta\varphi+\varphi^2-\varphi\varphi_o}{\varphi\cdot\varphi_o}\right) \\
&= \frac{h_{af}}{h_o}\frac{(\varphi-\eta)\cdot(\varphi-\varphi_o)}{\varphi\cdot\varphi_o}
\end{aligned}$$

Since the wall temperature of a system without film will be lowered after the film is added, φ is larger than φ_o. And typically, $T_w < T_{aw,}$ because heat is transferred from the heat source (main flow) into the wall. As a result, φ is generally higher than η.

Thus $\frac{(\varphi-\eta)\cdot(\varphi-\varphi_o)}{\varphi\cdot\varphi_o} > 0$ and as a result Eq. 1 under-predicts Heat Flux Ratio and over-predicts the actual heat flux reduction.

Comparisons of HFR from simulations and calculation results from Eq. 1 and Eq. 12 are shown in Fig. 8. An excellent agreement is found between the CFD simulation and the calculated results based on Eq. 12, as it is supposed to be since Eq. 12 is theoretically exact within the CFD precision. For a quick estimate of HFR using Eq. 12, the φ could be approximated as $\varphi = a + b\,(x/d)^n$ in this study, for example.

Strong irregularities of HFR curves of all three cases using a single φ-value for each case are noticed at x/d about 5.6. These irregularities are caused by the divergence of h_{af} in the conjugated case (Case 1.2) when T_w approaches T_{aw} and heat flux is approaching zero and undergoing reversal of direction. More detailed discussion of h_{af} will be presented later. This is very different from the continuous smooth curves of

the CFD predicted HFR and the varying wall temperature case calculated via Eqs. 1 or 12; both cases bear the correct physics.

Discussion on Using Heated or Cooled Wall Conditions for Film Cooling Experimental Setup

The actual film-cooling airfoils are subject to a complicated conjugate heat transfer phenomenon. For the convenience of setting up an experiment, a simplified experimental test section has been often employed by imposing a heated or cooled boundary condition. Discussion of Myth 3 has expressed concern on this simplified practice. First of all under heated wall condition, the heat flow direction is opposite to the real case where heat transfers into the airfoil, making such set-ups less meaningful in simulating real case film cooling scenarios. Secondly, different directions of the temperature gradient in the boundary layer will result in different variable properties effects on h-values. To illustrate the issues involved, two cases of constant wall temperature T_w= 325K and 375K (corresponding to $\varphi = 0.75$ and 0.25, respectively) and three cases of uniformly heated and cooled cases with $q'' = \pm 3$ and 6 kW/m^2 are simulated. These five cases are simulated for both with and without film, so a total of 10 different cases (Cases 4-8) are listed in Table 2. The results of wall temperature and film cooling effectiveness are shown in Fig. 9 and discussed below.

Conjugate Case --- It is noticed φ_{conj} is slightly lower than η in a small area immediately downstream of the jet hole and is higher than η in rest of downstream region. A higher value of φ indicates better film cooling effect. Thus a higher φ_{conj} compared with η means a better cooling effect is achieved in the conjugated case than the adiabatic wall case. The extra cooling effect comes from the internal cooling included in the conjugated case. However φ_{conj} is lower than η in the neighborhood of the jet hole area because the conduction effect through the wall transfers heat from the hotter downstream region to the cooler upstream area and overpowers the internal cooling effect. Upstream of the film hole, φ_{conj} value is about 0.6 indicating the effect of internal cooling without film cooling effect.

Uniformly Cooled Wall Cases --- For the two uniformly cooled wall cases with heat fluxes at 3kW/m^2 and 6kW/m^2, it is noticed that in the area downstream of the film hole, φ values are greater than 1, which is not realistic in a typical cooled turbine airfoil system. This indicates that the heat sink imposed on the wall exceeds the maximum cooling power of the actual system and results in an unreal lower wall temperature than the coolant temperature.

Looking at upstream temperature of the cooled wall case at 3kW/m^2, φ is less than 1, which correctly indicates the convective cooling effect by the wall. A jump of increased value of φ crossing the coolant hole is seen, indicating that additional cooling effect is provided by the film injection than the imposed cooled wall condition at the coolant hole area. Meanwhile the jump is less noticeable in the stronger cooling case (6kW/m^2) meaning film injection does not contribute much to an already more strongly cooled wall.

Uniformly Heated Wall Cases --- Negative φ value is found upstream of the film hole. This is resulted from a higher wall temperature than the main stream temperature, which is a natural feature of an actively heated wall condition because the wall is the heat source but absolutely unrealistic for an operational turbine system.

φ jumps from the unrealistic negative values to reasonable values crossing the film injection hole, indicating the significant effect of film cooling. φ is lower than the adiabatic case showing a less effective film cooling performance over a heated wall comparing with an insulated wall. The heated wall arrangement also preheats the coolant film resulting in a significantly reduced overall cooling effect. From this analysis, it is clear that the practice of heating the wall to simulate turbine airfoil film cooling is wrong, and the results are misleading. Again, the physics of a hot airfoil in a conjugate airfoil cooling condition is totally different from the hot airfoil generated by a heated source. In a conjugate case, the temperature of a hot wall is the consequence of penetration of heat from the main stream gas and spread through the metal wall; this means the hot airfoil temperature is passively achieved. This is very different from the hot surface produced by an actively heated source, which generates heat as an energy source no matter what the film cooling effect is. Evidence can be found from the negative φ values generated upstream the film hole from the heated wall case, which is not seen in conjugate case and cooled wall case. Heated wall acts as an active heat source and as a result, the concept of using T_{aw} as the driving temperature potential is no longer valid since a competing heat source is added into the system and heat transfer on the airfoil is not solely determined by T_{aw}. Consequently, using T_{aw} in the heated wall film cooling analysis compounds the problems that should be avoided.

Again, the heated wall can be used as the corrected boundary condition only if all the heat flow direction is consistently reversed, i.e. using a heating jet with a temperature higher than the main gas stream ($T_j > T_g$).

Film Heat Transfer Coefficients

From the derivation of Eq. 1, it is clear that using h_{af} from the conjugate case will cause no ambiguity in HFR calculation. But in the conventional practice, h_{af} measured under constant heat flux or constant temperature wall condition has often been used instead. Although, this conventional practice has been discussed earlier in this paper as not physically correct, it is interesting to investigate how would the h_{af} be affected under these inappropriate conditions.

Heat Transfer Coefficient without Film --- The h-value without cooling film is investigated for six cases of different boundary conditions including a conjugate case, two constant temperature wall cases (325K and 375K), uniformly cooled and heated wall cases (-3kW/m^2 and +3kW/m^2), strongly cooled (-6kW/m^2) wall. The results are compared in Fig. 10 with the well established correlation for forced turbulent convection on a flat plate [17]:

$$Nu_x = 0.029\ Re_x^{0.8}\ Pr^{0.4} \qquad (13)$$

It is found that all the results are higher than the turbulent correlation of Eq. 13. Both constant wall temperature wall cases and the uniformly heated case achieve lower Nu than the conjugate case. A change of constant temperature wall cases from T_w =325K to 375K leads to a change of 5% in Nu. This is a 50% change of wall temperature boundary condition based on the temperature scale T_g-T_j =100K. Uniformly cooled cases result in 6-12% higher Nu. In summary, the change of wall boundary condition affects Nu within an envelope of $\pm$ 12% centered at the conjugate case with no-film condition.

Heat Transfer Coefficient with Film-Cooling --- First it needs to be noted that the definition of h_{af} is built upon the concept of adiabatic film temperature as $h_{af} = q''/(T_{aw}-T_w)$. The adiabatic film temperature must be known before h_{af} can be acquired.

The film-cooling heat transfer coefficient results for different boundary conditions are shown in Fig. 11a and the ratio of (h_{af}/ h_o) for all cases are shown in Fig. 11b. Comparing with the no-film cases, the value of h_{af} has increased about 100% from h_o for most part of the cooling surface. Near the injection hole region, h-value is enhanced as high as 500%. Nusselt numbers for the two uniformly cooled cases are almost identical and close to the conjugated case. For the heated wall case, Nu is lower than the conjugate case and the difference can be as high as 15%.

Divergence of h_{af} is found for conjugate case at x/d $\approx$ 5.6 and constant temperature wall (T_w=325K) case at x/d=38. The divergence of h_{af} arises from the mathematical treatment of h_{af} at zero heat flux. As h_{af} is defined as $h_{af} = q'' / (T_{aw}-T_w)$, when T_w approaches T_{aw}, h_{af} diverges. Figure 9a shows the wall temperature profiles of both the conjugate case and the constant wall temperature case (T_w =375K) intercept the curve of the adiabatic film temperature. The locations of the interceptions are where divergence of h_{af} value occurs. This implies that using h_{af} will encounter mathematical problem in the actual conjugate airfoil cooling condition if the local T_w approaches T_{aw}. Having been explained before, this is caused by the reverse heat conduction in the wall. However, if the wall is included to obtain T_w as in Case 2, h_{af} will not diverge since all T_{aw} of Case 2 is higher than Tw, conj (See Fig. 7). Recall that in the region of x/d <6, the negative heat flux occurs and T_w of Case 2 doesn't fare the negative heat flux well.

In the discussion of Myth 3, the concern of using the isothermal jet film heat transfer coefficient as h_{af} was expressed because the effect of coolant jet temperature is not included in the heat transfer coefficient. To investigate this issue, three additional cases using isothermal jet are computed by CFD and shown in Fig. 11a. It can be seen, the isothermal jet cases will be about 20-25% lower than the cooling jet conjugate case.

Film injection exerts a strong effect on h_{af} augmentation near the injection hole region. But different thermal boundary conditions investigated in this study do not seem to impose much different effects on h_{af} in the near hole region. This is not unexpected because the film cooling effect is supposed to be strong and dominant by the flow behavior**,** not the thermal boundary condition, immediately downstream of the

injection hole. If the blowing ratio or the blowing hole geometry changes, the film effectiveness would have a more discernable difference because the flow structure would have altered. As the flow moves further downstream, the effect of the thermal boundary condition becomes more discernable.

Similar explanation can be made for the relatively lower h_{af} from the heated wall condition case, comparing with the cooled wall cases. Cooling wall will take the heat out of the film which is continuously heated by the main stream, thus helps to maintain the coolant film distinguishable from the main hot gas. Fig. 11b shows the trend of the ratio of h_{af}/h_o is similar to h_{af}, but with less variation from case to case.

In summary, the conventional practice of using uniformly heated wall as the boundary condition to simulate film cooling condition, although it does not provide correct physics, can provide the h_{af} value within 10-15% of the conjugate case value. The isothermal jet heat transfer coefficient will be about 20-25% off from the cooling jet conjugate case. That indicates that the uniformly cooled wall cases fair better than heated cases. Near the film hole (x/d <6), the variation of h_{af} values diminishes. Calculation of h_{af} will encounter undefined condition when T_w approaches T_{aw}. But ironically, this does not happen to the heated wall cases because T_{aw} is always higher than T_w. It needs to be remembered that even though the h_{af} and h_{af}/h_o results of heated and cooled cases are within 20% of the conjugate value, the φ value can be 100-200% off (see Fig. 9b).

Simulation at Elevated Gas Turbine Operating Condition

Even though the cases studied in the main text are simulated under a typical laboratory condition, the discussions made and conclusion arrived in the main text should not be significantly affected by the elevated operating conditions in a gas turbine system. To support this statement, cases under elevated condition are simulated in this section. The GT operating condition simulated represents a general condition in an F-frame type GT without trying to match the specific condition of any brand name or model. The material properties and boundary conditions are summarized in Table 3. Variable properties of both air and blade are adopted as a function of temperature and pressure.

The results of HFR are plotted in Figs. 12 and 13, corresponding to Figs. 8a and 8b under the lab condition. It can be seen that only minor differences can be found comparing with the HFR results from the lab condition simulation. The magnitude of reversed heat flux is reduced near the injection hole. All the issues discussed and conclusions made in the main text with the laboratory conditions are valid under elevated gas turbine operating condition.

Table 3 Summary of boundary conditions and material properties under elevated engine condition

Engine condition			
Operational pressure	P (atm)	15	
Main stream inlet	T_g (K)	1400	2060°F
	u_g(m/s)	80	Uniform
	Tu	3%	Turbulence Intensity
	Re_l x10^{-6}	1.6	l=0.32m
Jet inlet	T_j(K)	750	890°F
	u_j (m/s)	56	Mach=0.1, Uniform
	Tu	3%	Turbulence intensity
	Re_d x10^{-6}	0.05	d=4mm
$M=(\rho u)_j/(\rho u)_g$	M	1.3	Blowing ratio
Outlet	P (atm)	15	Constant pressure
Conjugate cooling wall	T_{ci} (K)	750	
	h_i (W/m^2-K)**	1800	
Blade*	k (W/m-K)	16.9	at T=422K
		26.5	at T=811K
		31.4	at T=1033K
		35.3	at T=1144K
Air	ρ (kg/m^3)	3.43	at T=1400K, P=15 atm
	k (W/m-K)	0.1	
	μ (x10^{-6} kg/m-s)	55.7	
	ν (x10^{-6} m^2/s)	16	

CONCLUSION

In this study several conventional myths and concerned practices for film cooling research have been discussed. A series of computational experiments have been conducted to simulate the physical processes of film cooling including both the actual condition and simplified conditions that have been traditionally employed.

The appropriateness of employing the concept of adiabatic wall temperature as the driving temperature was first questioned because the heat source is from the main hot gas stream, not coming from the near-wall viscous dissipation like in the compressible flow condition. However, the analysis supports this concept to be used in the film cooling by showing that T_{aw} has been able to correctly determine the heat flux direction

including the reversed heat flux flowing from the wall to the gas due to conduction in the wall. The T_{aw} obtained by theoretical zero wall thickness fares better as the driving temperature than T_{aw} obtained from a conjugate study. Since T_{aw} is not always higher than T_w, the more precise way to credit the contribution of T_{aw} is that it can be used as a good reference temperature to correctly determine the heat flux direction. When $T_{aw} > T_w$, the heat flux moves from the gas to the wall and vice versa.

Using the values for φ (0.5 ~ 0.7) as a constant to calculate the heat flux ratio (HFR) has been questioned and investigated. Implicitly, a constant φ-value implies a constant film cooling effectiveness or a constant T_w over the entire surface, which is not consistent with the fact in most cases (unless the constant wall temperature condition is imposed). Several major issues have been showcased through the CFD cases. Negative values of film cooling effectiveness (φ) occurs in some simulated cases showing the commonly adopted value φ=0.5~0.7 could be un-realistic and give false HFR. Results show that the origin of the unrealistic negative HFR given by the constant φ cases arise from the assumption of a wall temperature at which the system can't be possibly achieve. The original HFR equation derived by Mick and Mayle [1] implicitly implied that the wall temperature of the film-cooled surface to be the same as the no-film case. A new HFR equation is derived by removing this implicit assumption and accounts for the wall temperature difference between with and without film conditions. The difference between the old and new equation can contribute to about 20% of the heat flux ratio value. The revised system of equations is:

$$\frac{q''}{q''_o} = \frac{h_{af}}{h_o}\left(1 - \frac{\eta}{\varphi_o}\right) + \frac{h_{af}}{h_o}\frac{\varphi - \varphi_o}{\varphi_o} \quad \text{(Heat Flux Ratio, HFR)} \qquad (12)$$

$$\eta = (T_g - T_{aw}) / (T_g - T_j) \quad \text{(Adiabatic film cooling effectiveness)} \qquad (2)$$

$$h_{af} = q'' / (T_{aw} - T_w) \quad \text{(Adiabatic heat transfer coefficient)} \qquad (3)$$

$$\varphi = (T_g - T_w) / (T_g - T_j) \quad \text{(Film cooling effectiveness)} \qquad (5)$$

$$q''_o = h_o (T_g - T_{wo}) \quad \text{(Convection without film)} \qquad (14)$$

The conventional practice of employing a heated wall with hotter main stream flow and cold film injection are found to be fundamentally wrong because the heated wall serves as an energy source and provides the heat flux moving in a wrong direction. Employing isothermal jet ($T_j = T_g$) experiment to obtain the heat transfer coefficient only includes the effect of the fluid mechanics (which adversely affect cooling) but the effect of jet temperature (which assists cooling) is not counted. As much as 25% difference in h-value is generated as a result.

Wall conduction is important and needs to be simulated in both experiment and CFD analysis. Wall conduction smears the temperature distribution and reduces film cooling effectiveness. A conjugate wall cooling simulation shows that reversed heat transfer from surface to gas that gives a minus HFR is possible due to the heat conduction from the downstream hotter region into the near film hole cooler region.

Only 2D cases are discussed in this paper because they provide a more clear way to discuss the physics.

3D cases will involve a more complicated flow structure, but the conclusions should not be affected. 3D cases will be discussed in a future paper.

ACKNOWLEDGEMENT

This study is supported by the Louisiana Governor's Energy Initiative via the Clean Power and Energy Research Consortium (CPERC) and administered by the Louisiana Board of Regents.

REFERENCE

[1] W.J. Mick, R.E. Mayle, Stagnation film cooling and heat transfer, including its effect within the hole pattern, ASME J. of Turbomachinery 110 (1988) 66-72.

[2] The Gas Turbine Handbook, Office of Fossil Energy, National Energy Technology Libratory, U.S. Department of Energy, 2006, PP. 310-318.

[3] B. Sen, D.L. Schmidt, and D.G. Bogard, Film cooling with compound angle holes: heat transfer, ASME J. of Turbomachinery 118 (1996) 800-806.

[4] S. Ou, J.C. Han, Influence of mainstream turbulence on leading edge film cooling heat transfer through two rows of inclined film slots, ASME International Gas Turbine and Aeroengine Congress and Exposition 36, 1991.

[5] Y. Lu, A. Dhungel, S.V. Ekkad, R.S. Bunker, Effect of trench width and depth on film cooling from cylindrical holes embedded in trenches, ASME J. Turbomachinery 131 (1) (2009) 011003.

[6] R.J. Goldstein, Film cooling advances in heat transfer 7 (1971) 321-379.

[7] K. Harrison, and D.G. Bogard, Use of the adiabatic wall temperature in film cooling to predict wall heat flux and temperature, ISROMAC Paper 12 (2008) 20187.

[8] B.D. Mouzon, E.J. Terrell, J.E. Albert, D.G. Bogard, Net heat flux reduction and overall effectiveness for a turbine blade leading edge, ASME TurboExpo 2005, GT2005-69002.

[9] S.M. Coulthard, R.J. Volino, K.A. Flack, Effect of Jet Pulsing on Film Cooling-Part II: Heat Transfer Results, ASME J. Turbomachinery 129 (2007) 232-246.

[10] C.M. Bell, H. Hamakawa1, P.M. Ligrani, Film cooling from shaped holes, ASME J. Heat Transfer, 122 (2000) 224-232.

[11] R.A. Brittingham, J.H. Leylek, A detailed analysis of film cooling physics: Part IV—compound-angle injection with shaped holes, ASME J. Turbomachinery 122 (2002) 133-145.

[12] B.E. Launder, D.B. Spalding, Lectures in Mathematical Models of Turbulence, Academic Press, London, England, 1972.

[13] M. Wolfstein, The velocity and temperature distribution of one-dimensional flow with turbulence

augmentation and pressure gradient, Int. J. Heat Mass Transfer 12 (1969) 301-318.

[14] Fluent Manual, Version 6.2.16, Fluent, Inc. 2005.

[15] X. Li and T. Wang, Effects of various modeling on mist film cooling, ASME Journal of Heat Transfer 129 (2007) 472-482.

[16] D.H. Rhee, Y.S. Lee, H.H Cho, Film cooling effectiveness and heat transfer of rectangular-shaped film cooling holes, ASME Turbo Expo 3 (2002) 21-32.

[17] P.H. Oothsuizen, D. Naylor, An Introduction to Convective Heat Transfer Analysis, second ed, McGraw-Hill, New York, 1999

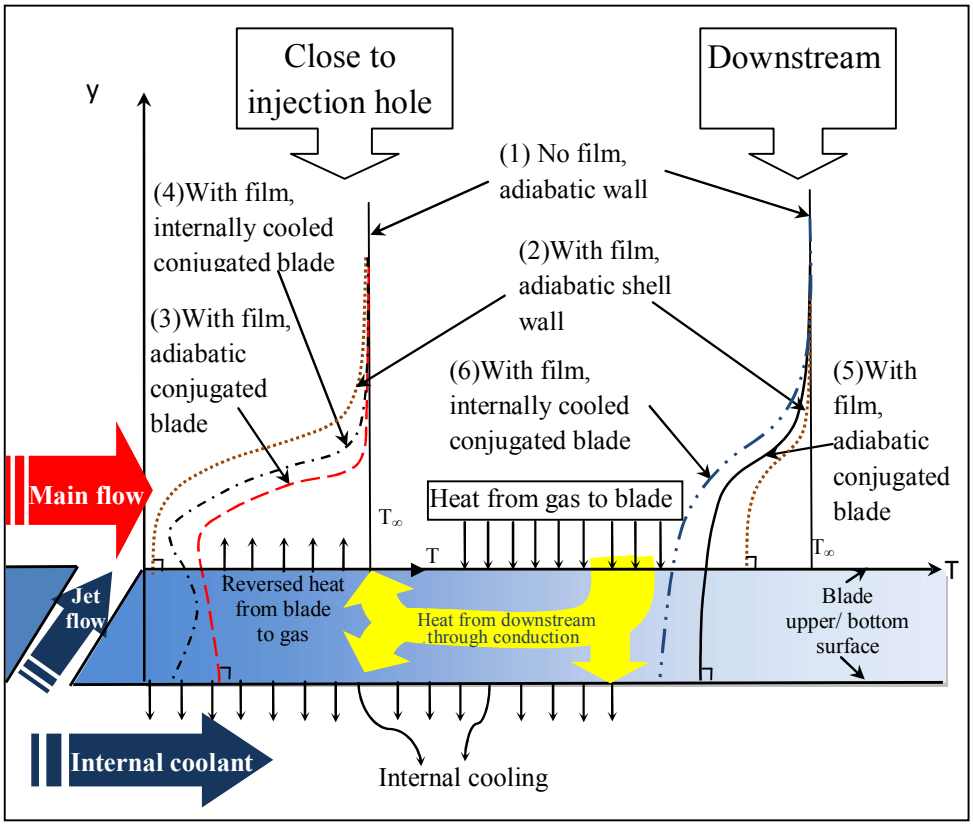

Figure 1 Qualitatively temperature profiles of a typical internally and film cooled blade at two locations: one near the injection hole region with potentially reversed heat transfer and the other located further downstream.

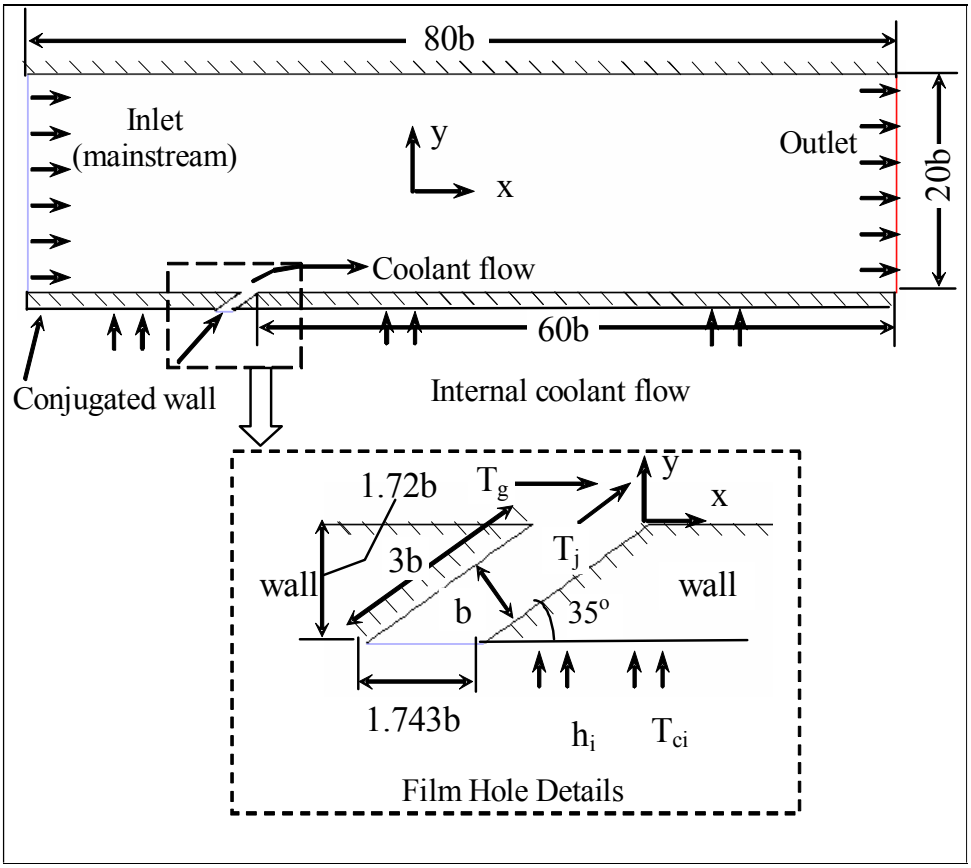

Figure 2 Computational domain

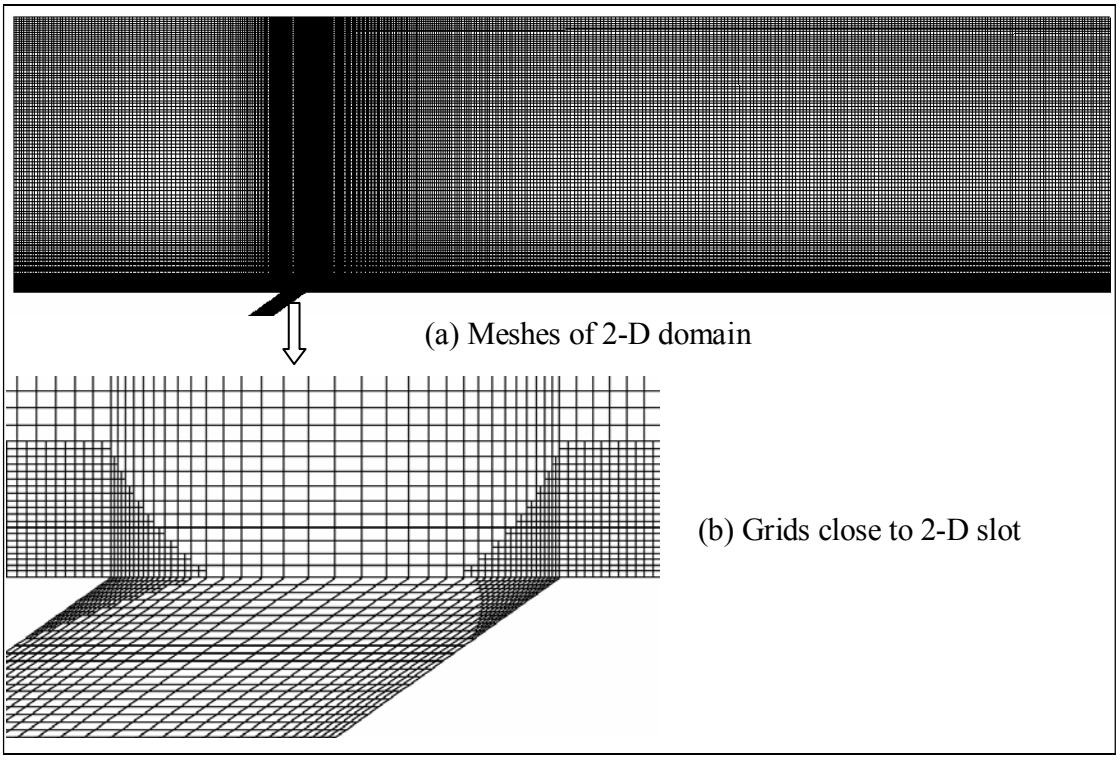

Figure 3 Computational Meshes

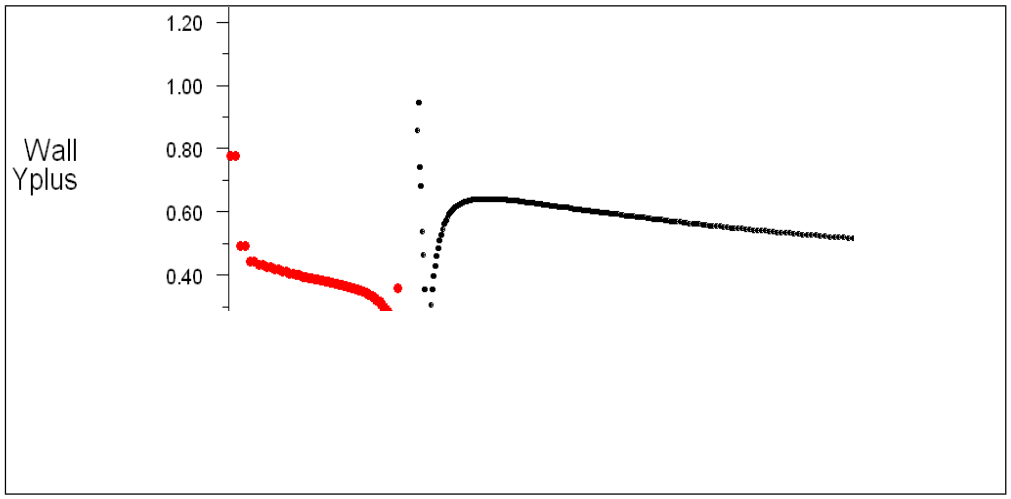

Figure 4 Y+ distribution of the first mesh near the wall

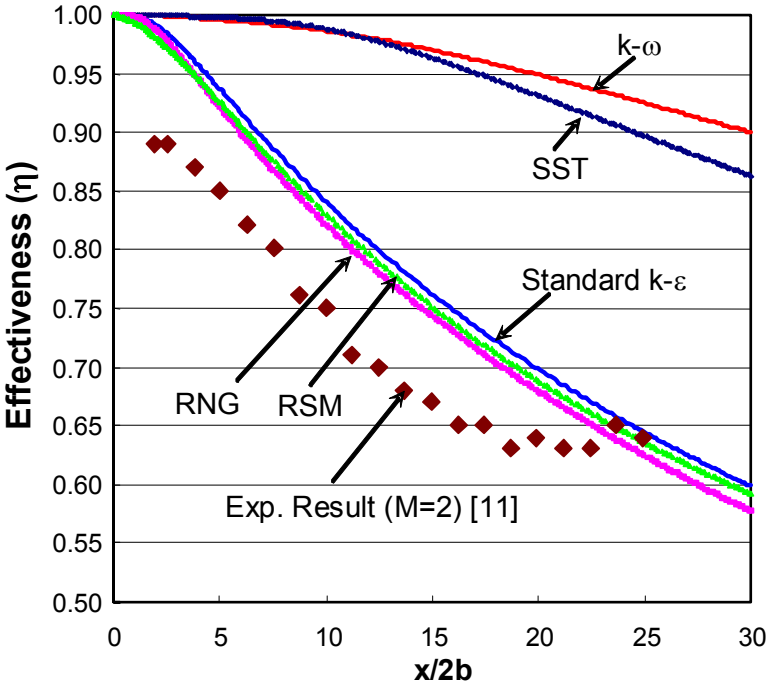

Figure 5 Effect of turbulence models on single-phase film cooling performance (Li and Wang [15])

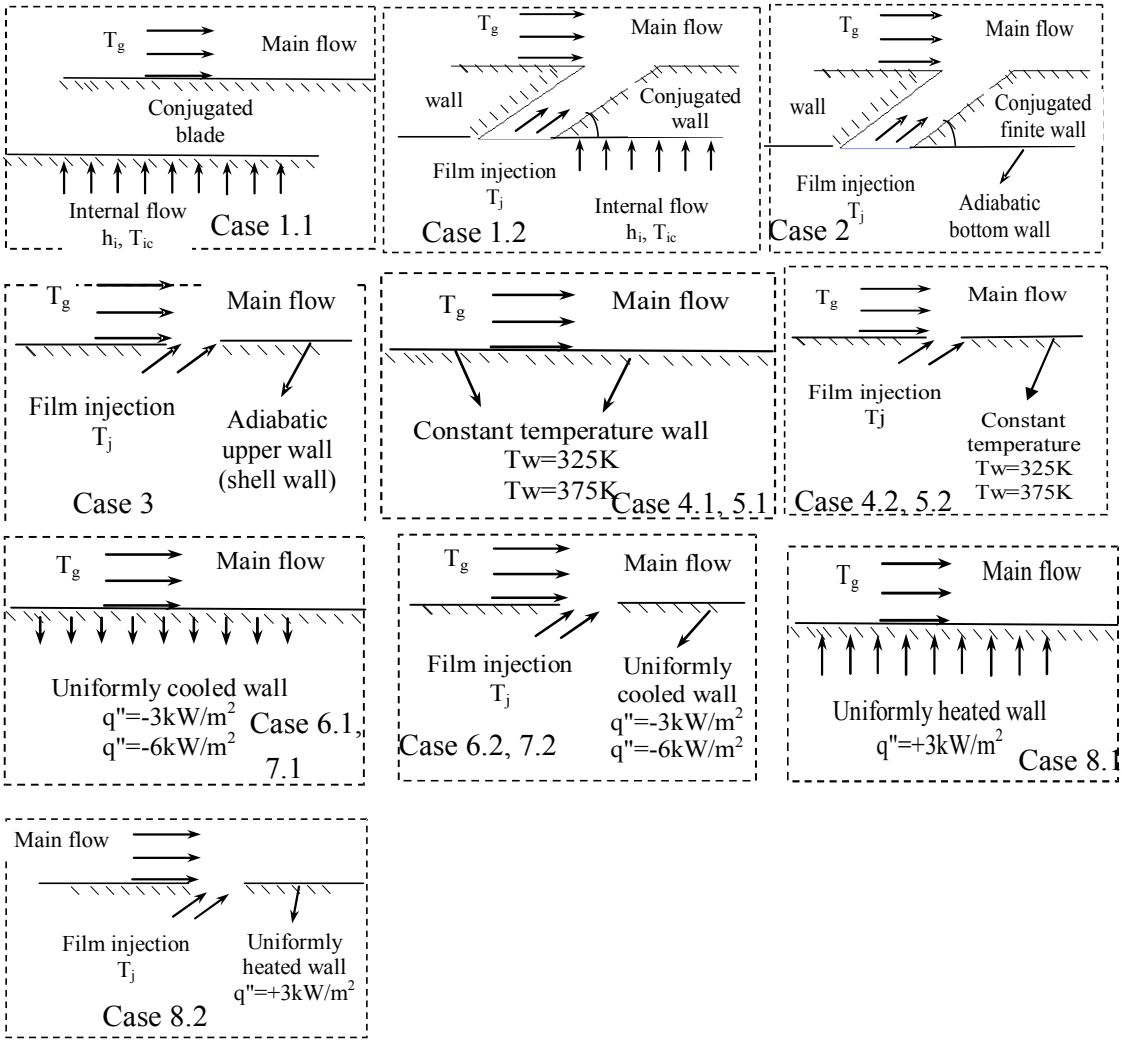

Figure 6 Illustrations of boundary condition set-up for different cases

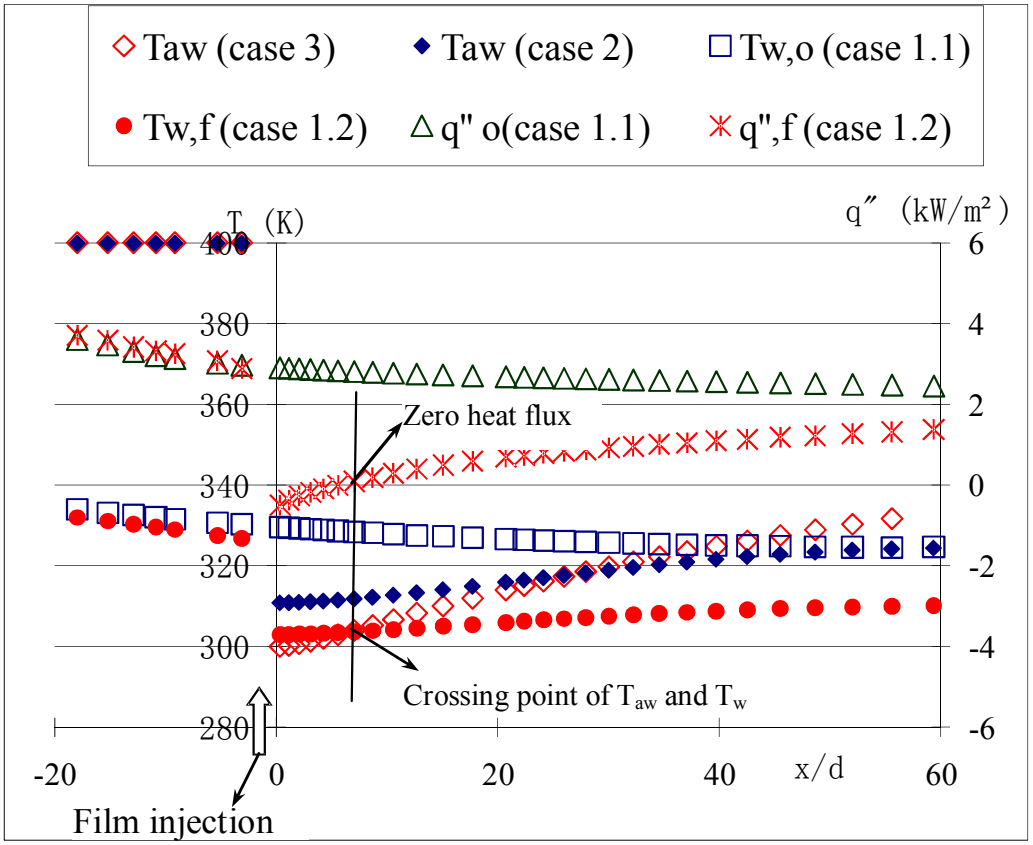

Figure 7 Wall surface temperature and heat flux distributions for Cases 1.1, 1.2, 2 and 3 for discussion of T_{aw}.

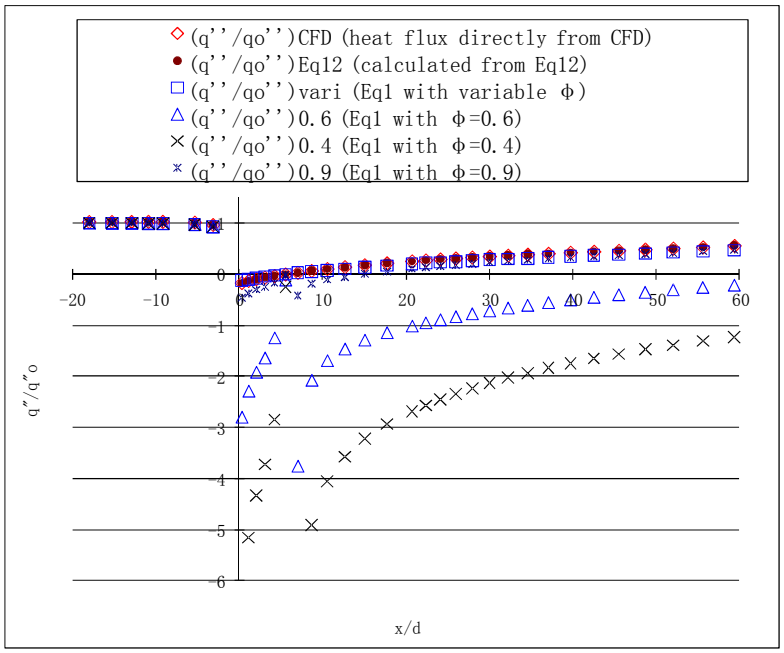

(a)

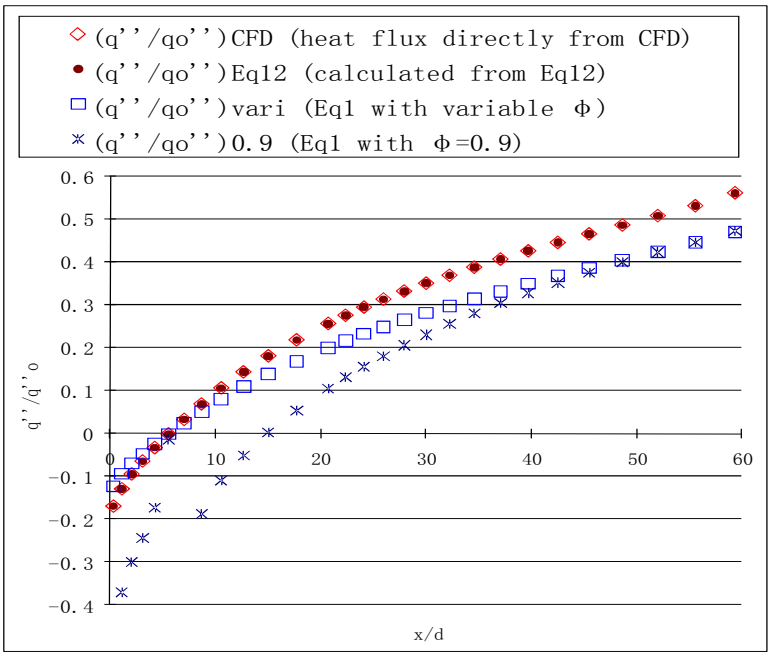

(b)

Figure 8 (a) Heat flux ratio (HFR) comparison between CFD predicted results and calculated results via Eq. 1. (b) An enlarged view of HFR (q"/q"$_o$) distributions to show four closely agreed cases and the region of heat flux direction reversal

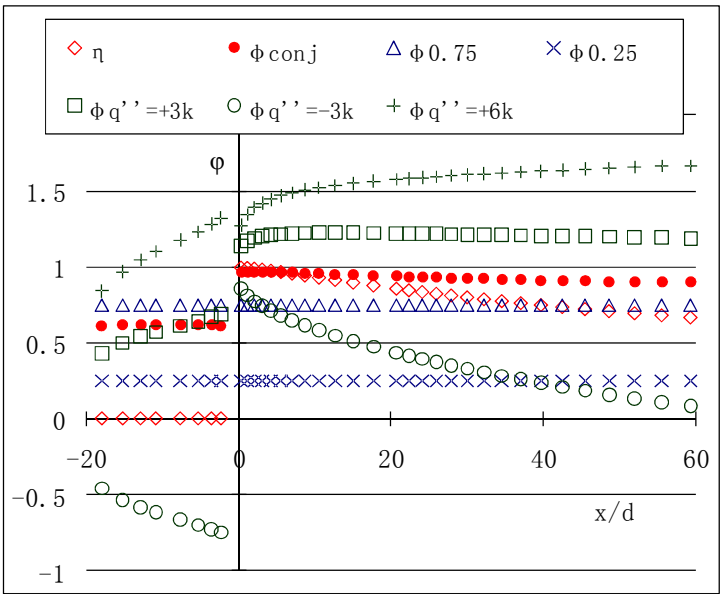

(a)

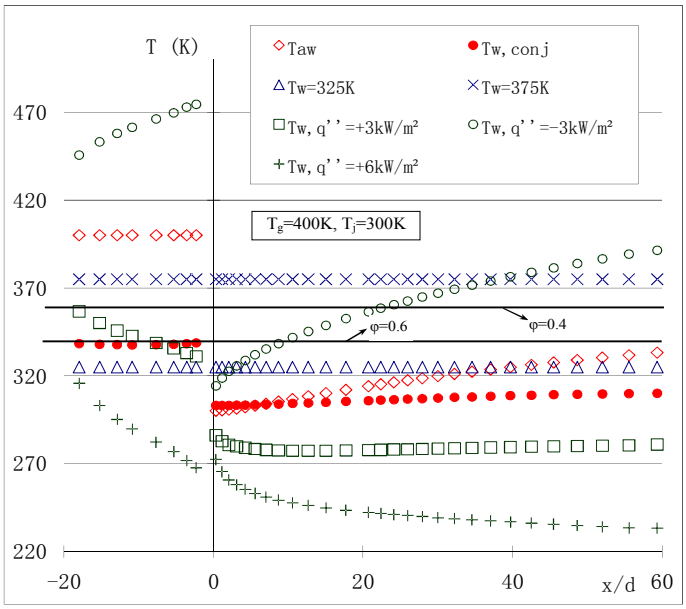

(b)

Figure 9 (a) Adiabatic film temperature and wall temperature (b) Film cooling effectiveness (φ) and Adiabatic film cooling effectiveness (η) under different wall conditions. Cases of φ = 0.4 and 0.6 correspond to T_w = 360K and 340K respectively. Their values can be easily represented by horizontal lines in both figures, so they are not shown to make the figure clearer.

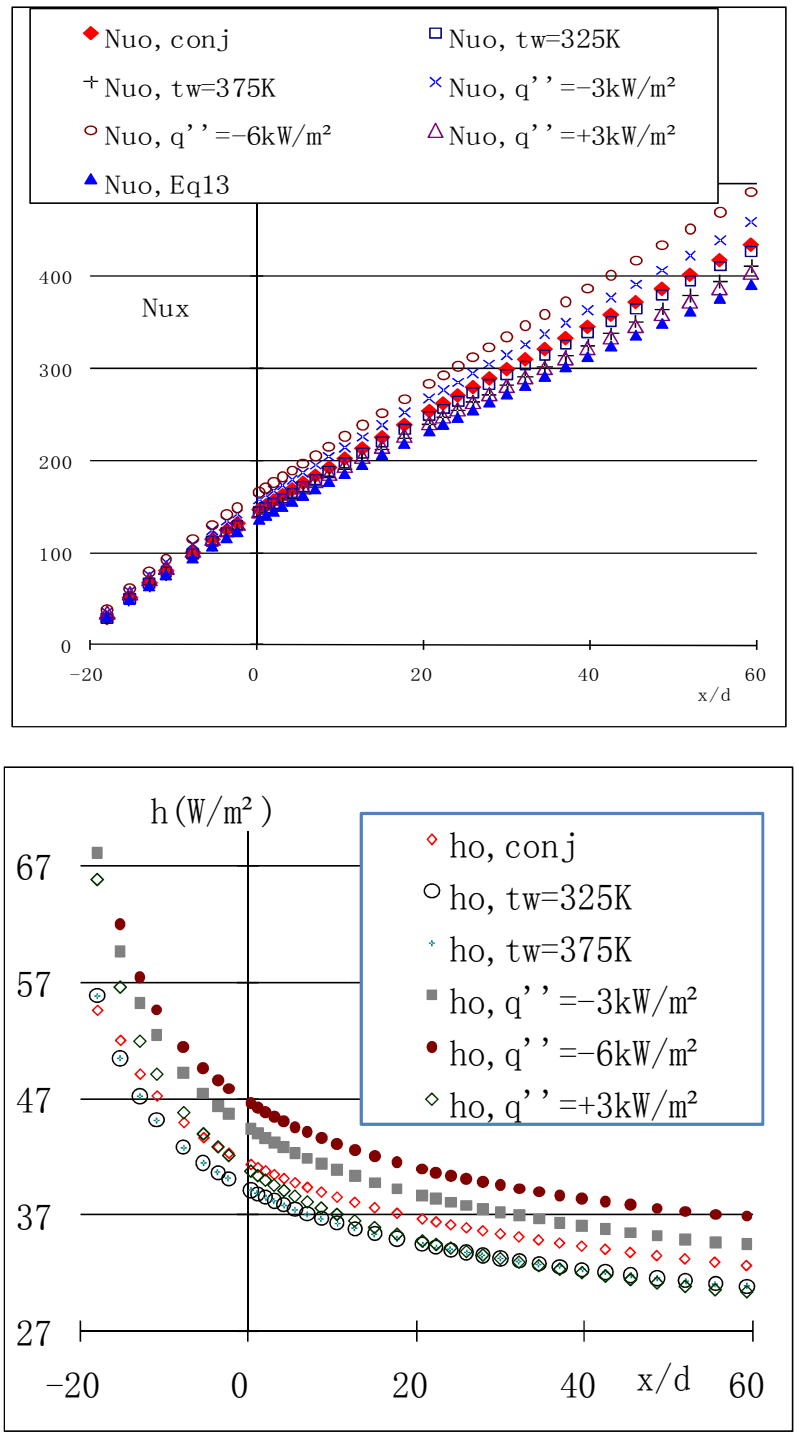

Figure 10 Heat transfer coefficient of without-film cases (a) Nu (b) h-value

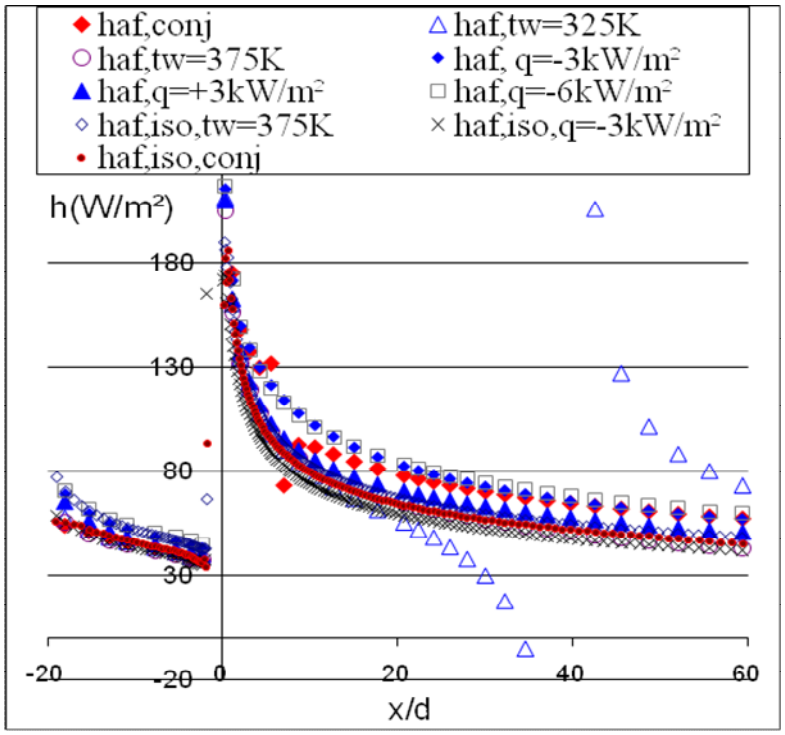

(a) h_{af} comparison

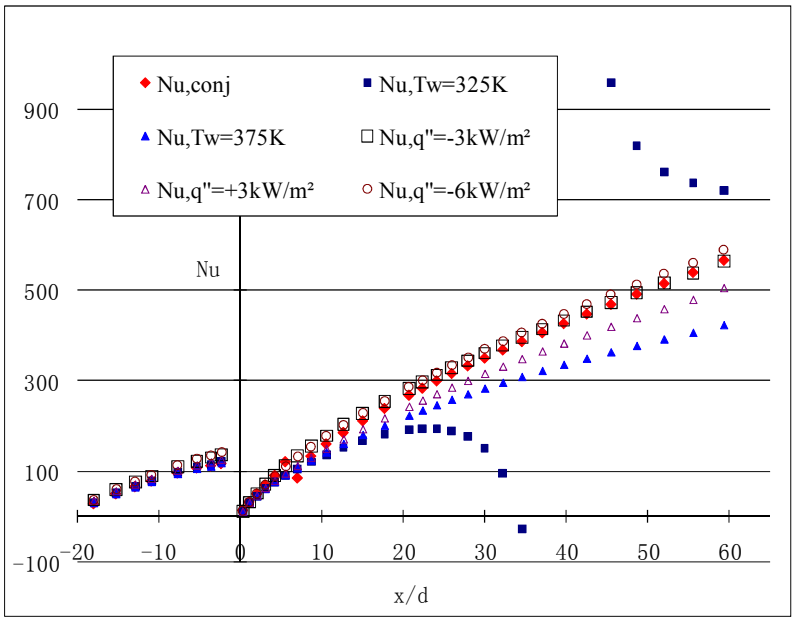

(b) Nu comparison

Figure 11 Comparisons of cases of different boundary conditions: (a) h_{af}, (b)Nu

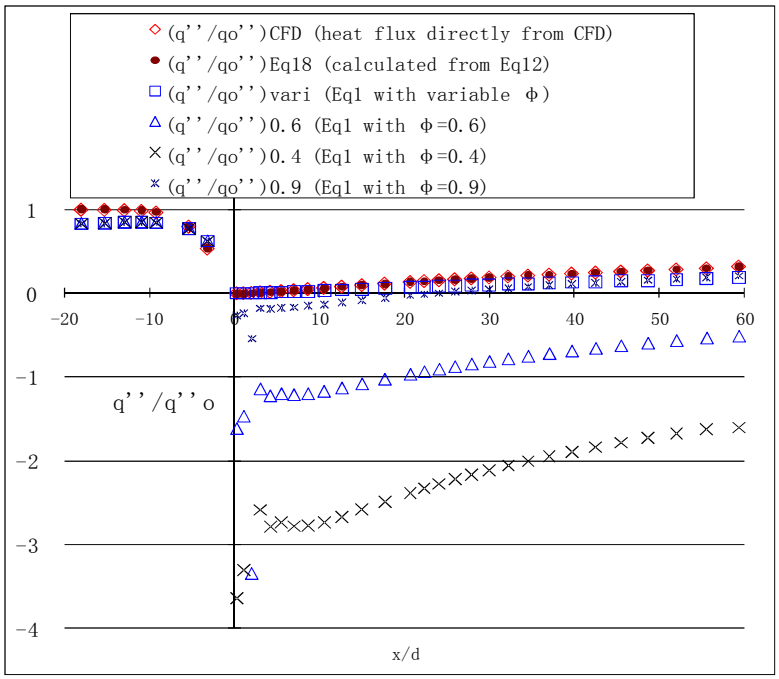

Figure 12 Heat flux ratio (HFR) comparison between CFD results under engine condition and calculated results via Eq. 1.

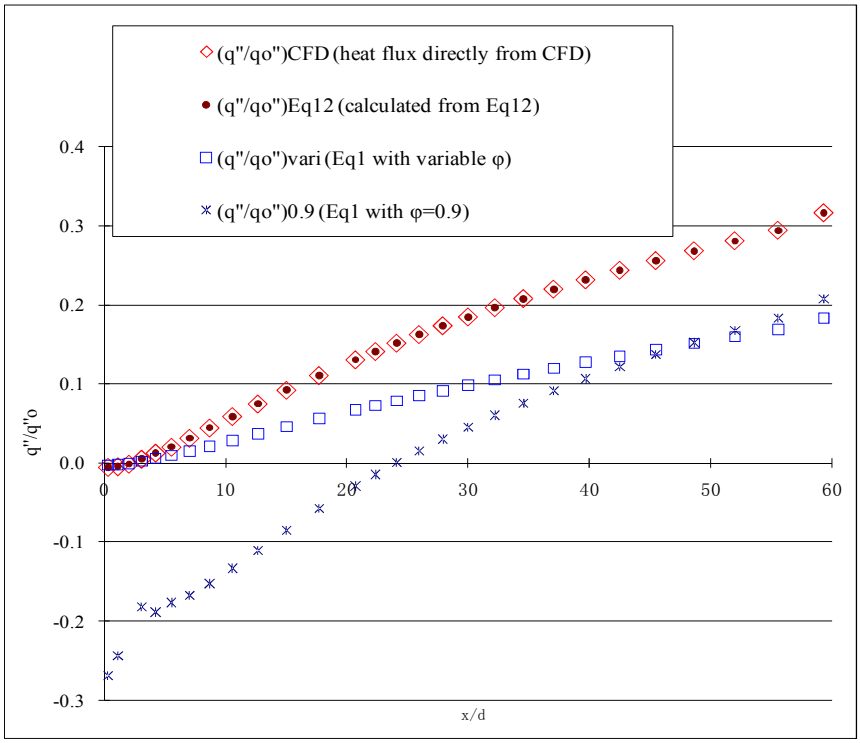

Figure 13 Enlarged view of HFR (q"/q"$_o$) distributions to show four closely agreed cases and the region of heat flux direction reversal

APPENDIX C
EVALUATION OF THE EFFECT OF THE TEST SECTION OPEN-TOP DESIGN

As mentioned in the Test Section Setup section of Chapter 2, an open-top design for the test section is implemented. In order to verify that the effects of the open top will not disturb the main flow uniformity, a Pitot tube is used to measure the flow profile in the opening area. A stand is built to hold the Pitot tube hanging from the top to measure the flow velocity at five locations from X/D = 8 to X/D = 40. For each stream-wise location, six measurement points in the vertical direction (Y-direction) are monitored. The reference point for the vertical direction, Y/D = 0, is set at the top surface of the test section top plate. Two points (Y/D = -2 and -4) are measured inside the test section and three are outside (Y/D = 1.5, 3, and 4). The measurement set up is illustrated in Fig. C-1.

As shown in the velocity profile plotted in Fig. C-2, an entrainment type flow is recognized. At X/D < 16, which is the most important area in this study, the flow inside the test section is barely disturbed. The entrainment flow is hardly discernable and limited to about 1.5D above the top plate of the test section. At X/D = 24 and beyond , entrainment flow is detected at the height of the top plate and at about 1 inch (4D) above the top plate height, but it decays quickly to zero. Thus, it is concluded that the open-top design does not alter the main flow uniformity significantly. As also mentioned in Chapter 2, since this study investigates the difference between the film cooling effectiveness of mist and air-only flow, this minor flow mixing over the open-top region is not critical as long as the flow inside the duct is identical from experiment to experiment.

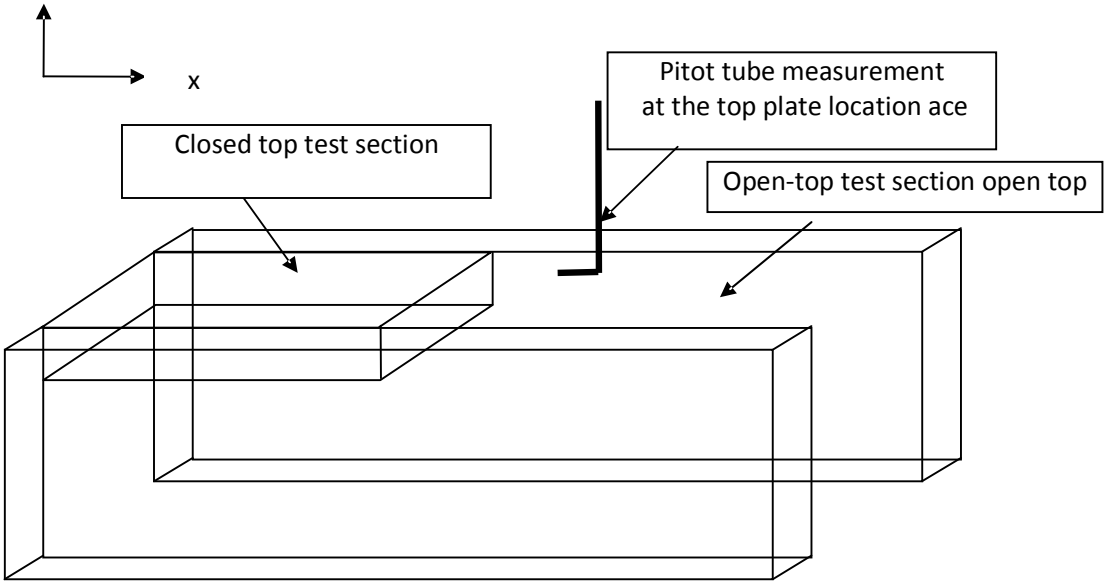

Figure C-1 Illustration of the open-top test section design

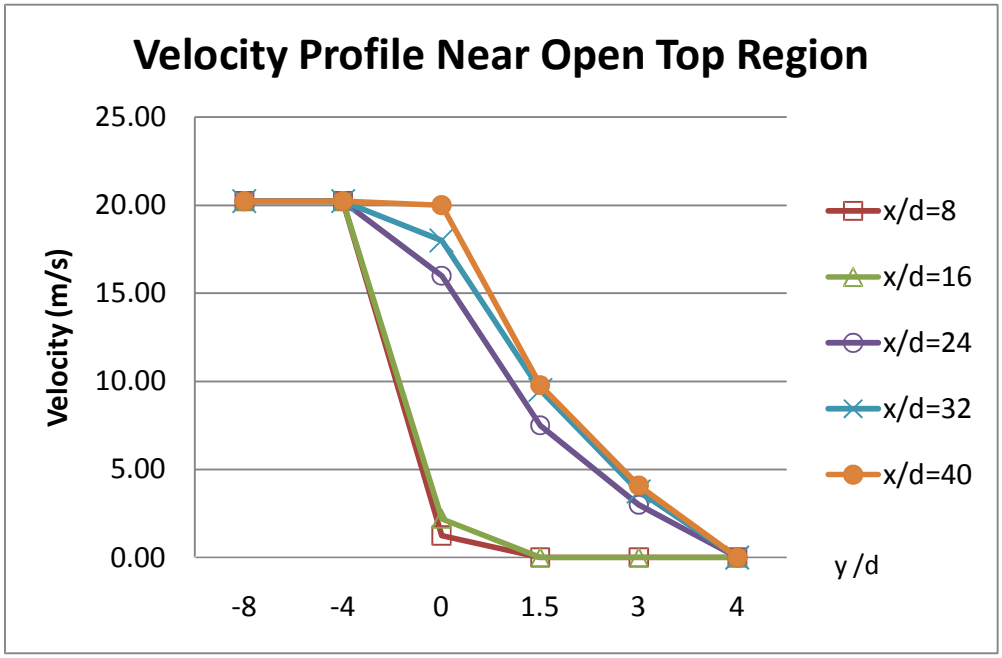

Figure C-2 Velocity profile near open top region

VITA

Lei Zhao received his Bachelor of Science degree from the University of Science and Technology of China, Hefei, China in 2005. He joined the Master's program in the Mechanical Engineering Department of the University of New Orleans in Fall 2006 and received his M.S. degree in 2008. Then he continued his Ph.D. study under the supervision of Dr. Ting Wang working on an experimental study of mist/air film cooling with application in gas turbine airfoils. He received his Ph.D. degree in May, 2012.